Regimes and scaling laws for convection with and without rotation

Robert S. Long

Submitted in accordance with the requirements for the degree of
Doctor of Philosophy

The University of Leeds

EPSRC Centre for Doctoral Training in Fluid Dynamics

February 2021

Declaration

The candidate confirms that the work submitted is his own, except where work which has formed part of jointly authored publications has been included. The contribution of the candidate and the other authors to this work has been explicitly indicated below. The candidate confirms that appropriate credit has been given within the thesis where reference has been made to the work of others.

The work presented in Chapter 3 resulted in the following publication (Long et al., 2020b)

- **Long, R.S.**, Mound, J.E., Davies, C.J., Tobias, S.M. 2019 Thermal boundary layer structure in convection with and without rotation. *Physical Review Fluids* (2020)

Robert Long conducted the simulations, performed the analysis and wrote the article while Jon Mound, Chris Davies and Steven Tobias undertook standard advisory roles.

The work presented in Chapter 4 resulted in the following publication (Long et al., 2020a)

- **Long, R.S.**, Mound, J.E., Davies, C.J., Tobias, S.M. 2020 Scaling behaviour in spherical shell rotating convection with fixed-flux thermal boundary conditions. *Journal of Fluid Mechanics* (2020)

A subset of numerical models used in this work were ran by Jon Mound and Chris Davies. Robert Long ran additional simulations, performed the analysis and wrote the article while Jon Mound, Chris Davies and Steven Tobias undertook standard advisory roles.

Acknowledgements

First and foremost I want to thank my supervisory team of Jon Mound, Chris Davies and Steven Tobias all of whom played a pivotal role in my success and development as a scientist. I would like to thank Jon for his never-ending knowledge of all things geophysics and good humour, Chris for his boundless enthusiasm, and last but not least Steve for his continuous support and quick one liners. To all three of you, I am extremely grateful for being allowed to pursue my own ideas while being there to offer support and advice when I faltered.

I would like to thank Jon Aurnou for his hospitality during my research visit to UCLA and Jewel Abbate for being a great lab partner when working on *Calimero*. I also owe thanks to Carolina Lithgow-Bertelloni for being very generous with her time and the wider Crust2Core crew for embracing me as one of their own.

I acknowledge the EPSRC Centre for Doctoral Training in Fluid Dynamics (grant number EP/L01615X/1) for the studentship funding my studies and additional funding allowing me to attend conferences. I want to thank Peter Jimack for his attentiveness and availability throughout my time in the CDT. I am grateful for further funding from the RAS, SEDI, IPGP, and the Leeds for Life foundation to support with travel to international conferences. I would also like to thank UKSEDI and the UKFN for financial aid in attending multiple national meetings.

During my time at Leeds I have been spoilt by having both the Deep Earth research group and the Astro- geophysical fluid dynamics group. Thanks to everyone for your contagious enthusiasm from which I have gained excitement for many fields outside of my own work!

I need to give a special shoutout to my Leeds drinking buddies Colin, Josh, Andy, Eva and Tom, and all of the students and academics from ETH, Paris, and beyond who have made every conference fun and memorable!

Abstract

The geodynamo is maintained by turbulent rotating convection in Earth's liquid iron outer core. Core dynamics are inaccessible to direct measurement and our understanding comes from a combination of observations, theoretical arguments, laboratory experiments and numerical simulations. The vast range of spatial and temporal scales present prevent numerical or physical experiments from being able to reproduce the convective state of Earth's core exactly. This motivates systematic studies in which we attempt to understand the fundamentals of convection over the broad range of accessible parameter space with a view to identifying asymptotic behaviour; if such behaviour is found, then this could allow extrapolation to Earth's core values.

We present a combined numerical-laboratory survey of hydrodynamic convection to elucidate the role of different boundary conditions, geometries and the influence of rotation over a wide range of parameter space. We focus on transitions in thermal convection with a particular interest in the constraining effects of rotation.

The transition from rapidly rotating to weakly rotating convection is hypothesised to be controlled by the thermal boundary layers. Using plane-layer Rayleigh-Bénard convection simulations we determine a robust definition of the thermal boundary layer which can be used for non-rotating or rotating convection with different thermal boundary conditions. Different physical regimes of convection are identified in a rotating spherical shell by correlating changes in both local and global flow diagnostics. We identify a regime of quasi-geostrophic turbulence which may be relevant to describing the dynamics of Earth's core.

Laboratory experiments and local plane-layer simulations are thought to be analogues for convection in the polar region of a spherical shell and unsurprisingly these modelling approaches do not agree with full spherical shell calculations. In an attempt to unify these different modelling approaches we harvest a fluid region at high latitude and are able to explicitly show good agreement between experiments and local simulations with polar convection. Ultimately this work provides a platform to investigate convection in a regime which bridges that of Earth's core.

Contents

1 Introduction **1**
1.1 The structure of Earth's interior . . . 1
1.2 Force balances of the geodynamo . . . 3
1.2.1 Dynamo simulations . . . 6
1.3 Convection studies . . . 8
1.3.1 Rayleigh-Bénard convection . . . 9
1.3.2 Rotating Rayleigh-Bénard convection . . . 14
1.3.3 Spherical shell rotating convection . . . 19
1.4 Summary . . . 24
1.5 Project aims and thesis outline . . . 26

2 Theory and Numerical Implementation **29**
2.1 Boussinesq approximation . . . 29
2.2 Plane layer convection . . . 30
2.2.1 Governing equations . . . 30
2.2.2 Boundary conditions . . . 33
2.2.3 Numerical implementation . . . 34
2.2.4 Convergence criteria . . . 38
2.3 Spherical shell convection . . . 41
2.3.1 Governing equations . . . 41
2.3.2 Boundary conditions . . . 42
2.3.3 Numerical implementation . . . 42
2.3.4 Convergence criteria . . . 44
2.4 Statistical methods . . . 45
2.5 Summary . . . 46

3 Defining the thermal boundary layer in convection with and without rotation **47**
3.1 Introduction . . . 47
3.1.1 Research question . . . 50
3.2 Defining the thermal boundary layer . . . 51
3.2.1 Established methods . . . 51
3.2.2 Crossover in heat transport contributions . . . 52
3.2.3 On the validity of two dimensional Rayleigh-Bénard convection . . . 52
3.3 Thermal boundary layer thickness . . . 54

3.3.1 Influence of thermal boundary conditions . . . 55
3.3.2 Prandtl number dependence . . . 56
3.3.3 Effects of including rotation . . . 56
3.4 Conclusions . . . 59

4 Dynamical Regimes and Scaling Behaviour of Rotating Convection 63
4.1 Introduction . . . 63
4.1.1 Rayleigh-Bénard convection . . . 64
4.1.2 Spherical shell convection . . . 65
4.1.3 Research question . . . 66
4.2 Scaling law analysis; theoretical predictions . . . 67
4.2.1 Diagnostic measurements . . . 67
4.2.2 Flow speeds and length scales . . . 69
4.2.3 Mechanical boundary layers . . . 72
4.2.4 Heat transfer and thermal boundary layers . . . 72
4.2.5 Transition parameters . . . 73
4.3 Regimes of rotating convection . . . 74
4.3.1 Non-rotating regime . . . 75
4.3.2 Transitional regime . . . 79
4.3.3 Weakly nonlinear regime . . . 81
4.3.4 Rapidly rotating regime . . . 83
4.3.5 Convective mixing . . . 88
4.3.6 Composite scaling laws . . . 90
4.4 Conclusions . . . 91

5 A comparison of numerical and laboratory models of convection in the polar region 95
5.1 Introduction . . . 95
5.1.1 Nusselt number scaling . . . 98
5.1.2 Reynolds number scaling . . . 99
5.1.3 Research question . . . 100
5.2 Experimental procedure . . . 100
5.2.1 Thermometry . . . 101
5.2.2 Laser Doppler Velocimetry (LDV) . . . 106
5.2.3 Visualisations . . . 107
5.3 Harvesting a local cylinder from the spherical shell . . . 107
5.4 Scaling laws for heat and momentum transport . . . 108
5.4.1 Non-rotating convection . . . 108
5.4.2 Rotating convection . . . 110
5.5 Conclusions . . . 116

6 Conclusion 119
6.1 Project aims . . . 119

6.2 Simplifying assumptions 122
6.3 Future extensions 124
6.4 Final thoughts 126

A Model Database - Summary of Simulations **127**
A.1 Spherical shell simulations 127
A.2 Plane layer simulations 130

List of Figures

1.1 Schematic showing the structure of Earth's interior . . . 2
1.2 1-D density structure of the Earth given by PREM . . . 3
1.3 Visualisation of an extreme dynamo . . . 6
1.4 Schematic of plane layer, cylindrical and spherical shell convection configurations . . . 8
1.5 Temperature distribution for conduction and fully convective Rayleigh-Bénard convection . . . 10
1.6 Laboratory Rayleigh-Bénard convection heat transfer data shown in $Nu - Ra$ space . . . 11
1.7 Laboratory Rayleigh-Bénard convection flow speed data shown in $Re - Ra$ space . . . 13
1.8 Critical Rayleigh number and onset wavenumber versus Ekman number for rotating Rayleigh-Bénard convection with no-slip boundary conditions . . . 15
1.9 Temperature distribution for rotating Rayleigh-Bénard convection in the rotationally constrained and weakly rotating regimes . . . 16
1.10 Rotating Rayleigh-Bénard convection heat transfer data shown in $Nu - Ra$ space . . . 17
1.11 Morphology of rapidly rotating convection at onset when $Pr \sim \mathcal{O}(1)$ . . . 20
1.12 Rotating spherical shell convection heat transfer data shown in $Nu - Ra$ space . . . 21
1.13 Heat transfer scaling exponents for rotationally constrained convection in plane layer and spherical shell geometries . . . 22
1.14 Summary of rotating convection regimes for plane layer and spherical shell geometries . . . 24

2.1 RBC cell illustrating fixed temperature and fixed heat-flux thermal boundary conditions . . . 32
2.2 Examples of a uniformly spaced grid and one defined by the zeroes of the chebyshev polynomials . . . 37
2.3 Trace of kinetic energy for RBC showing typical averaging period . . . 39
2.4 Convergence criteria illustrated for non-rotating RBC simulations . . . 40
2.5 A schematic of poloidal and toroidal fields in a spherical shell . . . 43

3.1 Methods of defining the thermal boundary layer shown for Rayleigh-Bénard convection with fixed temperature boundaries . . . 49

3.2 Comparison of the different methods to define thermal boundary layer thickness applied to 2D and 3D Rayleigh-Bénard convection 54
3.3 Heat transfer data for 2D Rayleigh-Bénard convection with different different thermal boundary conditions shown in $Nu - Ra$ space 56
3.4 Thermal boundary layer thickness versus Rayleigh number for non-rotating Rayleigh-Bénard convection 57
3.5 Methods of defining the thermal boundary layer shown for Rayleigh-Bénard convection with fixed heat-flux boundaries 58
3.6 Nusselt number and thermal boundary layer thickness for Rayleigh-Bénard convection with varying Pr 59
3.7 Methods of defining the thermal boundary layer shown for rotating Rayleigh-Bénard convection with fixed temperature boundaries 60
3.8 Nusselt number for rotating Rayleigh-Bénard convection with free-slip boundaries 61
3.9 Boundary layer thickness and temperature drop versus Rayleigh number for rotating Rayleigh-Bénard convection 62

4.1 Methods of defining the viscous and thermal boundary layers 70
4.2 Heat transfer data for our rotating spherical shell simulations shown in $Nu - Ra$ space 75
4.3 Contours of radial velocity qualitatively showing regimes of rotating spherical shell convection 76
4.4 Scaling behaviour of the Nusselt number, Reynolds number, convective length scale and viscous boundary layer thickness for transitional models with $E \geq 10^{-4}$ 78
4.5 Nusselt number compensated by its non-rotating scaling behaviour versus parameters proposed to control the transition away from rapidly rotating convection 80
4.6 Reynolds number and convective length scales compensated by their non-rotating scaling behaviours versus the transition parameter, $RaE^{8/5}$ 81
4.7 Heat transfer data in the weakly nonlinear regime shown in $Nu - Ra/Ra_c$ space 82
4.8 Convective length scale and Reynolds number versus VAC predictions for models in the weakly nonlinear regime 83
4.9 Convective length scale and Reynolds number versus IAC predictions for models outside of the weakly nonlinear regime 85
4.10 Viscous boundary layer thickness versus Ekman number shown for models in the rapidly rotating regime 86
4.11 Radial profiles of average temperature for different values of $RaE^{8/5}$ 89
4.12 Convective mixing efficiency quantified by the internal temperature gradients and internal temperatures 89
4.13 Thermal boundary layer thickness versus Nusselt number 90

4.14 Diagram summarising the regimes of rotating convection shown in Ra/Ra_c-E space 92

5.1 Schematic linking local and global models 98
5.2 Heat transfer comparison of local and global plotted in $Nu-Ra$ space . . . 99
5.3 Photograph and schematic of the laboratory experiment 'Calimero' 102
5.4 Schematic of the thermometry setup 104
5.5 Trace of temperature for an experimental run 105
5.6 Trace of velocity for an experimental run 106
5.7 Visualisations of laboratory convection 107
5.8 Visualisation of the polar harvest 108
5.9 Heat transfer of polar convection shown in $Nu-Ra$ space 109
5.10 Flow speeds of polar convection shown in $Re-Ra$ space 111
5.11 Heat transfer and flow speed data for rotating polar convection 113
5.12 Heat transfer scaling exponents for polar convection 116

6.1 Regime diagram placing Earth's core 121

List of Tables

1.1 Physical parameters and their values relevant for Earth's core 4
1.2 Non-dimensional parameters relevant for a convective dynamo 5
1.3 Summary of the heat transport and flow diagnostics in Rayleigh-Bénard convection 14
1.4 Summary of the heat transport and flow diagnostics in rotating Rayleigh-Bénard convection and rotating spherical shell convection 25

4.1 Parameters proposed to capture the boundary between the rapidly rotating and transitional regimes of convection 73
4.2 Nusselt-Rayleigh scaling exponents as a function of the Ekman number in the steep heat transfer regime 84
4.3 Parameters of the linear regression to the viscous boundary layer thicknesses 87
4.4 Summary of scaling behaviour for rotating spherical shell convection 94

5.1 Dimensionless parameters governing rotating convection - accessible parameter regimes for laboratory experiments and numerical simulations 97
5.2 Physical properties of water at 20 °C 101
5.3 Heat transfer scaling exponent for rotating polar convection 112
5.4 Flow speed scaling exponent for rotating polar convection 114

A.1 Summary of rotating spherical shell simulations - I 128
A.2 Summary of rotating spherical shell simulations - II 129
A.3 Summary of two-dimensional non-rotating convection simulations with fixed temperature thermal boundary conditions. 130
A.4 Summary of two-dimensional non-rotating convection simulations with fixed heat-flux thermal boundary conditions. 130
A.5 Summary of three-dimensional rotating convection simulations with Ekman number, $E = 10^{-7}$. The boundaries are stress-free and prescribed fixed temperature thermal boundary conditions. 131

Chapter 1

Introduction

All planets in the solar system, with the exception of Venus have, or once had intrinsic magnetic fields. For the Earth, records of the paleomagnetic data show that the geomagnetic field has persisted for the past 3.5 billion years (e.g. Tarduno et al., 2010) and possibly as long as 4.2 billion years (Tarduno et al., 2015). If not actively generated, the magnetic field would decay over a period of $\sim 10^4$ years, a magnetic diffusion time (Glatzmaier and Coe, 2007). The generation of magnetic field is believed to occur within the Earth's interior (Gauss, 1877) however the deep interior is too hot to maintain permanent magnetisation as minerals are above their Curie temperature (Stacey and Davis, 2008). So what is the responsible mechanism? Larmor (1919) suggested self-excited dynamo action where electrical currents are induced by the motions of liquid metals deep within the Earth.

This chapter introduces the source region of the geomagnetic field and the underlying mechanisms, and gives the geophysical context for this work. We briefly describe the structure of Earth's interior and consider the force balances theorised to exist in Earth's core. Next, we introduce the different model approaches often used to investigate core dynamics and end with a review of the heat and momentum transfer in these model systems.

1.1 The structure of Earth's interior

Earth's deep interior is inaccessible to direct measurements and much of our understanding comes from the seismic profile of the Earth. In the early 20th century seismologists observed a distinct pattern in the distribution of shear wave (S-wave) arrivals after large earthquakes and deduced that the Earth has a fluid metallic core (Jeffreys, 1926). Consequent seismic observations revealed that within the molten fluid core there exists a solid inner core (Lehmann, 1936). This inner core is gradually crystallising outwards due to the secular cooling of the whole planet (e.g. Jacobs, 1953; Shimizu et al., 2005).

Earth's deep interior is comprised of three main regions: at the centre, a solid iron inner core; above that the liquid metal outer core and the outermost 'solid' mantle (shown in figure 1.1). The 1-D density structure of the Earth according to the Preliminary Reference Earth Model (PREM, Dziewonski and Anderson, 1981) is shown in figure 1.2. Through the mantle PREM shows increasing seismic velocity with increasing depth and the boundary layer between the silicate mantle and liquid core is termed the D" region. The large velocity contrast across the core-mantle boundary (CMB) arises due to the transition from silicate rocky mantle to the dense iron alloy of the core, with the latter comprising of $\sim$ 85% iron, $\sim$ 5% nickel and some lighter elements (e.g. McDonough and Sun, 1995; Bazhanova et al., 2017). The shear–wave velocity is zero in the outer core because liquids cannot support shear waves. The density contrast across the inner-core boundary (ICB) corresponds to the solid-liquid interface where light elements are incorporated into the liquid phase as the inner core crystallises (e.g. Braginsky, 1963; Alfe et al., 2000). The outer core fluid is then enriched in light elements relative to the inner core, resulting in a denser iron-nickel solid core.

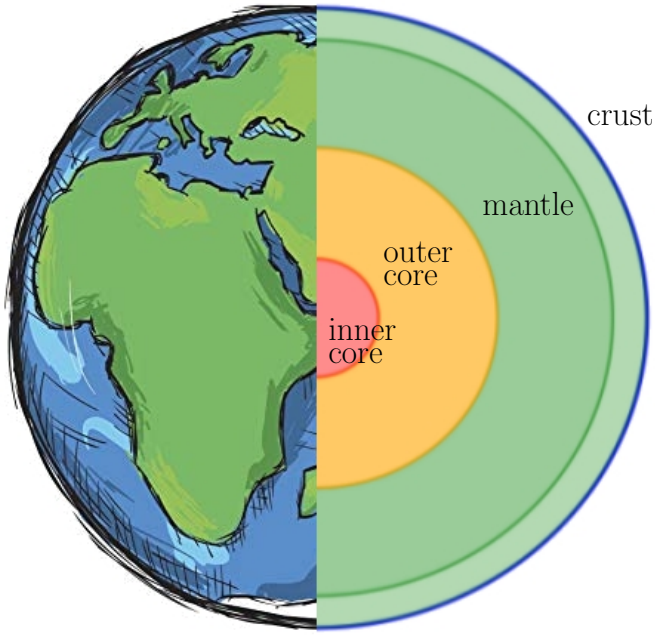

Figure 1.1: A schematic showing the structure of Earth's interior.

The liquid iron outer core is thought to have a low viscosity (similar to that of water at room temperature and pressure) at the high temperatures and pressures in Earth's core (de Wijs et al., 1998; Pozzo et al., 2013). The presence of the planetary scale magnetic field suggests that the liquid iron is undergoing vigorous motion with the primary driver thought to be convection resulting from both thermal and compositional effects (Gubbins and Roberts, 1987). Latent heat released at the ICB as the inner core freezes (e.g. Olson, 2007) and heat extracted by the mantle at the CMB drive thermal convection. The constituent elements, e.g. silicon, oxygen, hydrogen (e.g. Umemoto and Hirose, 2020) which are less dense than the ambient are precipitated into the core fluid at

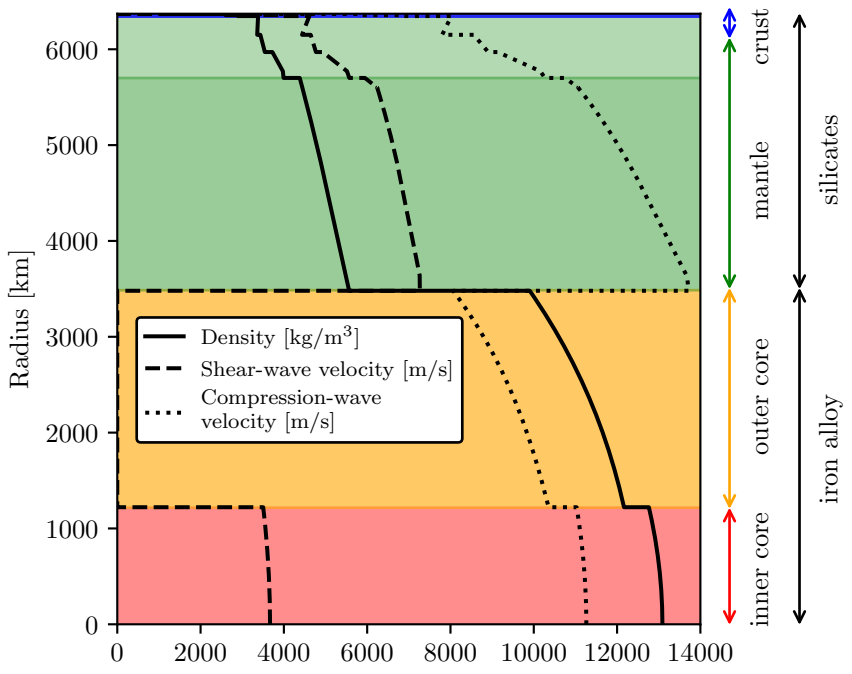

Figure 1.2: 1-D density structure of the Earth according to PREM (Dziewonski and Anderson, 1981). The shear and compression wave velocities along with density are shown as a function of radius. The different colours correspond to the different regions within Earth's interior and the mantle has two sub-regions seperated by a discontinuity at a depth of 660 km. The colours correspond to the same regions as in figure 1.1.

the ICB and rise up through the core leading to a source of compositional buoyancy. It is currently unclear about the proportionate contributions of thermal and compositional buoyancy (Lister and Buffett, 1995; Gubbins, 2001). Convection is the likely candidate for sustaining the geodynamo as it can provide an adequate source of power on a suitable timescale, which is not realised for other suggested mechanisms such as precession for tidal forcing.

1.2 Force balances of the geodynamo

The dynamo process in Earth's outer core, responsible for converting kinetic energy to magnetic energy, evolves subject to the physical laws of magnetohydrodynamics; consisting of the pre-Maxwell equations of electrodynamics, Ohm's law for a moving conductor and the conservations laws for momentum, mass and energy. In this section, we focus on just the momentum equation (with the other equations introduced in chapter 2) and investigate different possible force balances which could be responsible for governing the dynamics of Earth's core.

In dimensionless form, conservation of momentum is expressed by the Navier-

Stokes equation,

$$\underbrace{\frac{E}{Pr}\left[\frac{\partial \boldsymbol{u}}{\partial t}+(\boldsymbol{u}\cdot\boldsymbol{\nabla})\,\boldsymbol{u}\right]}_{\text{inertia}}+\underbrace{\mathbf{1}_z\times\boldsymbol{u}}_{\text{Coriolis}}=\underbrace{-\boldsymbol{\nabla}P}_{\text{pressure}}+\underbrace{E\nabla^2\boldsymbol{u}}_{\text{viscosity}}+\underbrace{\Lambda\boldsymbol{\nabla}\times\boldsymbol{B}\times\boldsymbol{B}}_{\text{Lorentz}}+\underbrace{RaET'\boldsymbol{r}}_{\text{Archimedean}}\,, \quad (1.1)$$

where $\boldsymbol{u}$ is the fluid velocity, P is pressure, T' is the temperature fluctuation about some steady state background profile, $\mathbf{1}_z$ is the unit vector that points in the direction of the rotation vector $\boldsymbol{\Omega}=\Omega\mathbf{1}_{\boldsymbol{z}}$, and gravity acts radially (with unit vector in the radial direction, $\mathbf{1}_r$). We have scaled length with the thickness of the spherical shell, h, time by the thermal diffusion time, h^2/κ, temperature by the temperature drop across the fluid layer, ΔT, and the magnetic field by some characteristic strength, B_0. Combinations of physical quantities (table 1.1) give the non-dimensional parameters governing the system; the Ekman number, E, the Prandtl number, Pr, the Elsasser number, Λ, and the Rayleigh number, Ra, defined as the ratio of forces in equation (1.1). See table 1.2 for a summary of these parameters.

Quantity	Symbol	Value
kinematic viscosity	ν	$5\times10^{-7}\,\mathrm{m^2\,s^{-1}}$
thermal diffusivity	κ	$1.3\times10^{-5}\,\mathrm{m^2\,s^{-1}}$
outer radius	r_o	$3.48\times10^{6}\,\mathrm{m}$
inner radius	r_i	$1.22\times10^{6}\,\mathrm{m}$
shell thickness	h	$2.26\times10^{6}\,\mathrm{m}$
rotation rate	Ω	$7.29\times10^{-5}\,\mathrm{s^{-1}}$
typical flow velocity	U	$10^{-4}\,\mathrm{m\,s^{-2}}$
magnetic field strength	B_o	$1\,\mathrm{mT}$

Table 1.1: Physical parameters of Earth's core. All values are given in Jones (2015) except for U which is taken from Holme and Olson (2007).

For increasingly more vigorous convection, the magnetic field strength increases and this growth of the magnetic field leads to convection occurring on the scale of the fluid layer (e.g. Schwaiger et al., 2019). The Elsasser number, Λ, defined as the ratio of the Lorentz and Coriolis forces is then expected to equilibrate at $\sim\mathcal{O}(1)$ (Malkus, 1959). This is often referred to as the strong-field regime as the Lorentz force is much stronger than viscous and inertial forces (e.g. Hollerbach, 1996). A magnetic field with $\Lambda\sim\mathcal{O}(1)$ promotes convection and core dynamics are then theorised to be in a magnetostrophic state, where the leading order force balance in equation (1.1) is between Coriolis, pressure and Lorentz forces (e.g. Wu and Roberts, 2013; Tobias, 2019),

$$\mathbf{1}_z\times\boldsymbol{u}\sim-\boldsymbol{\nabla}P+\Lambda\boldsymbol{\nabla}\times\boldsymbol{B}\times\boldsymbol{B}.$$

To allow assessment based on data available from geomagnetic observations, Λ has tradi-

tionally been estimated using the following definition

$$\Lambda = \frac{B_0^2}{2\rho\mu\eta\Omega}, \tag{1.2}$$

where μ is the magnetic permeability and η is the magnetic diffusivity. Characteristic values for Earth's core yield $\Lambda \sim \mathcal{O}(1)$ which supports the picture of a magnetostrophic balance. Equation (1.2) does not include any information about the length scale or flow speed of convection and may inaccurately evaluate the magnitude of forces.

Quantity	Symbol	Meaning	Definition	Earth's core
Ekman number	E	$\frac{\text{viscosity}}{\text{Coriolis}}$	$\frac{\nu}{2\Omega h^2}$	10^{-15}
Prandtl number	Pr	$\frac{\text{viscous diffusion}}{\text{thermal diffusion}}$	$\frac{\nu}{\kappa}$	$0.01 - 1$
Elsasser number	Λ	$\frac{\text{Lorentz}}{\text{Coriolis}}$	$\frac{B_o^2}{2\mu\rho\eta\Omega}$	1
Rayleigh number	Ra	$\frac{\text{Archimedean}}{\text{diffusion}}$	$\frac{\alpha g \Delta T h^3}{\nu\kappa}$	10^{25}

Table 1.2: Non-dimensional parameters governing the dynamics of a convective dynamo. These parameters correspond to those in equation (1.1). All of the physical values are taken from table 1.1.

An alternative measurement for the ratio of the Lorentz to Coriolis forces was proposed by Soderlund et al. (2012) termed the dynamical Elsasser number:

$$\Lambda_d = \frac{B_0^2}{2\rho\mu\Omega U h}. \tag{1.3}$$

Characteristic values for Earth's core yield $\Lambda_d \sim \mathcal{O}\left(10^{-2}\right)$ indicating that the Lorentz force is subdominant to the Coriolis and pressure forces. This suggests that core dynamics may be controlled at leading order by a geostrophic balance, the balance of pressure and Coriolis forces,

$$\mathbf{1}_z \times \boldsymbol{u} \sim -\boldsymbol{\nabla} P, \tag{1.4}$$

instead of magnetostrophy. This is supported by observations of temporal variations in Earth's magnetic field. We observe that the Earth's magnetic field is largely dipolar and the dipole is roughly aligned with the rotation axis (offset by $\approx 11°$). This symmetry highlights the importance of Earth's rotation on the dynamics of core convection.

1.2.1 Dynamo simulations

Observations of the geomagnetic field are complemented by high fidelity numerical dynamo simulations. These numerical dynamos often resemble hydrodynamic convection (e.g. King and Buffett, 2013; Soderlund et al., 2012, 2015). We consider the dynamo model ran at the most extreme parameters to date (Schaeffer et al., 2017) which exhibits a large magnetostrophic polar vortex in the tangent cylinder and *quasi-geostrophic* columnar fluid structures resembling non-magnetic convection outside of the tangent cylinder (see figure 1.3).

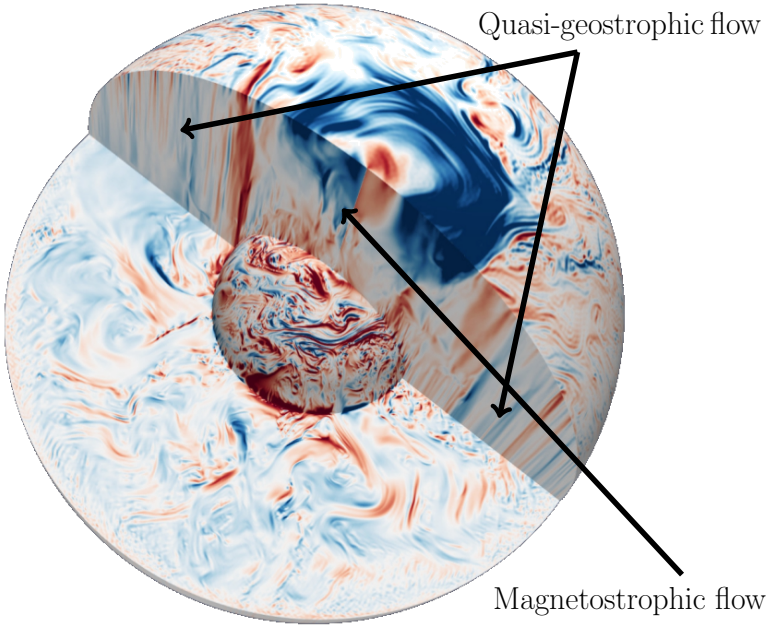

Figure 1.3: Contours showing a snapshot of azimuthal velocity for the most extreme convective dynamo simulation to date (having $E = 10^{-7}$). Image modified from Schaeffer et al. (2017).

Rapidly rotating fluids have a preference to align with the rotation axis described by the Taylor-Proudman constraint (Proudman, 1916; Taylor, 1917) and when $E \ll 1$ the resultant flows are organised into two-dimensional columnar morphologies. To see this, we take the curl of equation (1.4) which yields

$$\frac{\partial \boldsymbol{u}}{\partial z} = 0. \tag{1.5}$$

This is known as the Taylor-Proudman theorem and shows that geostrophic motions are two-dimensional and results from a balance between the Coriolis force and pressure gradients.

Studies of core flow based on the secular variation data find that QG flows best describe the observations (e.g. Pais and Jault, 2008) while theoretical considerations by Aurnou and King (2017) suggest that magnetostrophic dynamics may operate on smaller scales than are accessible to the resolution of current geomagnetic observations.

In addition to theoretical and observational considerations, numerical dynamo simulations have proved to be an important tool to further our understanding of dynamo action. Dynamo simulations have been present for more than 20 years (starting with the seminal work of Glatzmaier and Roberts, 1995) and have successfully reproduced many features of the geomagnetic field (e.g. Christensen et al., 2010) despite operating at parameters far from the expected conditions of Earth's core. When the magnitude of each force is calculated, numerical dynamos are found to be geostrophic at zeroth order, with buoyancy and Lorentz forces balancing the ageostrophic Coriolis force at first order (Wicht and Christensen, 2010; Soderlund et al., 2012, 2015; Schwaiger et al., 2019). The most extreme dynamo simulations to date (Yadav et al., 2016; Schaeffer et al., 2017; Sheyko et al., 2018) support this picture, having geostrophy at leading order and a balance of Lorentz, Archimedean and Coriolis forces at the next order (referred in the literature as QG-MAC). This dynamical balance may extend to the dynamics of Earth's core (Aubert et al., 2017) although this remains uncertain.

We can gain further insight about the nature of core dynamics by considering the Reynolds number, Re. The Reynolds number is a representative measure of how turbulent the flow is, defined by the ratio of inertial and viscous forces in the momentum equation (equation (1.1)),

$$Re = \frac{Uh}{\nu}. \tag{1.6}$$

Typically flows with $Re \gg \mathcal{O}\left(10^4\right)$ are considered turbulent (Batchelor, 2000). Estimating the value of Re for the core requires some characteristic velocity, U. The velocity of the core can be inferred by inverting magnetic field data, which gives an estimate of $10^{-4}\,\mathrm{m\,s^{-1}}$ (Holme and Olson, 2007). Although this may seem slow, the size of the core and its low viscosity imply this is a turbulent body of fluid. For the Earth's core, $Re \sim \mathcal{O}(10^9)$ (using values from table 1.1) implying that core convection is strongly chaotic and exhibits a vast range of spatio-temporal scales. The competition of chaotic three-dimensional fluid motions ($Re \gg 1$) and preference of the flow to order itself parallel to the rotation axis ($E \ll 1$) results in a state of fluid motion unique to rotating systems known as *geostrophic turbulence* (Pedlosky, 2013). Consistence with the Taylor-Proudman theorem states that geostrophic turbulence involves slowly evolving chaotic fluid motions (relative to the rate of rotation) in planes perpendicular to the rotation axis while motions parallel to the rotation axis are suppressed (e.g. Read, 2001). The field of 2D turbulence was heavily motivated by the chaotic motions in rapidly rotating sytems (e.g. Lilly, 1971).

To gain a complete understanding of the dynamics and evolution of the core, we cannot consider it in isolation and instead must consider how the liquid core couples to the solid inner core and the overlying mantle. At the ICB the fluid-solid boundary dictates that the appropriate boundary condition on the velocity is no-slip, i.e. the velocity must vanish. The viscosity of the mantle, $\nu = 10^{17}\,\mathrm{m^2\,s^{-1}}$ (Schubert et al., 2001) is much larger than that of the core and as a result at the CMB the velocity also conforms to a no-slip condition. The Earth's mantle and core convect on dramatically different time scales

shown by the typical velocity in the high viscosity mantle being $10^{-10}\,\mathrm{m\,s^{-1}}$ (Lallemand and Funiciello, 2009). The core convects a million times faster than the mantle and thus the core almost instantaneously responds to any change in the thermal structure of the mantle. On core time scales the radial temperature distribution of heat in the mantle is persistent and this keeps the heat flux coming out of the CMB constant. The preferable boundary condition for the core is therefore a fixed heat-flux boundary condition (Olson, 2003). It is difficult to determine the appropriate thermal conditions at the ICB and as a result there is some freedom in whether this is treated as a fixed temperature or fixed heat-flux driver of convection.

In this section we have shown that there is some debate about the governing force balance in Earth's core. Most of the evidence suggests that core dynamics are dominated by the Coriolis force with magnetic effects potentially only coming in at the next order. This has motivated much work to focus on non-magnetic thermal convection which will be discussed in the next section.

1.3 Convection studies

Over the past century, thermal convection has been extensively studied using a combination of experiments, numerical models and analytical methods. Originally, only convection in plane layer geometries was studied (Rayleigh, 1916; Bénard, 1900, 1901) with rotation added in later experiments (Rossby, 1969). Now, however plane-layer convection is complemented by a large amount of geophysically motivated work investigating convection in rotating spherical shell geometries (e.g. Aubert et al., 2017). The state of the art (see the review of Aurnou et al., 2015) is made up from contributions of computational models in spherical shell geometries, and both numerical and physical experiments in right-cylinders and Cartesian systems. The different geometries are shown in figure 1.4.

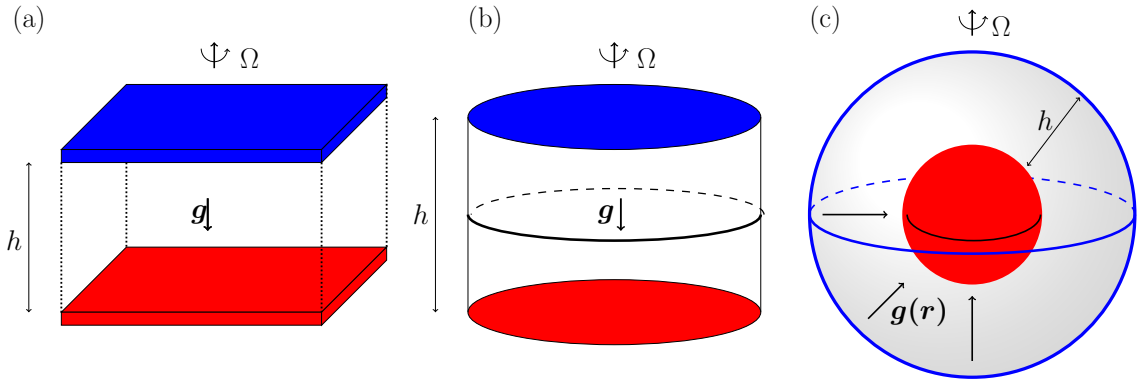

Figure 1.4: Schematic of the different configurations used to study convection; (a, b) Rayleigh-Bénard convection in plane layer and cylindrical geometries, (c) spherical shell geometry. The red(blue) boundaries are hot(cold). For rotating cases, the system rotates about the vertical with fixed angular velocity, Ω.

In the following sections we will discuss the scaling behaviour of the heat transport (Nusselt number), thermal boundary layer thickness, flow speed (Reynolds number) and the viscous thermal boundary layers for each configuration.

1.3.1 Rayleigh-Bénard convection

Non-rotating plane layer Rayleigh-Bénard convection (RBC) is a paradigm problem of turbulent fluid dynamics and has been the focus of many systematic surveys dating back to Malkus (1954). The RBC paradigm consists of a fluid layer contained between two rigid horizontal plates with gravity acting perpendicular to the plates (see figures 1.4a and 1.4b). The fluid is heated from below and cooled from above and when a sufficiently high temperature difference, ΔT, is maintained between the boundaries the fluid layer is destabilised. The non-dimensional parameters governing the system are the Rayleigh number, Ra (strength of buoyancy relative to thermal and viscous dissipation), the Prandtl number, Pr (ratio of viscous and thermal diffusivities) and Γ (the aspect ratio of the domain);

$$Ra = \frac{\alpha g \Delta T h^3}{\nu \kappa}, \quad Pr = \frac{\nu}{\kappa}, \quad \Gamma = \frac{L_x}{L_z}, \tag{1.7}$$

here α is the coefficient of thermal expansion, g is the gravitational acceleration, h is the depth of the fluid layer, ν is the viscous diffusivity, κ is the thermal diffusivity, L_x is length in the horizontal (typically taken equal in both directions) and L_z is length in the vertical. Except for when mentioned all the results presented here have moderate Pr; the experimental results use water, having $Pr = 7$, and the numerical simulations have $Pr = 1$.

For RBC, the fluid layer is destabilised when Ra is raised above some critical value, Ra_c, at which the convective instability onsets and for a given set of boundary conditions Ra_c is constant (Chandrasekhar, 1961). In the absence of flow ($Ra < Ra_c$) heat is transported purely by conduction and the corresponding temperature distribution can be seen in figures 1.5a and 1.5b. When $Ra > Ra_c$ heat is predominantly transported through advection in the fluid bulk and conduction in the thermal boundary layers which develop (see figures 1.5c and 1.5d).

The material properties of different fluids mean that Pr can vary over many orders of magnitude, taking values from $\mathcal{O}\left(10^{-5}\right)$ for plasmas to $\mathcal{O}\left(10^{3}\right)$ for alcohol type liquids (e.g. Lam et al., 2002). Most experiments use air or water as the working fluid having Pr $\approx$ 0.7, and 7, respectively (at room temperature) whereas liquid metals typically have $\mathcal{O}\left(10^{-3} - 10^{-1}\right)$ (due to their high thermal conductivity). Typically, convection experiments are performed in right-cylinders whereas plane-layer simulations employ horizontally periodic domains; despite this difference the two cases give similar heat transfer (e.g. King et al., 2012) and flow speed results (Hawkins et al., 2020). Everything discussed herein applies to both modelling approaches.

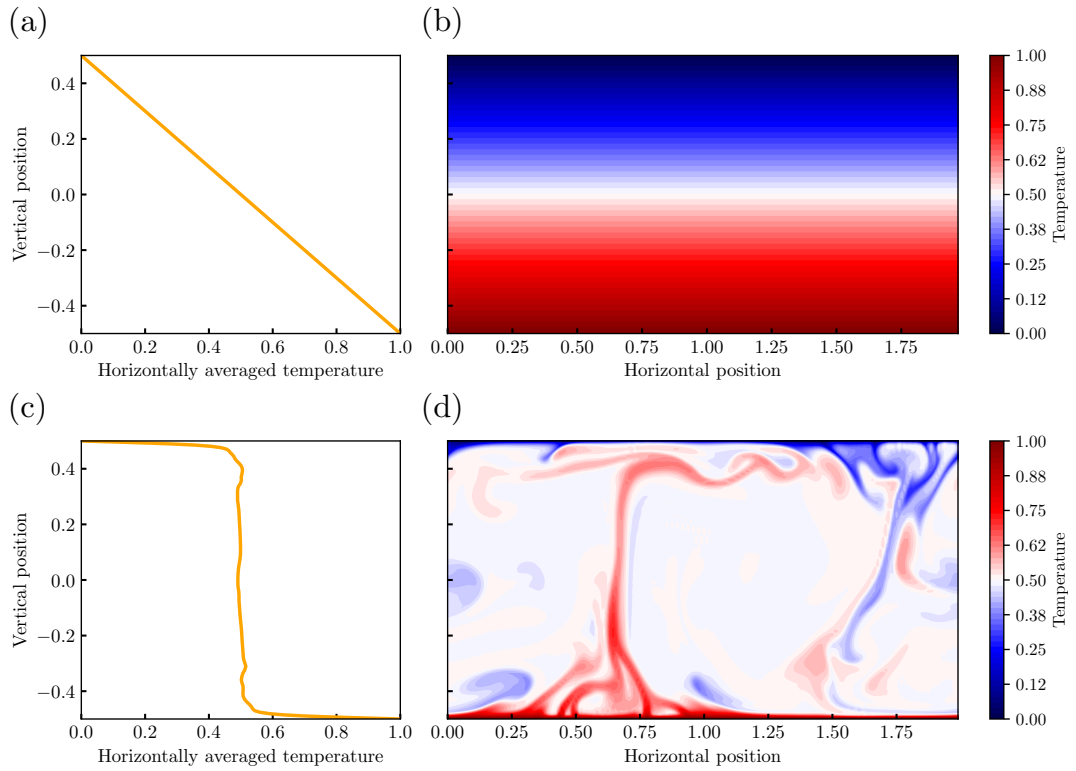

Figure 1.5: Temperature distribution for conduction having $Ra = Ra_c$ (figures a,b) and moderate convection with $Ra = 10^8$ (figures c,d). Figures (a,c) show the horizontally averaged temperature and (b,d) show snapshots of the temperature field. Both cases correspond to two-dimensional Rayleigh-Bénard convection with $Pr = 7$ and $\Gamma = 2$.

One of the most widely studied diagnostics of RBC is the efficiency with which convective fluid motions transfer heat; this is an easily obtained quantity in experiments and as a result has received a lot of attention in the literature (e.g. Rossby, 1969; Schmitz and Tilgner, 2010). The enhanced heat transfer due to convection is characterised by the Nusselt number, Nu, defined as

$$Nu = \frac{\text{total heat transfer}}{\text{conductive heat transfer}} = \frac{qh}{k\Delta T}, \tag{1.8}$$

where q is the total heat flux and k is the fluid's thermal conductivity. The conductive heat flux (that in the absence of flow) is

$$q_{cond} = k\Delta T/h. \tag{1.9}$$

It follows that $Nu = 1$ for purely conductive heat transfer and larger values of Nu correspond to more efficient heat transfer corresponding to increasingly vigorous flows. Studies using a given working fluid often search for scaling behaviour of the form $Nu \sim Ra^{\lambda}$. Both laboratory and numerical surveys at moderate forcings ($Ra \leq 10^{10}$) empirically find $Nu \sim Ra^{2/7}$ (e.g. Chillá et al., 1993; Glazier et al., 1999; Ahlers and Xu, 2001). Experimental data with $Pr = 7$ covering a large range of Ra values are shown in figure 1.6 along

with the $Nu \sim Ra^{2/7}$ prediction.

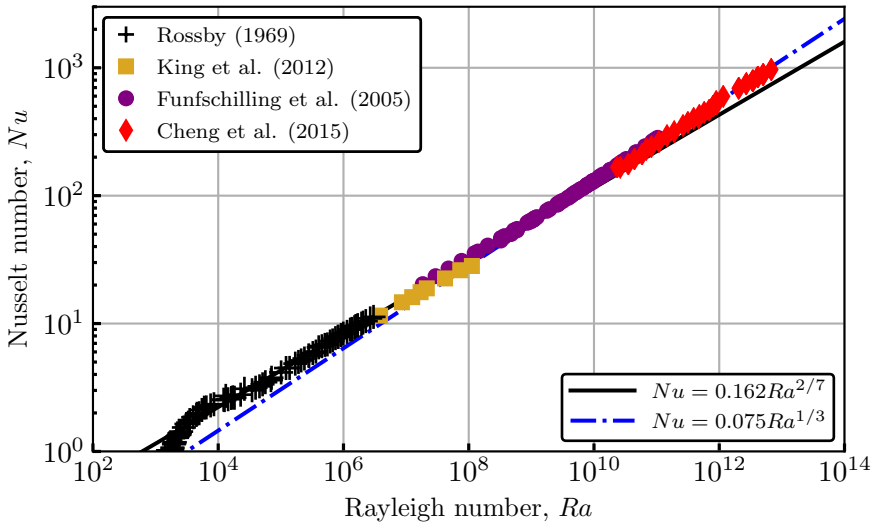

Figure 1.6: Heat transfer data from laboratory Rayleigh-Bénard convection experiments using water. The data is taken from Rossby (1969); Funfschilling et al. (2005); King et al. (2012); Cheng et al. (2015). The empirical $Nu \sim Ra^{2/7}$ (solid black) and theoretical $Nu \sim Ra^{1/3}$ (blue dot dash) scaling laws are shown with a transition at $Ra \approx 10^{10}$.

Assuming non-interacting boundary layers, the depth of the fluid layer does not enter the $Nu - Ra$ scaling (Malkus, 1954; Kraichnan, 1962) and predicts the classical scaling law

$$Nu \sim Ra^{1/3}. \tag{1.10}$$

Equation (1.10) has been confirmed by experiments carried out with $Ra \geq 10^{10}$ (e.g. Ahlers et al., 2009; Cheng et al., 2015) and numerical studies with $Pr = 1$ suggest this to be robust up to $Ra = 10^{15}$ (Iyer et al., 2020).

The $Nu \sim Ra^{1/3}$ scaling assumes that the bulk of the fluid volume is well mixed and isothermal with two quasi-static layers adjacent to the top and bottom boundaries; the thermal boundary layers, each of thickness, δ_κ. This configuration is shown in figures 1.5c and 1.5d and we see that approximately half of the temperature drop occurs in each of the thermal boundary layers. The vertical heat flux is conserved through horizontal planes and consequently the heat flux through the boundary layer is the total heat flux, $q_{\text{total}} = k\Delta T/2\delta_\kappa$. The Nusselt number can then be written as

$$Nu = \frac{q_{\text{total}}}{q_{\text{cond}}} = \frac{h}{2\delta_\kappa}. \tag{1.11}$$

Equation (1.10) can be obtained by considering the heat transfer scaling, $Nu \sim Ra^{\lambda}$. We substitute equation (1.11) for Nu and the definition of Ra (equation (1.7)) giving

$$\frac{h}{2\delta_\kappa} \sim \left(\frac{\alpha g \Delta T h^3}{\nu\kappa}\right)^{\lambda}.$$

If the thickness of the thermal boundary layers is independent of the fluid layer depth then

$$h \sim h^{3\lambda}, \quad \lambda = 1/3.$$

The results discussed above were for a fixed Prandtl number, $Pr \approx 7$, omitting any Pr dependence of Nu. Previous studies have shown that for $Pr \geq 0.2$ there is little to no dependence of the heat transport on Pr (Verzicco and Camussi, 1999; Ahlers and Xu, 2001; Iyer et al., 2020).

All of the heat transfer behaviour discussed above is observed from convection which is driven by fixed temperature boundaries, however Johnston and Doering (2009) showed that for $Ra > 10^6$, both fixed temperature and fixed heat-flux convection behave similarly.

The observed heat transfer diagnostics in RBC are well described by the Grossmann-Lohse theory (GLT) (Grossmann and Lohse, 2000, 2002, 2011). This theory is based on the exact relations for the viscous and thermal dissipation rates, ϵ_ν, and ϵ_κ, respectively

$$\epsilon_\nu = \frac{\nu^3}{h^4}\frac{(Nu-1)Ra}{Pr^2}, \quad \epsilon_\kappa = \frac{\kappa \Delta T^2}{h^2} Nu.$$

GLT splits the dissipation rates into contributions from the bulk and boundary layer contributions as the physics within these two regions is fundamentally different. In addition, the GLT assumes a large scale circulation (LSC) exists, defining a Reynolds number, Re, and that the viscous boundary layers behave as if they are of the laminar Prandtl-Blasius (PB) type (Prandtl, 1905; Blasius, 1908). While a LSC only formally exists in the presence of sidewalls, a near system size circulation is present when periodic sidewalls are employed as seen by the hot upwelling and cold downwelling in figure 1.5d.

Defining the Reynolds number, Re, in RBC experiments requires care as velocity is not a homogeneous field; the components and their respective magnitudes can vary across the domain. Typically, point measurements of the flow speed are taken either close to the sidewalls in order to measure the magnitude of the LSC (Qiu and Tong, 2001b) or at the centre of the domain to exclude the LSC (e.g. Zürner et al., 2019). In contrast, numerical simulations typically define Re using the volume average of all velocity components (e.g. King et al., 2013).

The observed $Re \sim Ra^\lambda$ behaviour recovers an exponent close to $\lambda = 1/2$ with values in the range $0.45 - 0.55$ (e.g. King et al., 2013; Zürner et al., 2019; Hawkins et al., 2020) shown in figure 1.7. This scaling behaviour is fairly robust and only the prefactor depends on the location at which the measurements are taken. The $Re - Ra$ relationship can be determined by using a free-fall velocity,

$$u_{\text{ff}} \sim \sqrt{\alpha g \Delta T h} \tag{1.12}$$

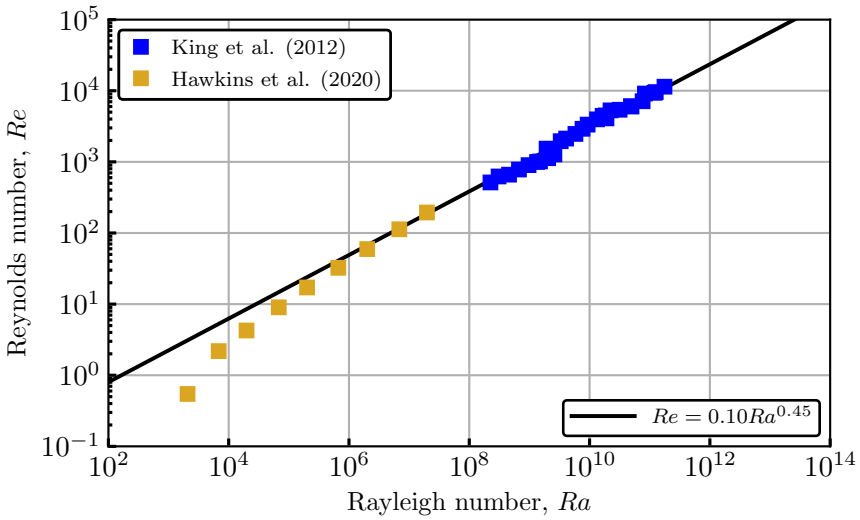

Figure 1.7: Flow speed data from laboratory and numerical Rayleigh-Bénard convection using water (Pr=7). The data is taken from King et al. (2013); Hawkins et al. (2020). The empirical $Re \sim Ra^{0.45}$ scaling law shown is from Qiu and Tong (2001b).

to estimate the system scale velocity in equation (1.6) giving

$$Re \sim Ra^{1/2} \tag{1.13}$$

when $Pr \sim \mathcal{O}(1)$ (Kraichnan, 1962; Grossmann and Lohse, 2002). Unlike Nu, Re is strongly affected by Prandtl number effects across the range $10^{-3} < Pr < 10$ and Verzicco and Camussi (1999) found $Re \sim Pr^{-0.94}$ for fixed $Ra = 6 \times 10^5$.

The GLT is further verified by testing the shape of the boundary layers against the PB prediction. The boundary layers in RBC contain strong fluctuating dynamics and when time averaging occurs at fixed heights the profiles are distinguishable from the PB prediction (Shishkina et al., 2010). Both the bulk and boundary layer dynamics are sampled as the measurement height can be either inside or outside of the boundary layer, e.g. during the emission of plumes. When analysed in a time-dependent frame which fluctuates with local and instantaneous boundary layer thicknesses, the boundary layer profiles are well described by PB theory (Zhou et al., 2010; Stevens et al., 2012; Shishkina et al., 2015). A prediction for the thickness of the viscous boundary layer is obtained by balancing the inertia of the fluid bulk with the viscous forces in the boundary layer of thickness, δ_ν,

$$\begin{aligned} \boldsymbol{u} \cdot \boldsymbol{\nabla} \boldsymbol{u} &\sim \nu \nabla^2 \boldsymbol{u}, \\ \frac{\delta_\nu}{h} &\sim Re^{-1/2}. \end{aligned} \tag{1.14}$$

The viscous boundary layers become thinner with increasingly more turbulent convection.

GLT predicts a set of equations describing $Nu(Ra, Pr)$ and $Re(Ra, Pr)$ over a vast range of parameter space and identifies different regimes with unique scaling behaviour

Quantity	Scaling	References
Nu	$Ra^{2/7} - Ra^{1/3}$	equation (1.10) and figure 1.6
δ_κ/h	Nu^{-1}	equation (1.11)
Re	$Ra^{0.45} - Ra^{0.55}$	equation (1.13) and figure 1.7
δ_ν/h	$Re^{-1/2}$	equation (1.14)

Table 1.3: Summary of results for the scaling behaviour of the Nusselt number, Nu, thermal boundary layer thickness, δ_κ/h, Reynolds number, Re, and viscous boundary layer thickness, δ_ν/h observed for Rayleigh-Bénard convection.

(see e.g table 2 and figure 2 in Grossmann and Lohse, 2000). These predictions account for the observed $Nu-Ra$ exponents of $\lambda = 2/7$, and $1/3$, and the range of $Re-Ra$ exponents.

In this section we have discussed the observations from numerical simulations and laboratory experiments of Rayleigh-Bénard convection regarding the scaling behaviour of the Nusselt number, thermal boundary layers, Reynolds number, and viscous boundary layers. We have also derived theoretical predictions which can describe these observations. A table summarising these findings is given in table 1.3.

1.3.2 Rotating Rayleigh-Bénard convection

The simplest configuration to investigate the interaction of rotation and convection is to take the RBC paradigm and rotate it about the vertical; with the rotation axis antiparallel to the gravity vector. The effect of rotation is encapsulated by the Ekman number, E, defined in table 1.2. When fluids undergo rotation there is a preference to form columnar structures aligned with the rotation axis (Greenspan, 1968; Pedlosky, 2013). These columnar flows are effectively invariant in the vertical direction as a result of the Taylor-Proudman constraint and they act to hinder convection. In the presence of increasingly strong Coriolis forces an increasingly high Rayleigh number is required for convection to onset. Linear stability analysis predicts both Ra_c and the critical wavenumber, m_c, at onset have power-law dependencies on E (Chandrasekhar, 1961) having expressions of the form

$$Ra_c \sim E^{-4/3}, \quad m_c \sim E^{-1/3}, \tag{1.15}$$

(see figure 1.8).

The columnar structures can be seen in contours of the temperature field in figure 1.9b. For a fixed Ekman number, columnar flow is present for moderate Ra values,

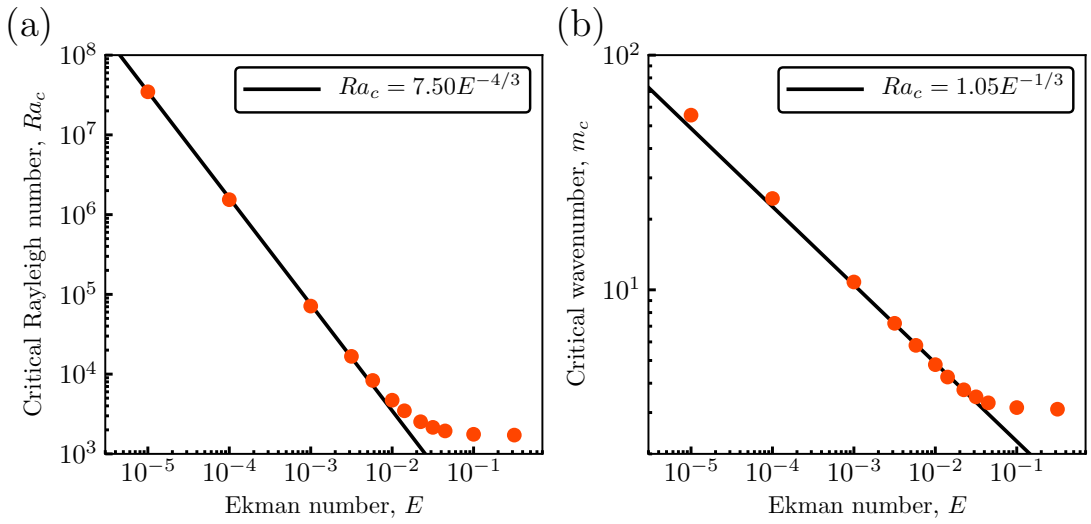

Figure 1.8: (a) Critical Rayleigh number, Ra_c, and (b) critical wavenumber, m_c, versus Ekman number for no-slip boundary conditions. The data is taken from Chandrasekhar (1961), table VIII.

whereas at sufficiently large Ra the Taylor-Proudman constraint is broken and the system is dominated by small scale turbulent structures (figure 1.9d). The two field morphologies give rise to different time average temperature profiles; the columnar regime is able to maintain interior temperature gradients (figure 1.9a) whereas the turbulent regime resembles non-rotating convection with an isothermal bulk and two thermal boundary layers accommodating the entire temperature drop (compare figure 1.9c with figure 1.5c).

As in the RBC case we will examine the $Nu - Ra$ data for rotating RBC, shown in figure 1.10. The rotating case differs from non-rotating RBC as there are two distinct scaling behaviours present, consistent with the two different field morphologies seen in figure 1.9. For a given E there is a steep $Nu - Ra$ scaling which transitions to a shallower scaling behaviour past some transitional value of Ra. When Ra is raised higher than this, the heat transfer follows non-rotating behaviour (figure 1.10) with some overshoot. RBC provides an upper limit for the heat transport in rotating convection at large Ra. Previous studies (Julien et al., 2012a; Grooms and Whitehead, 2014) found that in the columnar regime the heat transfer scaling becomes increasingly steep with decreasing E,

$$Nu \sim Ra^{\lambda(E)}. \tag{1.16}$$

The exponent ranges from $\lambda = 1.10$ for $E = 10^{-2}$ to $\lambda = 3.56$ for $E = 10^{-7}$. Cheng et al. (2015) showed that the scaling exponent increased monotonically with decreasing E following $\lambda \propto \ln|E^{-1}|$. Plane layer simulations with free-slip mechanical boundary conditions find conflicting results for the heat transport in the columnar regime, having a much lower scaling exponent saturating to the asymptotic scaling, $Nu \sim Ra^{3/2}E^2$ (Julien et al., 2012a). No-slip boundaries (and the vanishing velocity on the boundary) lead to the formation of viscous boundary layers which are not present for the free-slip boundaries;

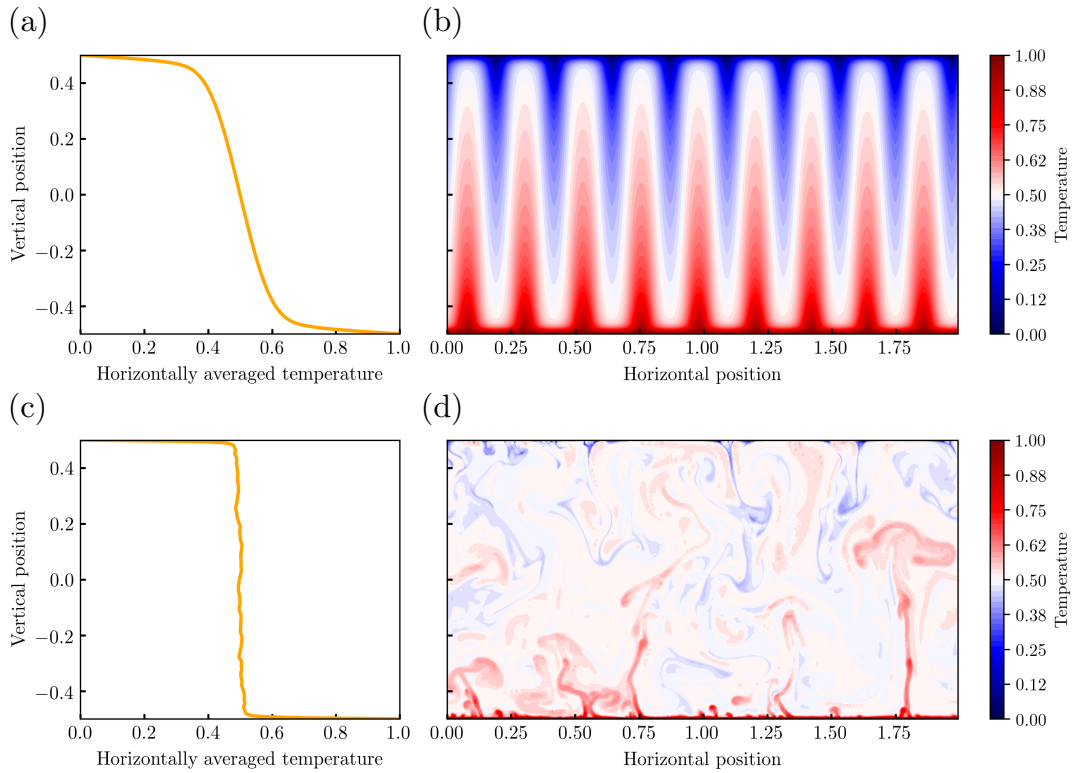

Figure 1.9: Temperature distribution for rotationally constrained convection having $Ra = 5 \times 10^6$ (figures a,b) and vigorous turbulent convection with $Ra = 3 \times 10^9$ (figures c,d). Both cases have $E = 10^{-4}$, $Pr = 7$, and $\Gamma = 2$. Figures (a,c) show the horizontally averaged temperature and (b,d) show snapshots of the temperature field.

are these boundary layers somehow responsible for the differences in the observed Nu scaling?

The viscous boundary layer in a rotating system is of the Ekman type and plays a leading role in controlling flows that depart from solid body rotation (Greenspan, 1968). The fluid bulk is geostrophic but geostrophy is broken in the boundary layers. Balancing Coriolis and viscous forces in the Ekman layer of thickness, δ_E, gives

$$2\boldsymbol{\Omega} \times \boldsymbol{u} \sim \nu \nabla^2 \boldsymbol{u},$$

$$\frac{\delta_E}{h} \sim E^{1/2}. \tag{1.17}$$

The Ekman layer drives a secondary flow referred to as Ekman pumping, or Ekman suction, and occurs whenever there is relative flow between the fluid and the solid boundary (Greenspan, 1968).

For no-slip boundaries the presence of Ekman layers and consequently Ekman pumping/suction is responsible for the enhanced heat transport leading to the larger $Nu-Ra$ scaling exponents (Stellmach et al., 2014; Plumley et al., 2016) such as those observed by Cheng et al. (2015); Kunnen et al. (2016).

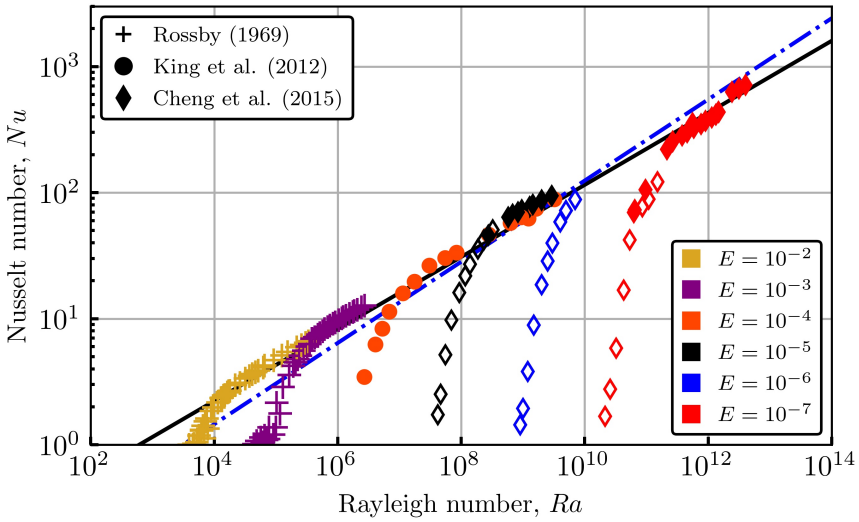

Figure 1.10: Rotating Rayleigh-Bénard convection heat transfer data. The data is taken from Rossby (1969); King et al. (2012); Cheng et al. (2015). All data use $Pr = 7$ and symbol colours correspond to different Ekman numbers. Filled markers are experimental data and empty markers are obtained from numerical simulations. As in figure 1.6 the empirical $Nu \sim Ra^{2/7}$ (solid black) and theoretical $Nu \sim Ra^{1/3}$ (blue dot dash) scaling laws are shown.

There is no equivalent of the robust GLT in rotating convection as the assumptions on the dissipation rates are not realised; in the rotating case, it is not clear that there is any regime in which either the fluid bulk or boundary layers have an insignificant contribution to the thermal and/or viscous dissipation rates. King et al. (2013) applied the GLT approach to rotating convection by arguing that only the contribution from the fluid bulk was needed. This choice followed from the viscous dissipation in the fluid bulk increasing with decreasing E due to the reduced length scales of convection while the volume percentage occupied by the Ekman layers also decreases. Balancing the production of kinetic energy with the time averaged (indicated by the overbar) viscous dissipation gives

$$\frac{\kappa^2}{h^4}(Nu - 1)Ra = \overline{(\boldsymbol{\nabla u})^2}.$$

The dissipation term in the bulk is approximated by U^2/ℓ^2 where U is some characteristic velocity and ℓ is the typical length scale of convection. This scaling is chosen by assuming that the relevant length scale for dissipation is the characteristic interior length scale, ℓ. This leads to the Reynolds number scaling

$$Re = \left(\frac{(Nu - 1)Ra}{Pr^2}\right)^{1/2} \frac{\ell}{h}. \tag{1.18}$$

The characteristic length scale for rotating convection is theorised to follow the viscous scaling

$$\frac{\ell}{h} \sim E^{1/3} \tag{1.19}$$

(e.g Chandrasekhar, 1961) which has also been confirmed numerically in the columnar regime using both DNS of the full system (King et al., 2013) and the asymptotically reduced nonlinear system of Sprague et al. (2006). Combining equations (1.18) and (1.19) allows a prediction of the flow speed based on the non-dimensional parameters. The resultant scaling,

$$Re \sim \left(\frac{(Nu-1)Ra}{Pr^2} \right)^{1/2} E^{1/3}, \tag{1.20}$$

is often referred to as the VAC (viscous-Archimedean–Coriolis) scaling, for the triple force balance on which it is based. Despite the length scale used (equation (1.19)) scaling similar to the onset length scale (equation (1.15)), equation (1.20) has been shown to describe rotationally constrained convection past onset and into the nonlinear regime (King et al., 2013).

Many works have investigated the transition between the columnar and turbulent regimes of rotating convection by comparing the $Nu - Ra$ scaling behaviour of the two regimes (King et al., 2009; Liu and Ecke, 2009; Cheng et al., 2019). Originally this transition was theorised to be controlled by the global balance between the Coriolis and buoyancy forces, parametrised by the convective Rossby number (Gilman, 1977),

$$Ro_c = \left(\frac{RaE^2}{Pr} \right)^{1/2}. \tag{1.21}$$

Ro_c is obtained by considering the standard Rossby number representing the ratio of inertial and Coriolis forces,

$$Ro = \frac{U}{2\Omega h}$$

and using the free-fall velocity as the velocity scale (equation (1.12)). If the transition was captured by this parameterisation then we would expect, $Ro_c \sim \mathcal{O}(1)$, however recent studies have shown that the non-rotating heat transfer behaviour can be observed even with $Ro_c \sim 10^{-2} - 10^{-1}$ (e.g. Cheng et al., 2015).

King et al. (2009) showed that the transition in Nu can be described by the relative thicknesses of the thermal and Ekman boundary layers. When $\delta_E < \delta_\kappa$, Ekman pumping throttles the heat transport giving rise to the steep $Nu - Ra$ scaling, whereas if $\delta_\kappa < \delta_E$ the effect of rotation should be weak leading to the non-rotating $Nu - Ra$ behaviour. When $Nu \sim Ra^{2/7}$ the crossover in boundary layer thicknesses occurs when

$$\delta_\kappa \sim \delta_E, \quad Ra^{-2/7} \sim E^{1/2},$$

predicting a transition at

$$RaE^{7/4} \sim \mathcal{O}(1). \tag{1.22}$$

When applied to a suite of numerical simulations having $3 \times 10^{-6} \leq E \leq 10^{-2}$, King et al.

(2009) empirically determined the prefactor which was indeed of $\sim \mathcal{O}(1)$;

$$RaE^{7/4} = 1.4. \tag{1.23}$$

This methodology was further developed in King et al. (2012) and when larger Ra values are considered and the $Nu \sim Ra^{1/3}$ is observed the transition was found to occur at $RaE^{3/2} = 10$.

Simulations with free-slip boundary conditions produce similar regime transitions (Schmitz and Tilgner, 2010) and so Julien et al. (2012b) argue that the Ekman layer cannot be responsible, since no viscous boundary layer exists on the free-slip boundaries. The dependence of the transition seen by Schmitz and Tilgner (2010) indicates that even in the free-slip case there is a critical balance between the viscous and rotational time scales analogous to that of the Ekman layer. We note that since the work of King et al. (2009, 2012) many authors have proposed different parameters to control the transition and we refer the reader to the recent review of Cheng et al. (2018) (see their table 1 and references therein) for an overview. We will revisit the hypotheses for the regime transition in the next section.

1.3.3 Spherical shell rotating convection

Although the spherical geometry is the natural choice to studying planetary style rotating convection, the majority of the rotating RBC laboratory experiments developed have been carried out in planar and cylindrical cells, in which the rotation axis and the gravity vector are aligned. The complementary approach combining numerical and laboratory experiments in planar or cylindrical geometries has enabled vast coverage of parameter space (Stellmach et al., 2014; Aurnou et al., 2015). The question is then whether the planar RBC results can be directly applied to rotating convection in spherical geometry in which the fluid is heated from the inner boundary and cooled from the outer boundary (figure 1.4c).

Laboratory experiments in spherical geometry are scarce owing to the difficulty in generating a radial acceleration emulating gravity. Most investigations use the centrifugal force as a proxy for the radial gravitational acceleration (Busse and Carrigan, 1974; Cardin and Olson, 1994; Sumita and Olson, 2003). The combination of gravity and the centrifugal acceleration generates surfaces of gravity potential close to spherical surfaces in the lower hemisphere and was originally used to study the onset of convection (Busse and Carrigan, 1974; Cordero and Busse, 1992). For a review see Cardin and Olson (2010). Sumita and Olson (2003) used this method to study convection with low Ekman number, $E = 5\times10^{-6}$, and vigorous forcing, $200Ra_c \lesssim Ra \lesssim 600Ra_c$. In this parameter range they obtained $Nu \sim Ra^{0.4}$, comparable to the 1/3 exponent of non-rotating RBC and concluded that the Coriolis force only plays a minor role on the heat transport. This observation may be explained when placed in terms of the different regimes of rotating convection which

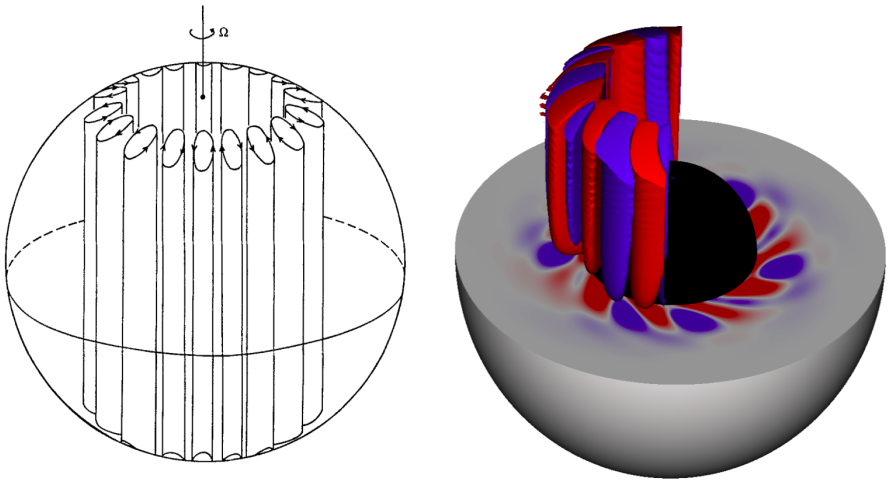

Figure 1.11: Preferred structure of convection near onset for rapidly rotating convection with $Pr \sim \mathcal{O}(1)$. (a) Qualitative sketch from Busse (1970). (b) Isosurfaces of meridional velocity from a simulation with $Pr = 1$, $E = 10^{-5}$ and $Ra = 1.1Ra_c$.

we will outline in this section. This section now focuses on analytical approaches and numerical models of spherical shell convection which have been developed since the 1970s as a complementary approach to the plane layer laboratory experiments (e.g. Gilman, 1977; Tilgner and Busse, 1997).

In agreement with the plane layer case, analytical work in the limit of $E \ll 1$ and $E/Pr \ll 1$, assuming a uniform distribution of heat sources showed that the onset of convection occurs when $Ra_c \sim E^{-4/3}$ (Roberts, 1968; Busse, 1970; Jones et al., 2000). At onset the flow takes the form of drifting thermal Rossby waves localised to the inner boundary and extending across the entire domain in the vertical (see figure 1.11). We note that two types of flows can occur at onset depending on the value of Pr. For $Pr \gtrsim \mathcal{O}(1)$ *columnar* convection (e.g. Busse, 1970) has rolls of intercepting the outer spherical surface at mid latitudes (as in figure 1.11b). In contrast, when $Pr < 1$, *inertial convection* has convection rolls that are trapped near the outer region of the fluid shell in the equatorial region with large azimuthal scale similar to the radial scale (e.g. Zhang and Busse, 1987). These columns are relatively thin, having an azimuthal wavenumber of $m_c \sim E^{-1/3}$. The columns exist in pairs, with the number determined by m_c, neighbouring rolls rotate alternatively in the prograde and retrograde directions. For fixed temperature boundaries, m_c is a monotonically increasing function of E. Fixed heat-flux boundary conditions do not greatly alter the morphology at onset but tend to favour longer length scales, with only a small change in Ra_c (Takehiro et al., 1999). At asymptotically small E there is no dependence of Ra_c or m_c on the choice of boundary conditions. At finite E, however, Gibbons et al. (2007) showed that m_c is a discontinuous function of E and Pr when fixed heat-flux boundary conditions are used.

In rotating spherical shell convection the $Nu - Ra$ behaviour is qualitatively similar to the rotating RBC case in that there is a steep scaling for moderate Ra values which

shallows off to the non-rotating behaviour as Ra is raised sufficiently high (Gastine et al., 2016; Mound and Davies, 2017). Figure 1.12 shows heat transport data for convection in a rotating spherical shell. The spherical shell data is unique in that there is a shallow tail close to onset for cases with $E < 10^{-4}$ (Yadav et al., 2015; Gastine et al., 2016; Mound and Davies, 2017). Gastine et al. (2016) found that the shallow scaling at low Ra ($< 6Ra_c$) follows the weakly nonlinear perturbation theory carried out by Busse and Or (1986); Gillet and Jones (2006) predicting the heat transport is proportional to the supercriticality,

$$Nu - 1 \sim \frac{Ra}{Ra_c} - 1.$$

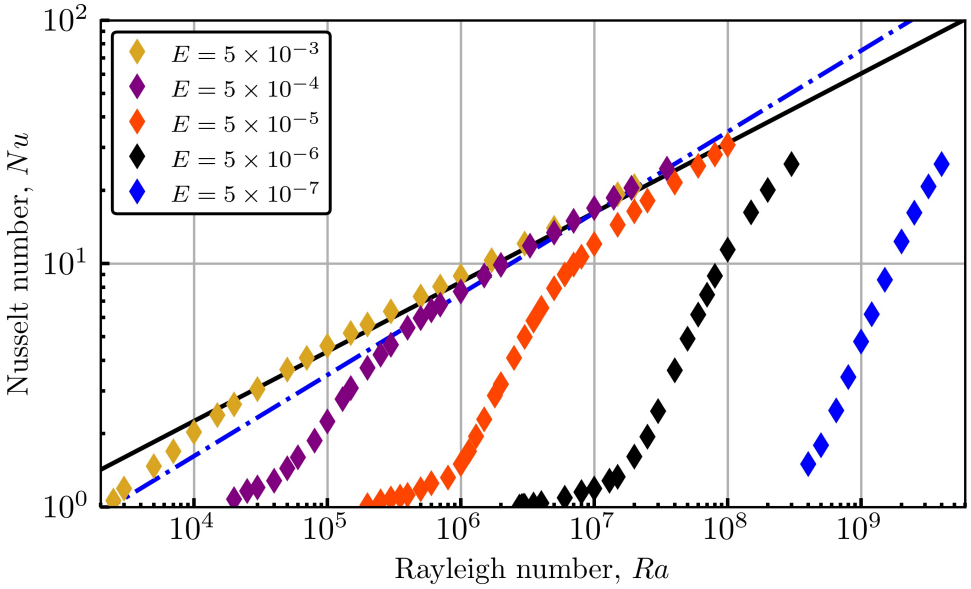

Figure 1.12: Rotating spherical shell heat transfer data. The data is taken from Gastine et al. (2016). All simulations have $Pr = 1$ and the symbol colours correspond to different Ekman numbers. As in figure 1.6 the empirical $Nu \sim Ra^{2/7}$ (solid black) and theoretical $Nu \sim Ra^{1/3}$ (blue dot dash) scaling laws are shown.

In the steep heat transfer regime, the scaling exponent increases with decreasing E, in agreement with the rotating RBC case. Though Mound and Davies (2017) found a continuous increase for the parameter range considered, Gastine et al. (2016) observed saturation at $Nu \sim Ra^{3/2}E^2$. This scaling might imply that an asymptotic regime has been reached as it is derived in the absence of thermal and viscous diffusion at asymptotically low E (Jones, 2015). Plane layer studies find exponents that are much larger than those observed in spherical shells (see figure 1.13) and this is likely due to Ekman pumping being maximised in plane layer cases which have gravity aligned with the rotation axis (Greenspan, 1968). Ekman boundary layers have been shown to allow states of enhanced heat transport and deviations from the asymptotic $Nu \sim Ra^{3/2}E^2$ behaviour (Stellmach et al., 2014; Plumley et al., 2016, 2017) and this could explain the steeper heat transport exponents. As before, for a given E if Ra is raised sufficiently high, the heat transport follows non-rotating behaviour, $Nu \sim Ra^{2/7}$ (Yadav et al., 2015; Gastine et al., 2016;

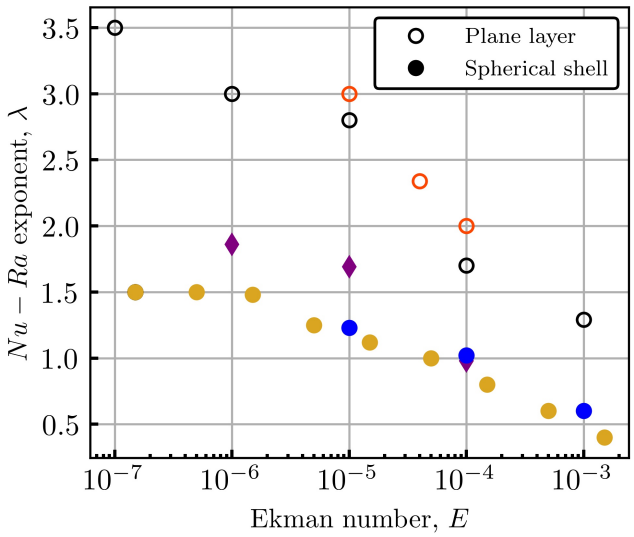

Figure 1.13: Heat transfer scaling exponents in the rotationally constrained regime versus Ekman number. The exponents from plane layer and spherical shell studies are shown as empty and filled markers respectively. Exponents correspond to data reported by King et al. (2012) (red markers), Cheng et al. (2015) (black markers), Yadav et al. (2015) (blue markers), Gastine et al. (2016) (yellow markers), and Mound and Davies (2017) (purple markers). Mound and Davies (2017) is the only data set using fixed heat-flux boundary conditions.

Mound and Davies, 2017). Unlike the plane layer data, the heat transport in spherical shells does not overshoot the non-rotating scaling and approaches this behaviour smoothly (compare figure 1.10 with figure 1.12).

Geometry can play a key role in determining the behaviour of convecting fluids, and in contrast to plane-layer RBC, convection in rotating spherical shells can self-consistently excite strong axisymmetric azimuthal (zonal) flows (Gilman, 1977). These zonal flows are excited by Reynolds stresses as a result of the curved boundaries in spherical domains (Busse and Hood, 1982). The Reynolds number in rotating spherical shells can therefore be decomposed into two meaningful contributions; Re_c, based on the convective flow, and Re_z, based on the zonal flow,

$$Re = Re_c + Re_z$$

The zonal flows do not contribute to the net heat transfer but for free-slip boundaries they represent a large amount of the total kinetic energy (e.g. Christensen, 2002; Gastine and Wicht, 2012) as their saturation is controlled by the weak friction effects in the bulk. In no-slip cases the zonal flows are much weaker than their free-slip equivalents due to the larger friction in the Ekman boundary layers which more efficiently inhibit zonal flows (Aubert, 2005; Jones and Schubert, 2007). Even for no-slip cases the zonal flow can correspond to as much as 20% of the total kinetic energy (Yadav et al., 2015) and so herein we will discuss results attaining to the convective flow, Re_c.

The weakly nonlinear heat transfer is accompanied by convective flow governed by the VAC force balance (Gillet and Jones, 2006; Gastine et al., 2016) with convective length scale and Reynolds number,

$$\frac{\ell}{h} \sim E^{1/3}, \quad \text{and} \quad Re_c \sim \left(\frac{(Nu-1)Ra}{Pr^2}\right)^{1/2} E^{1/3}.$$

This regime has the same scaling behaviour of ℓ/h and Re_c as rotating RBC. Gastine et al. (2016) found that the steep heat transfer scaling, $Nu \sim Ra^{\lambda(E)}$, is maintained by a balance between inertial, Archimedean and Coriolis forces (termed IAC) within the fluid bulk and viscous effects in the Ekman boundary layers. Formally this can be expressed within the GLT framework as

$$Re = a\left(\frac{Ra(Nu-1)}{Pr^2}\right)^{2/5} E^{1/5} + b\left(\frac{Ra(Nu-1)}{Pr^2}\right)^{1/2} E^{1/4};$$

the two terms on the right hand side correspond to the bulk and boundary layer contributions to Re_c, respectively. The parameters a and b are empirically determined and Gastine et al. (2016) found that the data in the rapidly rotating regime is well described with $a = 0.066$ and $b = 4.843$. When the heat transport follows, $Nu \sim Ra^{2/7}$, the Reynolds number also behaves as if non-rotating and follows $Re \sim Ra^{0.46-0.50}$ (Gastine et al., 2015, 2016) consistent with the GLT.

The systematic study of Gastine et al. (2016) identified four regimes of rotating convection. The weakly nonlinear regime transitions to the rapidly rotating regime (at low E) at $Ra = 6Ra_c$. The boundary layer transition (observed in the plane layer cases) demarcating the change from the steep heat transfer scaling to the non-rotating behaviour is shown to not hold for convection in rotating spherical shells (Gastine et al., 2016; Mound and Davies, 2017). Instead the transition is better parametrised by determining when the thermal boundary layer loses geostrophic balance (Gastine et al., 2016; Mound and Davies, 2017) occuring at $RaE^{8/5} \sim \mathcal{O}(1)$ (Julien et al., 2012a).

A summary of the regimes and scaling behaviour of rotating convection for both geometries considered is given in figure 1.14 and table 1.4.

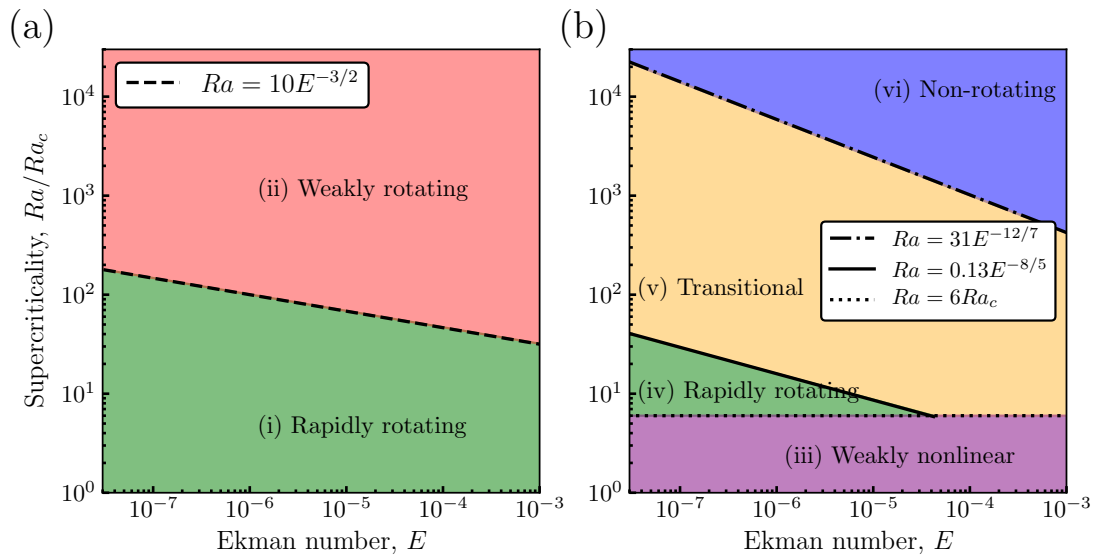

Figure 1.14: Summary of the regimes or rotating convection for (a) rotating Rayleigh-Bénard convection and (b) convection in a rotating spherical shell.

1.4 Summary

In this chapter, we introduced the geodynamo, which is self sustained by convective motions of liquid iron in Earth's outer core. We briefly summarised the force balances theorised to hold in Earth's core and used this to motivate an investigation of hydrodynamic convection in a rotating spherical shell. The behaviour of the heat and momentum transfer for different systems used to study convection is summarised and this provides the baseline for the work presented in this thesis. The results discussed come from convection driven by fixed temperature boundaries and we will investigate if these reported results are robust when considering convection driven by fixed heat-flux.

We focus on deriving and testing scaling relationships between the dependent and independent variables over the accessible parameter space. We want to find scaling laws that hold over many orders of magnitude and so we focus on power-law relationships. If asymptotic behaviour emerges (which is consistent with some physical expectation or intuition) for the output of our models then this allows extrapolation and discussion of the dynamics present in Earth's core.

	Nu	δ_κ/h	Re	δ_ν/h
(i) Rapidly rotating	$Ra^{\lambda(E)}$	$Nu^{-1+f(Ra,E)}$	$B^{1/2}E^{1/3}$	$E^{1/2}$
(ii) Weakly rotating	$Ra^{2/7-1/3}$	Nu^{-1}	$B^{1/2}E^{1/3}$	$Re^{-1/2}$
(iii) Weakly nonlinear	$\gamma_0\left(\frac{Ra}{Ra_c}-1\right)+1$	–	$B^{1/2}E^{1/3}$	–
(iv) Rapidly rotating	$Ra^{\lambda(E)}$	$Nu^{-1+f(Ra,E)}$	$\gamma_1 B^{2/5}E^{1/5}+\gamma_2 B^{1/2}E^{1/4}$	$E^{1/2}$
(vi) Non-rotating	$Ra^{2/7-1/3}$	Nu^{-1}	$Ra^{1/2}$	$Re^{-1/2}$

Table 1.4: Summary of results for the scaling behaviour of the Nusselt number, Nu, thermal boundary layer thickness, δ_κ/h, Reynolds number, Re, and viscous boundary layer thickness, δ_ν/h. The regimes correspond to those in figure 1.14. The convective power is given as $B = Ra(Nu-1)Pr^{-2}$.

1.5 Project aims and thesis outline

The aim of this thesis is to use numerical simulations to investigate the dynamics of rotating convection driven by a fixed heat-flux. Specifically, we want to test recent observations regarding the existance of different regimes of rotating convection and to unify the different behaviours observed in global spherical models and local plane layer models. To this end, the aims of the thesis are:

1. Can we define a robust method for defining the thermal boundary layer in rotating convection?
   (a) Test the robustness of established methods originating from fixed temperature non-rotating plane layer experiments.
   (b) Use physical arguments to derive a method of defining the boundary layer which is insensitive to the chosen configuration, e.g. thermal boundary conditions, presence of rotation, or geometry.
2. Do different physical regimes of convection exist in a rotating spherical shell?
   (a) Perform a systematic survey and isolate changes in the scaling behaviour of heat transport and flow diagnostics to create a regime diagram.
   (b) Determine the relevant regime and corresponding implications for Earth's core.
3. Can we unify the different observations from local plane layer and global spherical shell convection models?
   (a) Determine if the heat transfer behaviour of local models is consistent with results from the polar region of global models.
   (b) Compare the flow speed scaling behaviour of the global model with the contribution of the polar region.

Following this chapter, in which we gave background regarding Earth's interior, core dynamics and thermal convection, Chapter 2 describes the theoretical framework for modelling convection, including the governing equations and numerical implementation.

In Chapter 3 we evaluate different methods commonly used to define the thermal boundary layer in Rayleigh-Bénard convection and present a definition derived from the temperature equation. A parameter survey of rotating spherical shell convection is presented in Chapter 4 from which we identify four different dynamical regimes of rotating convection. We show that the thermal boundary layers are vital in determining the upper bound of rapidly rotating convection. In Chapter 5 we compare heat transfer and flow speed data from the polar region of global simulations with measurements taken from laboratory experiments using water.

Chapter 6 summarises the contents of this thesis and the underlying simplifications before concluding with a discussion of future avenues for this field of research.

Chapter 2

Theory and Numerical Implementation

The models used to study convection with and without rotation (discussed in chapter 1) can take different forms depending on the underlying motivation and assumptions. There are a number of textbooks that give a comprehensive overview of the relevant equations, see e.g. Chandrasekhar (1961); Pedlosky (2013); Batchelor (2000). This chapter introduces the governing equations and boundary conditions for the models we use to study convection. The governing equations are formulated for thermal convection with and without rotation and we derive different non-dimensional parameters based on the choice of thermal boundary conditions. We describe the numerical implementation with which we simulate convection in both plane layer and spherical shell geometries, and discuss the criteria for a simulation to be considered accurate and well converged.

2.1 Boussinesq approximation

The evolution of fluid motion is described by the equations governing the conservation of mass, momentum and energy (presented in subsection 2.2.1) solved subject to appropriate boundary conditions. In order to close the system an equation of state is required. In their primitive form the governing equations are complex and difficult to solve directly; however, one way of simplifying these equations is by using the Boussinesq approximation (formally justified by scaling analysis, Spiegel and Veronis, 1960). The Boussinesq approximation considers flows with small density variations as incompressible with the leading order effects due to density variations only retained in the buoyancy force. We treat all thermodynamic variables as constant, except for temperature, T, and the density in the buoyancy force, ρ, which is approximated by the Boussinesq equation of state

$$\rho = \rho_o \left(1 - \alpha(T - T_o)\right), \tag{2.1}$$

where α is the coefficient of thermal expansion, and T_o and ρ_o are reference values of temperature and density, respectively. Under the Boussinesq approximation density is independent of pressure implying that pressure changes are transmitted through the system instantaneously.

Equation (2.1) holds for a wide range of fluids due to the smallness of α; with typical values of $10^{-5}\,\mathrm{K}^{-1}$ for liquid metals (e.g. Chen et al., 2007) and $10^{-4}\,\mathrm{K}^{-1}$ for water (Lide, 2004). For the Boussinesq approximation to be applied to planetary cores we must consider T as the departure from the adiabatic temperature (e.g. Spiegel and Veronis, 1960). The two different models discussed in this chapter consider thermal convection of a Boussinesq fluid.

While the Boussinesq approximation is commonly used to simplify convection systems (and we will use it in this thesis) it is not clear that this is completely suitable when applied to Earth's core. We will list the major uncertainties associated with the Boussinesq approximation here for completeness. The Boussinesq approximation not only disregards compressibility in the momentum and continuity equations (which introduces an inaccuracy) but also neglects adiabatic cooling in the heat equation (Anufriev and Hejda, 2010). Consequently, the rate of work done by the gravitational and buoyancy forces, as well as viscous dissipation are implicitly assumed small relative to the heat flux through the core; these terms, however, are not negligible in Earth's core heat budget (e.g. Anufriev et al., 2005). Boussinesq models are unlikely to be able to capture a thermodynamically consistent picture of core convection.

2.2 Plane layer convection

Rayleigh-Bénard convection (RBC), introduced in chapter 1, is the simplest configuration used to study thermal convection. RBC provides a framework from which we can gain insight into the physics underpinning convection. Simulations in a plane layer have a clear benefit over spherical shell calculations as they are significantly less computationally expensive and allow more extreme values of the control parameters to be used. Within this section, we will outline the mathematical formulation of convection in a plane layer and describe our numerical implementation of the mathematical model.

2.2.1 Governing equations

We solve the standard equations governing the conservation of mass, momentum and heat for thermal convection with and without rotation. Conservation of mass is given by the continuity equation,

$$\frac{\partial \rho}{\partial t} + \boldsymbol{\nabla} \cdot (\rho \boldsymbol{u}) = 0,$$

where $\boldsymbol{u}$ is the flow velocity. Under the Boussinesq approximation this reduces to

$$\boldsymbol{\nabla} \cdot \boldsymbol{u} = 0, \tag{2.2}$$

(e.g. Landau and Lifshitz, 1987). Equation (2.2) shows the velocity field to be solenoidal and the flow is incompressible.

The Navier-Stokes equation describes the conservation of momentum and in a frame of reference rotating with angular velocity, $\boldsymbol{\Omega}$, the Navier-Stokes equation relevant for our system is

$$\rho_0 \left(\frac{\partial \boldsymbol{u}}{\partial t} + (\boldsymbol{u} \cdot \boldsymbol{\nabla}) \boldsymbol{u} \right) + 2\rho_0 \boldsymbol{\Omega} \times \boldsymbol{u} = -\boldsymbol{\nabla} \widetilde{P} + \rho \boldsymbol{g} + \rho_0 \nu \nabla^2 \boldsymbol{u}, \tag{2.3}$$

where ν is the kinematic viscosity of the fluid. The relationship between ρ and ρ_0 is given in equation (2.1). The gravitational acceleration acts vertically downward, $\boldsymbol{g} = g\mathbf{1}_z$, and the system is rotated about the vertical, $\boldsymbol{\Omega} = \Omega \mathbf{1}_z$. The pressure, $\widetilde{P}$, has incorporated the centrifugal acceleration, $\rho_o |\boldsymbol{\Omega} \times \boldsymbol{r}|^2/2$, which arises from choosing a non-inertial reference frame (e.g. Pedlosky, 2013). Equation (2.3) is an expression of Newton's second law of motion; the advective derivative (first term on the LHS) evolves subject to the Coriolis, pressure gradient, buoyancy and viscous forces. In the absence of rotation, that is $\boldsymbol{\Omega} = 0$ in equation (2.3), the Navier-Stokes equation for non-rotating convection can be written as

$$\rho_0 \left(\frac{\partial \boldsymbol{u}}{\partial t} + (\boldsymbol{u} \cdot \boldsymbol{\nabla}) \boldsymbol{u} \right) = -\boldsymbol{\nabla} P + \rho \boldsymbol{g} + \rho_0 \nu \nabla^2 \boldsymbol{u}. \tag{2.4}$$

Assuming a thermal energy source the simplest energy conservation law is the temperature equation (e.g. Chandrasekhar, 1961),

$$\frac{\partial T}{\partial t} + (\boldsymbol{u} \cdot \boldsymbol{\nabla}) T = \kappa \nabla^2 T + S_T, \tag{2.5}$$

where κ is thermal diffusivity and S_T represents any internal sources of heat. In equation (2.5) we have neglected adiabatic heating and viscous dissipation as a consequence of the Boussinesq approximation (Anufriev et al., 2005).

The two main internal heat sources in a planetary core are radiogenic heating and secular cooling. Ab initio studies quantifying the effect of radiogenic elements (e.g. Potassium) suggest that given their concentration in Earth's core they are unlikely to contribute to the thermal evolution in a meaningful way (e.g. Xiong et al., 2018). Only purely bottom heated convection is considered in this thesis and any internal sources of heat (e.g. radioactive elements in the core) are neglected; moving forward we take $S_T = 0$.

To convert the governing equations into a more useful form we turn to dimensional analysis, which allows simulations and experiments to be compared on a like-for-like basis. For different values of the physical parameters within the governing equations (e.g. layer depth, temperature difference, etc) we would expect different resultant flows. Crucially,

it is the dimensionless groupings of these parameters that give rise to these different flows and the distinct regimes of behaviour outlined in figure 1.14 and table 1.4. By expressing the governing equations in dimensionless form, we are able to compare simulations and experiments that have different values of the physical parameters, on a like-for-like basis, based on the values of these dimensionless groupings.

To write equations (2.2) to (2.5) in dimensionless form we must scale each quantity by some characteristic scale; the relevant length scale of the system is the depth of the fluid layer, h, the characteristic timescale is the time for a thermal anomaly to diffuse through the system - the thermal diffusion time, h^2/κ, and we scale temperature by some scale denoted T^*. The treatment of the temperature scale, T^*, depends on the nature of the thermal boundary conditions; for fixed temperature boundaries the natural scale is the temperature difference between the two boundaries, $T^* \sim \Delta T = T_{\text{hot}} - T_{\text{cold}}$, whereas for fixed heat-flux boundaries we scale $T^* \sim \beta/h$, where β is the imposed vertical heat flux across the boundaries, $\beta = -\partial T/\partial z$. The two different configurations of thermal boundary conditions can be seen in figure 2.1.

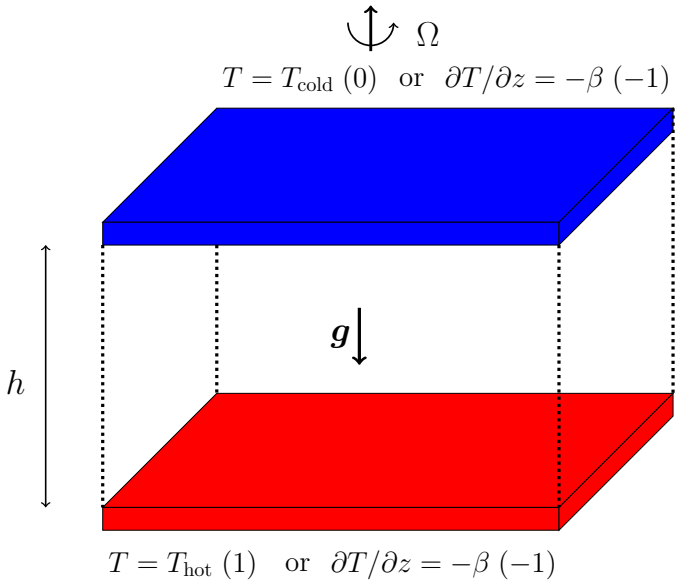

Figure 2.1: Convection cell, periodic in the horizontal, showing the different thermal boundary conditions: fixed temperature and fixed heat-flux. The boundary conditions are shown in dimensionless form with non-dimensional values given in brackets.

After a change of variables (achieved by scaling each quantity with its characteristic value) the non-dimensional governing equations are the conservation of mass,

$$\boldsymbol{\nabla} \cdot \boldsymbol{u} = 0, \tag{2.6}$$

conservation of energy,

$$\frac{\partial T}{\partial t} + (\boldsymbol{u} \cdot \boldsymbol{\nabla})\, T = \nabla^2 T, \tag{2.7}$$

and the conservation of momentum for either non-rotating (equation (2.8a)) or rotating

convection (equation (2.8b));

$$\frac{1}{Pr}\left(\frac{\partial \boldsymbol{u}}{\partial t}+(\boldsymbol{u}\cdot\boldsymbol{\nabla})\,\boldsymbol{u}\right)=-\boldsymbol{\nabla}P+\widehat{R}T'\mathbf{1}_z+\nabla^2\boldsymbol{u}, \tag{2.8a}$$

$$\frac{E}{Pr}\left(\frac{\partial \boldsymbol{u}}{\partial t}+(\boldsymbol{u}\cdot\boldsymbol{\nabla})\,\boldsymbol{u}\right)+\mathbf{1}_z\times\boldsymbol{u}=-\boldsymbol{\nabla}\widetilde{P}+E\widehat{R}T'\mathbf{1}_z+E\nabla^2\boldsymbol{u}. \tag{2.8b}$$

Although we use the same notation, note that all variables and operators are now dimensionless and unless specified we will consider dimensionless variables throughout the rest of the thesis. The control parameters are the Prandtl number,

$$Pr=\frac{\nu}{\kappa},$$

the Ekman number,

$$E=\frac{\nu}{2\Omega h^2},$$

and the thermal forcing parameter, $\widehat{R}$. The definition of $\widehat{R}$ is a measure of the imposed thermal forcing and depends on the thermal boundary conditions. When the boundaries are held at fixed temperatures the forcing parameter is the standard Rayleigh number

$$\widehat{R}=Ra=\frac{\alpha g\Delta T h^3}{\nu\kappa}. \tag{2.9}$$

In contrast, when a vertical heat flux is maintained, in place of equation (2.9) we have the flux-Rayleigh number

$$\widehat{R}=Ra_F=\frac{\alpha\beta g h^4}{\nu\kappa}. \tag{2.10}$$

2.2.2 Boundary conditions

The conservation laws for mass, momentum and energy need to be solved subject to a sufficient number of boundary conditions. The RBC paradigm is horizontally periodic with the fluid layer confined between impermeable top and bottom boundaries located at $z=\pm L_z/2=\pm 1/2$. For the top and bottom boundaries we implement the two standard choices for both the thermal and mechanical boundary conditions, which we discuss here.

Thermal boundary conditions

The two classical choices for the thermal boundary conditions are those of prescribing a fixed temperature at the boundaries or prescribing a fixed heat-flux (see figure 2.1). As discussed in chapter 1 both choices are warranted; with fixed temperature boundaries commonly used in laboratory experiments and the fixed heat-flux condition being relevant to Earth's core.

Isothermal boundaries are defined as

$$T = 1, 0 \quad \text{at} \quad z = \mp 1/2, \tag{2.11}$$

and fixed heat-flux boundary conditions state

$$\frac{\partial T}{\partial z} = -1 \quad \text{at} \quad z = \pm 1/2. \tag{2.12}$$

Our non-dimensional thermal boundary conditions are the same as those of Johnston and Doering (2009).

Mechanical boundary conditions

For laboratory convection or the interaction between the fluid core and solid mantle, the fluid-solid interface is described by the no-slip condition at the boundaries,

$$\boldsymbol{u} = 0 \quad \text{at} \quad z = \pm L_z/2. \tag{2.13}$$

The requirement of the velocity vanishing on the boundary ($\boldsymbol{u} = 0$) leads to the development of thin viscous boundary layers within which $\boldsymbol{u}$ changes rapidly from the free-stream value to the value on the boundary (e.g. Landau and Lifshitz, 1987). For non-rotating convection these boundary layers are of the Prandtl-Blasius type (Prandtl, 1905; Blasius, 1908) and are characterised by the balance of inertia in the fluid bulk with viscous effects in the boundary layer. When rotation is present the mechanical boundary layer is of the Ekman type and within the Ekman layer, the Coriolis force balances viscosity leading to Ekman pumping effects (e.g. Greenspan, 1968; Zhang and Liao, 2017). We gave details of boundary layers in both non-rotating and rotating convection in subsection 1.3.1 and subsection 1.3.2, respectively.

If a fluid-fluid interface is considered or viscous effects are assumed to be negligible, the appropriate choice of mechanical boundary conditions are free-slip. The free-slip condition requires tangential stress to vanish on the boundaries (e.g. Batchelor, 2000). For an impenetrable boundary with free-slip conditions, the velocity, $\boldsymbol{u} = [u_x,\ u_y,\ u_z]$, must satisfy

$$\frac{\partial u_x}{\partial z} = 0,\ \frac{\partial u_y}{\partial z} = 0,\ u_z = 0 \quad \text{at} \quad z = \pm 1/2. \tag{2.14}$$

In contrast to the no-slip case, the free-slip condition does not force rapid changes in $\boldsymbol{u}$ near the boundary and the classical mechanical boundary layers are not present.

2.2.3 Numerical implementation

The governing equations describing the conservation of momentum (equations (2.8a) and (2.8b)), mass (equation (2.6)) and energy (equation (2.7)) are continuous and need to be discretised in both time and space in order to be solved numerically. Typically, the

choice of one numerical scheme over another is determined by accuracy, stability, memory requirements and efficiency. Methods for evaluating accuracy and stability exist; however, these criteria can only be estimated for simple model equations (e.g. Ashgriz and Mostaghimi, 2002).

Of the different numerical approaches to spatial discretisation the most straightforward would be to use a local scheme such as finite differences or finite volumes (Anderson et al., 2016). Local grid-based methods are appealing as they only require local communication, making them capable of large scale parallelisation. In spite of this, global spectral methods prove to be more suitable when the solution varies significantly with time or space, when very long time integration is needed, or when high spatial resolution is necessary (Cheng and Brebbia, 2015). Spectral methods expand the dependent variables in orthogonal functions providing information everywhere (not just at the grid points) and provide very high accuracy. For N grid points in real space, the error is $\mathcal{O}(e^{-N})$ decreasing with increasing resolution far quicker than any polynomial (Gottlieb and Orszag, 1977). Expressing variables in their spectral form makes for exact computation of derivatives. However, the formation of nonlinear terms is computationally expensive in spectral space, as convolutions are required. Instead, multiplications to form the nonlinear terms are carried out in physical space before the resulting product is transformed back to spectral space to continue with the time marching. It is for this reason that the method is termed pseudospectral, as opposed to fully spectral, where nonlinear terms are calculated in spectral space. Much lower resolution is needed for spectral methods relative to local methods (to achieve the same level of accuracy) and this results in a considerable reduction of memory and computational time, especially for three-dimensional problems.

If the problem size and number of processors used becomes sufficiently large, local methods should become more efficient than global methods however it is unclear if this takeover could materialize at realistic conditions. The pseudospectral method still performs competitively with the computational resources currently available and is by far the most popular choice for simulating convection and dynamo action (Matsui et al., 2016).

In this thesis we only consider pseudo-spectral methods. Our plane layer simulations are performed using the open-source pseudospectral code Dedalus (Burns et al., 2020, also see `http://dedalus-project.org`). Dedalus is a framework for solving partial differential equations using spectral methods and has been widely applied to convection (Couston et al., 2018; Tobias et al., 2018; Currie and Tobias, 2019; Vallis et al., 2019). Here we will describe the spatial and temporal discretisation schemes that we use for our simulations.

Spatial discretisation

Spatial discretisation is achieved using a Fourier-Chebyshev pseudospectral method outlined in many texts; see e.g. Boyd (2001); Quarteroni et al. (2006); Glatzmaier (2013). The development of efficient Fast Fourier Transform (FFT) algorithms on which spectral methods are built, are key to their efficiency (Frigo and Johnson, 2005).

A spectral method consists of expressing the dependent variables as a combination of time-independent, spatially varying basis functions. A transform, built around the FFT, is used to translate between physical variables evaluated at grid points and spectral coefficients.

Our domains are horizontally periodic and the natural choice of basis functions is then a Fourier basis in the horizontal coordinate(s). Here we show the methodology for the horizontal coordinate, x. Fourier bases consist of complex exponential modes,

$$\phi_k(x) = \exp(ikx), \tag{2.15}$$

defined over the (native) interval $[0, 2\pi]$ for wavenumbers, k. The governing equations are discretised and solved on a uniformly spaced grid given by

$$x_g = \frac{2\pi g}{N_h}, \quad g = 0, \ \ldots, \ N_h - 1. \tag{2.16}$$

The number of grid points is denoted as N_h (with the subscript h denoting horizontally). Each quanitity, f, is represented as a symmetric sum over both positive and negative wavenumbers

$$f(x) = \sum_{-k_m}^{k_m} f_k \phi_k(x), \tag{2.17}$$

where k_m is the maximum resolved wavenumber, $k_m = \left\lfloor \dfrac{N_c - 1}{2} \right\rfloor$, and N_c is the number of modes kept in the Fourier expansion. The expansion coefficients are given explicitly by

$$f_k = \frac{1}{N_h} \sum_{g=0}^{N_h - 1} f(x_g)\phi_k(x_g) \tag{2.18}$$

and are computed using the FFT. Dedalus uses the FFTW python libraries (Burns et al., 2020) and rescales the results to our normalisation.

For the finite non-periodic vertical direction we use a Chebyshev basis which has an uneven grid spacing and has increased resolution near the boundaries. The Chebyshev-T polynomials expanded in z are given by

$$T_n(z) = \cos\left(n \arccos(z)\right), \tag{2.19}$$

defined on the (native) interval $[-1, 1]$ for order, n. The polynomials T_n are not to be

confused with temperature, T. This grid uses the Gauss-chebyshev quadrature nodes (interior grid)

$$z_g = -\cos\left(\frac{\pi(g+1/2)}{N_\mathrm{v}}\right), \quad g = 0,\ \ldots,\ N_\mathrm{v}-1. \tag{2.20}$$

The number of grid points in the vertical is denoted N_v. Towards the centre of the interval, the grid approaches being uniformly distributed with $\delta z \approx \pi/N_\mathrm{v}$ whilst towards the ends of the interval the grid points cluster quadratically allowing fine boundary layer gradients to be resolved (see figure 2.2).

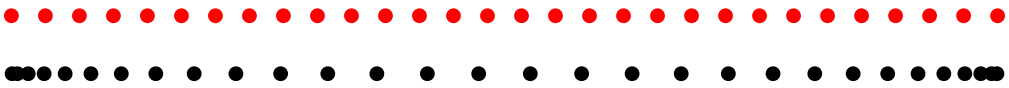

Figure 2.2: Examples of a uniformly spaced grid (red markers) and non-uniform grid based on the Chebyshev zeroes (black markers); 30 grid points are shown in each case. The latter shows clustering toward the edges of the domain.

Each function, f, is represented as

$$f(z) = \sum_{n=0}^{N_c-1} f_n T_n(z). \tag{2.21}$$

The expansion coefficients are given explicitly by

$$f_n = \frac{2-\delta_{n,0}}{N_\mathrm{v}} \sum_{g=0}^{N_\mathrm{v}-1} f(z_g) T_n(z_g), \tag{2.22}$$

where δ_{ij} is the Kronecker delta. These coefficients are transformed using a change of variables, $z = \cos(\theta)$, and are computed using the discrete cosine transform implemented within FFTW.

Temporal discretisation

The treatment of strong nonlinearities in the governing equations typically demand high order time-stepping methods. Implicit schemes offer increased stability allowing for large time steps, however larger matrices need to be inverted at each timestep. Temporal discretisation is typically achieved through a mixed implicit-explicit scheme and we use a Runge-Kutta (RK) method. We use a method referred to as RK443, which combines four stage diagonally implicit RK with four stage explicit RK and is third order accurate (Ascher et al., 1997).

Linear terms (pressure gradient, Coriolis, buoyancy and viscous terms in the

momentum equation) are treated implicitly, whilst nonlinear terms are treated explicitly to reduce the size of the resultant matrices. The governing constraint on the timestep is the Courant-Friedrichs-Lewy (CFL) condition which dictates the stable timestep size, Δt, as a function of spatial resolution, Δh (e.g. Anderson et al., 2016). The CFL condition,

$$\Delta t = A_{\mathrm{CFL}} \min(\Delta h/|\boldsymbol{u}|), \quad 0 < A_{CFL} < 1 \tag{2.23}$$

enforces the constraint that the timestep must be be less than the time taken for fluid to flow between two adjacent grid points (Courant, 1928).

2.2.4 Convergence criteria

All numerical studies must ensure that the results are properly converged. Numerical resolution in direct numerical simulations (DNS) of convection is vital in capturing the small scale plumes emitted from the thermal boundary layers (Grötzbach, 1983; Stevens et al., 2010). In this section we outline the tests that ensure we have sufficient spatial and temporal resolution for each of our simulations. The criteria determined to test if a simulation is well converged rely on time-averaged quantities; this temporal averaging is necessary due to the transient behaviour of the solutions.

All of our simulations are initialised from rest with a conductive profile to which we impose small random perturbations to the temperature field. Once run for a sufficient amount of time, the transient response to the initial condition is passed; for unsteady convection, the solution tends to settle to some statistically-steady state about which it fluctuates (see figure 2.3). Meaningful statistics can only be obtained if the simulations are run for a sufficiently long duration which does not include the initial transient.

The governing equations are non-dimensionalised using the thermal diffusion time, $\tau_d = h^2/\kappa$, however in the fully nonlinear regime it is more useful to think in terms of advective time units. An advection time unit is the time taken for a parcel of fluid to traverse the layer, $\tau_a = h/U$, with U being the characteristic flow velocity. The Peclét number, Pe, is the ratio of time scales and allows conversion to advection time units, $Pe = RePr = \tau_d/\tau_a$ (the Reynolds number, Re, is defined in chapter 1). All models are averaged for at least 100 advective time units. An example of a time averaging period can be seen in figure 2.3 which shows the trace of kinetic energy. We denote time averaged quantities with an overbar,

$$\overline{f} = \frac{1}{\Delta t}\int_{t_0}^{t_0+\Delta t} f \, \mathrm{d}t.$$

The first measure of convergence we will discuss is based on conservation of energy. For Boussinesq convection there is a simple yet exact relation for the conservation of energy termed the *mean kinetic energy balance*. Taking the scalar product of velocity

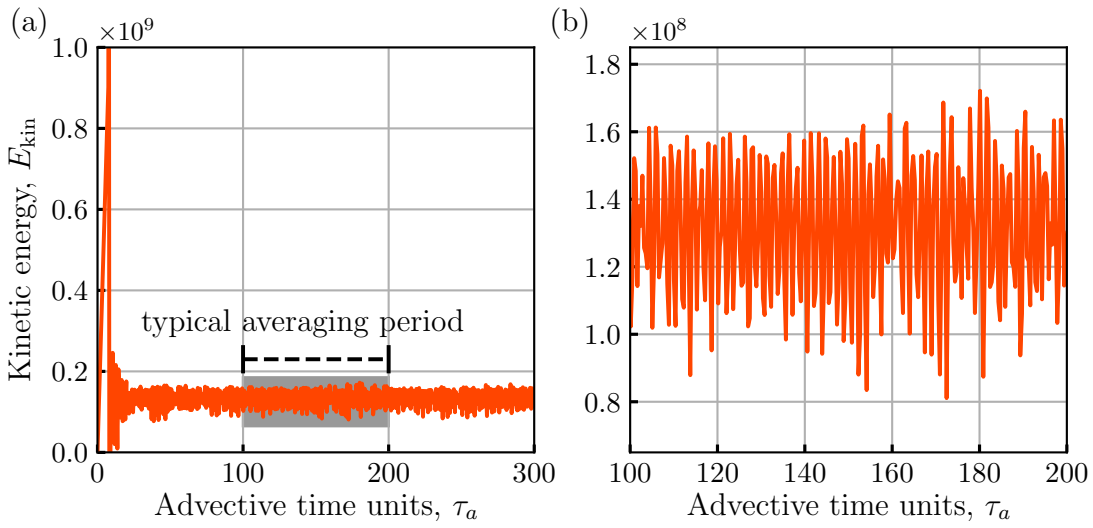

Figure 2.3: Trace of kinetic energy for Rayleigh-Bénard convection with fixed temperature boundaries, $Ra = 10^7$ and $Pr = 1$. A typical averaging period is highlighted in (a) with the grey shaded region being magnified in (b).

with the momentum equation (equations (2.8a) and (2.8b)) and averaging in both time and over the fluid volume, V, the mean energy equation for both non-rotating and rotating convection is

$$\int_V \underbrace{\widehat{R}\overline{Tu_z}}_{B_P} - \underbrace{\overline{(\boldsymbol{\nabla}\times\boldsymbol{u})^2}}_{\epsilon_\nu}\,\mathrm{d}V = 0, \tag{2.24}$$

where $\widehat{R}$ is the thermal forcing parameter which depends on the thermal boundary conditions (subsection 2.2.1). This shows a balance between buoyant energy production, B_P, and viscous dissipation, ϵ_ν. A model is considered well converged if the residual balance between these two terms is less than 1% (e.g. King et al., 2012, 2013). We show the percentage error of these two terms,

$$E_{\text{err}} = 100 \cdot \frac{|B_P - \epsilon_\nu|}{B_P}$$

for our non-rotating RBC simulations in figure 2.4a. We see in figure 2.4a that the error increases with increasing supercriticality, Ra/Ra_c. This occurs because at larger values of Ra/Ra_c the convection is more turbulent and larger fluctuations can occur in a more sporadic manner; increased averaging periods are necessary to satisfy our convergence criteria. Note that if the larger Ra/Ra_c simulations were run for longer, then the error would decrease further.

Alongside mechanical equilibrium, we check that the system is in thermal equilibrium by testing the conservation of vertical heat-flux, which is quantified by different definitions of the Nusselt number. For simulations with fixed temperature boundaries, thermal equilibrium is checked by comparing the heat fluxes through the top and bottom

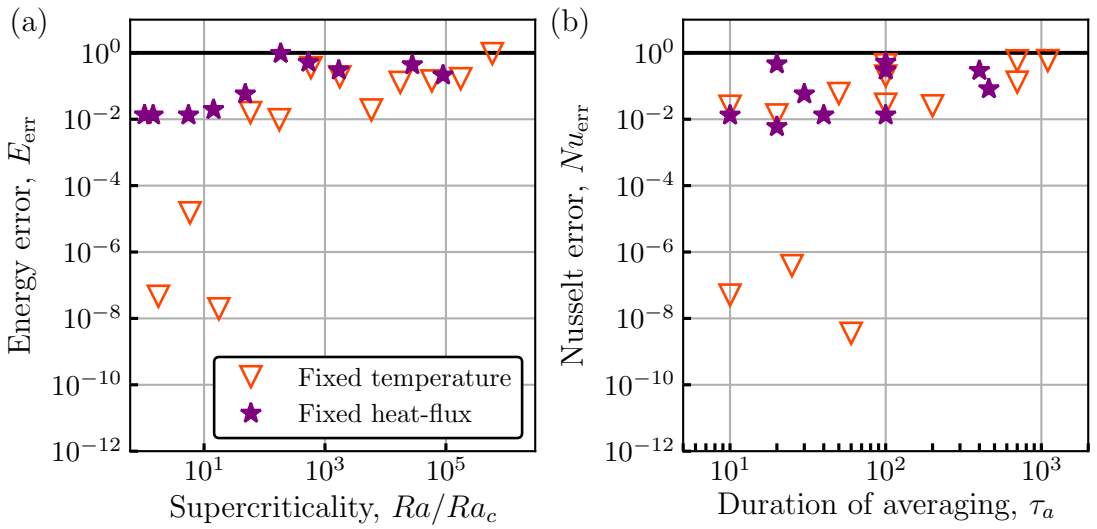

Figure 2.4: Convergence for the non-rotating Rayleigh-Bénard convection simulations with $Pr = 1$. We show (a) the residual error of the balance of kinetic energy production and viscous dissipation (equation (2.24)) versus supercriticality and (b) the residual error of the Nusselt number (equation (2.26)) versus duration of temporal averaging. The black lines correspond to a residual of 1%.

boundaries and the volumetric average,

$$Nu_{t,b} = \left.\frac{\partial\langle\overline{T}\rangle}{\partial z}\right|_{z=\pm 1/2}, \quad Nu_V = \int_V \overline{u_z T + \frac{\partial T}{\partial z}}\, dV, \tag{2.25}$$

the subscripts t, b and V correspond to the top boundary, bottom boundary and volume averaged values, respectively. Figure 2.4b shows the residual error, Nu_{err}, defined as

$$Nu_{\text{err}} = 100 \cdot \frac{\max(|Nu_t - Nu_V|,\ |Nu_t - Nu_b|,\ |Nu_b - Nu_V|)}{Nu_V} \tag{2.26}$$

for all non-rotating simulations driven by isothermal boundaries.

When convection is driven by boundaries prescribed a fixed heat-flux, increasing the Rayleigh number increases the efficiency of convective mixing which leads to a decrease in the temperature drop, ΔT, across the fluid layer (Goluskin, 2016). The Nusselt number is then inversely proportional to ΔT (e.g. Otero et al., 2002)

$$Nu_F = \frac{1}{\Delta T}. \tag{2.27}$$

We ensure that for all simulations with fixed heat-flux boundaries that Nu_F agrees with Nu_V to within 1%, see figure 2.4b.

We compute the thickness of the mechanical boundary layers based on the location of the local maxima in the vertical profile of horizontal velocity, $U_h = \sqrt{u_x^2 + u_y^2}$ (e.g. King et al., 2013), or $U_h = |u_x|$ in 2D. For all simulations there are at least 10 points in

both boundary layers with most simulations having roughly double this; the details of all simulations presented in this thesis are given in appendix A. This resolution is thought to be sufficient for boundary layers in RBC (e.g. Stevens et al., 2010).

2.3 Spherical shell convection

In this section we consider convection in a rotating spherical shell. The spherical shell is defined in spherical coordinates, (r, θ, ϕ), by the inner and outer boundaries located at radii, r_i, and r_o, respectively. The spherical shell geometry is characterised by the radius ratio, $r_i/r_o = 0.35$ which is chosen as to best match Earth's core. In all cases the spherical shell is considered to rotate uniformly about the vertical axis, $\boldsymbol{\Omega} = \Omega \mathbf{1}_z$.

2.3.1 Governing equations

The equations governing convection in a rotating spherical shell take a similar form to that of the plane layer cases discussed previously. Conservation of mass, momentum and energy are described, respectively, by

$$\boldsymbol{\nabla} \cdot \boldsymbol{u} = 0, \tag{2.28}$$

$$\frac{E}{Pr}\left(\frac{\partial \boldsymbol{u}}{\partial t} + (\boldsymbol{u} \cdot \boldsymbol{\nabla})\,\boldsymbol{u}\right) + \boldsymbol{\Omega} \times \boldsymbol{u} = -\boldsymbol{\nabla} P + \widehat{R} E T' \boldsymbol{r} + E \nabla^2 \boldsymbol{u}, \tag{2.29}$$

$$\frac{\partial T}{\partial t} + (\boldsymbol{u} \cdot \boldsymbol{\nabla})\, T = \nabla^2 T \tag{2.30}$$

where T' is the temperature fluctuation about the conductive profile and $\widehat{R}$ is the thermal forcing parameter. The appropriate form of the gravitational acceleration for Earth's core acts radially and varies linearly with radius such that $\boldsymbol{g} = -(g_o/r_o)\boldsymbol{r}$, where g_o is the gravitational acceleration at the outer boundary, radius r_o. The control parameters of the system are the Ekman number, E, and Prandtl number, Pr, (defined in subsection 2.2.1) and the thermal forcing parameter, $\widehat{R}$, is given by either

$$\text{fixed temperature}: \quad \widehat{R} = Ra = \frac{\alpha g_o \Delta T h^3}{\nu \kappa},$$

$$\text{fixed heat flux}: \quad \widehat{R} = Ra_F = \frac{\alpha g_o \beta h^2}{\nu \kappa}$$

2.3.2 Boundary conditions

In all spherical simulations we consider rigid impenetrable boundaries and implement the no-slip condition

$$\boldsymbol{u} = 0 \quad \text{at} \quad r = r_i,\, r_o.$$

The majority of our simulations employ fixed heat-flux thermal boundary conditions but in chapter 5 we compare the results with convection driven between fixed temperature boundaries. Fixed heat-flux conditions are given by

$$\frac{\partial T}{\partial r} = \beta \quad \text{at} \quad r = r_i,\, r_o,$$

and for fixed temperature we have

$$T = T_i,\, T_o \quad \text{at} \quad r = r_i,\, r_o.$$

2.3.3 Numerical implementation

In this work the pseudospectral *Leeds Spherical Dynamo* (LSD) Code (Willis et al., 2007) is used for all numerical simulations in spherical geometry. The Leeds Spherical Dynamo has been used in many studies of both hydrodynamic (e.g. Davies et al., 2013; Mound and Davies, 2017) and magnetic convection (e.g. Jones et al., 2011; Hori et al., 2018) and passes the dynamo benchmark of Christensen et al. (2001). The pseudospectral method employed by the LSD will be outlined here and a detailed description of the pseudospectral method can be found in Willis et al. (2007); Davies et al. (2011).

The fluid velocity is divergent-free (equation (2.28)) and can be decomposed into toroidal and poloidal parts (Backus, 1958),

$$\boldsymbol{u} = \boldsymbol{\nabla} \times (\mathcal{T}\boldsymbol{r}) + \boldsymbol{\nabla} \times \boldsymbol{\nabla} \times (\mathcal{P}\boldsymbol{r}), \tag{2.31}$$

where $\mathcal{T}$ and $\mathcal{P}$ represent the toroidal and poloidal scalars, respectively. The toroidal–poloidal decomposition identically satsfies the incompressibility condition while reducing the number of scalar equations for $\boldsymbol{u}$ from three to two. A toroidal field does not have a radial component and is confined within the sphere; we show examples of torioidal and poloidal field lines in figure 2.5. It is clear that the curl of a toroidal field is poloidal, but the reverse is also true (Gubbins and Roberts, 1987).

The components $\boldsymbol{u} = [u_r,\, u_\theta,\, u_\phi]$ can be recovered from $\mathcal{T}$ and $\mathcal{P}$ by

$$u_r = -r\nabla_H^2 \mathcal{P}, \tag{2.32}$$

$$u_\theta = \frac{1}{\sin(\theta)}\frac{\partial \mathcal{T}}{\partial \phi} + \frac{1}{r}\frac{\partial}{\partial r}\left(\frac{\partial \mathcal{P}}{\partial \theta}\right), \tag{2.33}$$

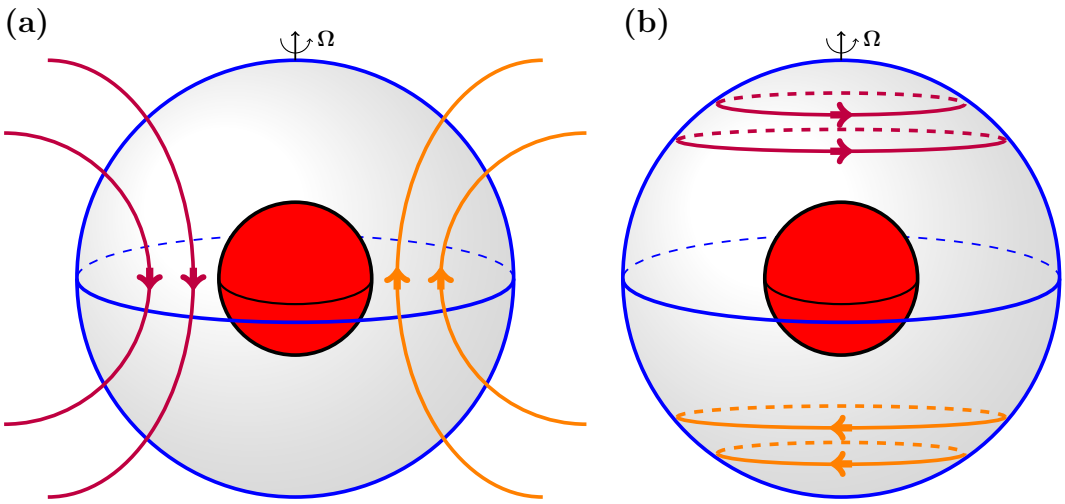

Figure 2.5: Illustration of the poloidal-toroidal decomposition in a spherical shell with (a) poloidal and (b) toroidal field lines shown in orange and purple. The orange and purple curves show field lines in opposite directions.

$$u_\phi = -\frac{\partial \mathcal{T}}{\partial \theta} + \frac{1}{r\sin(\theta)}\frac{\partial}{\partial r}\left(r\frac{\partial \mathcal{P}}{\partial r}\right), \tag{2.34}$$

here ∇_H^2 is the horizontal Laplacian,

$$\nabla_H^2 = \frac{1}{r^2\sin(\theta)}\frac{\partial}{\partial \theta}\left(\sin(\theta)\frac{\partial}{\partial \theta}\right) + \frac{1}{r^2\sin^2(\theta)}\frac{\partial^2}{\partial^2 \phi}. \tag{2.35}$$

In standard procedure we operate with $\boldsymbol{r}\cdot\boldsymbol{\nabla}\times$ and $\boldsymbol{r}\cdot\boldsymbol{\nabla}\times\boldsymbol{\nabla}\times$ on the momentum equation (equation (2.29)) resulting in two scalar equations. It is important to note that by taking the curl of the momentum equations the pressure gradient vanishes.

Spatial discretisation

For the spherical simulations spatial discretisation is achieved by using spherical harmonics on each spherical surface and in radius we employ a finite difference scheme.

The toroidal, poloidal and temperature scalars are expanded in series of orthogonal functions with spherical harmonics being the natural choice,

$$\psi(r,\theta,\phi,t) = \sum_{l=0}^{\infty}\sum_{m=0}^{\infty}\psi_l^m(r,t)Y_l^m(\theta,\phi). \tag{2.36}$$

Here $\psi \in \{\mathcal{T},\mathcal{P},T\}$ and ψ_l^m are coefficients for each of the dependent variables. The spherical harmonics $Y_l^m(\theta,\phi)$ are given by

$$Y_l^m(\theta,\phi) = P_l^m\left(\cos(\theta)\right)\exp(im\phi). \tag{2.37}$$

The associated Legendre functions of degree, l, and order, m, are denoted P_l^m. Harmonics with $l = m = 0$ are zero for $\boldsymbol{u}$ due to incompressibility (equation (2.28)). The spherical harmonic expansion makes use of Schmidt normalisation (McElhinny and McFadden, 1998)

$$\begin{aligned}\int_0^{2\pi}\int_0^{\pi} Y_l^m(\theta,\phi)Y_o^n(\theta,\phi)\sin(\theta)\,\mathrm{d}\theta\,\mathrm{d}\phi &= 0, \quad l \neq o, \quad m \neq -n \\ &= 2\pi\frac{2(2-\delta_{m0})}{2l+1}, \quad \text{otherwise,}\end{aligned} \tag{2.38}$$

where δ_{ij} is the Kronecker delta.

To represent the radial variation of the unknowns we employ a second order finite difference scheme. Instead of using regularly spaced grid points, we place the grid points at the zeroes of the Chebyshev polynomals. These polynomials cluster points close to the boundaries which is a desirable property for resolving the sharp gradients within the boundary layers.

Linear parts of the code are evaluated in spectral space by operating on spherical harmonic coefficients as these operations do not couple harmonic modes. Nonlinear terms and radial derivatives are evaluated in physical space and transformed back to spectral space using the spherical transform method (Orszag, 1971), the spherical transform is the most computationally intensive operation performed at each time step. Once all quantities are transformed to spectral space, this is also where timestepping is conducted.

Temporal discretisation

Time stepping is performed in spectral space using a predictor-corrector scheme (e.g. Anderson et al., 2016). The nonlinear terms, as well as the Coriolis and Archimedean terms are treated explicitly with diffusion terms being treated implicitly.

2.3.4 Convergence criteria

We use the same criteria outlined for the plane layer simulations. The time averaged quantities are obtained after averaging solutions (typically) for 100 advective time units, however, this is too computationally expensive for the most demanding runs which are averaged for at least ten advection times. The spherical shell models are checked to be in energetic equilibrium with the balance in equation (2.24) satisfied to within 1% (all simulations are summarised in appendix A).

The expression of thermal equilibrium for the spherical shell cases is slightly different from the plane layer discussed before. We test the Nusselt number expressed in

terms of fluxes, Nu_F, with the definition based on the global temperature difference, Nu_T,

$$Nu_F = \frac{\langle\langle \overline{\boldsymbol{q}} \cdot \mathbf{1}_r \rangle_H \rangle_r}{\left\langle -\partial \langle \overline{T} \rangle_H / \partial r \right\rangle_r}, \quad Nu_T = \frac{\Delta T_c}{\Delta \langle \overline{T} \rangle_H}, \tag{2.39}$$

where T_c is the conductive temperature profile (the temperature profile in the absence of flow). Averages over spherical surfaces and in the radial direction are respectively denoted by

$$\langle f(r,\theta,\phi) \rangle_H = \frac{1}{4\pi r^2} \int_0^{\pi} \int_0^{2\pi} f(r,\theta,\phi)\, r^2 \sin(\theta)\, \mathrm{d}\phi\, \mathrm{d}\theta,$$

$$\langle f(r) \rangle_r = \frac{1}{h} \int_{r_i}^{r_o} f(r) \mathrm{d}r.$$

For fixed heat–flux convection Nu_T has the temperature drop across the fluid layer, ΔT, on the denominator as increasing vigour of convection acts to reduce the temperature difference across the fluid layer (see also Goluskin, 2016)

2.4 Statistical methods

One of this work's main goals is to characterise convection through scaling law analysis. We will empirically determine scaling laws which are compared against theoretical predictions derived from the governing equations. The best fit laws are computed using a least squares inversion. The control parameters are varied over orders of magnitude and so we restrict our analysis to power laws of the form

$$\hat{\mathcal{Y}} = \gamma_0 \prod_{j=1}^{p-1} x_j^{\gamma_j}.$$

If we consider an example; our system uses a fixed radius ratio and Prandtl number and we want to identify the behaviour of the Nusselt number as

$$Nu = \gamma_0 Ra^{\gamma_1} E^{\gamma_2}.$$

Simulation output is collected in $\mathcal{Y}$ and predictions $\hat{\mathcal{Y}}$ are calculated from the independent variables x_j. The number of data, n, is the size of $\mathcal{Y}$ and the number of free parameters is p (prefactor and exponents). We take the logarithm to transform this into a linear problem such that

$$\log|\hat{\mathcal{Y}}| = \log|\gamma_0| + \sum_{j=1}^{p-1} \gamma_j \log|x_j|.$$

The least-squares inversion is used to calculate the prefactor γ_0 and exponents γ_j. We quantify the goodness-of-fit for the scaling laws using the coefficient of determination, R^2 (rounded to two decimal places). As another method of measuring the misfit between data and fitted values, we define the mean relative misfit (Christensen and Aubert, 2006)

to the original data $\mathcal{Y}$,

$$\chi = 100\sqrt{\frac{1}{n}\sum_{i=1}^{n}\left(\frac{\mathcal{Y}_i - \hat{\mathcal{Y}}_i}{\mathcal{Y}_i}\right)^2}. \tag{2.40}$$

For cases where the R^2 and χ values are not reported, they satisfy $R^2 \geq 0.97$ and $\chi < 5\%$ and are considered to be good fits to the data. When two scaling laws do similarly well at describing the model data we compare the scaling laws quantitatively through statistical F-tests (Snedecor and Cochran, 1989). An F-test checks if two scalings can be distinguished by testing their misfits against the null hypothesis that they have equal variance (to within some tolerance). We take the ratio of the residual variances from the two scalings and compare with the 95% confidence interval from an F-distribution with the same degrees of freedom as the model populations (Snedecor and Cochran, 1989).

2.5 Summary

In this chapter, we have outlined the mathematical formulation and numerical implementation we use to simulate thermal convection with and without rotation in Cartesian and spherical shell geometries. The simulations presented in the following results chapters all satisfy the convergence criteria we outline here, with the solutions being in thermal and energetic equilibrium. We also ensure sufficient spatial resolution to resolve the thin boundary layers that form close to the non-penetrable boundaries.

The plane layer simulations are introduced in chapter 3 and spherical shell models are in chapter 4 with both revisited in chapter 5.

Chapter 3

Defining the thermal boundary layer in convection with and without rotation

3.1 Introduction

Thermally driven flows are important in many natural settings including planetary atmospheres (Heimpel et al., 2005), solar and stellar bodies (Miesch, 2000), and Earth's liquid metal outer core (Braginsky and Roberts, 1995). Turbulent rotating convection is responsible for internally generated magnetic fields (Busse, 2002) and the emitted heat flux patterns of planets and stars (Heimpel et al., 2005). However, the convective state of these systems cannot be reproduced by numerical or physical experiments owing to the vast range of spatial and temporal scales that need to be resolved. It is common practice to study the idealised system of Rayleigh-Bénard convection (RBC), however, to understand real systems we must incorporate the effects of rotation and different boundary conditions.

Historically, the dynamics of RBC has been characterised by the heat transfer owing to the ease of using temperature sensors in laboratory experiments (Rossby, 1969; Funfschilling et al., 2005; Aurnou, 2007). The majority of studies assume global heat transport dynamics implicitly describe the bulk dynamics, however, more recent studies conclude that the convective heat transport is determined by the boundary layer processes (King et al., 2009; Stellmach et al., 2014; Julien et al., 2012a). The theoretical framework of Grossmann and Lohse (2000) describes the heat transport in RBC over a large range of parameter space by explicitly separating the dissipation contributions from the boundary layer and fluid bulk (Grossmann and Lohse, 2000, 2002, 2011). In rotating RBC two regimes of heat transport exist, one being rotationally constrained and one weakly rotating resembling RBC. This transition is thought to be described by the dynamics of the thermal boundary layer; two key arguments include that of King et al. (2009) who sug-

gested that the transition to the weakly rotating regime occurs when the thermal boundary layer becomes thinner than the mechanical boundary layer and Julien et al. (2012b) who proposed that the transition occurs when the thermal boundary layer loses geostrophic balance. The approach presented in this chapter is to consider the thermal boundary layer in isolation, this is in some sense only a first step. The thermal and mechanical boundary layers overlap and interact with one-another dynamically, robust boundary layer definitions set the groundwork for in depth studies which can better capture these dynamical interactions which are intimately linked to flow transitions. To elucidate the physics of flow transitions in thermal convection it would be useful to have a robust definition of the thermal boundary layer that can be broadly applied to different configurations.

We consider Rayleigh-Bénard convection (RBC) with and without rotation. For a fixed aspect ratio, the non-dimensional parameters governing the non-rotating system are the Rayleigh number, Ra, characterising the importance of buoyancy forcing to viscous effects, and the Prandtl number, Pr, the ratio of the viscous and thermal diffusivities, given respectively as

$$Ra = \frac{\alpha g \Delta T h^3}{\nu \kappa}, \; Pr = \frac{\nu}{\kappa}. \tag{3.1}$$

α denotes the thermal expansion coefficient, g the gravitational acceleration, ν the kinematic viscosity, and κ the thermal diffusivity. An in-depth overview of RBC and the mathematical formulation are given in chapter 2. Convective fluid motions transport heat across the fluid layer and their efficiency is quantified by the Nusselt number, Nu, defined as the ratio of total heat transport to that by conduction alone. The Nusselt number is defined as

$$Nu = \frac{qh}{k\Delta T} \tag{3.2}$$

where q is the heat flux and k is the fluid's thermal conductivity.

In the absence of rotation, turbulent convection mixes the fluid bulk and the temperature within the interior becomes more isothermal as Ra is increased. For Boussinesq convection the entire temperature drop across the fluid layer is then accommodated by the (nearly) symmetric thermal boundary layers (TBLs). In this idealised case, the amount of heat transported across the layer can be related to the thickness of the TBL, δ. Within the TBL, heat transport is purely conductive and so we expect (Malkus, 1954; Spiegel, 1971)

$$\frac{\delta}{h} \sim \frac{1}{2Nu}. \tag{3.3}$$

The thermal boundary layers are laminar (and conductive) over the range of Ra investigated in this study.

An important issue in the study of convective fluid dynamics is then to determine the thickness of the TBL and the corresponding temperature distribution within the TBL. Estimates of the TBL originally started in non-rotating convection experiments using moderate Pr fluids such as water. Two methods have been widely used to define δ relying on either the temporally and horizontally averaged temperature profile, ϑ, or on

the root-mean-square temperature fluctuation, σ. In the first method, which we refer to as 'linear intersection', the extrapolation of the linear portion of ϑ near the boundary to the isothermal value defines δ (Belmonte et al., 1994; Verzicco and Camussi, 1999; Breuer et al., 2004; Liu and Ecke, 2011). The second method, termed 'local maxima' defines δ by the location of the local maxima in the σ profile (Tilgner et al., 1993; King et al., 2012, 2013). An example of both methods can be seen in figure 3.1(a) which shows the TBL of a numerical solution.

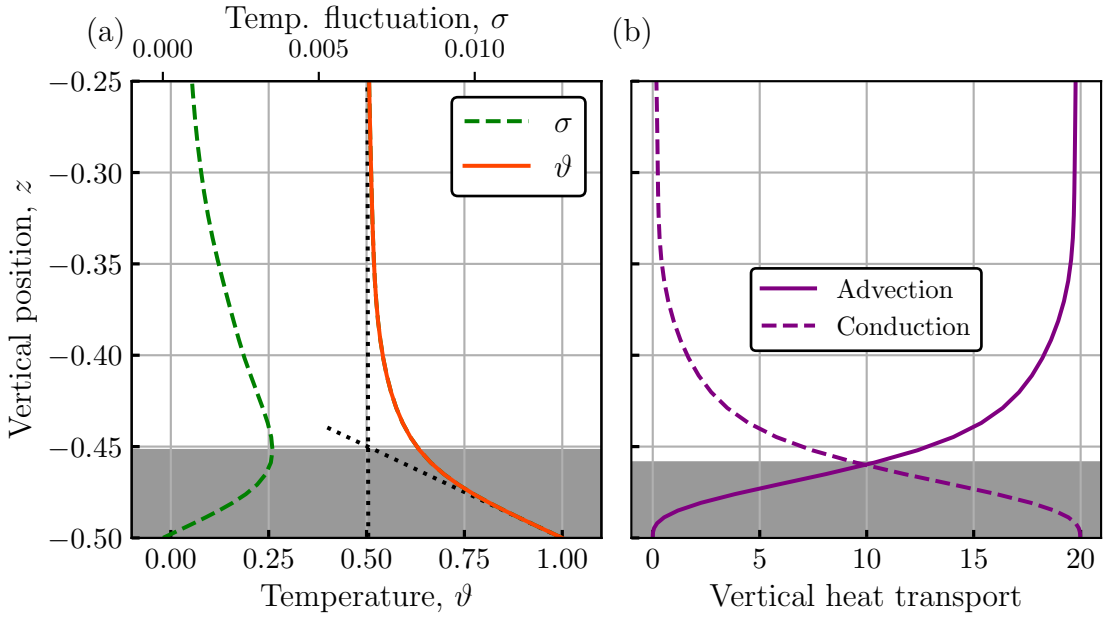

Figure 3.1: Vertical profiles of the average temperature, θ (solid orange line), and RMS temperature fluctuation, σ (dashed blue line) are shown in (a). The vertical profiles of advective (solid) and conductive (dashed) heat transport contributions are shown in (b). The dotted black lines show linear fits to ϑ at mid-depth and close to the boundary. The grey shaded regions show the thermal boundary layer thickness defined by the local maxima method in (a) and the heat transport method in (b). Profiles are obtained from a two-dimensional simulation with $Ra = 3 \times 10^6$.

Laboratory experiments of RBC typically drive convection by prescribing a fixed temperature on the boundaries rather than a fixed heat-flux (Xin and Xia, 1997; Du Puits et al., 2007; Cheng et al., 2015). Thermal boundary conditions have significant effects near convective onset, with fixed heat-flux conditions decreasing the critical Rayleigh number and increasing the preferred wavelength (Hurle et al., 1967). The longer wavelength of fixed heat-flux convection may also be important in determining convective patterns in the fully nonlinear regime (Von Hardenberg et al., 2008). In the turbulent regime Johnston and Doering (2009) showed that over the range $10^6 \leq Ra \leq 10^{10}$ the time averaged temperature profiles and values of Nu are indistinguishable between fixed temperature and fixed heat-flux conditions. If the Nu values are the same between both cases then we should expect δ to also be indistinguishable. Over a similar range of Ra the experimental study of Verzicco and Sreenivasan (2008) found that although the temperature profiles were indistinguishable between the different thermal boundary conditions, the profiles of

σ behaved very differently. Applying the local maxima method to a fixed heat-flux boundary, Verzicco and Sreenivasan (2008) found that the peak was always on the boundary, predicting $\delta = 0$; they instead chose to treat this boundary using the linear intersection method. We will address this discrepancy in sections 3.2 and 3.3 where we introduce an alternative method based on the vertical heat transport. This definition is shown in figure 3.1(b).

In contrast with the RBC paradigm, astro- and geophysical flows can be strongly influenced by the effects of rotation (Jones, 2011; Aurnou et al., 2015). For the simplest model of rotating RBC, the fluid layer is rotated about the vertical with constant angular frequency, Ω. A third dimensionless parameter, the Ekman number, E, measures the relative importance of viscosity to rotation,

$$E = \frac{\nu}{2\Omega h^2}. \tag{3.4}$$

Different regimes of rotating convection exist based on the relative importance of rotation and buoyancy forces (King et al., 2009; Schmitz and Tilgner, 2009; Gastine et al., 2016). For a given E, below some transitional value of Ra there is rotationally constrained convection, and above this there is weakly rotating convection. Rotationally constrained flows have a tendency to form columnar flow structures aligned with the rotation axis (Greenspan, 1968; Pedlosky, 2013). These columnar structures are able to sustain interior temperature gradients over many orders of Ra (Julien et al., 1996). For a fixed value of Ra the size of the interior temperature gradients increases with decreasing E (King et al., 2013) and within this regime δ is poorly described by equation (3.3). The weakly rotating regime resembles non-rotating convection having an isothermal fluid bulk and boundary layers described by equation (3.3) (King et al., 2013). The standard definitions of the TBL have not been systematically tested in rotating RBC and in this chapter we report the outcome of this investigation.

3.1.1 Research question

We present a numerical investigation of convection with and without rotation to examine the robustness of existing methods for defining the TBL thickness. **Can we define a robust method for defining the thermal boundary layer in rotating convection?**

We use simulations of Rayleigh-Bénard convection with two different thermal boundary conditions; fixed temperature and fixed heat-flux and a suite of rotating simulations with fixed temperature boundaries. This is the first systematic study of different methods used to define the thermal boundary layer in rotating convection. The limitations of the different methods leads us to suggest an alternative approach based on the vertical heat transport.

3.2 Defining the thermal boundary layer

A number of different methods have been proposed to define the edge and hence the width of the TBL (Julien et al., 2012b) and of these methods we describe the two most widely applied definitions; the linear intersection and local maxima methods. Following this we suggest a definition based on basic physical arguments informed by the heat equation termed the 'heat transport' method.

3.2.1 Established methods

The methods of defining the thermal boundary layer rely on spatially and temporally averaged quantities. We define temporal and horizontal (over a plane) averages shown acting on an arbitrary function, f:

$$\overline{f} = \frac{1}{\Delta t}\int_{t_0}^{t_0+\Delta t} f \,\mathrm{d}t, \tag{3.5}$$

$$\langle f(\boldsymbol{x})\rangle = \frac{1}{A}\int_{A} f(\boldsymbol{x}) \,\mathrm{d}A, \tag{3.6}$$

respectively, where Δt is the duration of the time averaging. For the 2D simulations, $\boldsymbol{x} = [x, z]$ and $A = L_x$ (where L_x is the extent of the horizontal). In the 3D rotating cases, $\boldsymbol{u} = [x, y, z]$ and $A = L_x L_y$ (where L_y is the extent in the second horizontal coordinate).

Linear intersection method

The linear intersection method is derived from the shape of the ϑ profile (figure 3.1a); a simple geometric argument is made to define δ. The linear (conductive) profile near the boundary is extrapolated to the linear gradient fit at mid-depth and this location defines δ (Verzicco and Camussi, 1999; Breuer et al., 2004; Liu and Ecke, 2011). For an isothermal bulk (as observed in non-rotating convection) this is equivalent to extrapolating the profile near the boundary to the isothermal value.

Local maxima method

The local maxima method assumes that the RMS temperature fluctuations, σ,

$$\sigma = \sqrt{\overline{\left\langle (T-\vartheta)^2 \right\rangle}}, \tag{3.7}$$

have pronounced local maxima close to the boundaries. The location of these maxima corresponds to the location at which thermal plumes emitted from the TBL are mixed into the fluid bulk (Tilgner et al., 1993). Consequently, this location also defines δ (Tilgner,

1996; King et al., 2013; Kunnen et al., 2016).

3.2.2 Crossover in heat transport contributions

We suggest an alternative definition of the TBL based on physical arguments on the conservation of heat. Boussinesq convection with no internal heat sources must conserve thermal energy, which can only be transferred via advection and conduction (see the heat equation given in chapter 2). The dimensionless temperature conservation can be written in terms of the total heat flux, $\boldsymbol{q}$

$$\partial_t T = -\boldsymbol{\nabla}\cdot\boldsymbol{q}, \quad \boldsymbol{q} = \underbrace{\boldsymbol{u}T}_{\text{advection}} - \underbrace{\boldsymbol{\nabla}T}_{\text{conduction}} . \tag{3.8}$$

The vertical heat flux is then given by

$$\mathbf{1}_z\cdot\boldsymbol{q} = wT - \partial_z T. \tag{3.9}$$

Within the TBL, conduction is dominant (advection is expected to be unimportant owing to the small vertical velocities near the non-penetrative boundaries). For non-rotating convection, advective heat transport is dominant in the fluid bulk as the local temperature gradients are negligible. We suggest that a physically relevant definition for the TBL is given by the intersection of the two contributions in equation (3.9) (see figure 3.1b), we refer to this as the 'heat transport' method moving forward.

3.2.3 On the validity of two dimensional Rayleigh-Bénard convection

Fully resolved three-dimensional simulations of RBC are computationally expensive and so where appropriate convection in two-dimensional geometries can be advantageous in allowing us to access more extreme values of the control parameters or a survey of many simulations.

Although most laboratory convection experiments use water as the working fluid with $Pr = 7$ most numerical studies use $Pr = 1$ to minimise computational expense. Schmalzl et al. (2004) compared thermal convection in two- and three-dimensional simulations with different values of Pr. When $Pr < 1$ the convective flows are largely toroidal and 2D simulations are not appropriate as they are incapable of capturing toroidal motion. Both global diagnostics (Reynolds number and Nusselt number) and local measurements (thermal and viscous boundary layer thicknesses), however, were found to be in good agreement between 2D and 3D simulations for $1 \leq Pr \leq 100$. In particular we highlight figure 4b in Schmalzl et al. (2004) which shows almost indistinguishable temperature profiles between 2D and 3D cases.

For $Pr \geq 1$ there is only a weak dependence of the heat transport on Pr. At a

fixed value of $Ra = 10^6$, Schmalzl et al. (2004) found $Nu \sim Pr^{-0.032}$ for $1 \leq Pr \leq 100$. This gives us a useful test of evaluating the different methods of defining the TBL.

We primarily focus on convection of a $Pr = 1$ fluid but we do briefly consider the effects of different Pr in subsection 3.3.2 by considering $Pr = 10,\ 100$. Figure 3.2 shows comparison profiles of (a,d) temperature, (b,e) rms temperature fluctuation and (c,f) heat fluxes for $Ra = 10^6$ and $Pr = 1$ in (a,b,c) 2D and (d,e,f) 3D. Despite the fundamental difference between 2D and 3D turbulence the time averaged diagnostics used in defining the thermal boundary layers exhibit similar behaviour. There are some noticeable differences, e.g. the amplitude of the peak of the temperature fluctuation but clearly each method can be well approximated by the two-dimensional counterpart. We show only the results for $Pr = 1$ as they are suitable for this study but we also observe these similarities for $Pr = 10,\ 100$.

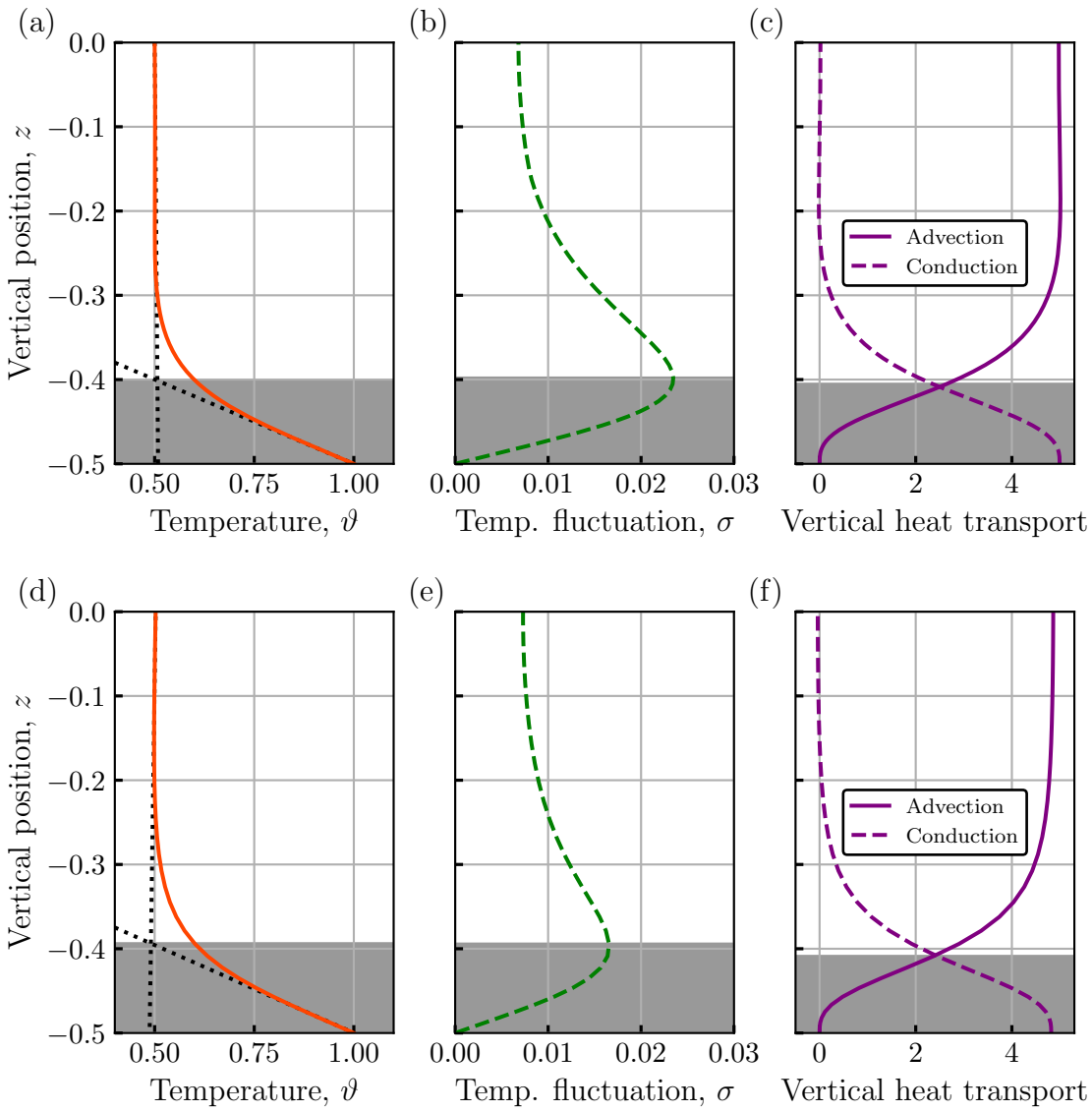

Figure 3.2: Illustrative examples of the different methods used to define the thermal boundary layer thickness are shown for non-rotating convection driven by fixed temperature boundaries. Results are from 2D (a,b,c) and 3D (d,e,f) calculations with $Ra = 10^5$. Only the lower half of the domain is shown. The subplots show vertical profiles of (a,d) temperature, ϑ, (b,e) RMS fluctuation, σ, and (c,f) vertical heat transport - advective and conductive contributions are shown as the solid and dashed lines respectively. The grey shaded region in each subplot shows the thermal boundary layer defined in each case.

3.3 Thermal boundary layer thickness

We will systematically investigate the robustness of each of the three methods to define δ. First, we will consider the influence of the thermal boundary conditions on each method using simulations of RBC. Secondly, we examine the Pr dependence on each method's performance and finally, we investigate how each method performs when rotation is present. We test the methods through comparison with theoretical expectations, check self-consistency as well as consistency between different methods. All numerical

simulations presented in this chapter are described in §2.2.

3.3.1 Influence of thermal boundary conditions

Equation (3.3) links δ with the global heat transport. To write this in terms of input parameters we use the $Nu - Ra$ scaling behaviour. Above $Ra = 10^6$ (and up to $Ra \leq 3 \times 10^8$) we find that the heat transfer data for both the fixed heat-flux and fixed temperature cases collapses onto a single scaling law (see figure 3.3),

$$Nu = 0.138 Ra^{0.286}. \tag{3.10}$$

This behaviour is in good agreement with the $Nu \sim Ra^{2/7}$ behaviour found for similar ranges of Ra (King et al., 2009; Johnston and Doering, 2009; Clarke et al., 2020). It follows that the TBL thickness should scale as

$$\frac{\delta}{h} \sim Ra^{-2/7}. \tag{3.11}$$

Figure 3.4(a) shows that for fixed temperature boundaries all three methods are in good agreement with the theoretical prediction of equation (3.11). The empirical fits to the data with $Ra \geq 10^6$ gives $\delta_{\mathrm{LI}} = 2.52 Ra^{-0.26\pm0.02}$, $\delta_{\mathrm{LM}} = 2.46 Ra^{-0.26\pm0.02}$, $\delta_{\mathrm{HT}} = 2.63 Ra^{-0.28\pm0.03}$ for the linear intersection, local maxima and heat transport methods respectively. All three fits have similar values of the mean relative misfit, χ (defined in equation (2.40)) in the range $1.4 - 3.0\%$. In all cases the error in the empirically determined exponents arise from an unbiased estimator for the covariance of the data and then consequently using the covariance matrix. In contrast, figure 3.4(b) shows that for fixed heat-flux boundaries the linear intersection and heat transport methods agree with the scaling prediction having empirical fits $\delta_{\mathrm{LI}} = 2.47 Ra^{-0.26\pm0.02}$ and $\delta_{\mathrm{HT}} = 3.31 Ra^{-0.28\pm0.04}$, respectively. The local maxima method gives a very different behaviour when $Ra \geq 10^6$, $\delta_{\mathrm{LM}} = 0.04 Ra^{-0.15}$ and a large misfit value, $\chi = 29.3\%$.

The linear intersection method works for either configuration because the temperature profile exhibits an isothermal fluid interior and two laminar thermal boundary layers which are insensitive to the choice of boundary conditions (see figure 3.1(a), figure 3.5(a)). Similarly, the heat transport definition is suitable for either boundary conditions (figure 3.1(b) and figure 3.5(b)) and agrees well with the linear intersection prediction. In contrast, the local maxima method is suitable for boundaries with a prescribed fixed temperature as there is zero fluctuation on the boundary allowing well pronounced local maxima. In the fixed heat-flux case the fluctuations are free to evolve and the local maxima (when they do exist) are not well constrained (see figure 3.5(a)). For the cases where a TBL can be identified, it can be as much as an order of magnitude smaller than the other definitions. The TBL thickness determined by the local maxima method scales as $\delta_{\mathrm{LM}} \sim Ra^{-0.59}$ for $Ra \leq 10^7$ which is steeper than any behaviour that we know of. The cases with highest Ra plateau off due to the value being bounded by numerical resolution.

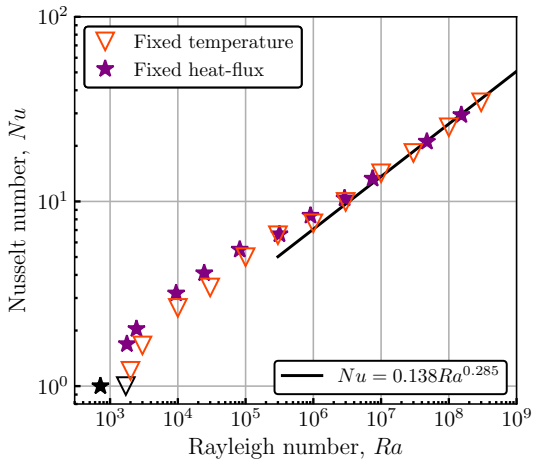

Figure 3.3: Nusselt number, Nu, versus Rayleigh number, Ra, for two-dimensional Rayleigh-Bénard convection. The shape and colour correspond to the thermal boundary conditions used. The black markers correspond to the onset values, Ra_c. The empirical fit, $Nu = 0.138Ra^{0.285}$ is shown as the solid line.

3.3.2 Prandtl number dependence

The heat transport method has been shown to work for both fixed temperature and fixed heat-flux boundary conditions. To further test the validity of this method, we will now consider RBC with varying Prandtl number. We ran five simulations with $Pr = 10$ and five with $Pr = 100$ sampling $Ra = 10^5 - 10^7$ all with isothermal boundary conditions; these simulations are shown in figure 3.6. Over this limited range we find only a weak dependence on the $Nu - Ra$ scaling for which we empirically determine

$$Nu \sim Ra^{0.285} Pr^{-0.02}.$$

This is consistent with the behaviour observed by Schmalzl et al. (2004).

We applied each of the three methods to define the TBL to these models, all of which performed successfully and give similar boundary layer thicknesses. The scaling was indistinguishable from the prediction given by equation (3.11). In figure 3.6(b) we show the heat transport prediction of the TBL and see only a small dependence on Pr. We conclude that all three methods used to predict the boundary layer can be applied when $Pr > 1$.

3.3.3 Effects of including rotation

Unlike non-rotating convection there is no well established scaling behaviour for the heat transfer in rotating systems with no-slip boundaries. The heat transfer scales as $Nu \sim Ra^{\lambda(E)}$ and λ increases monotonically with decreasing E (King et al., 2009; Cheng et al., 2015) due to larger Ekman pumping effects. Consequently, there is no prediction for the

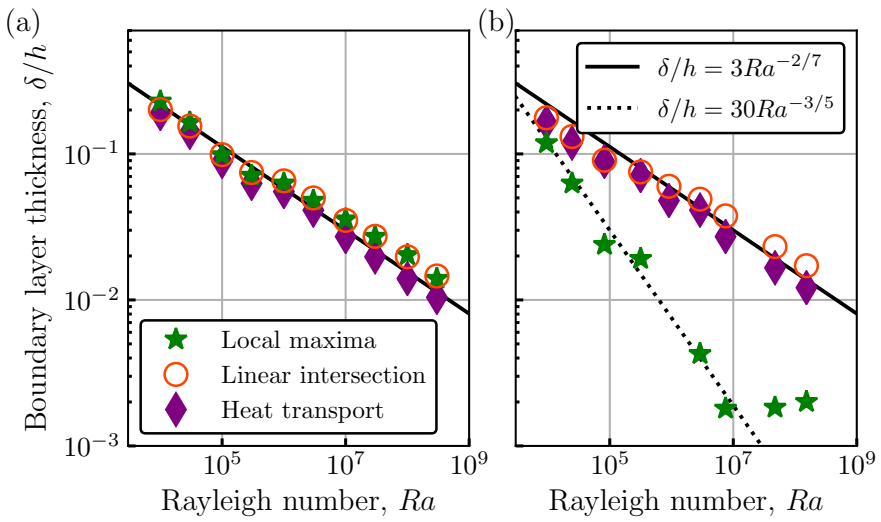

Figure 3.4: Boundary layer thickness as a function of Rayleigh number for each of the different methods; (a) shows fixed temperature cases and (b) fixed heat-flux cases. The linear intersection (orange circles), local maxima (green stars) and heat transport (purple diamonds) methods are shown along with the scaling prediction shown as the dashed line. The scaling prediction of equation (3.10) is shown as the solid line and the empirical fit is shown for the fixed heat-flux case.

scaling behaviour of δ which holds over all $Ra - E$ parameter space.

In rapidly rotating convection a significant fraction of the temperature difference is accommodated in the fluid bulk (figure 3.7(a)). There is no current consensus on how the magnitude of these internal temperature gradients depends on the input parameters (Julien et al., 2012b; King et al., 2013). If we assume that the bulk rather than the boundary layers (as in non-rotating convection) controls the heat transport and assume viscous dissipation is negligible in the interior, Nu becomes independent of diffusive effects and follows the scaling (Julien et al., 2012a; Jones, 2015)

$$Nu \sim Ra^{3/2} E^2 Pr^{-1/2}. \tag{3.12}$$

This heat transfer behaviour has been observed in rapidly rotating convection (at low E) when free-slip boundaries are used (Stellmach et al., 2014). An alternative expression for the ratio of total heat transport to conductive heat transport is given by

$$Nu = \frac{\delta\vartheta}{\Delta\vartheta}\frac{h}{\delta}, \tag{3.13}$$

where $\delta\vartheta$ is the temperature drop across the TBL. This expression is obtained by assuming that over the thickness, δ, the temperature profile is linear and we estimate conductive heat transport near the boundary as $\partial_z T \sim \delta\vartheta/\delta$ and non-dimensionalising appropriately. Equation (3.13) provides a consistency check for each of the three methods proposed to define δ by comparing the exact value of Nu (given by the vertical temperature gradient across the boundary, $Nu = -\partial_z T$) with the prediction of equation (3.13) from the

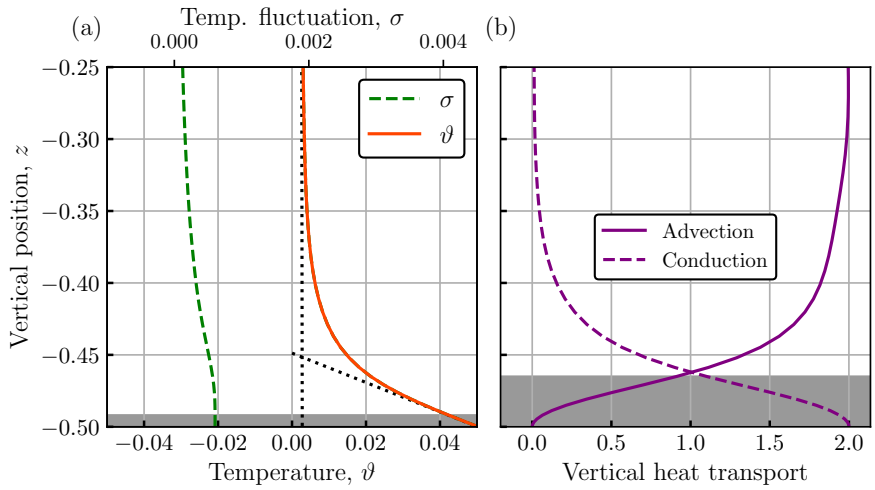

Figure 3.5: Vertical profiles of the average temperature, θ (solid orange line), and RMS temperature fluctuation, σ (dashed blue line) are shown in (a). The vertical profiles of advective (solid) and conductive (dashed) heat transport contributions are shown in (b). The dotted black lines show linear fits to ϑ at mid-depth and close to the boundary. The grey shaded regions show the thermal boundary layer thickness defined by the local maxima method in (a) and the heat transport method in (b). Profiles are obtained from a two-dimensional simulation with $Ra = 2.89 \times 10^6$.

determined values of δ/h and $\delta\vartheta/\Delta\vartheta$. An appropriate definition of the boundary layer should consistently predict the actual temperature difference across the boundary with an estimate based on the system scale (equation (3.13)).

Figure 3.8(a) shows that our suite of rotating convection simulations with $E = 10^{-7}$ conform to the diffusion-free scaling behaviour (equation (3.12)). In figure 3.8(b) we show the relative error in the predictions of Nu for each method of defining δ. The local maxima and heat transport methods give excellent agreement with Nu and their predictions typically have an error of approximately 1%. The linear intersection method predicts Nu with an error of $3-6\%$. The error in the predictions of Nu (using equation (3.13)) can be interpreted by investigating the scaling behaviour of δ and $\delta\vartheta$. For rotating convection we find that the TBL thickness predicted by the local maxima and heat transport methods scales as $\delta_{\mathrm{HT}} \sim Ra^{-1.9\pm0.04}$ (figure 3.9) with the temperature drop across the boundary layer, $\delta\vartheta \sim Ra^{-0.56\pm0.05}$. These methods accurately recover the $Nu - Ra$ scaling in equation (3.12) and the two scaling laws are in agreement with models derived in the limit of asymptotically small E (Julien et al., 2012b). The linear intersection is distinguishably different with $\delta_{\mathrm{LI}} \sim Ra^{-1.5\pm0.03}$ (figure 3.9 (a)) and $\delta\vartheta \sim Ra^{-0.09\pm0.01}$ (figure 3.9 (b)). The linear intersection method predicts thicker boundary layers than the other methods in the fully nonlinear regime and has a lower scaling exponent for the $Ra-$dependence of both δ/h and $\delta\vartheta/\Delta\vartheta$. This leads to the linear intersection method predicting $Nu \sim Ra^{1.41}$ giving a larger error when compared with the observed scaling $Nu \sim Ra^{3/2}$. We note that our data covers only a single decade in Ra and it is difficult to distinguish between the empirical scaling laws which have quite similar exponents, however, if Nu is estimated by

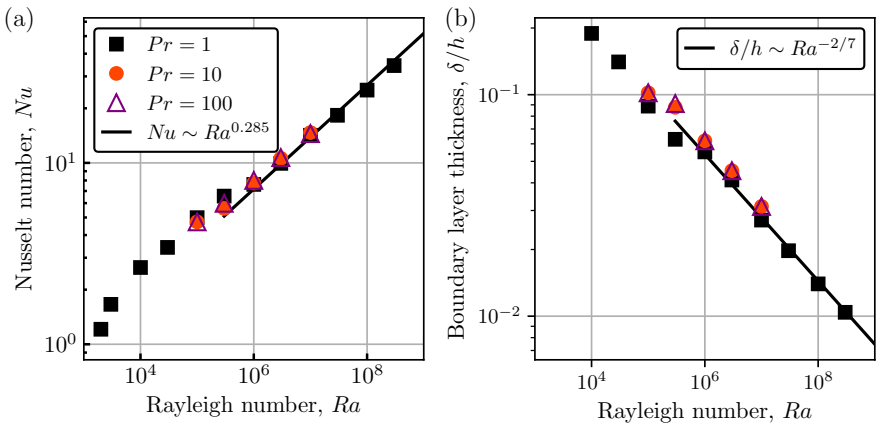

Figure 3.6: Nusselt number (a) and boundary layer thickness predicted by the heat transport method (b) versus Rayleigh number. The black lines show the determined behaviour of cases with $Pr = 1$ and the symbol shape/colour indicates the value of Pr.

δ defined using the linear intersection method Nu is off by $\approx 5\%$.

3.4 Conclusions

We have investigated two commonly used methods for defining the thermal boundary layer using simulations of Rayleigh-Bénard convection with and without rotation. We have shown that the local maxima method works well for specific configurations whereas the linear intersection method can be applied more generally. The location of the maxima in the RMS temperature fluctuation succeeds in predicting the thermal boundary layer thickness for fixed temperature convection but fails when the boundaries are prescribed a fixed heat-flux. In the fixed heat-flux case the temperature fluctuation on the boundary is non-zero and the local maxima that develop are not well pronounced. This helps explain the observation of Verzicco and Sreenivasan (2008) who found that the local maxima method predicted a boundary layer of zero thickness when the boundary was prescribed a fixed heat-flux. The intersection of linear fits near the boundary and in the interior is applicable to well mixed systems but is less intuitively applied when interior gradients are present (typically seen in rotationally constrained convection). When defined using the linear intersection method, the thermal boundary layer thickness and the associated temperature drop perform less well than the other methods in terms of predicting the Nusselt number. Clearly, both established methods are limited and we show that the most robust treatment of the thermal boundary layer thickness is achieved by locating the crossover in advective and conductive contributions to the heat transport. This heat transport method can be applied to either fixed temperature or fixed heat-flux thermal boundary conditions in both rotating and non-rotating systems.

The non-rotating simulations presented in this paper are two-dimensional with a fixed aspect ratio, $\Gamma = 2$, and Prandtl number, $Pr = 1$. The comparative study of

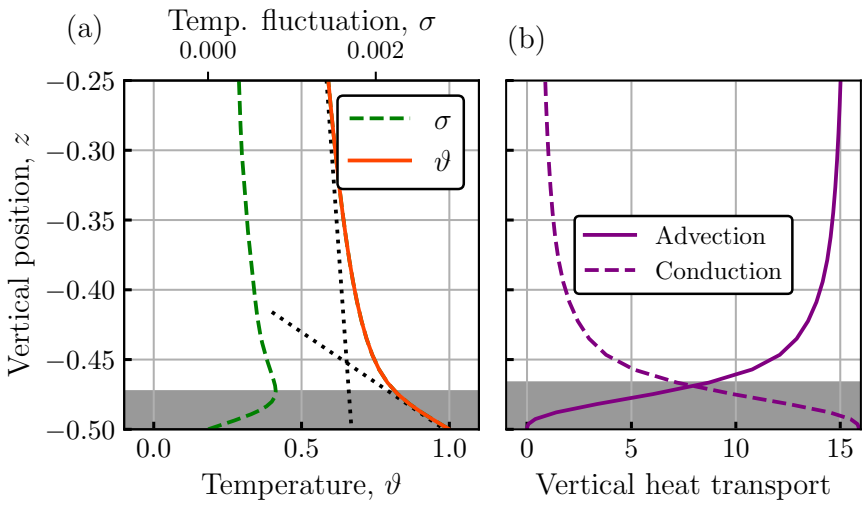

Figure 3.7: Results from the model with $Ra = 5 \times 10^{11}$, $E = 10^{-7}$ and fixed temperature boundaries. Only the lowest quarter of the domain is shown to focus on behaviour near the boundary. (Left) Vertical profiles of temperature (solid-orange) and RMS fluctuation (dashed-green). The dotted black lines show linear fits to ϑ at mid-depth and close to the boundaries. The grey shaded region shows the thermal boundary layer defined by the maxima in the σ profile. (Right) Vertical profiles of advective (solid-purple) and conductive (dashed-purple) heat transport. The grey shaded regions show the intersection of the heat transport contributions.

Schmalzl et al. (2004) showed that for $Pr \geq 1$ there is good agreement between two- and three-dimensional convection simulations; in particular the temperature profiles are almost indistinguishable.

We tested the performance of the different methods when Pr was changed by running a suite of simulations with $\Gamma = 2$, $Ra = 10^5 - 10^7$ and Prandtl number, $Pr = 10, 100$. The heat transport method can be applied regardless of Pr whereas for high Pr ($Pr = 100$) the linear intersection method becomes difficult to implement due to an overshoot in the temperature profile of its mean value (Hansen et al., 1992; Schmalzl et al., 2002). Our analysis of each method to define the TBL can be broadly applied to convection simulations for any Rayleigh number and Prandtl numbers of unity or above.

In contrast to numerical simulations, laboratory convection does not have access to the same wealth of diagnostic capabilities. Experimental studies of a single plume have measured velocity and temperature simultaneously with sufficient resolution to locate the crossover in vertical heat transport (Cagney et al., 2015; Cagney and Lithgow-Bertelloni, 2016). This methodology has recently been extended to rotating convection experiments which are now able to measure heat-transfer and flow speed data simultaneously (Hawkins et al., 2020) and so the heat transport method can be applied in a laboratory setting.

The methodology employed by the heat transport method could prove useful for identifying boundary layers for any scalar field governed by an advection-diffusion equation; e.g. the boundary layer in compositional convection (Bouffard et al., 2017).

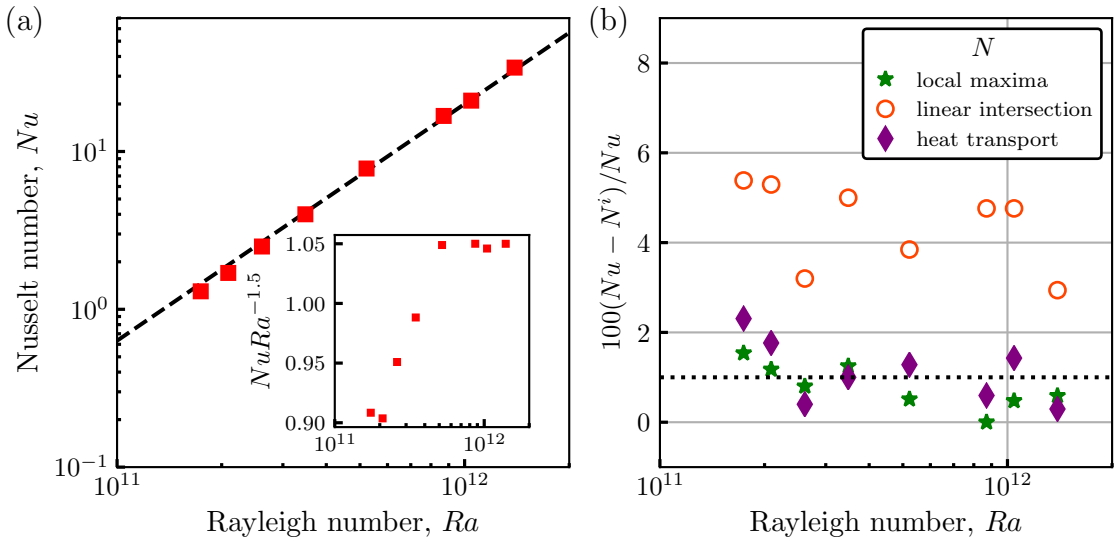

Figure 3.8: (a) Nusselt number versus Rayleigh number for convection between free-slip boundaries with $E = 10^{-7}$. The diffusive-free scaling (equation (3.12)) is shown as the dashed line. (b) Percentage error in the Nusselt number prediction of equation (3.13) for each of the three methods predicting the thermal boundary layer thickness. The dotted line corresponds to an error of 1%.

The linear intersection method has been widely applied to rotating convection simulations and by quantifying the difference of this definition with the heat transport method allows us to compare the two definitions on a like-for-like basis.

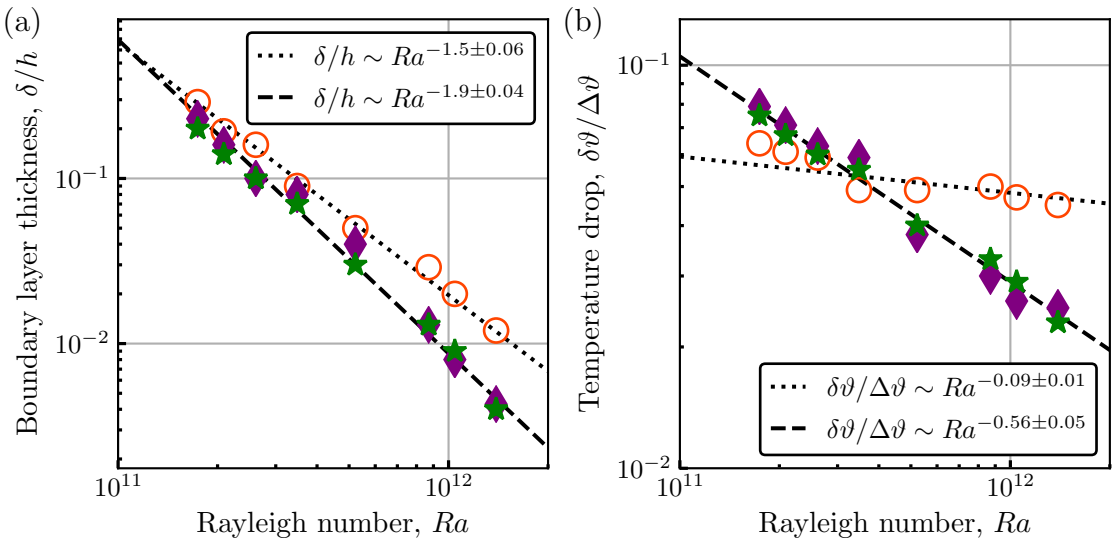

Figure 3.9: Boundary layer thickness (a) and temperature drop across the boundary layer (b) for rotating convection versus Rayleigh number. The linear intersection (orange circles), local maxima (green stars) and heat transport (purple diamonds) methods are shown along with the empirical fits shown as dashed and dotted lines. The local maxima and heat transport scalings are indistinguishable in this case and therefore jointly fit.

Chapter 4

Dynamical Regimes and Scaling Behaviour of Rotating Convection

4.1 Introduction

Convection plays a key role in the interior dynamics of many planets and stars. Spherical geometry and rotation are important in many of these natural convecting systems, including Earth's liquid metal outer core, solar and stellar interiors, and planetary atmospheres. The length scales associated with core convection in the Earth, range from narrow columns on the order of 10 m to system size flow structures (Jones, 2015). Similarly the range of timescales varies from the rotation period on the diurnal scale, to inertial waves on the decadal scale, and geomagnetic reversals which occur on average a few times every million years (Holme and Olson, 2007). The convective state of these astrophysical and geophysical systems, and the resulting heat transport, cannot be probed directly via numerical or physical experiment as the parameters of the system give rise to highly complex spatial and temporal behaviour. Consequently, a large body of work exists (described below) deriving and testing scaling relationships for convection between the independent and dependent variables.

We focus here on how rotation affects the scaling behaviour of both global and local diagnostics describing the heat transport (Nusselt number, interior temperature gradients, interior temperatures, thermal boundary layers) and flow properties (Reynolds number, convective length scales, viscous boundary layers). In what follows we will discuss the different scaling behaviours previously observed in both the plane-layer and spherical shell geometries and the different physical regimes of rotating convection.

4.1.1 Rayleigh-Bénard convection

Rotating RBC has been shown to display dynamics in one of two regimes; rapidly rotating (RR) and weakly-rotating (WR) as evidenced by global heat transfer behaviour measured by the Nusselt number, Nu (e.g. King et al., 2009; Schmitz and Tilgner, 2010). Nu is defined as the ratio of the total heat transport (sum of convective and conductive contributions) to the conductive heat transport. Here, we briefly review some relevant results for rotating RBC and refer the reader to Plumley and Julien (2019) for a detailed discussion of $Nu - Ra$ behaviour. With no-slip mechanical boundary conditions RR convection exhibits suppressed heat transfer relative to non-rotating convection with the scaling exponent increasing monotonically with decreasing Ekman number, $Nu \sim Ra^{\lambda(E)}$ (e.g. Cheng et al., 2015; Kunnen et al., 2016). Plane layer simulations with stress free boundaries however find that the heat transport saturates at the asymptotic scaling $Nu \sim Ra^{3/2}E^2$ (Julien et al., 2012a). In the no-slip case, the presence of Ekman boundary layer effects can enhance the heat transport leading to larger scaling exponents (e.g. Stellmach et al., 2014; Plumley et al., 2016) such as those observed by Cheng et al. (2015) and Kunnen et al. (2016). Heat transfer in the WR regime behaves similarly to that for convection without rotation: the empirical $Nu \sim Ra^{2/7}$ scaling is observed for moderate Rayleigh numbers ($Ra \leq 10^{10}$) before saturating at $Nu \sim Ra^{1/3}$ for sufficiently high values of Ra ($Ra \geq 10^{10}$) (Cheng et al., 2015).

Three main parameters have been suggested to control the transition from RR to WR convection. King et al. (2009, 2012) suggest that the transition between the RR and WR regimes occurs when the thermal boundary layer becomes thinner than the viscous boundary layer, occurring at either $RaE^{7/4} \sim \mathcal{O}(1)$ or $RaE^{3/2} \sim \mathcal{O}(1)$ depending on whether $Nu \sim Ra^{2/7}$ or $Nu \sim Ra^{1/3}$ (for the range of Ra studied here we find the $Nu \sim Ra^{2/7}$ scaling behaviour and consequently test the $RaE^{7/4}$ boundary layer crossing parameter, see subsection 1.3.2 for details). Alternatively, models with asymptotically small E by Julien et al. (2012b) suggest that the transition occurs when the thermal boundary layers are no longer in geostrophic balance, predicting a transition at $RaE^{8/5} \sim \mathcal{O}(1)$. Other works advocate the convective Rossby number, $Ro_c = \sqrt{RaE^2/Pr} \sim \mathcal{O}(1)$ (Gilman, 1977) to demarcate the transition. There is no consensus on what controls the RR-WR transition and various other options have also been considered (see Cheng et al., 2018, table 1 for an overview). The transition from RR to WR heat transfer behaviour is accompanied by vanishing interior temperature gradients, $\mathrm{d}T_{\mathrm{int}}$ (typically defined at mid-depth). $\mathrm{d}T_{\mathrm{int}}$ scales inversely with supercriticality in the RR regime (Julien et al., 2012b).

Despite the similar heat transfer behaviour between WR and non-rotating (NR) convection, the flow properties continue to be influenced by rotation even in the WR regime. The typical horizontal length scale associated with the convective flow follows the classic viscous scaling, $\ell/h \sim E^{1/3}$ for both RR and WR convection (King et al., 2013). In contrast, for NR convection the flow exhibits three-dimensional turbulence

and the typical length scale is then inversely proportional to the heat transport, $\ell/h \sim Nu^{-1/2}$ (King et al., 2013). Combining with the $Nu \sim Ra^{2/7}$ behaviour, one obtains $\ell/h \sim Ra^{-1/7}$. The Coriolis force does no work and it affects the flow speed (Reynolds number, Re_c) scaling solely by changing the length scales. A triple force balance between viscous, Archimedean and Coriolis forces (VAC balance) gives a scaling prediction for the flow speed, $Re_c \sim (Ra(Nu-1))^{1/2}E^{1/3}$ in both the RR and WR regimes (King et al., 2013). The different length scale observed in NR convection leads to a flow speed scaling, $Re_c \sim (Ra - Ra/Nu)^{1/2}$ (King et al., 2013).

A complete specification of the flow requires a description of the mechanical and thermal boundary layers. In the RR and WR regimes Coriolis forces balance viscosity in the region close to the walls leading to the Ekman boundary layer of thickness, $\delta_E \sim E^{1/2}$ (Greenspan, 1968). In NR convection the Prandtl-Blasius theory (e.g. Kundu and Cohen, 1990) predicts a viscous boundary layer of thickness, $\delta_\nu \sim Re_c^{-1/2}$. While some studies confirm this behaviour others find an empirical scaling $\delta_\nu \sim Re_c^{-1/4}$ (Lam et al., 2002). This discrepancy was attributed to the boundary layers being either passive or active (Qiu and Xia, 1998a,b) however more recent work has shown that the different scaling exponents follow from the adopted definition of the viscous boundary layer (Breuer et al., 2004; Gastine et al., 2015, see also figure 4.1a for the two different methods of defining a thermal boundary layer). Within the thermal boundary layers heat is transported almost purely by conduction and so for non-rotating convection the layer thickness scales as $\delta_\kappa \sim Nu^{-1}$. This scaling is observed to hold in the WR regime and provides a reasonable first order approximation in RR convection (King et al., 2013).

4.1.2 Spherical shell convection

Recently the first systematic study of rotating convection in a spherical shell geometry was published by Gastine et al. (2016). Similar to RBC, distinct regimes have been identified; and we follow Gastine et al. (2016) by defining the weakly nonlinear (WN), rapidly rotating (RR), transitional, and non-rotating (NR) regimes. When comparing quantitatively with Gastine et al. (2015, 2016) we account for the factor two difference in their definition of the Ekman number.

Close to the onset of convection, the WN regime exists and persists for low values of supercriticality (e.g. Yadav et al., 2015). In this regime inertial forces are small and the heat transfer follows the perturbation analysis of Gillet and Jones (2006): $Nu - 1 \sim Ra/Ra_c - 1$. Gastine et al. (2016) found the WN regime exists for $Ra_c \leq Ra \leq 6Ra$, where Ra_c is the critical value for instability. The RR regime is found for $E \leq 5 \times 10^{-5}$ and is characterised by a steeper heat transfer scaling than the WN regime. As in the plane layer case the $Nu - Ra$ scaling exponents increases with decreasing E. Though Mound and Davies (2017) found a continuous increase for the parameter range considered, Gastine et al. (2016) observed saturation at $Nu \propto Ra^{3/2}E^2$. This scaling might imply that an

asymptotic regime has been reached as it is derived in the absence of thermal and viscous diffusion at asymptotically low E (Jones, 2015). The $Nu \propto Ra^{3/2}E^2$ heat transfer scaling is predicted to hold until the thermal boundary layer loses geostrophic balance, which defines a transition to WR convection when $RaE^{8/5} = \mathcal{O}(1)$ (Julien et al., 2012a). At numerically accessible values of E ($\geq 10^{-7}$) it is found that, above some transitional value of Ra, the $Nu - Ra$ scaling exponent continually changes in the transitional regime until the non-rotating scaling $Nu \sim Ra^{2/7} - Ra^{1/3}$ (Gastine et al., 2015) is recovered in the NR regime. Gastine et al. (2016) found that the heat transport scaling conforms to the NR behaviour when $Ra > 328E^{-12/7}$. As in RBC the transition to the NR scaling occurs alongside vanishing interior temperature gradients (Gastine et al., 2015).

The characteristic length scale and speed of the convective flow in the WN regime is described by the VAC balance, predicting $\ell/h \sim E^{1/3}$, and $Re_c \sim (Ra(Nu-1))^{1/2}E^{1/3}$ (Gastine et al., 2016) as in rotating RBC. In the RR regime inertial effects dominate over viscous forces and Gastine et al. (2016) found that the length scale approaches the Rhines scale of convection, $\ell/h \sim (Re_cE)^{1/2}$ (Rhines, 1975) for $E = 3 \times 10^{-7}$. The appearance of the Rhines scale suggests that the fluid bulk has reached a triple force balance between inertia, Archimedean and Coriolis forces (referred to as the IAC balance) (e.g. Aubert et al., 2001). Within the RR regime Gastine et al. (2016) found that Re_c is described by decomposing the flow speed into contributions from the fluid bulk and the viscous boundary layers. Within the transitional regime no scaling laws can be defined. In the NR regime rotational effects are subdominant and the typical length scale of the flow follows $\ell \sim Ra^{-3/14} - Ra^{-1/3}$ (Gastine et al., 2015) where the range arises from the $Nu - Ra$ scaling. The flow speed in the NR regime depends only on the Rayleigh number with an exponent that varies in a manner that is consistent with the theory of Grossmann and Lohse (2000), $Re_c \sim Ra^{0.4-0.6}$ (Gastine et al., 2015).

As in the plane layer configuration, the mechanical boundary layers in the RR regime are of the Ekman type (Gastine et al., 2016) and the NR regime recovers the traditional Prandtl-Blasius viscous boundary layer thickness scaling, $\delta_\nu \sim Re_c^{-1/2}$ (Gastine et al., 2015). Similar to RBC the thermal boundary layers follow the typical $\delta_\kappa \sim Nu^{-1}$ scaling in the NR regime and a non-trivial dependence on E is observed in the RR regime (Gastine et al., 2015). In a spherical shell the inner and outer boundary layers can have different thicknesses due to the asymmetry in surface area as a function of radius (Gastine et al., 2015).

4.1.3 Research question

We report the first systematic study of hydrodynamic rotating convection in an Earth-like configuration. Our model employs no–slip non–penetrative boundaries prescribed a fixed heat-flux, a radius ratio of $r_i/r_o = 0.35$, and a gravity profile that varies linearly with

radius (these choices are motivated by the discussion in chapter 1). The one parameter survey that exists employs fixed temperature thermal boundary conditions, a thicker shell, $r_i/r_o = 0.60$, and a gravity profile of the form $g \sim r^{-2}$ (Gastine et al., 2016) as would be appropriate for studying gas giants. The inverse square gravity profile also has the benefit of allowing an analytical expression for the buoyancy production (Gastine et al., 2016), which is not available when considering a linear gravity profile. **Are these differences important in determining the different regimes of rotating convection?**

Previous studies have found that the choice of aspect ratio and thermal boundary conditions can influence behaviour in rotating convection systems. Asymmetry between the inner and outer spherical boundaries leads to different aspect ratio systems having distinct temperature distributions with larger temperature drops occurring at the inner boundary relative to the outer boundary (Gastine et al., 2015). The aspect ratio also changes the critical Rayleigh number at onset (Al-Shamali et al., 2004) and can alter the morphology of convection driven magnetic fields (Lhuillier et al., 2019). Fixed heat–flux boundary conditions prefer longer wavelengths than the equivalent fixed temperature case at onset (Gibbons et al., 2007) and lead to larger scale convective flows in the fully nonlinear regime (Sakuraba and Roberts, 2009) although this diffence may not be present for very strongly supercritical dynamos (e.g. Aubert et al., 2017). However, it is not yet known whether these effects influence global heat transfer and flow scaling behaviour across broad ranges of parameter space.

4.2 Scaling law analysis; theoretical predictions

4.2.1 Diagnostic measurements

We use several diagnostics to quantify the effect of different control parameters on the flow and temperature fields. We define temporal and horizontal (over a spherical surface) averages shown acting on an arbitrary function, f:

$$\overline{f} = \frac{1}{\Delta t}\int_{t_0}^{t_0+\Delta t} f \, \mathrm{d}t, \tag{4.1}$$

$$\langle f\,(r,\theta,\phi)\rangle = \frac{1}{4\pi}\int_0^{\pi}\int_0^{2\pi} f\,(r,\theta,\phi)\sin(\theta)\,\mathrm{d}\phi\,\mathrm{d}\theta, \tag{4.2}$$

respectively, where Δt is the duration of the time averaging.

The Nusselt number measures the global efficiency of heat transport by convection and conduction to that transferred by conduction alone:

$$Nu = \frac{\int (u_r T - \partial T/\partial r)\,\mathrm{d}r}{\int |\partial T/\partial r|\mathrm{d}r}.$$

For our model configuration it can be shown that this is equivalent to

$$Nu = \frac{\int (\mathrm{d}T_c/\mathrm{d}r)\mathrm{d}r}{\int (\mathrm{d}\overline{\langle T \rangle}/\mathrm{d}r)\mathrm{d}r} = \frac{\Delta T_c}{\overline{\Delta \langle T \rangle}}, \tag{4.3}$$

(Mound and Davies, 2017) where $\overline{\Delta \langle T \rangle}$ is the difference in average temperature between the inner and outer boundaries.

The characteristic velocity measured by the Reynolds number, Re, is derived from the time-averaged dimensionless kinetic energy, $E_k = \frac{1}{2} \iiint_{V_s} \overline{\boldsymbol{u}^2} \mathrm{d}V$

$$Re = \sqrt{\frac{2E_k}{V_s}}, \tag{4.4}$$

where V_s is the non–dimensional fluid volume. The axisymmetric zonal flow can contribute a significant amount of the total kinetic energy, however, this flow does not contribute to the radial heat transfer. We extract the Reynolds number of the convective flow, Re_c, from the kinetic energy by excluding the contribution from the axisymmetric ($m = 0$) mode.

Characteristic length scales of the flow are determined from the time averaged kinetic energy spectrum (e.g. Wicht and Christensen, 2010; King and Buffett, 2013) with the dominant horizontal wavelength of the flow, ℓ, defined as

$$\frac{\ell}{h} = \pi \frac{E_k}{\sum l \overline{\langle \boldsymbol{u}_l \cdot \boldsymbol{u}_l \rangle}}, \tag{4.5}$$

where $\boldsymbol{u}_l$ is the flow component at degree l.

We will show that scaling laws for Re_c depend on both the buoyancy production, B, as well as the convective length scale. For hydrodynamic convection of a Boussinesq fluid in the spherical shell geometry, the rate of change of kinetic energy arises from the imbalance between viscous dissipation and kinetic energy production due to buoyancy (e.g. King and Buffett, 2013). We compute B directly from this energy balance using a first order difference scheme for dE_k/dt

$$B = \frac{dE_k}{dt} + E \int_{V_s} \left(\boldsymbol{\nabla} \times \boldsymbol{u}\right)^2 \, \mathrm{d}V_s, \tag{4.6}$$

the second term on the right hand side is the viscous dissipation. By combining the flow speed and heat transfer scaling laws in a given regime we can obtain scalings of outputs in terms of the input parameters. The flow speed scaling in a given regime is dependent on the kinetic energy due to buoyancy production. Comparing our definition for the buoyant energy production, B, with King and Buffett (2013) we can write

$$B = \frac{Ra(Nu - 1)}{Pr^2}. \tag{4.7}$$

Unlike non-rotating convection, rotationally-constrained convection is capable of sustaining persistent interior temperature gradients even at high values of the Rayleigh number (e.g. Julien et al., 1996; King et al., 2010). The temperature is normalised to the range 0 and 1 as follows

$$\overline{\langle\vartheta\rangle} = \frac{\overline{\langle T\rangle} - \min(\overline{\langle T\rangle})}{\max(\overline{\langle T\rangle}) - \min(\overline{\langle T\rangle})}.$$

We calculate the temperature and temperature gradient at mid-shell radius by

$$T_{\text{int}} = \overline{\langle\vartheta\rangle}\Big|_{r=r_m}, \quad \mathrm{d}T_{\text{int}} = \frac{\mathrm{d}\overline{\langle\vartheta\rangle}}{\mathrm{d}r}\Big|_{r=r_m}, \tag{4.8}$$

respectively, where $r_m = \dfrac{r_i + r_o}{2}$.

Two different approaches are typically considered to define the thickness of the viscous boundary layer, δ_ν, both of which utilise the time and horizontally averaged velocity,

$$Re_h(r) = \overline{\left\langle \left(Re_\theta^2 + Re_\phi^2\right)^{1/2} \right\rangle},$$

here the subscripts denote the components of Re. Our model implements no–slip mechanical boundary conditions and as a result Re_h exhibits steep local increases as one moves away from the boundaries with well-defined local maxima (figure 4.1a). One way to define δ_ν is to measure the radial distance between the boundaries and the closest maxima of Re_h (Belmonte et al., 1994; Kerr and Herring, 2000) here called the "local maxima method". Alternatively, δ_ν, can be estimated as the radial distance at which the linear fit to Re_h near the boundary intersects the tangent of the local maxima (Breuer et al., 2004; Gastine et al., 2016) herein referred to as the "linear intersection method". The two methods are known to produce different boundary layer thicknesses (see figure 4.1a) with the local maxima method predicting much thicker boundary layers (e.g. Gastine et al., 2015). Except where explicitly mentioned we use the linear intersection method to define the viscous boundary layer thickness.

For the treatment of the thermal boundary layers we use the method based on the mean radial temperature profile, $\langle\overline{\vartheta}\rangle$, (e.g. Breuer et al., 2004; Liu and Ecke, 2011) which defines the edge of the thermal boundary layer, δ_κ, by the location at which the linear fit to $\langle\overline{\vartheta}\rangle$ near the boundary intersects the linear fit to the profile at mid-depth (figure 4.1b).

4.2.2 Flow speeds and length scales

We compare model output with theoretical predictions of the scaling behaviour derived from the dimensional momentum and vorticity equations,

$$\frac{\partial \boldsymbol{u}}{\partial t} = -\left(\boldsymbol{u}\cdot\boldsymbol{\nabla}\right)\boldsymbol{u} - 2\boldsymbol{\Omega}\times\boldsymbol{u} - \frac{1}{\rho_0}\boldsymbol{\nabla}\widetilde{P} + \alpha T'\boldsymbol{g} + \nu\nabla^2\boldsymbol{u}, \tag{4.9}$$

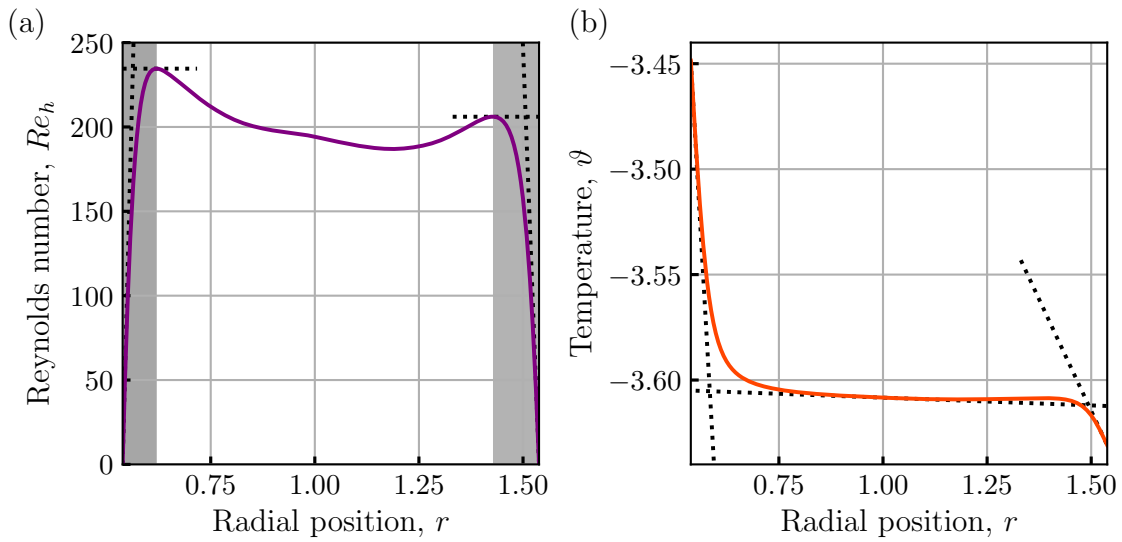

Figure 4.1: (a) Example radial profile of the time and horizontally averaged velocity, $Re_h(r)$ showing how δ_ν is defined. The viscous boundary layers can either be defined by the local maxima of Re_h (highlighted by the grey shaded region) or by the intersection of the linear fit to Re_h near the boundaries and with the tangent to the local maxima (black dotted lines). (b) Example radial profile of the time and horizontally averaged temperature showing how δ_κ is defined. The thermal boundary layers are defined by the intersection of the linear fit to $\langle\overline{\vartheta}\rangle$ near the boundaries and at mid-depth. Profiles obtained from the numerical model with $E = 10^{-3}$ and $\widetilde{Ra} = 1.3 \times 10^4$.

$$\frac{\partial \boldsymbol{\omega}}{\partial t} = -\left(\boldsymbol{u}\cdot\boldsymbol{\nabla}\right)\boldsymbol{\omega} - 2\boldsymbol{\Omega}\cdot\boldsymbol{\nabla}\boldsymbol{u} + \boldsymbol{\nabla}\times\left(\alpha T'\boldsymbol{g}\right) + \nu\nabla^2\boldsymbol{\omega}, \tag{4.10}$$

respectively.

Scaling arguments for Re_c begin with a thermal wind balance, that is balancing Coriolis and buoyancy terms in equation (4.10). Assuming that spatial derivatives scale as $\boldsymbol{\nabla} \sim 1/\ell$, except for the axial gradient $\partial/\partial z$ which scales as $1/h$; i.e., convection takes the form of tall thin columns, we obtain

$$U \sim \frac{\alpha T' g h}{2\Omega\ell}$$

for some characteristic velocity, U. Following King and Buffett (2013) we multiply by U and assume that $U\alpha T'g = \overline{U_r \alpha T' g}$, which gives the non-dimensional flow speed scaling

$$Re_c = \left(BE\frac{h}{\ell}\right)^{1/2}. \tag{4.11}$$

Equation (4.11) shows that the behaviour of ℓ determines the flow speed scalings. The leading order force balance in rapidly rotating systems is geostrophic but purely geostrophic flows cannot generate mean heat transport. At second order the flow must

be ageostrophic and the Taylor-Proudman (TP) theorem is broken either by viscosity or inertia. A viscously broken TP constraint yields

$$2\boldsymbol{\Omega}\cdot\boldsymbol{\nabla}\boldsymbol{u}\sim\nu\nabla^2\boldsymbol{\omega},$$

$$\frac{\ell}{h}\sim E^{1/3}, \tag{4.12}$$

(Chandrasekhar, 1961). Alternatively, if viscous forces are negligible and instead inertial forces are responsible for breaking the TP constraint, this predicts

$$2\boldsymbol{\Omega}\cdot\boldsymbol{\nabla}\boldsymbol{u}\sim\boldsymbol{\nabla}\times(\boldsymbol{u}\cdot\boldsymbol{\nabla}\boldsymbol{u}),$$

$$\frac{\ell}{h}\sim(Re_cE)^{1/2}. \tag{4.13}$$

This is often referred to as the Rhines scale (Rhines, 1975; Cardin and Olson, 1994) and arises from the balance of vortex stretching and vortex advection. Substituting equation (4.12) or equation (4.13) into equation (4.11) gives two possible dimensionless flow scalings associated with the Viscous-Archimedean-Coriolis (VAC) and Inertial-Archimedean-Coriolis (IAC) balances respectively,

$$\text{VAC}:\ \frac{\ell}{h}\sim E^{1/3},\ Re_c\sim B^{1/2}E^{1/3}, \tag{4.14}$$

$$\text{IAC}:\ \frac{\ell}{h}\sim(Re_cE)^{1/2},\ Re_c\sim B^{2/5}E^{1/5}. \tag{4.15}$$

We now consider the theoretical expectations for non-rotating convection. Partitioning the advective and diffusive contributions in the heat equation,

$$\boldsymbol{u}\cdot\boldsymbol{\nabla}T\sim\kappa\nabla^2T,$$

King et al. (2013) derived a flow speed scaling in terms of the Nusselt number,

$$Re_c\sim Nu^2 \tag{4.16}$$

(see also Julien et al., 2012b). Assuming a well mixed fluid bulk, combining the flow speed scaling (equation (4.16)) with a theoretical estimate for the length scale based on the natural plume spacing,

$$\ell/h\sim Re^{1/2}(\delta_\kappa/h)^{3/2},$$

King et al. (2013) gives a scaling behaviour for ℓ/h in non–rotating convection,

$$\frac{\ell}{h}\sim Nu^{-1/2}. \tag{4.17}$$

4.2.3 Mechanical boundary layers

In non–rotating convection the viscous boundary layers are found to be laminar for the range of Rayleigh numbers currently accessible and are of the Prandtl–Blasius type (e.g. Stevens et al., 2010). Balancing inertia of the fluid bulk with the viscous forces in the boundary layer of thickness, δ_ν, yields

$$\boldsymbol{u}\cdot\boldsymbol{\nabla}\boldsymbol{u} \sim \nu\nabla^2\boldsymbol{u},$$

$$\frac{\delta_\nu}{h} \sim Re^{-1/2}. \tag{4.18}$$

In contrast, the Coriolis force is important in rotating convection and gives rise to Ekman boundary layers (e.g. Pedlosky, 2013). Balancing Coriolis and viscous forces in the Ekman layer of thickness, δ_E, gives

$$2\boldsymbol{\Omega}\times\boldsymbol{u} \sim \nu\nabla^2\boldsymbol{u},$$

$$\frac{\delta_E}{h} \sim E^{1/2}. \tag{4.19}$$

4.2.4 Heat transfer and thermal boundary layers

Along with the theoretical expectations of the flow characteristics, we can also make predictions for the heat transport scaling in rotating convection. The work of Grossmann and Lohse (2000) shows that for non–rotating convection there exists different regimes with unique scaling exponents. The dependence of heat transport in rotating convection on the control parameters, Ra, E, Pr, r_i/r_o, is still a topic of debate. Following Jones (2015), for a given radius ratio we assume that the heat transport scaling can be written as

$$Nu \sim Ra^{\lambda_1}E^{\lambda_2}Pr^{\lambda_3}, \tag{4.20}$$

with $\lambda_{1,2,3}$ being real exponents to be determined. The weakly nonlinear perturbation analysis of Gillet and Jones (2006) applies for marginally supercritical Rayleigh numbers with the exponent $\lambda_1 = 1$ giving

$$Nu \sim Ra/Ra_c. \tag{4.21}$$

At sufficiently large Ra, Nu joins the non–rotating branch, having an exponent of $2/7 \leq \lambda_1 \leq 1/3$. Jones (2015) hypothesised that a regime could exist between these states in which the fluid bulk limits the heat transport instead of the diffusive thermal boundary layers. If so, it is likely that the heat transport scaling will be independent of viscous and thermal diffusion, from equation (4.20) the independence of ν and κ respectively requires

$$-\lambda_1 + \lambda_2 + \lambda_3 = 0, \quad \lambda_1 + \lambda_3 = 1.$$

Linear theory predicts that $Ra_c \sim E^{-4/3}$ as $E \to 0$ so $\lambda_2 = 4\lambda_1/3$ gives the unique solution

$$Nu \sim Ra^{3/2}E^2Pr^{-1/2} \tag{4.22}$$

(Julien et al., 2012a). In the case of non–rotating convection, the total amount of heat transported by the fluid can be related to the thickness of the thermal boundary layer δ_κ. Within the thermal boundary layer heat is transported almost purely by conduction and for turbulent non-rotating convection (Spiegel, 1971)

$$\frac{\delta_\kappa}{h} \sim Nu^{-1}. \tag{4.23}$$

There is currently no accepted theoretical prediction for the scaling behaviour of δ_κ in the rotating case as the assumption of the temperature drop occurring predominantly in the boundary layers is less certain (e.g. King et al., 2012).

4.2.5 Transition parameters

The domain of validity in parameter space for each of these scaling laws cannot be determined a priori and typically is obtained empirically (e.g. Schmitz and Tilgner, 2010; Gastine et al., 2016). Recent studies have found conflicting results for the parameter demarcating the upper bound of the rapidly rotating regime (King et al., 2013; Gastine et al., 2016). There are three proposed ideas to capture this transition which are summarised in table 4.1 (with Prandtl number dependencies neglected).

Transition argument	Meaning	Reference
Convective Rossby number	$Ro_c = Ra^{1/2}E$	Gilman (1977)
Boundary layer crossing	$Ra_\delta = RaE^{7/4}$	King et al. (2010)
Degree of geostrophy	$Ra_G = RaE^{8/5}$	Julien et al. (2012a)

Table 4.1: Proposed parameters to demarcate the transition from rapidly rotating convection to the transitional regime. The naming convention is adopted throughout. A transition can be expected when the parameter is $\mathcal{O}(1)$. All Pr dependencies have been neglected.

The global-scale balance between the Coriolis and buoyancy forces can be expressed by the convective Rossby number,

$$Ro_c = \sqrt{RaE^2/Pr} \tag{4.24}$$

(Gilman, 1977; Aurnou, 2007).

King et al. (2009, 2012) proposed that, when the thermal boundary layer becomes thinner than the Ekman layer the effects of rotation are secondary. In non-rotating

convection the thickness of the thermal boundary layer scales as $\delta_\kappa/h \sim Ra^{-2/7}$ (for the moderate range of Ra studied here) and equating this with the Ekman layer scaling $\delta_E/h \sim E^{1/2}$ predicts the "boundary layer crossing" transitional value,

$$Ra_\delta = RaE^{7/4}. \tag{4.25}$$

Julien et al. (2012b) argued that the dynamics of the thermal boundary layers control the transition from rotationally constrained convection. The thermal boundary layer loses geostrophic balance when the local convective Rossby number is smaller than unity predicting the "Degree of geostrophy" transition parameter,

$$Ra_G = RaE^{8/5}, \tag{4.26}$$

where the Prandtl number dependence has been omitted (see also Gastine et al., 2016). For each parameter we would expect the transition to occur at $\mathcal{O}(1)$. We will test the applicability of each transition parameter in subsection 4.3.2.

4.3 Regimes of rotating convection

The heat transfer data for all of our runs is shown in figure 4.2. Figure 4.3 shows the morphology of the convective flow for models taken from different regions of Ekman-Rayleigh parameter space and we can qualitatively see distinct regimes which coincide with different behaviours observed in figure 4.2. The onset of the convective instability in rotating bottom-heated spherical shells materialises as a drifting thermal Rossby wave which develops in the vicinity of the tangent cylinder (Busse, 1970). In the limit of $E \ll 1$ and $E/Pr \to 0$ the critical Rayleigh number Ra_c and azimuthal wavenumber m_c follow

$$Ra_c \sim E^{-4/3}, \; m_c \sim E^{-1/3}. \tag{4.27}$$

The heat transfer data suggests four regimes (highlighted in figure 4.2); for a given value of E the slope of the $Nu - Ra$ scaling is shallow for low Ra (we call this the weakly nonlinear regime), the scaling exponent increases with Ra in what we call the rapidly rotating regime, and shallows again at the highest values of Ra in the non-rotating regime. The transitional regime connects the steep scaling in the rapidly rotating regime and the relatively shallow non-rotating behaviour. We investigate the flow physics which lead to these different heat transfer behaviours and how to demarcate the boundaries between these different regimes.

We first report the results from high E and Ra cases that show non-rotating behaviour as this defines an upper limit for the heat transport in rotating spherical shell

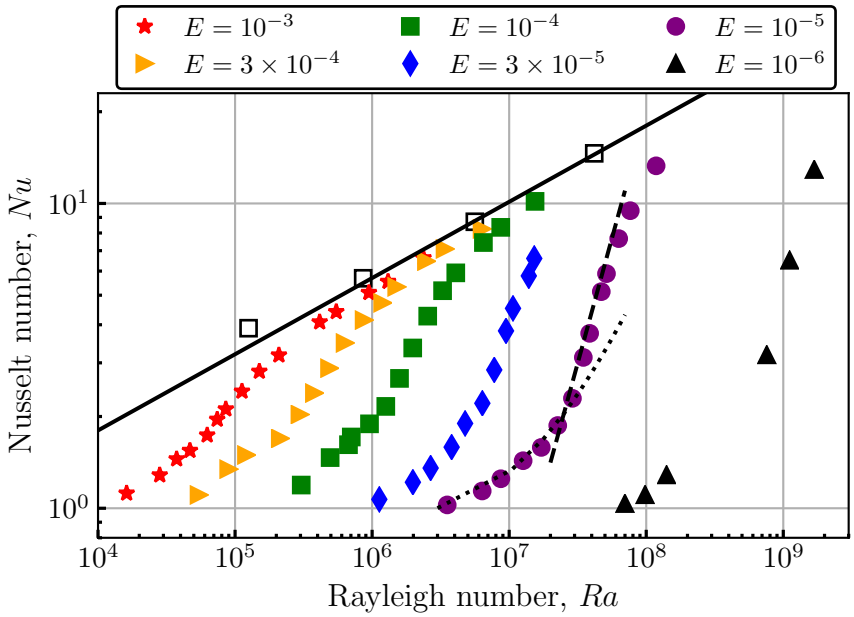

Figure 4.2: Nusselt number versus the Rayleigh number. Seven different Ekman numbers are explored denoted by symbol shape and colour. Close to onset the weakly nonlinear behaviour is indicated by the dotted line, the steep scaling behaviour at low E is illustrated by the dashed line, and the end-member non-rotating behaviour is shown by the solid line. Empty square markers correspond to non-rotating simulations.

convection (Grossmann and Lohse, 2000; Gastine et al., 2016). We then consider reduced Ra and highlight the continually changing behaviour in the transitional regime and identify the upper boundary of the rapidly rotating regime. The weakly nonlinear regime is described and its upper boundary identified. Then, we describe the rapidly rotating regime having defined its upper and lower bounds. Finally we discuss the efficiency of convective mixing in terms of interior temperature gradients, interior temperatures, and the thermal boundary layers.

4.3.1 Non-rotating regime

For a given value of the Ekman number, when the Rayleigh number is raised past some transitional value the dynamics of the system change and begin to follow non-rotating behaviour (King et al., 2009, 2013; Gastine et al., 2016). Motivated by the behaviour seen in figure 4.2 we will focus on the $E \geq 10^{-4}$ cases to investigate the transition to the non-rotating branch of heat transfer. Figure 4.4(a) shows that the local $Nu - Ra$ slope continually decreases until the most vigorously forced models ($Ra \geq 3 \times 10^5$) for $E = 10^{-3}$ follow a scaling of

$$Nu = 0.13 Ra^{2/7}. \tag{4.28}$$

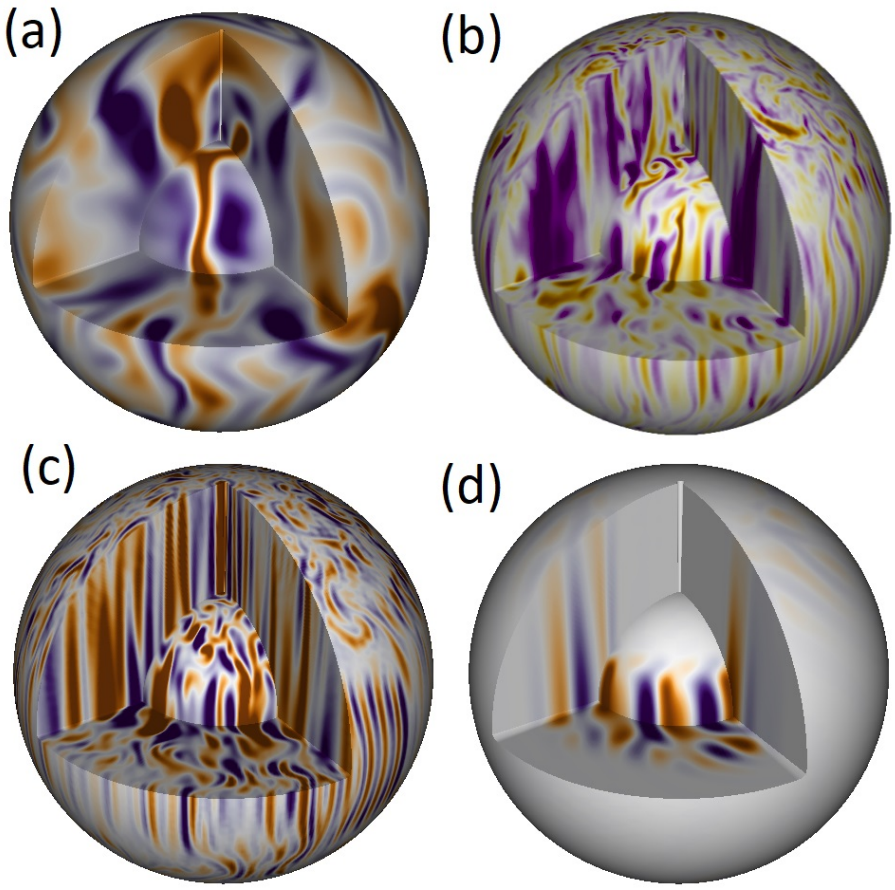

Figure 4.3: Contours of radial velocity shown on meridional and equatorial cuts, and spherical surfaces. The inner and outer surfaces correspond to radii of 10% and 90% of the domain. The different cases shown correspond to (a) a non-rotating model with $E = 10^{-3}$ and $Ra = 1.3 \times 10^6$, (b) a transitional model with $E = 10^{-5}$ and $Ra = 1.2 \times 10^8$, (c) a rapidly rotating model with $E = 10^{-5}$ and $Ra = 4.7 \times 10^7$, (d) a weakly nonlinear model with $E = 10^{-5}$ and $Ra = 8.7 \times 10^6$.

This scaling relation is consistent with other studies with $Ra < 10^{10}$ (Glazier et al., 1999; Cheng et al., 2015) and the analytical work of Grossmann and Lohse (2000) who show that this is a linear combination of two different analytically derived exponents (see their eq. 3.1).

Figure 4.4(b) shows Re_c plotted versus Nu. The least squares regression yields $Re_c = 6.39Nu^{1.88}$ with $R^2 = 1.00$ and $\chi = 1.23$. The empirical fit is indistinguishable from the predicted square law,

$$Re_c = 5Nu^2. \tag{4.29}$$

Combining the heat transfer and flow speed scalings (equations (4.28) and (4.29) respectively) yields

$$Re_c = 0.65Ra^{4/7}. \tag{4.30}$$

The theoretical scaling equation (4.16) is derived solely from the heat equation and equation (4.30) is therefore unlikely to be valid at asymptotically high Re when inertia plays a dominant role. At larger Ra values equation (4.16) is expected to transition to the asymptotic $Re_c \sim Ra^{1/2}$ behaviour as the ultimate regime of Grossmann and Lohse (2000) is reached.

Figure 4.4(c) shows that for $E = 10^{-3}$ cases the length scale is described by a least squares fit giving

$$\ell/h = 0.97Nu^{-0.48}, \tag{4.31}$$

in excellent agreement with equation (4.17). The $E = 3 \times 10^{-4}$ data may be approaching the same scaling behaviour but with a different prefactor implying there is still some secondary influence of rotation. Combining the scalings for the heat transfer and length scales (equations (4.28) and (4.31)) yields

$$\ell/h = 2.58Ra^{-0.14}. \tag{4.32}$$

In figure 4.4(d) we show that there is no systematic dependence of δ_ν/h on Re_c for the majority of models, even when other diagnostics follow non-rotating behaviours. Figure 4.4(d) shows that for the highest Ra cases with $E = 10^{-3}$, the theoretical $Re_c^{-1/2}$ scaling is approached for the boundary layers at both the inner and outer boundaries. The inner and outer boundary layer thicknesses have best fits

$$\delta_\nu^i/h = 0.82Re_c^{-0.52} \quad \text{and} \quad \delta_\nu^o/h = 0.96Re_c^{-0.50} \tag{4.33}$$

respectively. Combining the flow speed and boundary layer scalings gives (equation (4.30) and equation (4.33) respectively) yields

$$\delta_\nu^i/h = 0.53Ra^{-0.30} \quad \text{and} \quad \delta_\nu^o/h = 0.62Ra^{-0.29} \tag{4.34}$$

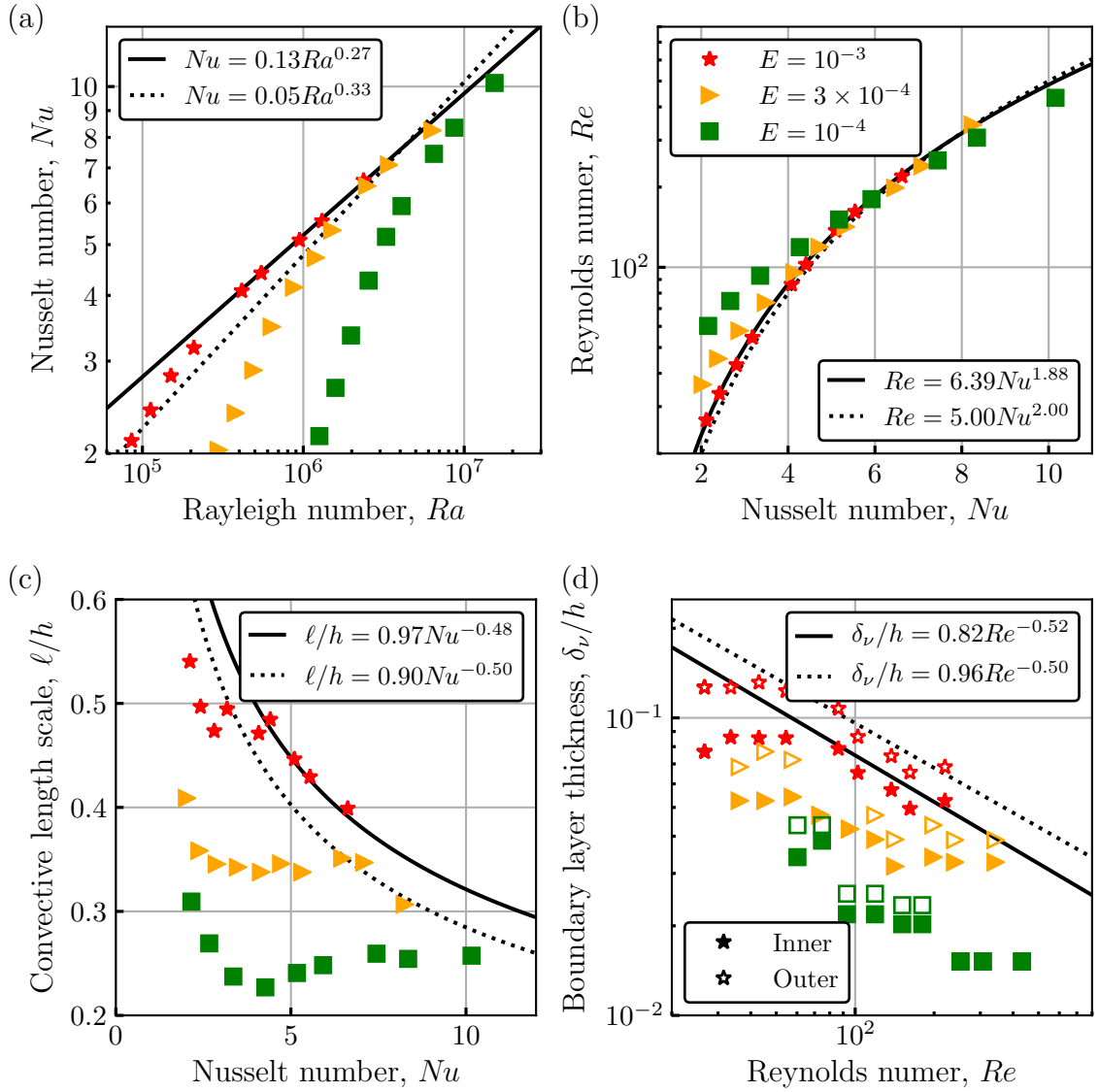

Figure 4.4: Models in the transitional regime with $E \geq 10^{-4}$ showing: (a) heat transfer scaling - the two scaling behaviours associated with non-rotating convection, $Nu \sim Ra^{2/7}$ and $Nu \sim Ra^{1/3}$ are shown as solid and dotted lines respectively, (b) flow speed scaling - solid and dotted lines show the empirical and theoretical scaling behaviours respectively, (c) typical length scales versus Nusselt number - solid line showing best fit to models with $E = 10^{-3}$, dotted line showing prediction with prefactor tuned for $E = 3 \times 10^{-4}$ models. (d) Viscous boundary layer thicknesses shown vs Reynolds number, solid/empty markers correspond to inner/outer boundary layer thicknesses. The solid and dotted lines show the empirical fits to δ_ν/h for the inner and outer boundary layers respectively.

for the inner and outer boundary layers respectively.

4.3.2 Transitional regime

We have seen that at high Ra the dynamics behave as if non-rotating, but to approach this behaviour there is a continuous transition of each quantity. In figure 4.2 we see that the steep heat transfer scaling for a given E exists for a different range of Ra values. Large Ekman number cases quickly depart to a shallower scaling whereas the lower Ekman number models exhibit the steep scaling behaviour up to higher values of Ra. Clearly a simple supercriticality condition does not demarcate the transition from the rapidly rotating regime to the transitional regime (see figure 4.2). Models in the transitional regime are sensitive to rotational effects but are not completely columnar in nature (see figure 4.3(b)). We have investigated the behaviour over a broad range of parameter space in this transitional regime of rotating convection in which the flow and heat transport properties continuously vary until many diagnostics recover behaviour associated with non-rotating convection (as previously reported by Gastine et al., 2016). The continuously changing behaviour (see figures 4.5 and 4.6) makes it impossible to obtain scaling laws in this regime and instead we focus on locating the lower boundary of this regime. To best demarcate the lower bound of the transitional regime we test each of the transition parameters.

The majority of our models have $Ro_c < 1$ and an order unity transition is not supported (figure 4.5(a)). The boundary crossing parameter, Ra_δ, performs better than Ro_c in terms of collapsing the data however there is still sufficient scatter showing a systematic Ekman dependence (figure 4.5(b)). The transition parameter of Julien et al. (2012a) performs best; the steep heat transfer data collapses onto a single line (figure 4.5(c)) and the F-test finds that the data becomes distinguishable from the linear fit when $Ra_G > 0.6$. The cases with $Ra_G > 0.6$ show a gradual change in behaviour until the data follows equation (4.28). The lower bound of the transitional regime is determined to be

$$Ra_G = 0.6, \quad \text{or} \quad Ra = 0.6E^{-8/5}. \tag{4.35}$$

This transition is found consistently if instead Re_c or ℓ is used as shown in figure 4.6. In subsection 4.3.4 we will discuss the importance of the transitional regime's lower bound given by equation (4.35) in terms of rapidly rotating convection.

To quantify the boundary between the transitional and non-rotating regimes we would require additional numerical simulations at larger Ra. However, it is interesting to note that our $E = 10^{-3}$ cases follow the non-rotating scaling behaviour above supercriticalities of $Ra/Ra_c = 70$ whereas models by (Gastine et al., 2016) do not approach this limit until supercriticalities of approximately 400. Some amount of this difference is likely as a result of how Ra_c is treated, Gastine et al. (2016) approximate $Ra_c \sim E^{-4/3}$.

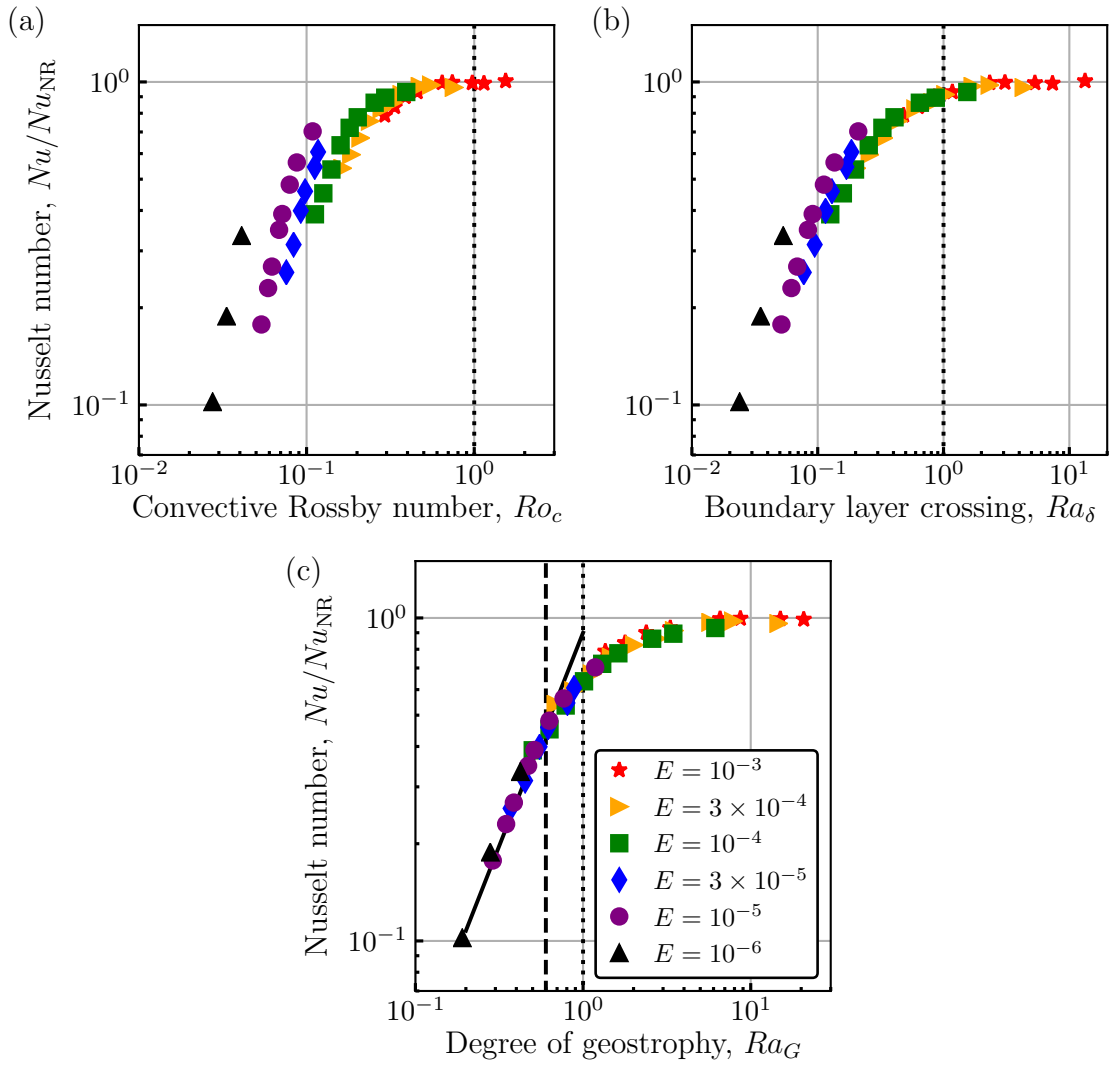

Figure 4.5: Nusselt number compensated by the non-rotating scaling, $Nu_{\mathrm{NR}} = 0.13Ra^{2/7}$ (equation (4.28)) versus proposed parameters to control the transition from rotationally constrained to weakly-rotating convection. The dotted lines are the expected locations where the data should deviate from the steep heat transfer behaviour and start transitioning to a plateau. In (c) the dashed line corresponds to $Ra_G = 0.6$, the location at which the data deviates from the linear relationship at lower values. For clarity only models with $Nu > 2$ are shown.

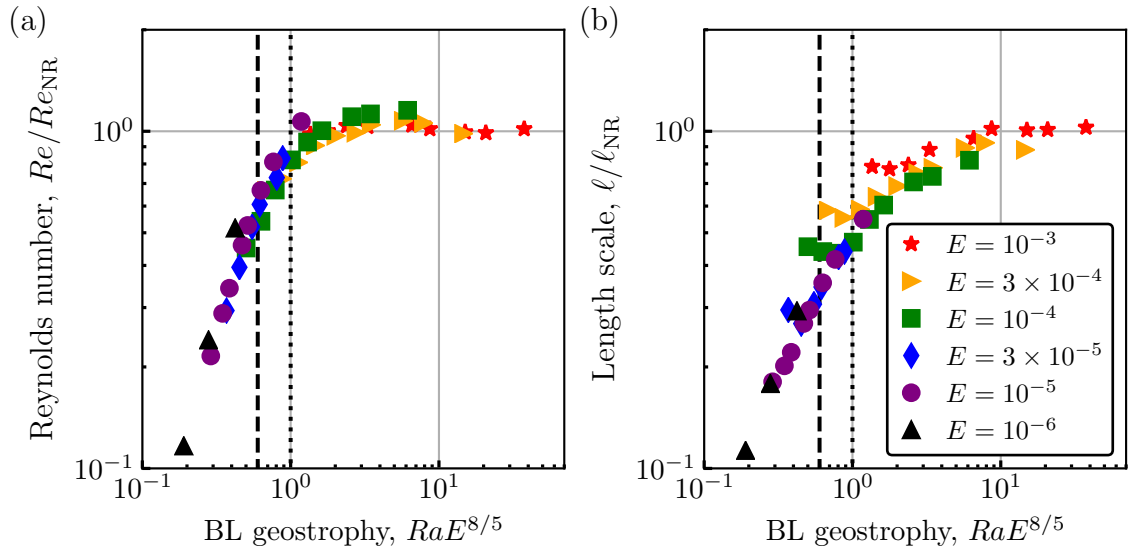

Figure 4.6: Compensated Reynolds number and convective length scale (normalised by the non-rotating scalings equations (4.30) and (4.31) respectively) versus the transition parameter, Ra_G. For clarity, only models with $Nu > 2$ are shown. The vertical lines have the same meanings as in figure 4.5.

4.3.3 Weakly nonlinear regime

After testing the high Ra cases, we now consider the cases close to onset as there is established theory to compare our results with. For Rayleigh numbers just above critical, a weakly nonlinear perturbation analysis (Gillet and Jones, 2006) predicts that the heat transport increases proportionally with supercriticality (equation (4.21)). Figure 4.7 shows $Nu - 1$ as a function of $Ra/Ra_c - 1$ for the models with $E \leq 10^{-4}$ and $Ra/Ra_c \leq 20$. The best fit to the data with $Ra/Ra_c \leq 8$ yields

$$Nu - 1 = 0.13\,(Ra/Ra_c - 1)^{1.04}\,, \tag{4.36}$$

with $R^2 = 0.99$ and $\chi = 18.55$. Data with $Ra/Ra_c > 8$ shows a clear departure from this scaling law and if included in the fitting a statistically different behaviour is found when checked with an F-test. We would not expect the weakly nonlinear theory to hold for $Nu > 2$ and equation (4.21) describes the data with $Ra \leq 8Ra_c$ reasonably well although a weak dependence on the Ekman number persists. We have included the $E = 10^{-4}$ data in figure 4.7 to illustrate that the weakly nonlinear behaviour is only observed for low E.

Figure 4.8(a) shows the average length scale ℓ/h plotted as a function of E for the numerical models close to onset ($Ra \leq 8Ra_c$) as to include only the models which exhibit the weakly nonlinear heat transfer scaling. The best fit to the data yields

$$\ell/h = 9.28E^{0.34}, \tag{4.37}$$

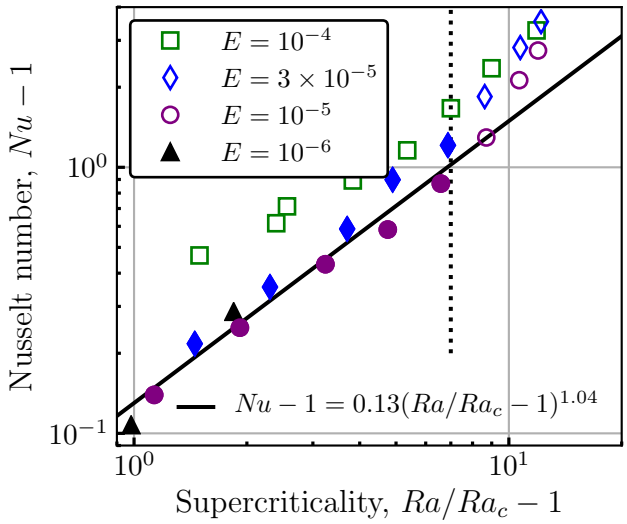

Figure 4.7: Nusselt number, $Nu - 1$, versus supercriticality, $Ra/Ra_c - 1$. Only the cases with $E \leq 10^{-4}$ and $Ra < 14Ra_c$ are displayed for clarity. The solid black line is the least squares fit to the filled marker data. The unfilled markers show a departure from this scaling which breaks down close to $Ra/Ra_c = 8$ shown as the vertical dotted line.

with $R^2 = 0.95$ and $\chi = 25.50$. For models with $E < 10^{-4}$ the misfit reduces to $\chi = 17.92$ implying that the typical length scale gradually approaches the theoretical VAC scaling (equation (4.12)) when $E < 10^{-4}$. The cases with higher Ekman numbers significantly depart from this scaling. Figure 4.8(b) shows Re_c versus the VAC prediction $B^{1/2}E^{1/3}$ for models with $Ra \leq 8Ra_c$. The least-squares fit to the data with $E < 10^{-4}$ yields

$$Re_c = 0.50 \left(B^{1/2}E^{1/3}\right)^{0.97}, \tag{4.38}$$

with $R^2 = 0.99$ and $\chi = 5.44$ which is in good agreement with the theory. The exponent being different from unity for the Reynolds number scaling is due to the length scaling not exactly matching the theory.

Figure 4.8 shows that the VAC theory for the length scales and flow speeds is valid for $E \leq 10^{-4}$ and breaks down at larger values of E. The $E - Ra$ parameter space corresponding to the weakly nonlinear regime of rotating convection is given by $Ra \leq 8Ra_c$, and $E \leq 10^{-4}$. We do not investigate the boundary layers in this regime as the flow is not fully developed and boundary layer analysis is not meaningful close to the onset of convection.

Combining equations (4.7), (4.14) and (4.21) allows us to write the scaling behaviour for the flow speed in the weakly nonlinear regime in terms of only the control parameters

$$Re_{\mathrm{WN}} \sim \left[Ra\left(\frac{Ra}{Ra_c} - 1\right)\right]^{1/2} E^{1/3}. \tag{4.39}$$

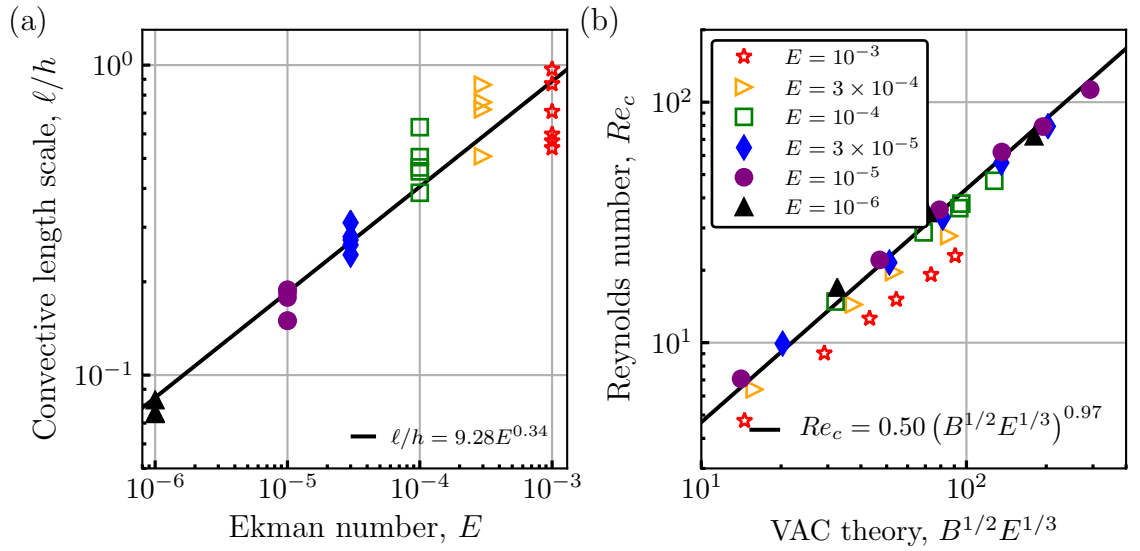

Figure 4.8: (a) Average flow length scale, ℓ/h, versus the Ekman number, E. (b) The Reynolds number, Re_c, versus the prediction of the VAC scaling, $B^{1/2}E^{1/3}$ (equation (4.14)). Only models with $Ra \leq 8Ra_c$ are shown. In both plots, the solid black lines correspond to the least-square fits to the data having $E < 10^{-4}$ (filled markers). The empty symbols are not included in the empirical fits.

4.3.4 Rapidly rotating regime

The weakly nonlinear scaling (equation (4.21)) describes the heat transport data until $Ra = 8Ra_c$ (subsection 4.3.3) after which the $Nu - Ra$ scaling becomes much steeper for moderate to low Ekman numbers. The regime of nonlinear and rotationally constrained convection is bounded above by $Ra_G = 0.6$ (see subsection 4.3.1) and exhibits heat transfer scaling exponents that increase with decreasing Ekman number (figure 4.2)

$$Nu \sim Ra^{\lambda(E)}, \tag{4.40}$$

as reported in previous studies in both plane layer (King et al., 2012; Cheng et al., 2015) and spherical shell geometries (Yadav et al., 2015; Gastine et al., 2016). Plane layer studies find exponents that are much larger than those observed in spherical shells (roughly a factor of two different) and this is likely due to Ekman pumping being maximised in plane layer cases which have gravity aligned with the rotation axis (Greenspan, 1968). In the absence of diffusion, equation (4.22) predicts $Nu \propto (RaE^{4/3})^{3/2}$. This scaling does a good job of collapsing the data, however our models do not follow the asymptotic scaling $Ra_c \sim E^{-4/3}$, as we are not at asymptotically low E. Furthermore table 4.2 shows that the steepest $Nu - Ra$ scaling exponents for $E \leq 10^{-5}$ exceed the value of 1.5 predicted by Jones (2015). Ekman boundary layers have been shown to allow states of enhanced heat transport and deviations from the asymptotic $Nu \propto Ra^{3/2}E^2$ behaviour (Stellmach et al., 2014; Plumley et al., 2016, 2017) and this could explain the steeper heat transfer exponents in the rapidly rotating regime.

Ekman number	Exponent
10^{-3}	0.56
3×10^{-4}	0.72
10^{-4}	0.97
3×10^{-5}	1.33
10^{-5}	1.66
10^{-6}	1.75

Table 4.2: Nusselt-Rayleigh scaling exponents given by the steepest heat transfer behaviour of four consecutive cases for each Ekman number. For $E = 10^{-6}$ we fit the three highest Ra cases. No clear asymptotic scaling behaviour has been found in our numerical models: the values of λ continously increase as a function of E^{-1} (e.g. Grooms and Whitehead, 2014; Cheng et al., 2015).

To quantify the steep heat transfer scaling behaviour above $Ra = 8Ra_c$, we fit each set of four consecutive Ra runs at a fixed Ekman number and take the linear best fit with maximum scaling exponent as in Mound and Davies (2017). For $E = 10^{-6}$ we fit a straight line through the three simulations with highest Ra values. The best-fitting values for λ as a function of the Ekman number are listed in table 4.2. We find that λ increases monotonically with decreasing E with a scaling close to $\lambda \propto \ln|E^{-1}|$, in agreement with Cheng et al. (2015).

It has been argued that the numerical dataset of Christensen and Aubert (2006) follows the VAC scaling beyond the weakly nonlinear regime of rotating convection (King and Buffett, 2013; Oruba and Dormy, 2014). We examined the scaling law that describes the length scale for the weakly nonlinear models, $\ell/h \sim 9.28E^{0.34}$ and found that it does not capture the variations in the rapidly rotating regime. Figure 4.9(a) shows the length scale versus Re_cE for all cases with $Ra > 8Ra_c$; at our lowest sampled Ekman numbers a systematic dependence seems to emerge,

$$\frac{\ell}{h} = 1.50(Re_cE)^{0.44}. \tag{4.41}$$

It is not surprising that the behaviour of the length scale only approaches the theoretical scaling equation (4.15) since the boundary layers still play a substantial role due to the high values of E used. Gastine et al. (2016) found that for their models with $E = 1.5 \times 10^{-7}$ the length scale showed the dependence, $\ell/h \sim (Re_cE)^{0.45}$ which is in good agreement with equation (4.13) and suggests that at low enough Ekman number

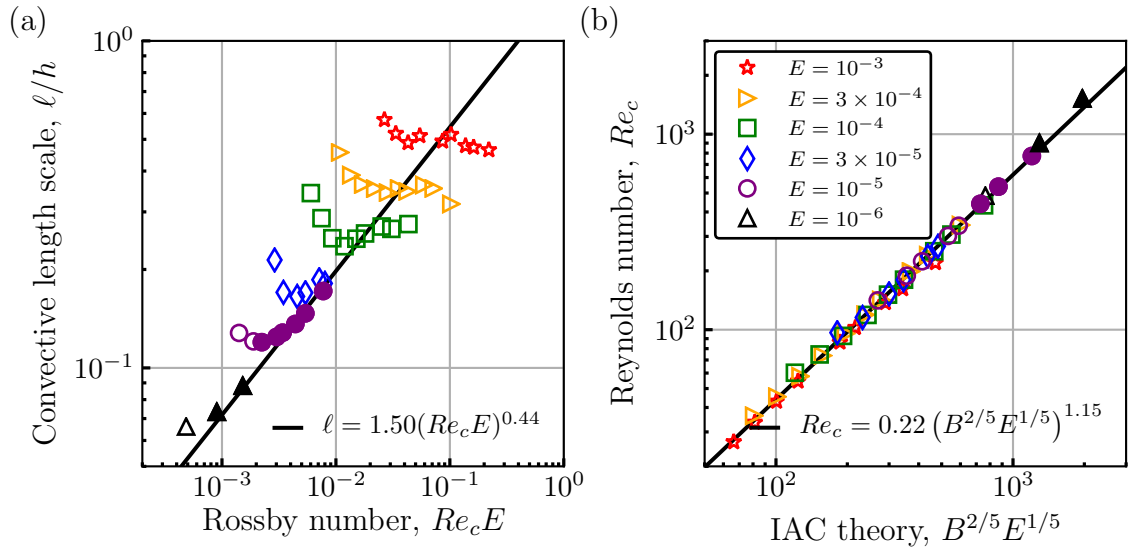

Figure 4.9: (a) Average flow length scale, ℓ/h, versus the Rossby number based on the convective flow, Re_cE, (b) convective flow speed, Re_c, versus the prediction of the IAC balance, $B^{2/5}E^{1/5}$ (equation (4.15)). Only models with $Ra \geq 8Ra_c$ are shown. In both plots, the solid black lines correspond to the least-square fits to the filled marker data. The empty symbols are not included in the empirical fits.

(perhaps only one-two orders of magnitude away from present values) the Rhines scaling could be confirmed (see also Guervilly et al., 2019, who observe the Rhines scaling in quasi-geostrophic models at much lower Ekman number than those accessible in our fully three-dimensional cases). Based on the relevant length scale being different from the theory we would not then expect the IAC scaling for the flow speed to be exactly reproduced. We do find a scaling law which sufficiently collapses the data for the rapidly rotating regime (figure 4.9(b)). The best fit yields

$$Re_c = 0.22(B^{2/5}E^{1/5})^{1.15} \tag{4.42}$$

which is statistically different from the IAC scaling (equation (4.15)) as expected, owing to the IAC length scale only being partially realised in our simulations. An exact IAC balance is not to be expected over the range of E values studied here as viscous boundary layer effects still make up a considerable contribution to the dynamics and boundary layer dissipation is not negligible for our range of Re_c (Gastine et al., 2015). The cases with larger Re_c better approach the IAC prediction (equation (4.15)).

We now investigate the behaviour of δ_ν/h in a systematic manner. For all cases with $Ra > 8Ra_c$ the least squares regression to the inner and outer boundary layer thicknesses using the linear intersection method gives $\delta^i_\nu/h \sim E^{0.40}$, $\delta^o_\nu/h \sim E^{0.47}$ respectively. If the additional constraint of rapid rotation is imposed, the best fit for the cases with $Ra > 8Ra_c$ and $E \leq 10^{-4}$ yields $\delta^i_\nu/h \sim E^{0.44}$, $\delta^o_\nu/h \sim E^{0.48}$, an improvement over the prior. If we consider only fully convecting models ($Ra > 8Ra_c$) which are rapidly rotating

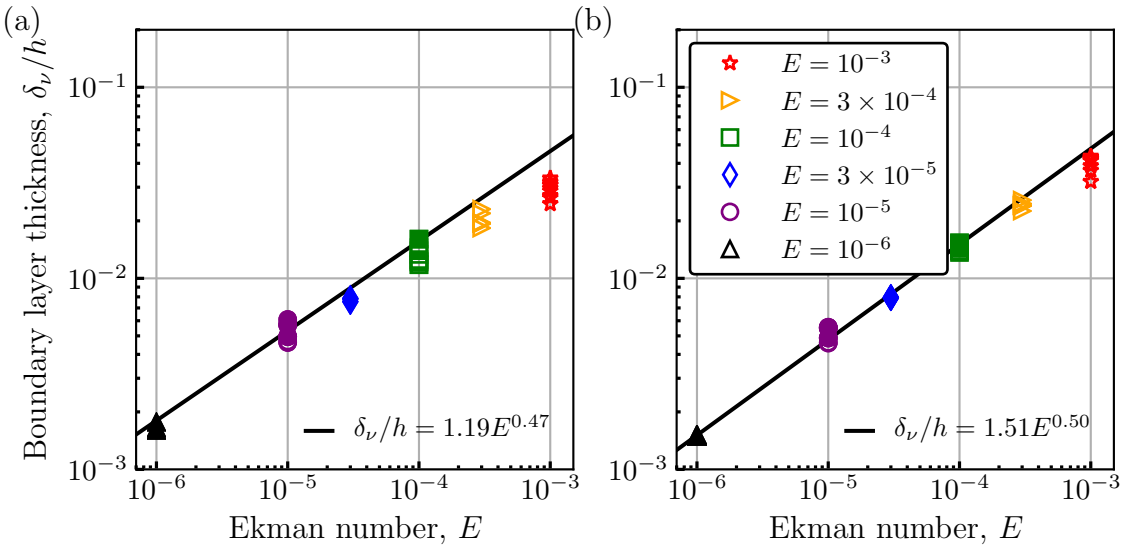

Figure 4.10: Viscous boundary layer thickness, δ_ν at the (a) inner and (b) outer boundary versus the Ekman number, E. The solid black lines correspond to the best fit to the 13 cases that fulfill $RaE^{8/5} < 0.6$, $E \leq 10^{-4}$ and $Nu > 2$ (filled markers). The least squares fit to the inner boundary has $R^2 = 0.99$ and $\chi = 9.24$ while the outer boundary has $R^2 = 1.00$ and $\chi = 6.16$.

($E \leq 10^{-4}$) and rotationally constrained ($RaE^{8/5} < 0.6$): the best fit then scales as

$$\delta_\nu^i/h = 1.19E^{0.47}, \ \delta_\nu^o/h = 1.51E^{0.50}, \tag{4.43}$$

in good agreement with equation (4.19), see figure 4.10. Interestingly, as we further constrain the models included in the fit we find that the relative misfit χ stays roughly the same and only the fitted exponent changes (see table 4.3). When comparing the definitions using the linear intersection and local maxima methods we find that the scaling exponents are statistically indistinguishable when compared using an F-test, though the prefactor of the linear intersection method is larger.

As reported in previous studies (e.g. Gastine et al., 2016) we find that the viscous boundary layer better follows the theoretical scaling at the outer boundary than it does for the inner boundary. We suspect this is because of the importance of curvature at the inner boundary, which would require a suite of models with varying radius ratio to test. At larger values of radius ratio the curvature effects should diminish and in the thin gap limit the the scaling behaviour of δ_ν^i/h should better follow the $E^{1/2}$ scaling with inner and outer boundary layers having equal thicknesses.

Similarly for the rapidly rotating regime we relate B to the control parameters, however in this regime the Nusselt-Rayleigh scaling exponent is a function of the Ekman number, combining equations (4.7), (4.15) and (4.40):

$$Re_{\mathrm{RR}} \sim \left[Ra\left(Ra^{\lambda(E)} - 1\right)\right]^{2/5} E^{1/5}. \tag{4.44}$$

		linear intersection				local maxima			
		prefactor	exponent	R^2	$\chi(\%)$	prefactor	exponent	R^2	$\chi(\%)$
$Nu > 2$	δ_ν^i/h	0.51	0.40	0.99	10.87	1.36	0.40	0.99	8.74
	δ_ν^o/h	1.05	0.47	1.00	7.48	3.42	0.48	1.00	7.29
$Nu > 2,\ E \leq 10^{-4}$	δ_ν^i/h	0.74	0.44	0.99	9.28	1.72	0.42	0.99	9.56
	δ_ν^o/h	1.27	0.48	1.00	5.84	3.82	0.49	1.00	7.13
$Nu > 2,\ E \leq 10^{-4},$	δ_ν^i/h	1.19	0.47	0.99	8.55	2.58	0.45	0.99	9.24
$RaE^{8/5} < 0.6$	δ_ν^o/h	1.51	0.50	1.00	6.67	4.88	0.51	1.00	6.16

Table 4.3: Prefactors, exponents, coefficients of determination and relative misfit of the empirical fit to the velocity boundary layer thickness, δ_ν/h as a function of E. Analysis is limited to fully convecting models having $Nu > 2$, the data is further tested by quantifying the importance of rotation by limiting the analysis to models with $E \leq 10^{-4}$, and then finally the we consider models which are also rotationally constrained having $RaE^{8/5} < 0.6$.

Finally, the length scale in the rapidly rotating regime can be written in terms of the input parameters by combining equations (4.40) and (4.44)

$$\left(\frac{\ell}{h}\right)_{\mathrm{RR}} \sim \left[Ra\left(Ra^{\lambda(E)}-1\right)\right]^{1/5} E^{3/5}. \tag{4.45}$$

4.3.5 Convective mixing

Here we quantify the efficiency of turbulent convection in mixing the bulk fluid by considering the temperature gradients, $\mathrm{d}T_{\mathrm{int}}$, and the temperatures, T_{int}, at mid-shell radius. Figure 4.11 shows radial profiles of the time and horizontally averaged temperature, $\langle\overline{\vartheta}\rangle$, for models with $E = 10^{-3}$ and $E = 10^{-5}$. Increasing the supercriticality changes the temperature distribution from a conductive profile toward that of a nearly isothermal fluid bulk (zero interior temperature gradients are realised only for our highest Ra simulations with $E = 10^{-3}$). Figure 4.12(a) shows the temperature gradient at mid-depth as a function of supercriticality. In agreement with Julien et al. (2012b) we find a simple scaling relation between $\mathrm{d}T_{\mathrm{int}}$ and Ra/Ra_c. With the exception of $E = 10^{-3}$ all models follow a relation of $\mathrm{d}T_{\mathrm{int}} = (Ra/Ra_c)^{-\gamma}$ where $0.61 < \gamma < 0.66$. We introduce a weak Ekman dependence to collapse the data for models in the rapidly rotating and transitional regimes,

$$\mathrm{d}T_{\mathrm{int}} = 0.63\,(Ra/Ra_c)^{-0.60}\,E^{-0.10}; \tag{4.46}$$

this scaling has $R^2 = 0.95$, and $\chi = 5.58$ for the data within the rapidly rotating regime, and $\chi = 32.22$ for models with $Ra > 8Ra_c$ and $Ra_G > 0.6$. This observation of a continuously decreasing temperature gradient with increasing Ra differs from the behaviour in plane layers which sees the mid-depth temperature gradient decrease for weak supercriticalities and plateau for turbulent quasi-geostrophic convection (e.g. Stellmach et al., 2014). Our findings are consistent with (Gastine et al., 2016) which suggests that either the geometry or degree of supercriticality is the reason for the different behaviour.

The increase in misfit suggests that this scaling law holds in the rapidly rotating regime, but not the transitional regime. We observe that decreasing $\mathrm{d}T_{\mathrm{int}}$ is accompanied with a decreasing interior temperature, T_{int} (see figures 4.11 and 4.12). Unlike the gradient we find no direct link between T_{int} and supercriticality (figure 4.12(b)). Instead we find that for some of the rapidly rotating regime and into the transitional regime, T_{int} scales with the transition parameter, $Ra_G = RaE^{8/5}$,

$$T_{\mathrm{int}} = 0.23\left(RaE^{8/5}\right)^{-0.28}, \tag{4.47}$$

which describes models with $Ra > 8Ra_c$ having $R^2 = 0.96$ and $\chi = 9.34$. The scaling exponent is statistically indistinguishable from a $-2/7$ law and suggests a link between the interior temperature and convective heat transfer. The transition from rapidly rotating to non-rotating convection is associated with a gradual lowering of the mean temperature gradient (King et al., 2010) until an end-member state is reached where the thermal

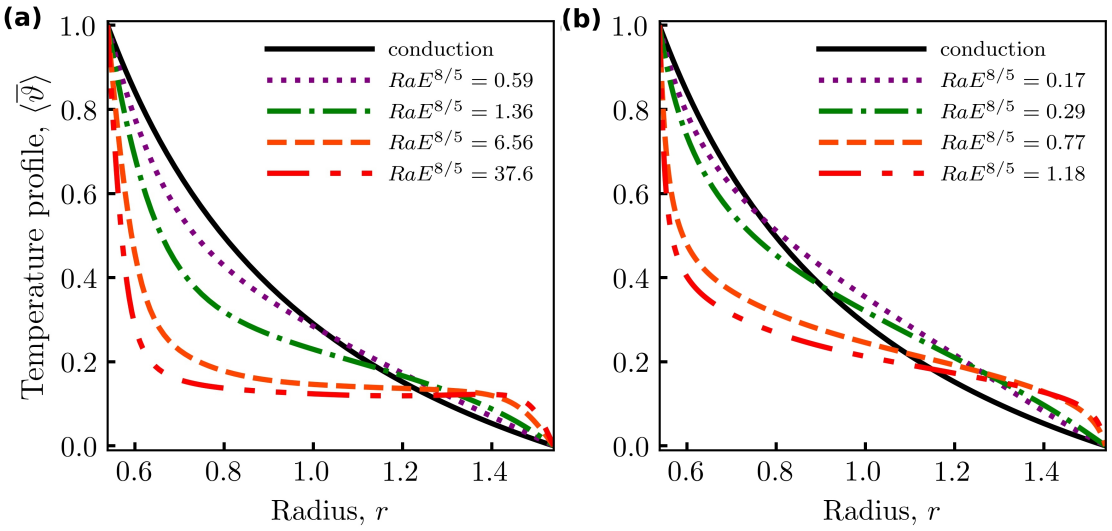

Figure 4.11: Radial profiles of the temporally and horizontally averaged temperature, $\langle\overline{\vartheta}\rangle$, for different values of the transition parameter, $Ra_G = RaE^{8/5}$, for Ekman numbers, (a) $E = 10^{-3}$ and (b) $E = 10^{-5}$. The solid black line corresponds to the conductive temperature profile.

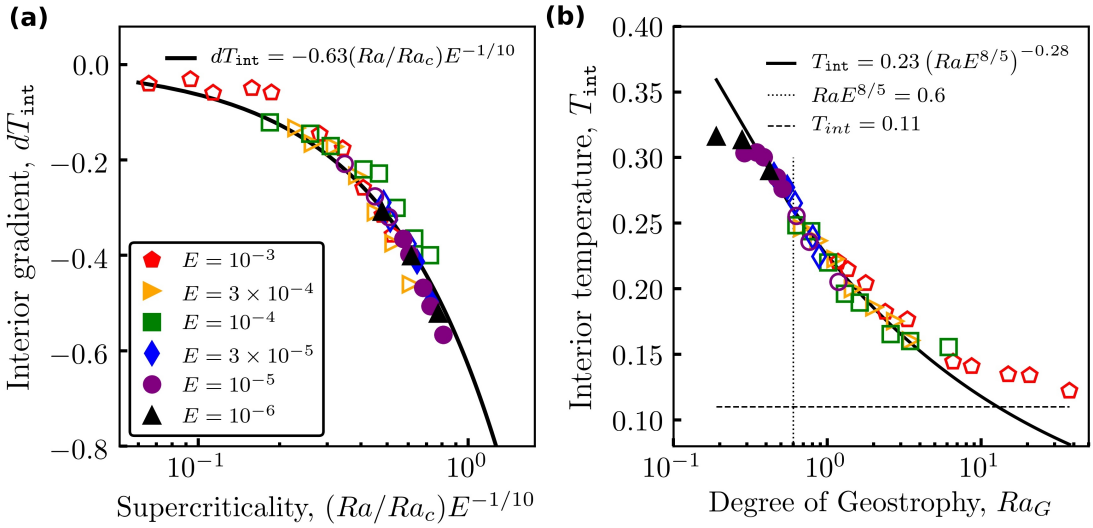

Figure 4.12: (a) Mean internal temperature gradient as measured at mid-depth, $dT_{\rm int}$, versus supercriticality, Ra/Ra_c, with a weak Ekman dependence added in order to best collapse the data. (b) Interior temperature evaluated at mid-depth, $T_{\rm int}$, versus the transition parameter, $Ra_G = Ra^E8/5$. The value 0.11 is shown as a dashed line and is the isothermal prediction of King et al. (2010). The filled markers are in the rapidly rotating regime and unfilled markers are cases in the transitional regime.

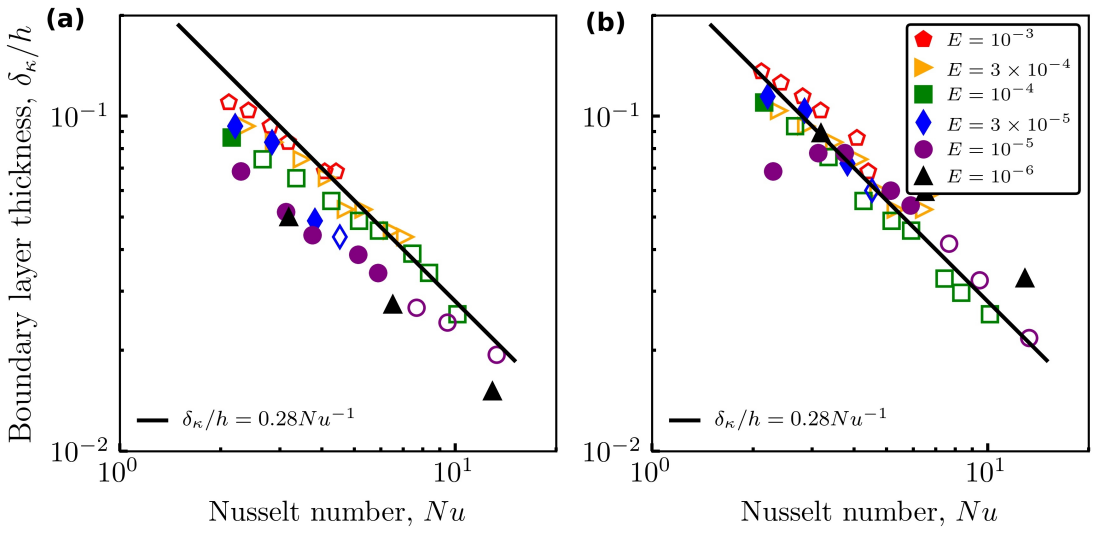

Figure 4.13: Thermal boundary layer thickness, δ_κ/h, at the (a) inner and (b) outer boundary as a function of the Nusselt number, Nu. The solid black line corresponds to the theoretical expectation, $\delta_\kappa/h \propto Nu^{-1}$. Only models with $Nu \geq 2$ are shown for clarity. The filled markers are in the rapidly rotating regime and unfilled markers are cases in the transitional regime.

boundary layers are responsible for the entire temperature drop across the system, for a perfectly well-mixed Boussinesq fluid we expect a zero mean temperature gradient in the fluid bulk.

The thickness of the thermal boundary layers in the transitional regime are well described by a Nu^{-1} law, and even in the rotationally constrained cases this provides a good first order description of the behaviour (see figure 4.13). In the rapidly rotating regime there is some non-trivial dependence of both the prefactor and scaling exponent on E and Ra as previously reported (Gastine et al., 2016),

$$\delta_\kappa = \zeta(Ra, E) Nu^{-1+f(Ra,E)}, \tag{4.48}$$

this is a purely qualitative description and we do not quantify this further.

4.3.6 Composite scaling laws

By combining the flow speed and heat transfer scaling laws in a given regime we can obtain scalings of outputs in terms of the input parameters. The flow speed scaling in a given regime is dependent on the kinetic energy due to buoyancy production. Comparing our definition for the buoyant energy production, B, with King and Buffett (2013) we can write

$$B = Ra(Nu - 1). \tag{4.49}$$

Combining equations (4.14), (4.21) and (4.49) allows us to write the scaling behaviour for the flow speed in the weakly nonlinear regime in terms of only the control parameters

$$Re_{\mathrm{WN}} \sim \left[Ra\left(\frac{Ra}{Ra_c}-1\right)\right]^{1/2} E^{1/3}. \tag{4.50}$$

Similarly for the rapidly rotating regime we relate B to the control parameters, however in this regime the Nusselt-Rayleigh scaling exponent is a function of the Ekman number, combining equations (4.15), (4.40) and (4.49):

$$Re_{\mathrm{RR}} \sim \left[Ra\left(Ra^{\lambda(E)}-1\right)\right]^{2/5} E^{1/5}. \tag{4.51}$$

Finally, the length scale in the rapidly rotating regime can be written in terms of the input parameters by combining equations (4.15) and (4.51)

$$\left(\frac{\ell}{h}\right)_{\mathrm{RR}} \sim \left[Ra\left(Ra^{\lambda(E)}-1\right)\right]^{1/5} E^{3/5}. \tag{4.52}$$

4.4 Conclusions

We have studied the scaling behaviour of rotating convection in a spherical shell geometry using direct numerical simulations. We have performed 74 numerical simulations spanning $10^{-6} \leq E \leq 10^{-3}$, flux Rayleigh numbers up to 800 times supercritical for $Pr = 1$. In all cases we prescribe a fixed heat flux at the no-slip boundaries, a linearly varying gravity distribution and the radius ratio $r_i/r_o = 0.35$. We have studied seven different diagnostics of the system across $E - Ra$ parameter space. These diagnostic quantities are the Nusselt number, Nu, the Reynolds number, Re_c, the flow length scale, ℓ/h, the mechanical boundary layer thickness, δ_ν/h, interior temperatures, T_{int}, interior temperature gradients, $\mathrm{d}T_{\mathrm{int}}$ and thermal boundary layer thicknesses, δ_κ/h. Observed changes in the scaling behaviours of these diagnostics are used to identify boundaries of distinct regimes of rotating convection summarised in figure 4.14. The scaling behaviours of these seven quantities are summarised in table 4.4.

The weakly nonlinear regime consists of columnar flow localised to the inner boundary with heat transfer predicted by weakly nonlinear theory and the convective flow described by a VAC balance. The rapidly rotating regime is turbulent with heat transfer throttled by Ekman pumping and the flow being characterised by an IAC balance in the bulk and VAC balance in the boundary layers. The upper bound of the rapidly rotating regime is demarcated by the parameter, $RaE^{8/5} = \mathcal{O}(1)$, of Julien et al. (2012b) in agreement with Gastine et al. (2016). The rotational constraint on the flow is gradually lost in the transitional regime before all diagnostics follow non-rotating scaling behaviour in the non-rotating regime.

Our systematic survey of convection in a rotating spherical shell reveals interest-

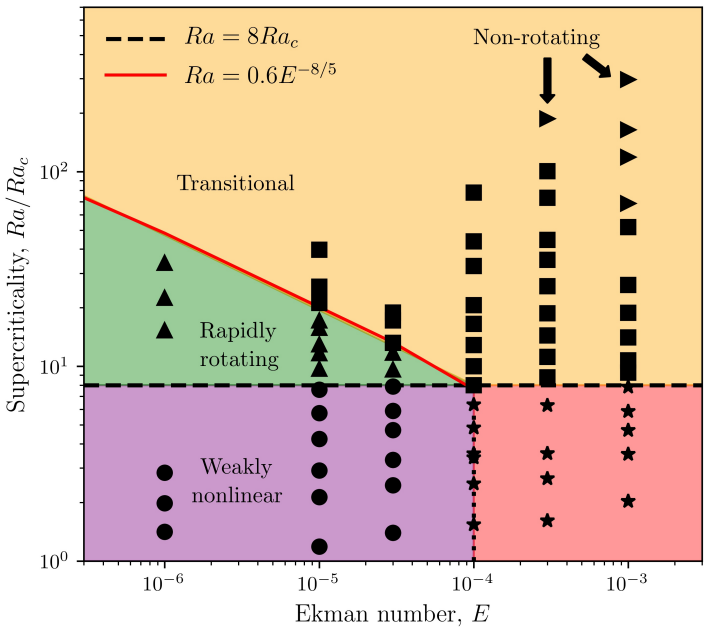

Figure 4.14: Regime diagram summarising the boundaries between different physical regimes of rotating convection. Each marker indicates a numerical simulation with symbol shape and background colour indicating regime; circles are in the weakly nonlinear regime (purple), upward pointing triangles in the rapidly rotating regime (green), squares in the transitional regime (yellow), and right facing triangles correspond to the non-rotating cases. The stars (pink) represent a unique regime at high E which we have not explored in this work. The dashed line shows $Ra = 8Ra_c$ and the solid red line shows the upper bound of the rapidly rotating regime demarcated by $Ra_G = RaE^{8/5} = 0.6$.

ing differences from the similar study of Gastine et al. (2016). There are three differences in model configuration between our study and Gastine et al. (2016); we use a smaller radius ratio, r_i/r_o (0.35 to their 0.60), a different gravity distribution (linear to their quadratic), and fixed-flux thermal boundary conditions (they use fixed temperature). It is not clear how each of these quantities affect the heat transfer and flow speed behaviour. For the weakly nonlinear and non-rotating regimes of rotating convection our results are in agreement with Gastine et al. (2016) however we observe differences in the scaling behaviour of the Reynolds number and Nusselt number in the rapidly-rotating regime. In the rapidly-rotating regime, Gastine et al. (2016) find that the heat transfer data saturates to the asymptotic scaling exponent of 1.50, whereas we find exponents as high as 1.75 with no signs of the scaling exponent reaching a limit. We find similar scaling behaviour of the convective length scale in this regime but different Reynolds number scaling behaviour. Our results suggest a more significant contribution of the viscous boundary layers to both the Reynolds number and Nusselt number scaling behaviours. Even for our lowest E cases Ekman pumping effects are still important to the globally averaged heat transport. Simulations in Cartesian geometries find much larger scaling exponents with values as high as 3.60 (Cheng et al., 2015) and this can be attributed to the efficiency of Ekman pumping being maximised as gravity is antiparallel to the rotation axis. Although the scaling behaviour in a given regime differs, we find very similar regime boundaries to Gastine et al. (2016) implying that the relative importance of rotation is the key factor in determining these regimes, with the other quantities having secondary effects.

Regime	weakly nonlinear		rotationally constrained		Non-rotating	
parameter	scaling	reference	scaling	reference	scaling	reference
Nu	$c_1\left(\frac{Ra}{Ra_c}-1\right)+1$	equation (4.36) figure 4.7	$\lambda(E)$	equation (4.40) table 4.2	$\rightarrow Ra^{2/7}-Ra^{1/3}$	equation (4.28) figure 4.4(a)
ℓ/h	$E^{1/3}$	equation (4.37) figure 4.8(a)	$(Re_cE)^{0.40}\rightarrow(Re_cE)^{1/2}$	equation (4.41) figure 4.9(a)	$\rightarrow c_2(E)Ra^{-1/7}$	equation (4.32) figure 4.4(c)
Re_c	$B^{1/2}E^{1/3}$	equation (4.38) figure 4.8(b)	$\left(B^{2/5}E^{1/5}\right)^{1.15}\rightarrow B^{2/5}E^{1/5}$	equation (4.42) figure 4.9(b)	$\rightarrow Ra^{4/7}$	equation (4.30) figure 4.4(b)
δ_ν/h	Undefined		$E^{1/2}$	equation (4.43) figure 4.10	$\rightarrow Ra^{-1/7}$	equation (4.34) figure 4.4(d)
$T_{\rm int}$	$\frac{r_i^2-r_or_i}{r_i^2-r_o^2}$	King et al. (2010)	$\left(RaE^{8/5}\right)^{-2/7}$	equation (4.47) figure 4.12(a)	$\rightarrow 0.11^*$	King et al. (2010) figure 4.12(a)
$\mathrm{d}T_{\rm int}$	$\frac{4r_ir_o}{(r_i-r_o)(r_i+r_o)^2}$	King et al. (2010)	$(Ra/Ra_c)^{-3/5}\,E^{-1/10}$	equation (4.46) figure 4.12(b)	$\rightarrow 0$	figure 4.12(b)
δ_κ/h	Undefined		$Ra^{-2/7+f(E,Ra)}$	equation (4.48) figure 4.13	$\rightarrow Ra^{-2/7}$	equation (4.48) figure 4.13

Table 4.4: Summary of results for the scaling behaviour of the Nusselt number, Nu, the characteristic length scale of convection, ℓ/h, the convective flow speed, Re_c, viscous boundary layer thickness, δ_ν/h, temperature at mid-shell depth, $T_{\rm int}$, internal temperature gradients defined at mid-shell depth, $\mathrm{d}T_{\rm int}$, and thermal boundary layer thickness, δ_κ/h. *The asymptotic value for the interior temperature $T_{\rm int}$ is derived under the assumption of the inner and outer boundary layers having equal thickness.

Chapter 5

A comparison of numerical and laboratory models of convection in the polar region

5.1 Introduction

The most widespread tool for investigating planetary core flows has been direct numerical simulations (DNS) of the magnetohydrodnamic equations in rotating spherical shell geometries (Christensen and Wicht, 2015; Wicht and Sanchez, 2019). At the most extreme parameter values currently accessible, numerical dynamos operate in a regime where the leading order force balance is geostrophic; the Coriolis force is balanced by pressure gradients (e.g. Soderlund et al., 2012; Schwaiger et al., 2019). We note that some studies debate the leading order balance present in the models, see e.g. Sheyko et al. (2018); Aubert (2019). Magnetic effects enter the force balance at the next order and this motivates the study of hydrodynamic rotating convection as an analogue of core dynamics. A variety of modelling approaches have been developed to investigate rapidly rotating convection and these can be broadly grouped into three categories: global (spherical shell) DNS, local (plane layer or cylindrical) DNS and laboratory (cylindrical) experiments. In what follows we will introduce and discuss these three approaches along with their respective advantages and disadvantages. The goal of this chapter is to systematically compare the different modelling approaches and to detail how they complement one another.

The accessible parameter ranges of each modelling approach is a key point of comparison and discussion. For a given aspect ratio, rotating convection is governed by three dimensionless control parameters: the Ekman number, E, the Rayleigh number, Ra, and the Prandtl number, Pr. These parameters are formally defined in table 5.1. The

expected parameter values for Earth's core are

$$E \sim \mathcal{O}(10^{-15}),\ Ra \sim \mathcal{O}(10^{25}),\ Pr \sim \mathcal{O}(0.1). \tag{5.1}$$

The control parameters are introduced and their values determined in §1.2. None of the modelling approaches are able to simultaneously access all of the values relevant to Earth's core (e.g. Aurnou et al., 2015).

Global DNS (introduced in subsection 1.3.3 and presented in chapter 4) are the natural choice for studying the dynamics of Earth's core and solve the hydrodynamic equations in a spherical shell geometry. Spherical models explicitly account for the boundary curvature and the radial gravity profile captures the misalignment of the rotation axis with the gravitational acceleration. These effects could be responsible for latitudinal variation in core convection. Global DNS are computationally expensive and the range of values that the control parameters can take are rather limited. These simulations are typically constrained to $E \geq 10^{-7}$ and $Ra \leq 3 \times 10^{10}$ (e.g. Gastine et al., 2016). Furthermore Earth's core is a liquid iron alloy with low Pr whereas numerical simulations are typically run with $Pr = 1$ (e.g. Christensen and Wicht, 2015) in order to reduce computational expense. A key advantage of DNS is that they have high spatial and temporal resolution as they store field values as a function of both time and space; this allows for many diagnostics to be quantified and investigated.

An alternative approach to characterise rotating convection is to consider a local fluid region at high latitude and aligned with the rotation axis (shown graphically in figure 5.1). In this region gravity is antiparallel to the rotation axis and by considering a right cylinder any curvature effects due to the spherical geometry are removed. This cylindrical configuration is easily accessible in a laboratory setting with convection being driven by heating from below and cooling from above (e.g. Aurnou and Olson, 2001; Rossby, 1969). Laboratory experiments are able to reach more extreme values of E and Ra than their global (numerical) counterparts. The most extreme experiments using water as the working fluid (with $Pr \approx 7$) have $E \geq 10^{-8}$ and $Ra \leq 10^{14}$ (Cheng et al., 2018, 2019). Unlike the DNS which typically use an idealised $Pr = 1$ fluid experiments can use low Pr fluids such as liquid gallium (Aurnou and Olson, 2001) or hydrochloric acid (Aujogue et al., 2018) with relative ease. A major restriction of experiments is the lack of available diagnostics; historically temperature measurements have been taken (Rossby, 1969; Funfschilling et al., 2005; Aurnou, 2007) and only recently have these been complemented by pointwise velocity measurements (Qiu and Tong, 2001a,b; Brown et al., 2007).

Motivated by comparison with laboratory experiments has driven interest in developing DNS in local geometries, either in cylindrical (e.g. Horn and Shishkina, 2014; Kooij et al., 2018) or periodic Cartesian domains (e.g. Stellmach and Hansen, 2004, 2008; Julien et al., 1996). The local DNS provide a middle ground; their accessible parameter space is more extreme than the global DNS and they provide the diagnostic capabilities

Quantity	Meaning	Definition	Global DNS	Local DNS	Experiments
Ekman number, E	$\frac{\text{viscosity}}{\text{Coriolis}}$	$\frac{\nu}{2\Omega h^2}$	$\geq 10^{-6}$	$\geq 5 \times 10^{-8}$	$\geq 10^{-8}$
Prandtl number, Pr	$\frac{\text{viscous diffusion}}{\text{thermal diffusion}}$	$\frac{\nu}{\kappa}$	≥ 1	≥ 0.01	≥ 0.01
Rayleigh number, Ra	$\frac{\text{buoyancy}}{\text{diffusion}}$	$\frac{\alpha g_o \Delta T h^3}{\nu\kappa}$	$\leq 3 \times 10^{10}$	$\leq 10^{11}$	$\leq 10^{14}$
Nusselt number, Nu	$\frac{\text{total heat transfer}}{\text{conductive transfer}}$	$\frac{qh}{k\Delta T}$	$1 - 10^2$	$1 - 3 \times 10^2$	$10 - 10^3$
Reynolds number, Re	$\frac{\text{inertia}}{\text{viscosity}}$	$\frac{Uh}{\nu}$	$\leq 10^3$	$\leq 10^3$	$3 \times 10^2 - 10^4$

Table 5.1: Typical values of the dimensionless parameters governing rotating convection. Here ν is the fluid's viscous diffusivity, Ω is the angular rotation rate, h is the depth of the fluid layer, κ is the thermal diffusivity, α is the coefficient of thermal expansion, g_o is the gravitational acceleration (defined at the outer boundary of spherical shell cases), q is the total heat flux, k is thermal conductivity and U is some characteristic flow velocity.

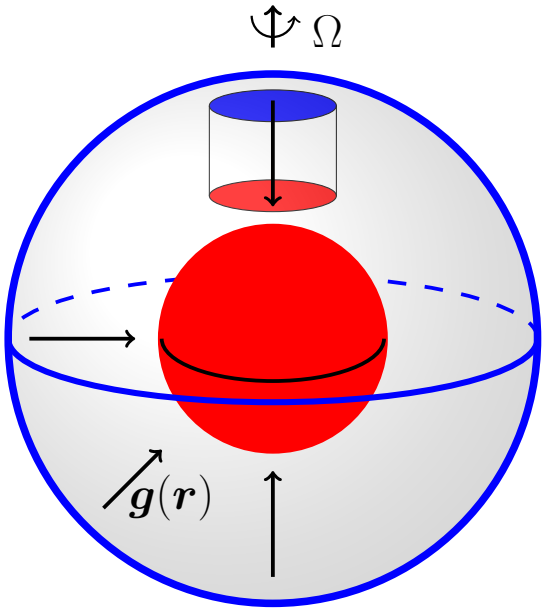

Figure 5.1: Schematic showing the connection between local and global models of core convection. The global spherical shell model is heated from the inner boundary and cooled from the outer boundary. The local models resemble high latitude convection heated from below and cooled from above.

that the experiments are missing. An obvious drawback of local DNS is the inability to capture boundary curvature (as in a spherical shell) and hence their direct application to understanding planetary flows is hindered. The heat transfer behaviour in local and global convection models can differ significantly (as described in chapter 1).

In this chapter we aim to systematically compare simultaneous velocity and heat transfer measurements from laboratory experiments with results from numerical simulations in local Cartesian and global spherical shell geometries. We first review the different heat transport and flow properties observed in the different modelling approaches. We aim to unify the different behaviours by bringing together three synergistic studies, laboratory experiments, local simulations and a cylindrical domain harvested from the polar region of our global simulations.

5.1.1 Nusselt number scaling

Historically, convection systems have been characterised by their heat transfer behaviour measured by the Nusselt number, Nu, (defined in table 5.1) as temperature sensors are easily used in the laboratory setting (e.g. Rossby, 1969; Ahlers and Xu, 2001). DNS in local geometries have focused on the scaling behaviour of Nu to compare and validate against laboratory experiments (e.g. Stellmach et al., 2014). The implicit assumption is that the heat transfer dynamics are representative of the large scale convection dynamics and any transitions in the scaling behaviour of Nu would also capture transitions in the flow. Recent studies have shown an explicit dependence of the Nu behaviour on the

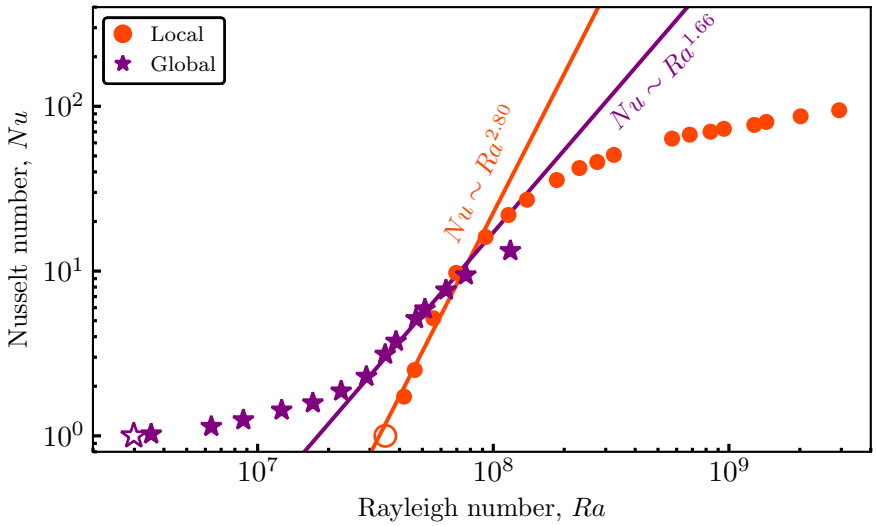

Figure 5.2: Nusselt number versus Rayleigh number for rotating convection with $E = 10^{-5}$. The symbol shape (and colour) indicate the type of model; global spherical shell models are shown as purple stars and plane-layer simulations are shown as orange circles. The empty markers denote the critical Rayleigh number at onset. All simulations have $Pr = 1$.

boundary layers dynamics (e.g. King et al., 2009; Julien et al., 2012b) and so it raises the question of how intimately linked the scaling behaviour of the bulk flow is to that of the global heat transfer.

The heat transport behaviour of rotating convection has been discussed previously in chapters 1, 3 and 4 and so we give only an overview here. Figure 5.2 shows Nu versus Ra for rotating convection with $E = 10^{-5}$; we show the difference between local plane layer models and global spherical shell models. The $Nu - Ra$ behaviour for the local models exists in one of two regimes; the rapidly rotating regime is characterised by a large $Nu - Ra$ scaling exponent, λ, whereas the weakly rotating regime resembles non-rotating convection with $\lambda = 2/7 - 1/3$. Similarly these two regimes exist for global models but in contrast, close to onset the global data exhibits a shallow tail in the weakly nonlinear regime before transitioning to the steep $Nu - Ra$ scaling. The weakly nonlinear regime is unique to spherical shells as the onset of convection is localised to the inner core boundary and conduction is responsible for transporting heat throughout most of the domain.

5.1.2 Reynolds number scaling

The flow speed is characterised by the Reynolds number, Re, defined by the ratio of inertial forces to viscous forces (table 5.1). Re has been measured for both non-rotating convection (Brown et al., 2007; Qiu and Tong, 2001a,b) and recently in rotating convection (Hawkins et al., 2020). In contrast to earlier numerical studies (e.g. King et al., 2013), Hawkins et al. (2020) found that the transitions in scaling behaviour of Nu and Re are

not intimately connected to one another (see their figure 11) which is in contrast to the correlated transition observed in spherical shell studies (see chapter 4 and Gastine et al., 2016). It is not clear if this difference is due to geometric effects or a result of the lower Ekman numbers achieved in the laboratory experiments.

5.1.3 Research question

In this chapter we systematically compare simultaneously measured convective velocities and heat transfer measurements from cylindrical laboratory experiments with results of numerical simulations in an infinite plane layer and spherical shell geometries. The experiments are performed in a right-cylinder with isothermal boundaries and water as the working fluid. We have run 3D horizontally periodic simulations and numerical simulations in a spherical shell with $Pr = 7$, fixed temperature boundaries and three different rotation rates corresponding to $E \in \{3 \times 10^{-6}, 1 \times 10^{-5}, 5 \times 10^{-5}\}$. We present the results of Nu and Re for the spherical shell simulations in two ways; we present both the globally averaged quantities and the contribution of the polar region. We explicitly isolate convection in the polar region of the spherical shell by harvesting a local cylindrical domain at high latitude. **Can we unify the different observations of local Cartesian and global spherical shell convection models?**

To answer this, we will describe the Nusselt number and Reynolds number scalings for each configuration and determine the regions of agreement between the different modelling approaches. This will elucidate the connection between laboratory experiments and spherical shell convection. The numerical implementation has been discussed previously and so here we focus on the experimental apparatus and methodology.

5.2 Experimental procedure

Convection experiments in spherical shells are troublesome to implement as they use the rotation rate to modify effective gravity to match the shell geometry (e.g. Sumita and Olson, 2003). In this work we use the standard experimental configuration consisting of a right-cylinder rotated about the vertical axis; we use the device *Calimero* housed at SPINlab, UCLA. The setup consists of a cylindrical convection tank having diameter and height of 20 cm that sits on top of a rotating pedestal. The working fluid is water with physical properties at a working temperature listed in table 5.2.

The convection tank sits atop the rotating table as part of the *stack*. The stack refers to everything above the table that co-rotates. Figure 5.3 shows a schematic of the set-up. The top of the rotating table is a stainless steel platform that allows the tank to be levelled. On this sits the bottom insulator and heat exchanger which is connected to the hotter boundary; this enforces the fixed temperature boundary conditions. Sat above

Property	Symbol	Units	Value
thermal expansivity	α	K^{-1}	2×10^{-4}
viscous diffusivity	ν	$\mathrm{m}^2\,\mathrm{s}^{-1}$	10^{-6}
thermal diffusivity	κ	$\mathrm{m}^2\,\mathrm{s}^{-1}$	1.4×10^{-7}
specific heat	C_p	$\mathrm{J\,kg}^{-1}\,\mathrm{K}^{-1}$	4180
thermal conductivity	k	$\mathrm{J\,m}^{-1}\,\mathrm{s}^{-1}\,\mathrm{K}^{-1}$	0.6
Prandtl number	ν/κ	–	7

Table 5.2: Physical properties of water at 20 °C (e.g. Lide, 2004; King, 2009). The majority of experiments are configured such that the average temperature is $\approx 20K$.

this are the bottom thermal block, acrylic tank and top thermal block with accompanying heat exchanger and insulator. These components combine to make the convection tank which contains the fluid. The stack is completed by the upper heat exchanger, insulation and stainless steel plate which provides a normal force to the system. Finally, the stack is topped with the expansion tank. Additional layers of insulation are added to the outside of the tank as to minimise any heat loss allowing us to treat the sidewall as a perfect insulator. This is necessary because non-negligible heat loss through the sidewall could lead to a height dependent Nusselt number, generating a number of dynamical and technical complications. System diagnostics include a series of thermistors (in both thermal blocks, fluid interior and external to the tank) and a laser doppler velocimetry (LDV) tool. The diagnostic hardware is shown in figure 5.3 and will be discussed in the following sections.

5.2.1 Thermometry

The thermal measurements in the experiments require accurate temperature sensors and can be broken down into four basic measurements; top and bottom boundary temperatures, internal fluid temperature, and external temperature.

Temperature measurements are made using 25 thermistors which use temperature dependent resistance elements. We use the widely applied Steinhart-Hart equation (Steinhart and Hart, 1968) which gives an empirical third-order approximation of the relationship between temperature, T, and resistance, R, given by

$$\frac{1}{T} = a + b \ln |R| + c(\ln |R|)^3, \tag{5.2}$$

(a)

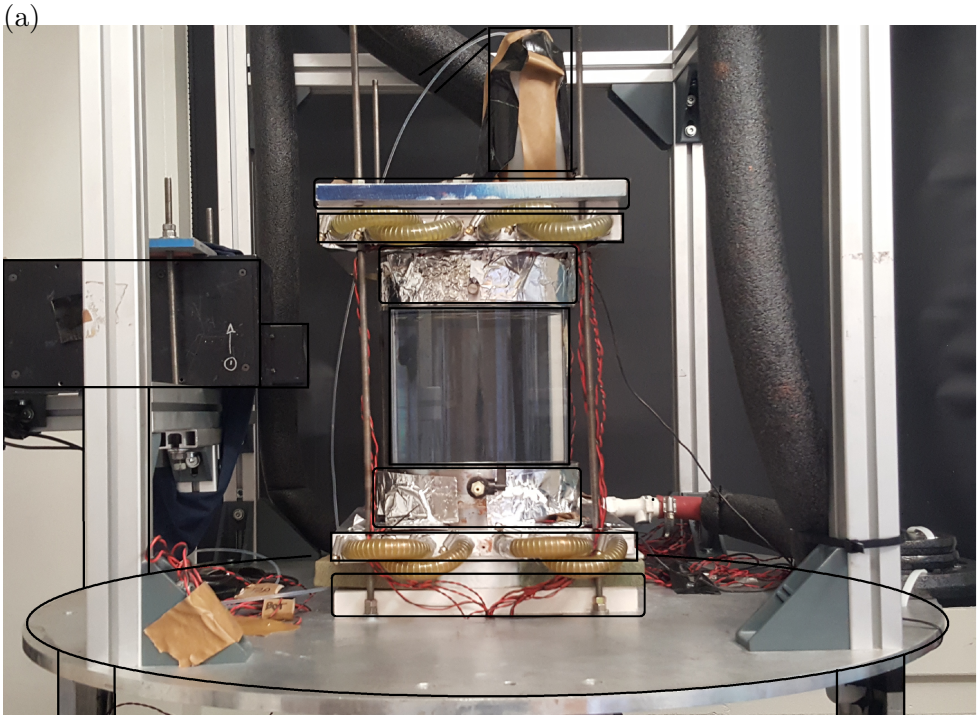

(b)

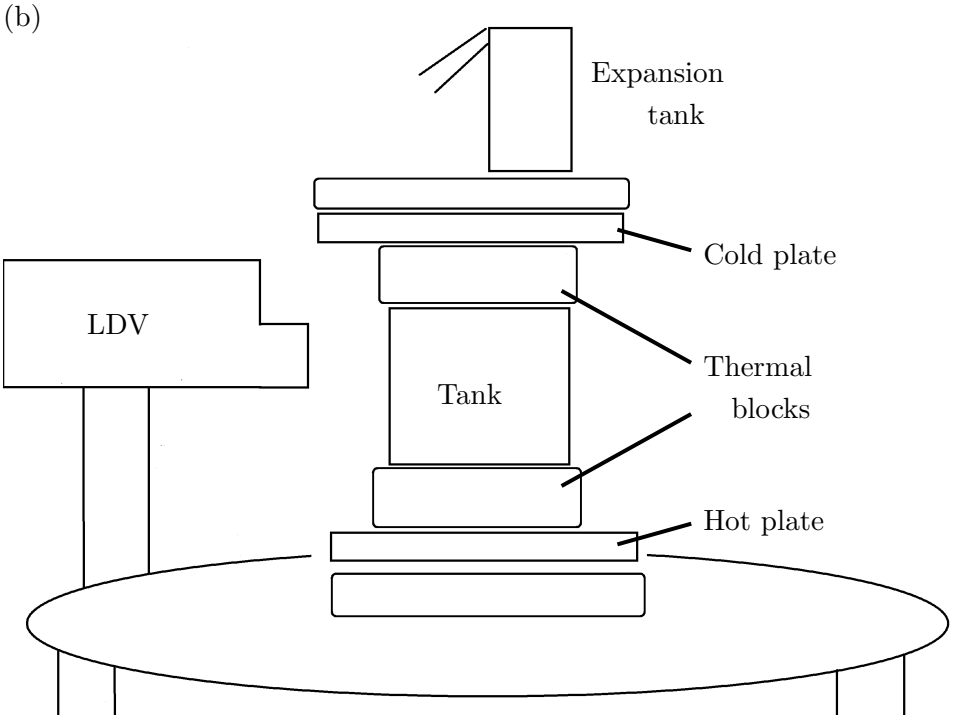

Figure 5.3: (a) Photograph and (b) schematic of the experimental set-up including the convection tank, heating plates, thermal blocks, expansion tank and laser doppler velocimeter (LDV).

If the coefficients a, b, and c are known, then temperature can be found from the resistivity. The resistivity of a given thermistor is measured by passing a small known current through it and measuring the resultant voltage drop. To calibrate the coefficients which are specific for each thermistor, we measure the resistivity of each resistor at three known temperatures spread over the expected range of operating temperatures (previous work suggests this is a sufficient number of test cases, King, 2009). The measurements are averaged in time to get three values for each of the thermistors corresponding to the three different temperatures, the coefficients for each thermistor are then solved for by inverting the Steinhart-Hart equation. Each of the amphenol thermistors has a resistivity of $10 \pm 0.06\,\mathrm{k\Omega}$. To calibrate the thermistors we immerse them in an isothermal bath and check their respective values, they are calibrated to within ± 0.01K.

In both of the thermal blocks we have 12 resistors, a vertically separated pair of thermistors are located at six locations spread equidistance in azimuth. The difference in average values of the bottom and top thermistor measurements give the mean temperature drop and consequently the Rayleigh number, Ra. The temperature drop across the fluid layer is measured by the difference of the thermistors vertically closest to the fluid layer,

$$\Delta T = \frac{1}{6}\left(\overline{\sum_{j=1}^{6} T_j^{\mathrm{bottom}}(t) - \sum_{j=1}^{6} T_j^{\mathrm{top}}(t)}\right), \tag{5.3}$$

where the overbar denotes an average in time. The thermistors record temperatures at a rate of 1 Hz. An external thermistor (pressed up against the side of the convection tank, at half height) is used to give a first order check of whether or not wall modes are present in the experiments, as previously reported (Aujogue et al., 2018; Aurnou et al., 2018). Wall modes are an instability that can occur when $Ra < Ra_c$ and their nonlinear interaction can effect the interior flow. Our measurements suggest that we are not in the regime for which wall modes are present.

We investigate the efficiency with which fluid motion transfers heat across the layer characterised by the Nusselt number. The Nusselt number, Nu, provides a global diagnostic measuring the ratio of total heat transfer to that in the absence of fluid flow

$$Nu = \frac{qh}{k\Delta T}, \tag{5.4}$$

where q is the heat flux, h is the depth of the fluid layer, k is the fluid's thermal conductivity and ΔT is the temperature drop across the layer. The heat flux is calculated as the input power, P per unit area. We measure P by computing the temperature drop within the aluminium thermal block,

$$P = \frac{\delta T k^{\mathrm{block}} A}{\lambda}, \tag{5.5}$$

where δT is the temperature drop measured within the thermal block, k^{block} is the thermal conductivity of aluminium ($167\,\mathrm{J\,s^{-1}\,m^{-1}\,K^{-1}}$, Olafsson et al., 1997), A the area of the fluid layer (πr^2) and λ is the distance between the thermistors within the thermal block

(this configuration is shown visually in figure 5.4). Figure 5.5 shows an illustrative example for the temperature traces of the thermistors used to define ΔT for a given experiment. For the range of temperature differences considered in this work, k can be considered constant (King, 2009).

The Nusselt number when expressed with only each independent variable occurring once (each variable having their own independent errors) can be written as

$$Nu = \frac{\delta T k^{\text{block}} h}{\Delta T k \lambda}, \tag{5.6}$$

(see figure 5.4 for definitions) the area of the fluid layer and thermal blocks are equal and cancel in this equation. We use given values of thermal conductivity for aluminium and water so the systematic error for the Nusselt number comes from measuring the heights and temperature drops associated with the fluid layer and the thermal blocks. Moving forward we use the subscript err to denote the precision error associated with the equipment used to measure the given quantity.

We quantify the error in measuring Nu by applying the propagation of errors technique. The error is solely expressed as multiplication/division meaning that the fractional uncertainties add in quadrature. There are four measured quantities which go into the defining Nu: h, ΔT, λ, and δT. We denote the error in accuracy of each measurement with the subscript err, applying the propagation of errors then gives

$$Nu_{\text{err}} = Nu\sqrt{\left(\frac{h_{\text{err}}}{h}\right)^2 + \left(\frac{\Delta T_{\text{err}}}{\Delta T}\right)^2 + \left(\frac{\lambda_{\text{err}}}{\lambda}\right)^2 + \left(\frac{\delta T_{\text{err}}}{\delta T}\right)^2}. \tag{5.7}$$

The errors are determined by the accuracy which with the given quantity can be measured.

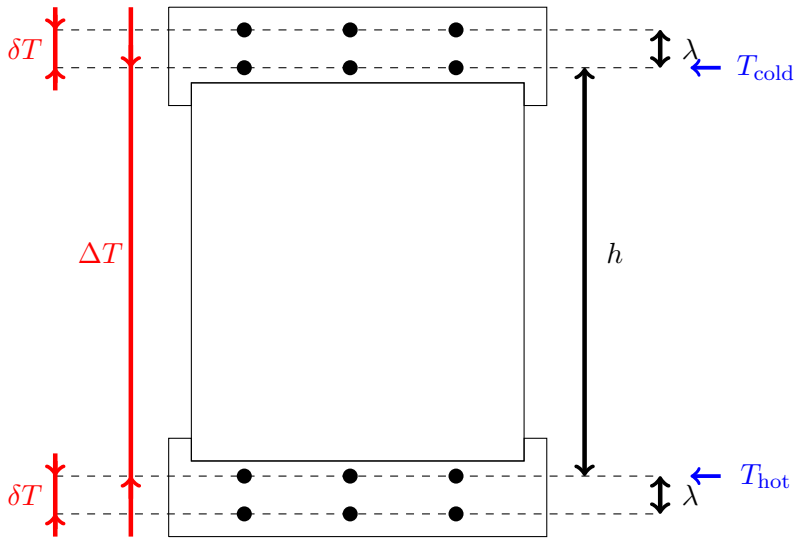

Figure 5.4: Schematic of the thermometry measurements used to define the Rayleigh number and Nusselt number in the experiments.

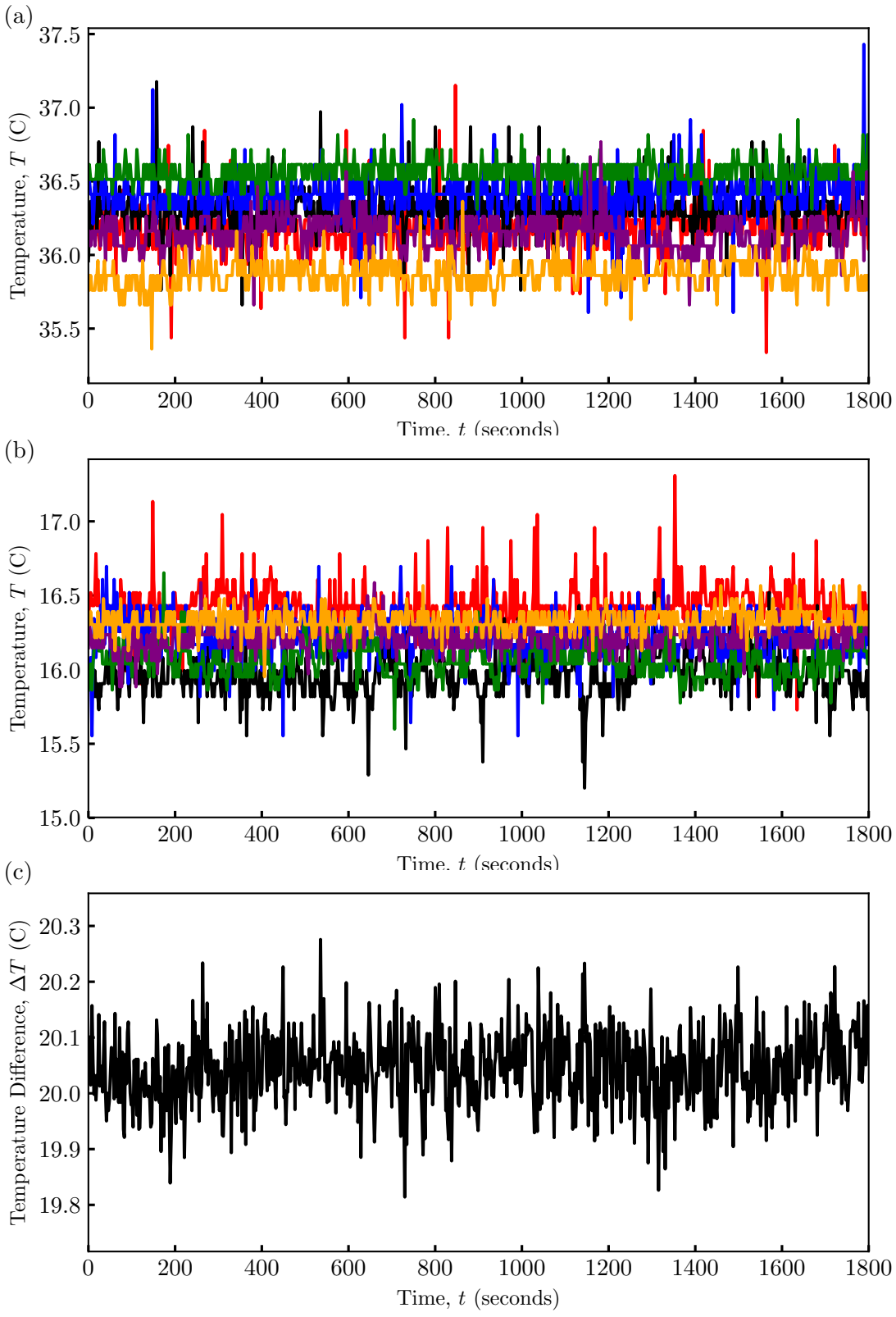

Figure 5.5: Temperature traces for non-rotating convection with $\Delta T = 20$. Temperature measurements in the upper and lower thermal blocks (a,b respectively). Each colour corresponds to the recording of a different thermal sensor. (c) Temperature difference across the fluid layer obtained by time-averaging the top and bottom data recordings.

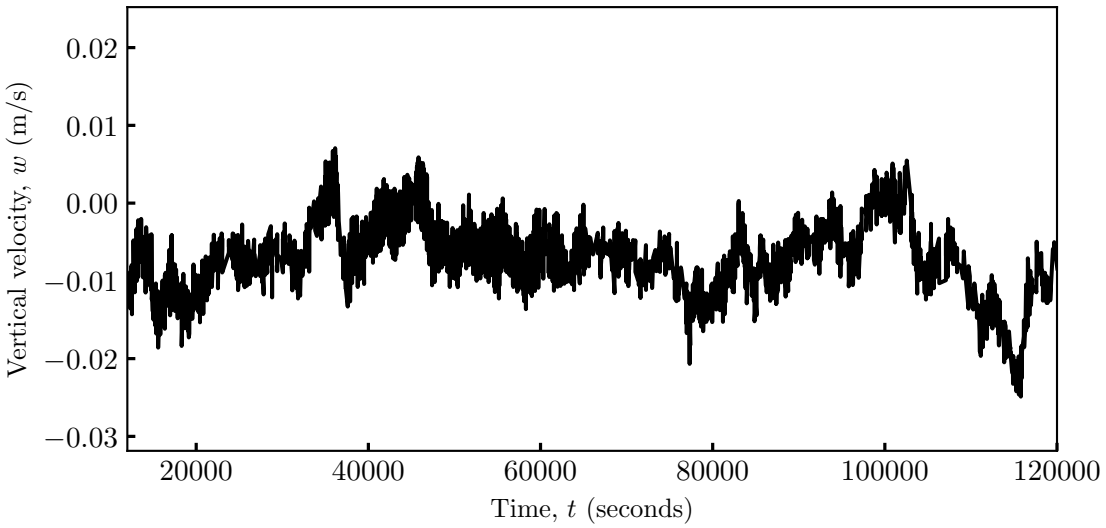

Figure 5.6: Vertical velocity trace for non-rotating convection with $\Delta T = 20$. The velocity measurements are taken using the LDV.

5.2.2 Laser Doppler Velocimetry (LDV)

The majority of convection experiments have only measured the heat transfer and simultaneous measurements of flow speed are a recent extension. Here we use laser doppler velocimetry (LDV, Drain, 1980; Bonner and Nossal, 1990) to measure vertical velocities at a fixed point in the domain. The LDV used in this work is a *Measurement Science Enterprise LDV instrument* that is mounted to the rotating frame and aligned axially (for an in-depth description of the LDV we refer the reader to Hawkins et al., 2020). LDV is a non-intrusive measurement technique that requires reflective signals; to get sufficient reflection we add a particle solution to the system. We chose TiO2 as our seeding agent which is mostly neutrally buoyant in water and has a high reflection coefficient (TiO2 is commonly used, Demir et al., 2011; Hu et al., 2014). The downside to using TiO2 is that it will eventually sediment to the bottom of the system (on the daily time scale) and clump to make bigger particles, we combat this by injecting more particles every few days as to ensure a consistent data rate. The particles are injected into the tank through the expansion tank and this process inevitably adds air bubbles which clump to the top boundary, however we find that even after all of the experiments are completed, the area of bubbles accounts for only 2% of the area of the top layer.

We define the Reynolds number, Re, using a vertical root mean square velocity w_{rms} from the velocity time series;

$$w_{\mathrm{rms}} = \sqrt{\frac{1}{N}\sum_{j=1}^{N}|w_j^2|}, \quad Re = \frac{w_{\mathrm{rms}}h}{\nu}. \tag{5.8}$$

An example velocity trace is shown in figure 5.6. In a similar fashion to the Nusselt

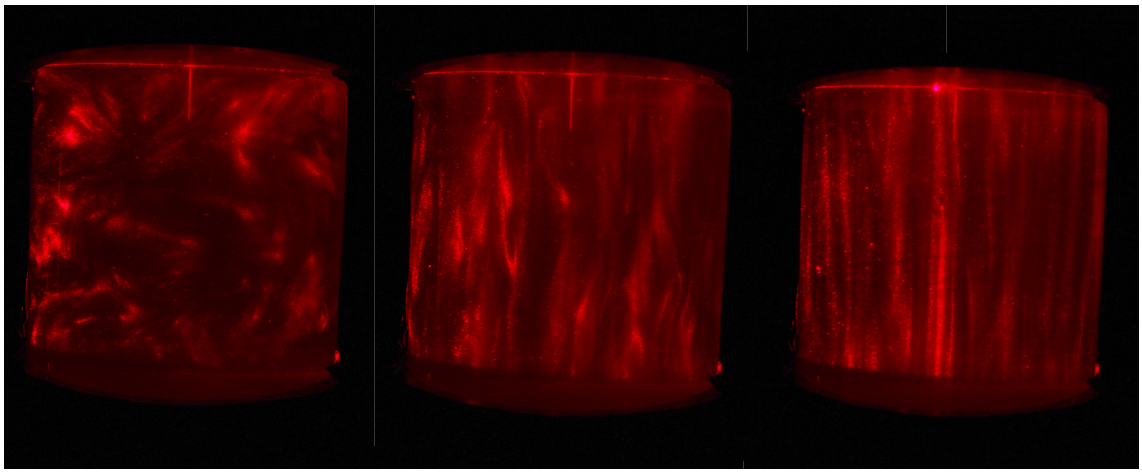

Figure 5.7: Visualisations of the laboratory experiments with $Ra = 1.3 \times 10^9$. The images correspond to non-rotating convection (left) and rotating convection with $E = 10^{-5}$ (middle) and $E = 10^{-6}$ (right).

number, we define the error of Re as

$$Re_{\text{err}} = Re\sqrt{\left(\frac{w_{\text{err}}}{w}\right)^2 + \left(\frac{h_{\text{err}}}{h}\right)^2 + \left(\frac{\nu_{\text{err}}}{\nu}\right)^2} \tag{5.9}$$

We assume that viscosity is fixed in our experiments and so $\nu_{\text{err}} = 0$.

5.2.3 Visualisations

After the experimental data were collected we procured a series of images and videos of the shear structures in the convective flow. To do this, the insulation was removed from the tank, a vertical laser sheet was shone through the tank, and Kalliroscope was added to the water. Kalliroscope is a long chain polymer allowing shear structures to be seen in the flow and has a high reflectivity making for clear photography. We used a digital camera to obtain still images and videos of the flow, example images of both non-rotating and rotating convection are shown in figure 5.7.

5.3 Harvesting a local cylinder from the spherical shell

A key goal of this chapter is to investigate convection in the polar region of the spherical shell simulations. We extract a local cylindrical domain from the global simulation; this cylinder is located above the inner core and centred about the rotation axis, spanning 5 degrees either side. The harvested cylinder is chosen as to have an aspect ratio (diameter/height) of unity as to match the geometry of the laboratory experiments. The cylinder is entirely within the fluid bulk minimising any curvature or boundary layer effects.

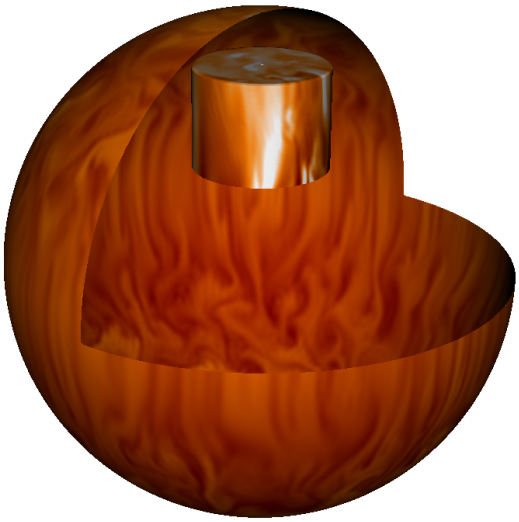

Figure 5.8: Visualisation of the cylindrical fluid domain harvested from the polar region of the spherical shell simulation. Contours of temperature are shown on a clipped spherical surface and on the cylindrical domain.

Practically, we achieve the harvest by converting all variables from spectral to physical space and then changing from spherical to cylindrical coordinates. Finally, the variables are interpolated onto a uniform grid to make evaluation of spatially averaged quantities straight forward.

5.4 Scaling laws for heat and momentum transport

We report a systematic comparison of the heat transport (Nusselt number, Nu) and momentum transport (Reynolds number, Re) for the different modelling approaches. We first present the results of non-rotating convection before discussing the rotating convection case.

5.4.1 Non-rotating convection

Non-rotating convection provides an upper bound on the heat transport for the rotating case (King et al., 2013; Gastine et al., 2016) and we begin by quantifying this behaviour. A key difference between the laboratory experiments and the local DNS arises due to the presence of sidewalls, in the experiment sidewalls drive a large scale circulation which is not present in the periodic simulations due to the absence of physical sidewalls. Our local DNS have aspect ratio, $\Gamma = 2$, with one hot upwelling and one cold downwelling, this mimics an almost system scale circulation.

We have performed eight laboratory experiments with $Ra \in [3 \times 10^8, 3 \times 10^9]$ (shown in figure 5.9). The lowest Ra experiment has a large error bar due to the limited sensitivity of the thermistors used to measure temperature. The two highest Ra runs show a different trend to the rest of the data and it is likely that these points are in a transitional region where the heat transfer changes from $Nu \sim Ra^{2/7}$ to $Nu \sim Ra^{1/3}$ (e.g. Cheng et al., 2015). The empirical fit to the data with $5 \times 10^8 \leq Ra \leq 2 \times 10^9$ gives

$$Nu = (0.15 \pm 0.02) Ra^{0.284 \pm 0.031}. \tag{5.10}$$

This behaviour is in good agreement with studies over similar ranges of Ra and Pr (Johnston and Doering, 2009; Cheng et al., 2015; Hawkins et al., 2020). The best fit to the local DNS is indistinguishable from equation (5.10) with $Nu = (0.16 \pm 0.01) Ra^{0.280 \pm 0.023}$.

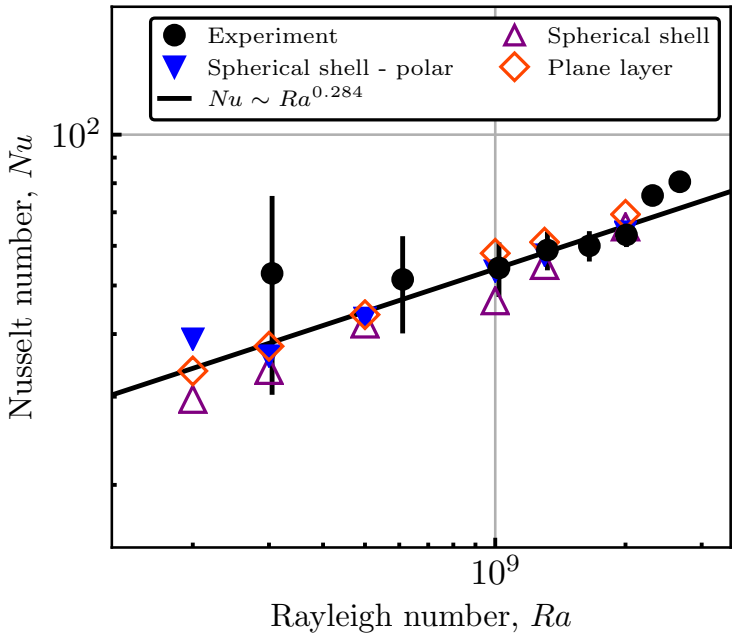

Figure 5.9: Nusselt number versus Rayleigh number. Each marker type corresponds to a different class of model. The empirical fit to the experimental data (black circles with error bars) with $5 \times 10^8 \leq Ra \leq 2 \times 10^9$ is shown as the black line.

The empirical fit to the global models agrees within error and there is no distinguishable difference between the volume averaged Nu and that associated with the polar harvest, both follow $Nu = (0.14 \pm 0.02) Ra^{0.29 \pm 0.03}$. For non-rotating convection the dynamics are dominated by three-dimensional turbulence and we find there is no geometric dependence of the heat transport, with all models following the same $Nu - Ra$ scaling.

For the same experiments we measured the momentum transfer which is found to scale as

$$Re = (0.01 \pm 0.002) Ra^{0.55 \pm 0.04} \tag{5.11}$$

(figure 5.10). This scaling exponent is larger than those previously reported experimen-

tally which find $Re \sim Ra^{0.45}$ (e.g. Qiu and Tong, 2001b; Hawkins et al., 2020). The existing scaling exponents and our data are within ± 0.05 of the theoretical prediction of Grossmann and Lohse (2000, 2001), $Re \sim Ra^{0.5}$. This difference in the Re scaling could be due to the spatial dependence of the large scale circulation that exists in cylindrical geometries; although exploration of this is beyond the scope of this work. Within the framework of Grossmann and Lohse (2000) Re is not a simple polynomial function of Ra and "subregimes" are characterised by a changing exponent, $Re \sim Ra^{\lambda}$ with $0.4 \leq \lambda \leq 0.6$; the fitted exponent of 0.55 is consistent with this. The $Re - Ra$ scaling for the local DNS is in better agreement with the experimental studies of Qiu and Tong (2001b); Hawkins et al. (2020); our local DNS data are described by $Re = (0.11 \pm 0.05)Ra^{0.44 \pm 0.01}$.

There is a slight discrepancy in the Re data shown in figure 5.10(a) with the plane layer and spherical shell DNS having smaller values at the same value of Ra than the corresponding experiments and polar harvest. For the DNS we define Re by a volume average whereas the experimental measurements and the polar harvest only sample the fluid bulk. In figure 5.10(b) we show the Re values of the DNS computed from a single spatial point in the fluid interior and this collapses all of the data onto a single scaling law. In the rotating case we will only discuss Re based on the fluid interior as to allow the fairest comparison of the experiments and simulations. Over the range of Ra studied here boundary layers can still contribute to the global momentum transport (see chapter 4) but the momentum transport in the fluid interior scales the same in all modelling approaches. For the parameter range explored here we would expect to be in the regime of Grossmann and Lohse (2000) in which dissipation is dominated by the mechanical boundary layer contribution. We have tested different spatial locations in both the plane layer and spherical shell DNS (inside and outside of the tangent cylinder) and there is little to no dependence on the observed value of Re. As per the heat transport, there is no geometric effect on the momentum transport in the nonlinear regime of non-rotating convection in a spherical shell.

5.4.2 Rotating convection

The $Nu - Ra$ and $Re - Ra$ data for all cases are shown in figure 5.11.

The onset of convection in a rotating spherical shell is a drifting thermal Rossby wave with columnar vortices localised to the inner core boundary. Close to onset, the weakly nonlinear regime does not have substantial flow within the tangent cylinder and as a result the polar region of the spherical shell is characterised by low Re until $Nu \approx 2$ (see figure 5.11). The weakly nonlinear regime is unique to spherical shell geometries and not present in the local models.

For increasingly supercritical cases, the $Nu - Ra$ behaviour is characterised by a steep scaling (with larger exponent) for some range of Ra before transitioning to a shallow scaling (and small exponent) at larger Ra. Figure 5.11(a,c,e) shows $Nu - Ra$ for different

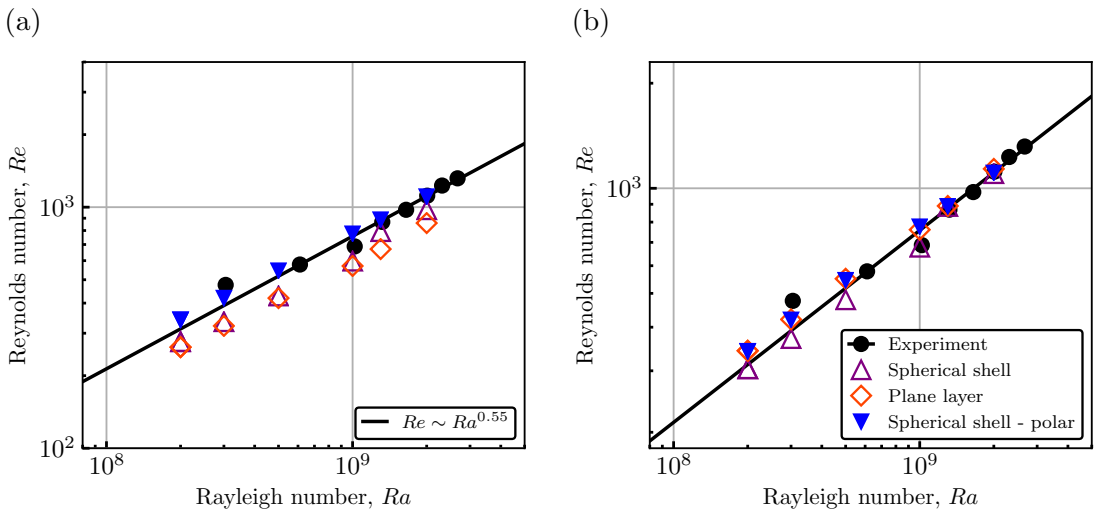

Figure 5.10: Reynolds number versus Rayleigh number. Each marker type corresponds to a different class of model. The empirical fit to the experimental data (black circles with error bars) is shown as the black line. For the simulations, the globally averaged Re is shown in (a) and that determined only by the fluid bulk is shown in (b).

Ekman numbers, $E = 5 \times 10^{-5},\ 10^{-5},\ 3 \times 10^{-6}$ respectively.

Within the rapidly rotating regime characterised by the steep scaling there is a clear distinction in the $Nu - Ra$ behaviour between the spherical shell data and the local DNS (and polar harvest) data for a given value of E. We quantify the heat transfer scaling exponent as $\lambda = \partial \ln |Nu| / \partial \ln |Ra|$. In the rapidly rotating regime λ increases with decreasing E and shows no sign of saturation over the explored parameter space. This monotonically increasing exponent is consistent with the findings of Cheng et al. (2015); Mound and Davies (2017). We observe a significant difference in behaviour of the local DNS and the spherical shell; the spherical shell is characterised by a much lower scaling exponent in the rapidly rotating regime (see figure 5.11 and table 5.3). This difference in behaviour hints at the importance of geometric effects for rotating convection.

The globally averaged Nu in a spherical shell is dominated by the equatorial region in which the heat transport is less efficient than in the tangent cylinder (e.g. Yadav et al., 2015). The efficient heat transport in the polar region is a consequence of maximised Ekman pumping effects (as the gravity vector and rotation axis are parallel) showing the importance of viscous effects for the range of Ekman number studied here. We list the fitted exponents of the rapidly rotating regimes in table 5.3 (we do not list a best fit to the spherical shell data with $E = 3 \times 10^{-6}$ as we cannot obtain a meaningful fit from our few data points). The harvested polar region differs from the spherical shell but is in good agreement with the local DNS with the fitted exponents agreeing to within error.

For sufficiently large Ra (at a given value of E) the $Nu - Ra$ data trends towards the non-rotating scaling behaviour shown as the black lines in each panel of figure 5.11. In the limited region of overlap the local DNS results are consistent with the experimental

Model	E	λ (rapidly rotating)	λ (weakly rotating)
Experiment	5×10^{-5}	N/A	0.28 ± 0.04
Experiment	10^{-5}	N/A	0.28 ± 0.04
Experiment	3×10^{-6}	N/A	0.31 ± 0.03
Plane layer	5×10^{-5}	2.01 ± 0.04	0.26 ± 0.02
Plane layer	10^{-5}	2.50 ± 0.01	0.29 ± 0.01
Plane layer	3×10^{-6}	2.78 ± 0.05	0.29 ± 0.05
Spherical shell	5×10^{-5}	1.24 ± 0.04	0.30 ± 0.03
Spherical shell	10^{-5}	1.64 ± 0.02	0.32 ± 0.02
Spherical shell - polar	5×10^{-5}	1.97 ± 0.03	0.28 ± 0.02
Spherical shell - polar	10^{-5}	2.48 ± 0.02	0.27 ± 0.02

Table 5.3: Heat transfer scaling exponents $\lambda = \partial \ln |Nu| / \partial \ln |Ra|$ of the rapidly rotating and weakly rotating regimes. λ is listed for the different modelling approaches and Ekman numbers shown in figure 5.11.

measurements. The $Nu - Ra$ scaling exponents for the weakly rotating regime are given in table 5.3 and shows that all modelling approaches follow the classical $Nu \sim Ra^{2/7}$ scaling (to within error).

The scaling behaviour of Re is qualitatively similarly to that of Nu in that there is a steep branch which shallows off at large Ra (see figure 5.11b,d,f). Similar to the heat transport scaling we investigate the scaling behaviour, $Re \sim Ra^{\lambda}$, and evaluate $\lambda = \partial \ln |Re| / \partial \ln |Ra|$ for both the rapidly rotating and weakly rotating branches. The fitted exponents and their errors are listed in table 5.4.

In the rapidly rotating regime, Re is larger for the global spherical shell than the polar harvest owing to the delayed onset of convection in the tangent cylinder. The local DNS and polar harvest have comparable values and scale similarly, with an exponent, $\lambda \approx 3$, whereas the spherical shell has $\lambda \leq 2.61$. An important difference between the steep trends in Nu and Re is that the exponent for Nu monotonically increases with decreasing E whereas the Re exponent is roughly constant. The steep $Re - Ra$ scaling transition

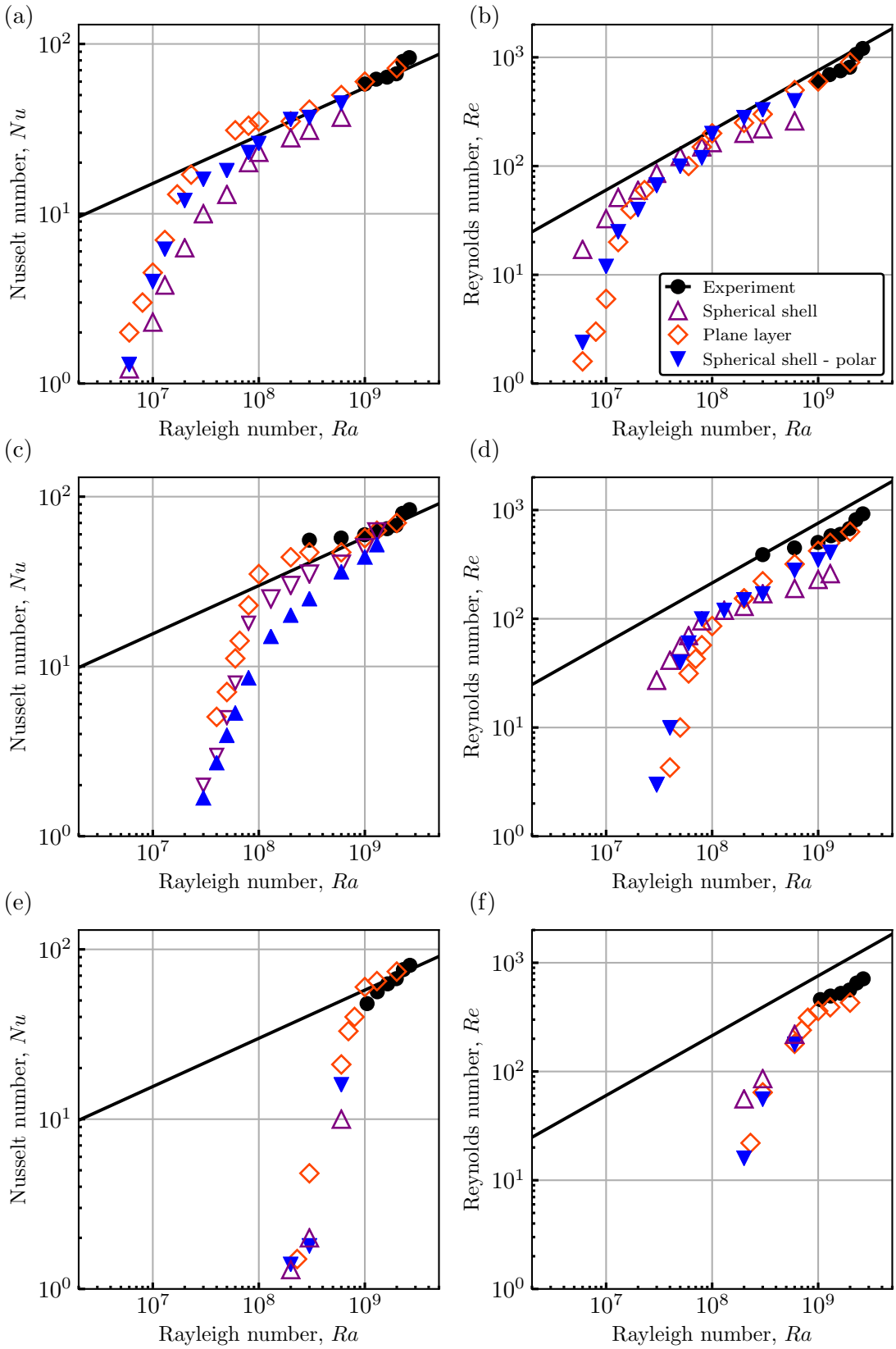

Figure 5.11: Nusselt number (a,c,e) and Reynolds number (b,d,f) shown as a function of Rayleigh number. Each row corresponds to data from experiments and simulations at different Ekman numbers, $E = 5 \times 10^{-5}$ (a,b), $E = 10^{-5}$ (c,d) and $E = 3 \times 10^{-6}$ (e,f). In each figure the solid black lines corresponds to the best fit of the non-rotating experimental data.

Model	E	λ (rapidly rotating)	λ (weakly rotating)
Experiment	5×10^{-5}	N/A	0.58 ± 0.04
Experiment	10^{-5}	N/A	0.53 ± 0.04
Experiment	3×10^{-6}	N/A	0.55 ± 0.03
Plane layer	5×10^{-5}	2.97 ± 0.03	0.57 ± 0.03
Plane layer	10^{-5}	2.96 ± 0.04	0.52 ± 0.01
Plane layer	3×10^{-6}	3.02 ± 0.05	0.51 ± 0.04
Spherical shell	5×10^{-5}	2.24 ± 0.02	0.50 ± 0.03
Spherical shell	10^{-5}	2.61 ± 0.03	0.49 ± 0.01
Spherical shell - polar	5×10^{-5}	2.92 ± 0.03	0.57 ± 0.02
Spherical shell - polar	10^{-5}	3.04 ± 0.04	0.51 ± 0.03

Table 5.4: Flow speed scaling exponents $\lambda = \partial \ln |Re| / \partial \ln |Ra|$ of the rapidly rotating and weakly rotating regimes. λ is listed for the different modelling approaches and Ekman numbers shown in figure 5.11.

to the shallower trend at the same Ra value as the $Nu - Ra$ transition. Interestingly, the transition to the weakly rotating regime is accompanied by the polar region of the spherical shell having a larger Re than the global average.

At sufficiently high Ra the weakly rotating branch is approached and in this regime the experimental data all scale with a similar exponent to that of the non-rotating experiments (see table 5.4). The prefactor, however, decreases with decreasing E leading to smaller Re values at a fixed Ra. The local DNS, laboratory experiments and polar harvest all scale the same in this regime and have similar values of Re. Our empirical fits are consistent with the predictions of Grossmann and Lohse (2000). In contrast, the global spherical shell has a distinctly different exponent which is smaller and the values themselves are lower. The difference in scaling exponents here may suggest that a different force balance is governing the dynamics. We will address this by considering the methodology applied in chapter 4.

To allow comparison with chapter 4 we will now investigate the scaling behaviour

of Re with respect to different force balances. The spherical shell models close to onset ($Nu \leq 2$) have negligible nonlinear effects and viscous forces determine the dynamics as in chapter 4. The flow speed is well defined by the VAC prediction, $Re_{\mathcal{V}}$,

$$Re = (0.64 \pm 0.03) Re_{\mathcal{V}}^{0.98 \pm 0.03}.$$

As Ra is increased convection becomes highly nonlinear and the inertial force takes over from viscosity in the global force balance. In order to adequately describe Re in the fully nonlinear regime of spherical shell convection we follow Gastine et al. (2016) in including contributions from both the interior and the boundary layers. The interior is governed by $Re_{\mathcal{I}}$ and the boundary layers by Re_{bl}. An empirical fit gives

$$Re = (2.13 \pm 0.05) Re_{\mathcal{I}}^{0.99 \pm 0.03} + (0.14 \pm 0.03) Re_{\mathrm{bl}}^{0.97 \pm 0.02}.$$

The difference in the prefactor highlights the more significant contribution of $Re_{\mathcal{I}}$ to the global average. This methodology can also be applied to the local DNS which gives

$$Re = (1.01 \pm 0.05) Re_{\mathcal{I}}^{0.99 \pm 0.01} + (0.23 \pm 0.02) Re_{\mathrm{bl}}^{0.98 \pm 0.01}.$$

Again, we see that the empirical scaling exponents are in great agreement with the theory and the lower prefactors correspond to the lower values of Re at equivalent parameters than the spherical shell cases. We fit the data using just $Re_{\mathcal{I}}$ and find that the inclusion of Re_{bl} significantly increases the goodness of fit to the globally averaged Re (reducing the misfit from ≈ 14 % to $\approx 3\%$).

Finally, we consider the experimental data, which are well described by the IAC prediction, $Re_{\mathcal{I}}$, with an empirical fit

$$Re = (0.81 \pm 0.02) Re_{\mathcal{I}}^{0.98 \pm 0.01}. \tag{5.12}$$

This is in good agreement with the recent study of Hawkins et al. (2020). It is not surprising that the experimental data is well described by the IAC prediction, $Re_{\mathcal{I}}$, as we have only taken point measurements in the fluid interior. The DNS, however, define Re based on the volume averaged velocity which includes both the interior and the boundary layers which is why they require an additional correction term in order to adequately describe the data. The three highest Ra simulations with $E = 5 \times 10^{-5}$ and $E = 10^{-5}$ are consistent with equation (5.12) which suggests that these models are in the same dynamical regime as the laboratory experiments.

We find that even when the $Nu - Ra$ scaling follows non-rotating behaviour, the Re scaling can still be determined by the Coriolis force. This observation is in agreement with Hawkins et al. (2020) but contrasts with global spherical studies. In chapter 4 we showed that for spherical shell convection the non-rotating $Nu - Ra$ is approached with the $Re - Ra$ approaching non-rotating behaviour simultaneously.

5.5 Conclusions

We have presented a suite of laboratory-numerical convection models with and without rotation to compare the different approaches used to model convection in the polar region of Earth's core. The heat transport in doubly periodic plane layer simulations agree well with cylindrical laboratory experiments and there is now evidence that the flow speeds also agree as recently reported by Hawkins et al. (2020). There is, however, significant differences in the scaling behaviour of the heat transport in spherical shell geometries and these local models. In an attempt to unify these observations we have also presented results using a novel approach of harvesting a local cylindrical domain from the polar region of our spherical shell simulations.

In the rapidly rotating regime the local models are characterised by larger scaling exponents than the spherical shell equivalent. The harvested polar region exhibits the same scaling as the local cases with throttled heat transport (figure 5.12). Ekman pumping is maximised when the rotation axis and the gravity vector are parallel suggesting that over the accessible range of E boundary layer effects are still important. In none of our models do we observe the diffusion free asymptotic behaviour, $Nu \sim Ra^{3/2}E^2$, predicted by Julien et al. (2012b).

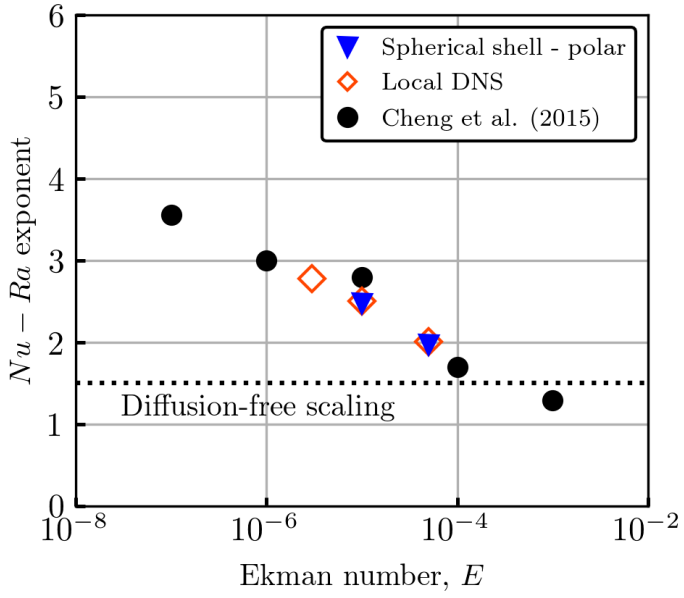

Figure 5.12: Heat transfer scaling exponents versus Ekman number for rapidly rotating convection. The orange and purple markers correspond to the simulations reported in this manuscript, the black plus markers correspond to the exponents of Cheng et al. (2015). The dotted line shows the diffusion-free theoretical prediction Julien et al. (2012b) which is not approached in our survey.

The convective flow speeds in rotating convection can be described by considering the appropriate contributions obtained from the thermal wind balance. We find that the IAC force balance gives an adequate first order description of the measured flow speeds

in the rapidly rotating regime. Our experiments take pointwise velocity measurements within the interior and are well described by the IAC prediction. In contrast, our DNS define Re from the volume averaged velocity field and the best way of describing the data is to include a correction to the IAC prediction corresponding to the boundary layer contribution.

Previous studies in spherical geometries find that the transition from the steep heat transfer to the non-rotating behaviour is accompanied by a transition in the flow speeds to a state where rotation is not important (Gastine et al., 2016, and chapter 4). In contrast, our results presented here are consistent with those of Hawkins et al. (2020) who find that Re can still be influenced by Coriolis forces even when the heat transport behaves as if non-rotating, i.e. quasi-geostrophic turbulence can support a non-rotating $Nu - Ra$ behaviour.

This is the first study to show quantitative agreement between simulations and laboratory experiments of rotating convection for the $Nu - Ra$ and $Re - Ra$ behaviour despite the two approaches having different and independent sources of error. We have shown that cylindrical laboratory experiments are a suitable analogue for convection at high latitudes within the tangent cylinder. Our result suggest that volume integrated quantities do not give a fundamental description of the dynamics in a spherical shell but the average of contributions from inside and outside the tangent cylinder, which are distinguishably different (see Schaeffer et al., 2017, for a complementary analysis and discussion). Regional analysis of core dynamics models akin to those in the atmospheric science community are needed to better characterise and understanding the different convective dynamics which can occur at different latitudes.

Chapter 6

Conclusion

The geodynamo is maintained by turbulent rotating convection in Earth's fluid core. Originally, convection was studied using laboratory experiments which employ fixed temperature boundary conditions. Consequently, the majority of numerical convection simulations have also focused on fixed temperature boundaries although for the cores of terrestrial planets the appropriate choice is fixed heat-flux owing to the vastly different material properties of the core and overlying mantle. This thesis has focused on the dynamics of convection driven by different thermal boundary conditions and we were particularly motivated to investigate the influence of rotation. This chapter summarises the key results obtained in the previous chapters and revisits the aims outlined in chapter 1. In closing we discuss some of the unresolved issues and describe future work.

6.1 Project aims

The aims and objectives of this project were outlined in §1.5 and guided the research presented in this thesis. The overarching motivation for this project was to understand the fundamental mechanisms underpinning the geodynamo. We focus on understanding the dynamics of convection driven by a fixed heat-flux in terms of both local dynamics (e.g. in the thermal boundary layers) and global dynamics in terms of defining different regimes of rotating convection. Finally, we perform a comparative study of numerical and laboratory models of convection in the polar region of Earth's core.

Can we identify a robust method for defining the thermal boundary layer in rotating convection?

In convection, boundary layer dynamics are important in determining the heat and momentum transport (e.g. Grossmann and Lohse, 2000) and in rotating convection the thermal boundary layer plays a key role in the transition from rotationally constrained to weakly rotating convection (King et al., 2009; Julien et al., 2012b). To elucidate the

physics of flow transitions in thermal convection a robust definition of the thermal boundary layer is needed that can be broadly applied to different configurations (e.g. thermal boundary conditions, values of the control parameters, etc.).

We have tested the two most commonly used methods to define the thermal boundary layer; the *linear intersection* method, based on the profile of time averaged temperature and the *local maxima* method, based on the root-mean-square temperature fluctuation. Both of these methods originate from studies of non-rotating convection driven by a fixed temperature gradient. In chapter 3 we show that the local maxima method cannot be used for boundaries with a prescribed heat-flux as a well defined local maxima in the temperature fluctuation does not exist. Unlike non-rotating convection which exhibits a well mixed fluid bulk, rotating convection can maintain interior temperature gradients. We show that when gradients are present the thermal boundary layer thickness defined using the linear intersection method, and the resultant temperature drop across the boundary layer are less accurate in recovering the Nusselt number.

We suggest an alternative method of defining the thermal boundary layer using simple physical arguments. The *heat transport* method defines the boundary layer thickness by the location at which the advective and diffusive contributions to the heat flux cross. This method is shown to work for non-rotating convection with no-slip boundaries having either a prescribed temperature or heat-flux, as well as rotating convection with free-slip boundaries.

Do different physical regimes of convection exist in a rotating spherical shell? Classically, different regimes of rotating convection have been hinted at from transitions in the scaling behaviour of the heat transport. More recently, heat transfer and flow speed measurements have been investigated simultaneously in global geometries (e.g. Gastine et al., 2016) and both local experiments (e.g. Hawkins et al., 2020) and simulations (e.g. King et al., 2013). We cannot reproduce the extreme values of the control parameters relevant to Earth's core in a computational model and one way of connecting the accessible parameter space to the geophysical motivation is through scaling laws. We survey the accessible parameter space and if an asymptotic regime is found for which the flow is turbulent and rotationally constrained then this may allow extrapolation to Earth's core parameters.

In chapter 4 we presented a systematic survey of parameter space and reported diagnostics from our suite of spherical shell rotating convection simulations with an aspect ratio, gravity profile and thermal boundary conditions relevant to Earth's core. We identified four distinct physical regimes of rotating convection with their boundaries defined by correlating changes in the scaling behaviour of the heat transport and flow properties. We find that convection is strongly constrained by rotation when the thermal boundary layers are in geostrophic balance, $RaE^{8/5} \lesssim 1$. Once the thermal boundary layers are no longer rotationally dominated, the rotational constraint on the flow is lost and all diagnostics transition to behave as if non-rotating. Ultimately, the different regimes are controlled by

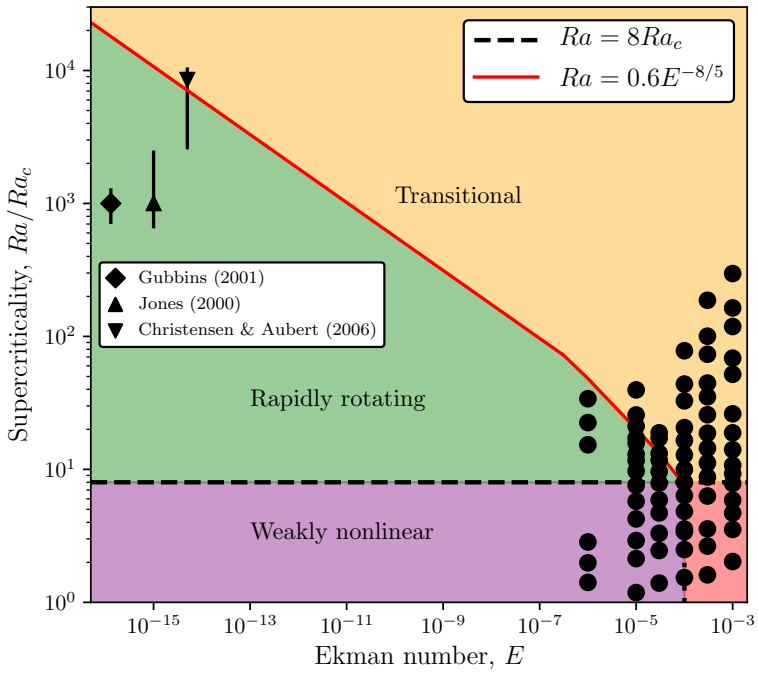

Figure 6.1: Regimes of rotating convection identified in chapter 4. Each black circle corresponds to a numerical simulation presented in chapter 4 and shows the accessible parameter space (of course up to $E = \infty$ is actually feasible). The axes are extended to geophysically relevant values and estimates for Earth's core are included (Jones et al., 2000; Gubbins, 2001; Christensen and Aubert, 2006).

the relative importance of the rotation and buoyancy forces.

Assuming that these regimes can be extrapolated from the accessible region of parameter space to geophysical conditions, estimates of material properties for Earth's core place it within the rapidly rotating regime (figure 6.1). This regime is characterised by quasi-geostrophic turbulence and is governed by a triple force balance of inertial, Coriolis and Archimedean forces in the fluid bulk with a viscous contribution from the boundary layers. The inertial balance predicts the characteristic length scale of core convection to be ~ 10 km which differs to the viscous balance predicting a length scale of ~ 100 m.

Can the different observations from local Cartesian and global spherical shell rotating convection models be unified?
The convective heat transport in an infinite plane layer is known to agree well with cylindrical laboratory experiments for both Rayleigh-Bénard convection and rotating convection (e.g. King et al., 2009; Cheng et al., 2015). Recent work has further shown that the convective flow speeds in these local cases are consistent with each other (e.g. Hawkins et al., 2020). Direct comparison between cylindrical experiments and global simulations remains difficult due to the distinctly different accessible parameter spaces the two approaches can access. However, in the rapidly rotating regime there are significant differences in the scaling behaviour of the heat transport in spherical shell and Cartesian simulations. The Cartesian cases more efficiently transport heat, having a steeper $Nu - Ra$ scaling behaviour than the spherical shell at equivalent values of the control parameters (differing by about a factor of two, compare e.g. King and Buffett, 2013; Mound and Davies, 2017).

In chapter 5 we presented a novel approach of unifying the different observations by comparing results with a cylindrical domain harvested from the polar region of spherical simulations. We have explicitly shown that the scaling behaviour of both the Nusselt number and Reynolds number in local models are similar to that of the polar region extracted from the spherical shell models. Over the accessible parameter space, boundary layer effects are still important in determining the dynamics; the polar region exhibits throttled heat transport relative to the global average. In the polar region, Ekman pumping is maximised owing to the rotation axis and gravity vector being aligned. The key difference between local and global models occurs close to onset, where convection in a spherical shell takes the form of a drifting thermal Rossby wave adjacent to the tangent cylinder and no analogue for this weakly nonlinear regime exists in local models.

6.2 Simplifying assumptions

The convection models considered in this thesis focus on purely thermal convection of an idealised fluid having $Pr = 1$. Here we will discuss the potential drawbacks of assuming a single buoyancy source and moderate Prandtl number.

1. Single source of buoyancy
   Although convective flows and the resultant magnetic field generation in Earth's core are driven by both thermal and compositional gradients (Jones, 2015; Wicht and Sanchez, 2019), it is common practice to study convection driven by a single buoyancy source. Most studies focus on purely thermal convection (allowing comparison with experiments) or the *co-density* formulation (Braginsky and Roberts, 1995) which replaces temperature and concentration by a single field variable. The key issue with this approach is that single-diffusive convection cannot account for differences in boundary conditions and the significantly different diffusivities of heat

and chemical constituents (Jones, 2015).

Studies of doubly-diffusive convection (DDC) have identified new regimes of convection (Mather and Simitev, 2020) and may be able to recover certain aspects of core dynamics. Based on the relative importance of the two buoyancy contributions, doubly-diffusive convection is capable of forming a stratified layer at the outer boundary and enhancement of the poloidal magnetic field (Manglik et al., 2010) or favouring different field morphologies by changing the generated helicity (Takahashi, 2014). Recent work by Mather and Simitev (2020) has started to address how thermal and double-diffusive convection differs and further study will determine to what extent single- and double-diffusive agree in describing core dynamics.

It is difficult to *a priori* determine how our results directly link to DDC, however, we can make some inferences. The thermal boundary layer is important in determining whether or not rotation governs global diagnostics in our thermal convection simulations. An important question is then whether the thermal or compositional boundary layer demarcate an equivalent transition in DDC. The heat transport method can be applied to any field governed by an advection-diffusion equation and used to define both the thermal and compositional boundary layers in DDC.

2. Moderate Prandtl number
   Owing to computational constraints most numerical convection models employ the peculiar case of a $Pr = 1$ fluid. In contrast we note that experiments typically use water as the working fluid having $Pr = 7$. Earth's core is a liquid iron alloy and due to their high thermal conductivities liquid metals typically have $Pr \sim \mathcal{O}(10^{-2}-10^{-1})$ (Lam et al., 2002). Numerical simulations using the codensity formulation invoke $Pr \sim \mathcal{O}(1)$ which assumes that turbulence is solely responsible for mixing in Earth's core, equilibrating all diffusivity coefficients. However, it is not clear that even if turbulent mixing is dominant that the compositional and temperature fields evolve the same way.

   Numerical simulations often use $Pr = 1$, however, thermal convection is likely to operate with $Pr < 1$ and compositional convection with $Pr > 1$. The precise ratio of compositional and thermal buoyancy sources is not certain so understanding the dynamics over a range of Pr is important. Numerical simulations of rotating plane-layer convection with $0.015 \leq Pr \leq 100$ find a significant Pr dependence on the heat transport and boundary layer dynamics resulting from changes in the flow morphology (Venugopal et al., 2020), an abrupt transition occurs when $Pr \sim \mathcal{O}(1)$. An important avenue is then to consider the end-member behaviour of diagnostics (e.g. flow speed) in the rapidly rotating regime at both low and high Pr.

   The geodynamo appears to exhibit features similar to those of convection driven

dynamos with large values of Pr ($\gg 1$) as well as those with $Pr \lesssim \mathcal{O}(1)$ (Simitev and Busse, 2005). The magnetic energy exceeds kinetic energy by a factor of 10^3 similar to that of a high Pr dynamo. The variations in field amplitude on the magnetic diffusion timescale and the torsional oscillations on a much shorter timescale (Bloxham et al., 2002) indicate a link with low Pr convective-dynamos (Busse and Simitev, 2004).

6.3 Future extensions

This thesis has developed an understanding of thermal convection through scaling law analysis and provides a baseline for further research. Ultimately, this has provided the framework to further understand hydrodynamic convection with the inclusion of more complicated physics. We have considered convection subject to homogeneous boundaries, however Earth's core is likely to have imposed heterogeneities. Non-zonal structure observed in the time averaged magnetic field (e.g. Gubbins and Kelly, 1993; Korte and Constable, 2006) likely results from core convection interacting with thermal, electromagnetic or topographic heterogeneities at the core-mantle boundary. An important extension to this work is to take these heterogeneities into consideration and investigate their effect on the derived scaling laws, which are often extrapolated to Earth's core. Below we discuss two cases that impose preferential length scales into the system; the heat flow pattern across the core-mantle boundary and the topography of the core-mantle boundary.

1. Core-mantle boundary heat flow
   Earth's core is thermally coupled to the overlying silicate mantle which convects much slower and supports larger lateral variations in material properties than the core. Core convection must be driven by a laterally varying heat-flux pattern at the core-mantle boundary (Olson, 2003) with the present-day heat-flux pattern obtained by seismic tomography (e.g. Masters et al., 1996). Seismic tomography reveals two dense large low shear velocity provinces at the base of the mantle; normal mode seismology gives their density which can be inverted to interpret these as hot provinces. Numerical dynamo models that have included this pattern of heat-flux successfully reproduce some features in the spatial and temporal structure of the geomagnetic field (Bloxham, 2000; Willis et al., 2007).

   Only one systematic study of spherical shell convection with heterogeneous thermal boundary conditions exists; Mound and Davies (2017) investigated the effect on the heat transfer. When present, the tomographic heat flux pattern can reorganise the flow near the CMB leading to a steepened $Nu - Ra$ scaling behaviour in the rapidly rotating regime (relative to the equivalent homogeneous case). How the heterogeneous heat-flux effects other quantities such as the Reynolds number remains an open question. Quantifying the effects of boundary heterogeneity on the flow morphology and scaling behaviour of the Reynolds number could prove important when extrapolating results to geophysically relevant parameters and interpreting

observations of core flow.

2. Core-mantle boundary topography
   Topographic coupling between the core and mantle is important to understand the axial torques (Hide, 1969; Kuang and Bloxham, 1993) and equatorial torques (Hide et al., 1996; Hulot et al., 1996) that the core exerts on the mantle. Seismic studies have probed the shape of the CMB and find topographic amplitudes as high as $\mathcal{O}(10)$ km (Morelli and Dziewonski, 1987; Sze and van der Hilst, 2003) with typical values of ± 2 km (Tanaka, 2010). Simple topography patterns have been investigated using quasi-geostrophic models of core convection (Calkins et al., 2012) which have found that significant longitudinal variations in radial heat flux along the ICB can be excited (although this study focused on convection near onset). Interestingly, the effects of topography become more significant as the Ekman number is reduced (Calkins et al., 2012) which suggests that this is an imporant effect for core convection.

   The main barrier to studying the effect of CMB topography is that the majority of spherical convection codes use spectral methods (Matsui et al., 2016) and are only suitable for perfectly spherical geometries. A bespoke numerical model will need to be developed using a different spatial discretisation, e.g. a spectral element method that allows CMB topography to be included in global convection simulations.

Numerical dynamos have been successful in reproducing many aspects of Earth's magnetic field including dipolar fields capable of reversing (Glatzmaier and Roberts, 1995; Christensen and Wicht, 2015). An ongoing issue is to quantify how Earth-like these dynamo models really are given that they are run in a vastly different region of parameter space to Earth's core. The recent study of Sprain et al. (2019) tested the ability of numerical geodynamo models to reproduce long-term behaviour of Earth's magnetic field such as the dipolarity and reversal rate. They show that present geodynamo models are unable to simultaneously capture all aspects of Earth's long term field behaviour. The simulations presented in Sprain et al. (2019) are run for many magnetic diffusion times and, due to the long duration, the parameter space explored is limited to $1.2\times10^{-4} \leq E \leq 10^{-3}$ and $1 \leq Ra/Ra_c \leq 100$ where Ra_c is derived from the onset of non-magnetic convection. One way forward is to search parameter space to try and find a model which can reproduce all long-term behaviour of the geomagnetic field. It will be important to examine different convective configurations, e.g. thermal convection driven by a fixed heat-flux at both the ICB and CMB versus compositional convection driven by a fixed flux at the ICB and no-flux at the CMB.

Even if a numerical dynamo model is found to reproduce the long-term behaviour of the geomagnetic field in a satisfactory manner, this does not inherently mean that the model is Earth-like. Dynamo theory suggests that a triple balance between Lorentz, Archimidean and Coriolis forces (termed MAC) is the dominant balance expected in Earth's core and determines the internal dynamics (e.g. Starchenko and Jones, 2002). A

dynamo model could reproduce features of the geomagnetic field but the behaviour could arise from a non-Earth-like force balance. The MAC balance only emerges in simulations when E is reduced to extreme values (Schaeffer et al., 2017; Schwaiger et al., 2019) with the exception of some simulations displaying a MAC balance at only the largest scales with $E = 10^{-4}$ (Aubert et al., 2017). Simulations at sufficiently low Ekman number that span sufficiently long timescales have not yet been realised. Future work should investigate if dynamo models in the rapidly rotating regime are able to reproduce long term aspects of the geomagnetic field with the dynamics also being maintained by a MAC balance.

6.4 Final thoughts

In this thesis we have systematically investigated convection using both laboratory experiments and numerical simulations. We have explored different geometries, different thermal boundary conditions and the effect of rotation over a wide range of parameter space. We have derived a robust method of treating the thermal boundary which is important in understanding flow transitions in thermal convection. In our parameter survey of convection in a rotating spherical shell, we find that boundary layer effects are still important even at the most extreme Ekman numbers explored, with the heat transport throttled when the rotation axis and gravitational acceleration are aligned (as Ekman pumping is maximised).

Our principal motivation is understanding the dynamics of Earth's core which underpin the geodynamo and we have performed scaling law analysis which could allow us to connect the accessible parameter regime with Earth's core values. We identify an asymptotic regime in our spherical shell convection models in which the flow is dominated by quasi-geostrophic turbulence; the flow is rotationally constrained whilst turbulent. This regime has small viscous effects localised to the thin boundary layers and is a good candidate for targeted dynamo simulations which aim to reproduce an Earth-like force balance. We have performed the first regional study of core dynamics explicitly illustrating the link between spherical shell convection and cylindrical laboratory experiments. This will provide a platform to separate the dynamics which occur inside and outside of the tangent cylinder. This work will provide a baseline to understand the effect of more complicated physics in the regime relevant to planetary cores.

Appendix A

Model Database - Summary of Simulations

Summary tables of the numerical simulations presented in this thesis. The convergence data is listed here with each model specified by the Ekman number, E and Rayleigh number, Ra. The duration of temporal averaging is given by τ, E_{err} denotes the energy residual and Nu_{err} the residual in Nusselt number (both of the latter quantities should be below 0.1). The spatial resolution in the mechanical boundary layers is listed as

1. N_i and N_o for the inner and outer boundaries, respectively (spherical shell)
2. N for the average (plane layer).

Finally, N_{res} gives the radial and horizontal resolutions, respectively.

A.1 Spherical shell simulations

E	Ra	τ	$E_{\rm err}$	$Nu_{\rm err}$	N_i	N_o	$N_{\rm res}$
10^{-3}	1.62×10^{4}	81	9.91×10^{-7}	8.98×10^{-5}	12	17	60 ,60
10^{-3}	2.82×10^{4}	193	4.13×10^{-7}	1.84×10^{-5}	13	17	64, 64
10^{-3}	3.75×10^{4}	483	4.95×10^{-5}	1.95×10^{-3}	13	16	64, 64
10^{-3}	4.68×10^{4}	4240	5.87×10^{-4}	1.03×10^{-3}	13	16	64, 64
10^{-3}	6.26×10^{4}	4005	6.93×10^{-5}	3.8×10^{-3}	13	16	64, 64
10^{-3}	8.56×10^{4}	605	6.1×10^{-5}	6.55×10^{-3}	15	18	80, 80
10^{-3}	7.41×10^{4}	1454	1.27×10^{-4}	1.84×10^{-3}	15	18	80, 80
10^{-3}	1.12×10^{5}	587	1.63×10^{-4}	2.28×10^{-4}	18	22	92, 92
10^{-3}	1.5×10^{5}	223	4.64×10^{-4}	5.38×10^{-3}	18	22	92, 92
10^{-3}	2.09×10^{5}	652	2.46×10^{-4}	1.34×10^{-3}	18	22	92, 92
10^{-3}	4.14×10^{5}	141	2.46×10^{-4}	1.71×10^{-3}	18	22	96, 96
10^{-3}	5.47×10^{5}	762	9.27×10^{-4}	8.3×10^{-3}	17	22	96, 96
10^{-3}	9.47×10^{5}	369	2.5×10^{-4}	4.63×10^{-3}	19	22	128, 128
10^{-3}	1.31×10^{6}	362	2.37×10^{-4}	3.51×10^{-3}	24	30	128, 128
10^{-3}	2.37×10^{6}	525	4.88×10^{-4}	4.51×10^{-3}	24	30	128, 128
3×10^{-4}	5.46×10^{4}	1213	7.76×10^{-4}	6.54×10^{-3}	23	27	64, 64
3×10^{-4}	8.98×10^{4}	200	3.2×10^{-7}	7.04×10^{-5}	12	21	64, 64
3×10^{-4}	1.21×10^{5}	96	2.54×10^{-7}	2.26×10^{-4}	12	20	64, 64
3×10^{-4}	2.14×10^{5}	103	1.58×10^{-8}	3.26×10^{-4}	12	19	64, 64
3×10^{-4}	2.97×10^{5}	438	1.82×10^{-3}	8.72×10^{-3}	12	12	80, 80
3×10^{-4}	3.79×10^{5}	444	1.35×10^{-3}	8.37×10^{-3}	14	15	92, 92
3×10^{-4}	4.89×10^{5}	928	7.57×10^{-4}	2.18×10^{-3}	14	16	92, 92
3×10^{-4}	6.35×10^{5}	787	1.81×10^{-4}	4.25×10^{-3}	14	16	92, 92
3×10^{-4}	8.74×10^{5}	739	2.21×10^{-4}	2.63×10^{-3}	14	16	92, 92
3×10^{-4}	1.19×10^{6}	198	2.75×10^{-4}	6.14×10^{-3}	14	16	96, 96
3×10^{-4}	1.51×10^{6}	492	2.1×10^{-4}	6.05×10^{-3}	14	17	96, 96
3×10^{-4}	2.49×10^{6}	370	2.4×10^{-4}	9.25×10^{-3}	14	17	96, 96
3×10^{-4}	3.4×10^{6}	720	4.66×10^{-4}	5.19×10^{-3}	14	18	128, 128
3×10^{-4}	6.34×10^{6}	101	2.01×10^{-6}	1.24×10^{-4}	10	26	128, 128
10^{-4}	3.04×10^{5}	107	6.98×10^{-4}	1.64×10^{-3}	10	10	64, 48
10^{-4}	6.72×10^{5}	90	1.27×10^{-6}	3.0×10^{-4}	10	23	64, 64
10^{-4}	4.94×10^{5}	79	1.71×10^{-3}	5.02×10^{-3}	9	19	64, 64
10^{-4}	7.05×10^{5}	68	2.38×10^{-3}	2.01×10^{-3}	12	12	60, 48
10^{-4}	9.57×10^{5}	97	1.26×10^{-3}	1.96×10^{-3}	12	11	80, 64
10^{-4}	1.26×10^{6}	539	2.63×10^{-4}	7.73×10^{-3}	12	13	80, 92
10^{-4}	1.58×10^{6}	90	2.85×10^{-5}	8.79×10^{-3}	10	11	92, 92
10^{-4}	1.98×10^{6}	84	2.26×10^{-5}	4.08×10^{-4}	9	10	80, 92
10^{-4}	2.54×10^{6}	557	1.11×10^{-4}	1.12×10^{-3}	15	18	96, 96
10^{-4}	3.27×10^{6}	75	3.49×10^{-4}	1.82×10^{-3}	12	13	128, 128
10^{-4}	4.08×10^{6}	87	6.46×10^{-4}	2.05×10^{-3}	12	13	96, 96
10^{-4}	6.49×10^{6}	75	1.05×10^{-3}	1.77×10^{-3}	15	18	96, 96
10^{-4}	8.68×10^{6}	60	9.55×10^{-4}	1.11×10^{-3}	16	18	128, 128
10^{-4}	1.54×10^{7}	96	7.99×10^{-7}	3.68×10^{-5}	35	7	128, 128

Table A.1: Summary of rotating spherical shell simulations - I

E	Ra	τ	E_{err}	Nu_{err}	N_i	N_o	N_{res}
3×10^{-5}	1.13×10^{6}	94	4.06×10^{-5}	8.11×10^{-5}	10	9	80, 80
3×10^{-5}	1.98×10^{6}	108	6.68×10^{-5}	4.49×10^{-3}	10	9	90, 90
3×10^{-5}	2.67×10^{6}	89	1.14×10^{-3}	6.74×10^{-3}	23	9	90, 90
3×10^{-5}	3.8×10^{6}	383	1.04×10^{-3}	5.73×10^{-3}	29	13	90, 90
3×10^{-5}	4.77×10^{6}	213	5.61×10^{-4}	7.88×10^{-3}	13	13	128, 128
3×10^{-5}	6.37×10^{6}	305	3.59×10^{-4}	8.07×10^{-3}	13	13	128, 128
3×10^{-5}	7.78×10^{6}	400	1.47×10^{-4}	6.63×10^{-3}	13	13	128, 128
3×10^{-5}	9.48×10^{6}	475	3.18×10^{-5}	2.11×10^{-4}	13	13	128, 128
3×10^{-5}	1.07×10^{7}	1919	1.08×10^{-4}	2.9×10^{-2}	15	15	128, 128
3×10^{-5}	1.39×10^{7}	1890	1.38×10^{-4}	9.43×10^{-3}	14	15	144, 144
3×10^{-5}	1.52×10^{7}	101	2.56×10^{-7}	1.04×10^{-5}	28	5	144, 144
10^{-5}	3.53×10^{6}	140	1.0×10^{-5}	3.76×10^{-3}	31	7	80, 64
10^{-5}	6.36×10^{6}	146	1.68×10^{-5}	4.76×10^{-5}	22	7	90, 90
10^{-5}	8.69×10^{6}	100	1.92×10^{-5}	3.91×10^{-4}	22	8	90, 80
10^{-5}	1.26×10^{7}	67	5.27×10^{-5}	1.08×10^{-3}	11	5	90, 128
10^{-5}	1.72×10^{7}	486	6.83×10^{-4}	2.63×10^{-3}	33	10	128, 128
10^{-5}	2.26×10^{7}	90	4.39×10^{-4}	1.83×10^{-4}	7	8	90, 128
10^{-5}	2.89×10^{7}	90	5.43×10^{-4}	5.21×10^{-4}	7	8	90, 128
10^{-5}	3.48×10^{7}	76	6.09×10^{-5}	3.37×10^{-4}	7	8	90, 128
10^{-5}	3.87×10^{7}	212	1.22×10^{-4}	6.49×10^{-4}	9	10	90, 128
10^{-5}	4.7×10^{7}	100	1.77×10^{-4}	5.03×10^{-4}	9	10	128, 144
10^{-5}	5.13×10^{7}	89	1.9×10^{-4}	4.1×10^{-4}	14	14	128, 144
10^{-5}	6.3×10^{7}	54	1.42×10^{-4}	1.03×10^{-3}	14	14	192, 192
10^{-5}	7.65×10^{7}	101	6.47×10^{-4}	9.17×10^{-4}	16	14	192, 192
10^{-5}	1.18×10^{8}	52	3.4×10^{-6}	6.84×10^{-6}	38	5	256, 256
10^{-6}	6.99×10^{7}	90	1.05×10^{-5}	1.47×10^{-4}	9	5	128, 128
10^{-6}	9.81×10^{7}	111	6.68×10^{-6}	4.06×10^{-3}	9	5	128, 128
10^{-6}	1.41×10^{8}	38	3.81×10^{-4}	5.97×10^{-3}	13	8	192, 192
10^{-6}	7.58×10^{8}	79	1.9×10^{-3}	6.14×10^{-3}	12	12	224, 224
10^{-6}	1.11×10^{9}	14	5.46×10^{-3}	6.21×10^{-3}	16	15	320, 320

Table A.2: Summary of rotating spherical shell simulations - II

A.2 Plane layer simulations

Ra	τ	E_{err}	Nu_{err}	N	N_{res}
2×10^3	60	3.56e-9	1.47e-13	12	64, 32
3×10^3	10	5.05e-8	4.64e-8	12	64, 32
10^4	10	2.46e-2	1.52e-5	10	64, 32
3×10^4	25	3.89e-7	1.95e-8	14	64, 32
10^5	20	1.35e-2	1.59e-2	12	64, 32
3×10^5	50	5.97e-2	9.71e-3	18	64, 32
10^6	100	4.37e-1	3.60e-1	15	128, 64
3×10^6	100	2.00e-1	1.90e-1	18	128, 64
10^7	100	2.83e-2	1.91e-2	24	128, 64
3×10^7	200	2.54e-2	1.29e-1	21	256, 128
10^8	700	1.31e-1	1.43e-1	19	256, 128
3×10^8	700	5.78e-1	1.67e-1	7	256, 128

Table A.3: Summary of two-dimensional non-rotating convection simulations with fixed temperature thermal boundary conditions.

Ra	τ	E_{err}	Nu_{err}	N	N_{res}
1.77×10^3	10	1.32e-3	1.35e-2	24	64, 32
2.45×10^3	40	1.34e-2	1.34e-2	12	64, 32
9.43×10^3	100	1.34e-2	1.34e-2	15	64, 32
2.45×10^4	20	5.96e-3	1.96e-2	16	64, 32
8.20×10^4	30	5.76e-2	5.75e-2	17	64, 32
3.16×10^5	20	4.64e-1	9.58e-2	9	64, 32
9.08×10^5	100	5.17e-1	5.20e-1	11	128, 64
2.89×10^6	100	3.01e-1	3.02e-1	10	128, 64
7.50×10^6	400	2.93e-1	4.37e-1	12	128, 64
4.74×10^7	460	8.23e-2	2.14e-1	15	256, 128
1.53×10^8	460	8.24e-2	2.14e-2	9	256, 128

Table A.4: Summary of two-dimensional non-rotating convection simulations with fixed heat-flux thermal boundary conditions.

Ra	τ	E_{err}	Nu_{err}	N	N_{res}
$1.74e11$	400	7.02e-2	8.72e-1	8	128, 64
$2.09e11$	200	3.42e-2	9.63e-2	10	128, 64
$2.61e11$	200	6.13e-1	4.48e-3	7	128, 64
$3.48e11$	300	9.78e-1	3.41e-1	19	256, 128
$5.22e11$	300	1.09e-3	2.87e-3	11	256, 128
$8.71e11$	600	4.33e-1	5.35e-2	10	512, 256
$1.04e12$	600	3.19e-1	3.17e-1	21	1024, 512
$1.39e12$	800	6.27e-2	2.65e-1	11	2048, 1024

Table A.5: Summary of three-dimensional rotating convection simulations with Ekman number, $E = 10^{-7}$. The boundaries are stress-free and prescribed fixed temperature thermal boundary conditions.

Bibliography

Ahlers, G. and Xu, X. 2001. Prandtl-number dependence of heat transport in turbulent Rayleigh-Bénard convection. *Physical Review Letters*. **86**(15), pp. 3320. Cited on pp. 10, 12, and 98.

Ahlers, G., Grossmann, S., and Lohse, D. 2009. Heat transfer and large scale dynamics in turbulent Rayleigh-Bénard convection. *Reviews of Modern Physics*. **81**(2), pp. 503. Cited on p. 11.

Al-Shamali, F., Heimpel, M., and Aurnou, J. 2004. Varying the spherical shell geometry in rotating thermal convection. *Geophysical & Astrophysical Fluid Dynamics*. **98**(2), pp. 153–169. Cited on p. 67.

Alfe, D., Gillan, M., and Price, G. 2000. Constraints on the composition of the Earth's core from ab initio calculations. *Nature*. **405**(6783), pp. 172. Cited on p. 2.

Anderson, D., Tannehill, J. C., and Pletcher, R. H. 2016. *Computational fluid mechanics and heat transfer*. CRC Press. Cited on pp. 35, 38, and 44.

Anufriev, A., Jones, C., and Soward, A. 2005. The Boussinesq and anelastic liquid approximations for convection in the Earth's core. *Physics of the Earth and Planetary Interiors*. **152**(3), pp. 163–190. Cited on pp. 30 and 31.

Anufriev, A. P. and Hejda, P. 2010. Earth's core convection: Boussinesq approximation or incompressible approach? *Geophysical and Astrophysical Fluid Dynamics*. **104**(1), pp. 65–83. Cited on p. 30.

Ascher, U. M., Ruuth, S. J., and Spiteri, R. J. 1997. Implicit-explicit Runge-Kutta methods for time-dependent partial differential equations. *Applied Numerical Mathematics*. **25**(2-3), pp. 151–167. Cited on p. 37.

Ashgriz, N. and Mostaghimi, J. 2002. An introduction to computational fluid dynamics. *Fluid flow handbook*. **1**, pp. 1–49. Cited on p. 35.

Aubert, J. 2005. Steady zonal flows in spherical shell dynamos. *Journal of Fluid Mechanics*. **542**, pp. 53–67. Cited on p. 22.

Aubert, J. 2019. Approaching Earth's core conditions in high-resolution geodynamo simulations. *Geophysical Journal International*. **219**(Supplement_1), pp. S137–S151. Cited on p. 95.

Aubert, J., Brito, D., Nataf, H.-C., Cardin, P., and Masson, J.-P. 2001. A systematic experimental study of rapidly rotating spherical convection in water and liquid gallium. *Physics of the Earth and Planetary Interiors*. **128**(1-4), pp. 51–74. Cited on p. 66.

Aubert, J., Gastine, T., and Fournier, A. 2017. Spherical convective dynamos in the rapidly rotating asymptotic regime. *Journal of Fluid Mechanics*. **813**, pp. 558–593. Cited on pp. 7, 8, 67, and 126.

Aujogue, K., Pothérat, A., Sreenivasan, B., and Debray, F. 2018. Experimental study of the convection in a rotating tangent cylinder. *Journal of Fluid Mechanics*. **843**, pp. 355–381. Cited on pp. 96 and 103.

Aurnou, J. 2007. Planetary core dynamics and convective heat transfer scaling. *Geophysical and Astrophysical Fluid Dynamics*. **101**(5-6), pp. 327–345. Cited on pp. 47, 73, and 96.

Aurnou, J. and King, E. 2017. The cross-over to magnetostrophic convection in planetary dynamo systems. *Proceedings of the Royal Society A: Mathematical, Physical and Engineering Sciences*. **473**(2199), pp. 20160731. Cited on p. 6.

Aurnou, J. and Olson, P. 2001. Experiments on Rayleigh-Bénard convection, magnetoconvection and rotating magnetoconvection in liquid gallium. *Journal of fluid mechanics*. **430**, pp. 283. Cited on p. 96.

Aurnou, J., Calkins, M., Cheng, J., Julien, K., King, E., Nieves, D., Soderlund, K. M., and Stellmach, S. 2015. Rotating convective turbulence in Earth and planetary cores. *Physics of the Earth and Planetary Interiors*. **246**, pp. 52–71. Cited on pp. 8, 19, 50, and 96.

Aurnou, J. M., Bertin, V., Grannan, A. M., Horn, S., and Vogt, T. 2018. Rotating thermal convection in liquid gallium: Multi-modal flow, absent steady columns. *Journal of Fluid Mechanics*. **846**, pp. 846–876. Cited on p. 103.

Backus, G. 1958. A class of self-sustaining dissipative spherical dynamos. *Annals of Physics*. **4**(4), pp. 372–447. Cited on p. 42.

Batchelor, G. 2000. *An Introduction to Fluid Dynamics*. Cambridge University Press. Cited on pp. 7, 29, and 34.

Bazhanova, Z. G., Roizen, V. V., and Oganov, A. R. 2017. High-pressure behavior of the Fe–S system and composition of the Earth's inner core. *Physics-Uspekhi*. **60**(10), pp. 1025. Cited on p. 2.

Belmonte, A., Tilgner, A., and Libchaber, A. 1994. Temperature and velocity boundary layers in turbulent convection. *Physical Review E*. **50**(1), pp. 269. Cited on pp. 49 and 69.

Bénard, H. 1900. Les tourbillons cellulaires dans une nappe liquide. *Rev. Gen. Sci. Pures Appl.* **11**, pp. 1261–1271. Cited on p. 8.

Bénard, H. 1901. Les tourbillons cellulaires dans une nappe liquide.-Méthodes optiques d'observation et d'enregistrement. *Journal de Physique Théorique et Appliquée*. **10**(1), pp. 254–266. Cited on p. 8.

Blasius, H. 1908. Grenzschichten in Flüssigkeiten mit kleiner Reibung. *Zeitschrift für Angewandte Mathematik und Physik*. **56**, pp. 1–37. Cited on pp. 12 and 34.

Bloxham, J. 2000. The effect of thermal core–mantle interactions on the palaeomagnetic secular variation. *Philosophical Transactions of the Royal Society of London. Series A: Mathematical, Physical and Engineering Sciences*. **358**(1768), pp. 1171–1179. Cited on p. 124.

Bloxham, J., Zatman, S., and Dumberry, M. 2002. The origin of geomagnetic jerks. *Nature*. **420**(6911), pp. 65–68. Cited on p. 124.

Bonner, R. F. and Nossal, R. Principles of laser-doppler flowmetry. In *Laser-Doppler blood flowmetry*, pp. 17–45. Springer, 1990. Cited on p. 106.

Bouffard, M., Labrosse, S., Choblet, G., Fournier, A., Aubert, J., and Tackley, P. J. 2017. A particle-in-cell method for studying double-diffusive convection in the liquid layers of planetary interiors. *Journal of Computational Physics*. **346**, pp. 552–571. Cited on p. 60.

Boyd, J. P. 2001. *Chebyshev and Fourier spectral methods*. Courier Corporation. Cited on p. 36.

Braginsky, S. Structure of the F layer and reasons for convection in the Earth's core. In *Soviet Phys. Dokl.*, volume 149, pp. 8–10, 1963. Cited on p. 2.

Braginsky, S. and Roberts, P. 1995. Equations governing convection in Earth's core and the geodynamo. *Geophysical & Astrophysical Fluid Dynamics*. **79**(1-4), pp. 1–97. Cited on pp. 47 and 122.

Breuer, M., Wessling, S., Schmalzl, J., and Hansen, U. 2004. Effect of inertia in Rayleigh-Bénard convection. *Physical Review E*. **69**(2), pp. 026302. Cited on pp. 49, 51, 65, and 69.

Brown, E., Funfschilling, D., and Ahlers, G. 2007. Anomalous Reynolds-number scaling in turbulent Rayleigh–Bénard convection. *Journal of Statistical Mechanics: Theory and Experiment*. **2007**(10), pp. P10005. Cited on pp. 96 and 99.

Burns, K. J., Vasil, G. M., Oishi, J. S., Lecoanet, D., and Brown, B. P. 2020. Dedalus: A flexible framework for numerical simulations with spectral methods. *Physical Review Research*. **2**(2), pp. 023068. Cited on pp. 35 and 36.

Busse, F. 2002. Convective flows in rapidly rotating spheres and their dynamo action. *Physics of fluids*. **14**(4), pp. 1301–1314. Cited on p. 47.

Busse, F. and Carrigan, C. 1974. Convection induced by centrifugal buoyancy. *Journal of Fluid Mechanics*. **62**(3), pp. 579–592. Cited on p. 19.

Busse, F. and Hood, L. 1982. Differential rotation driven by convection in a rapidly rotating annulus. *Geophysical & Astrophysical Fluid Dynamics*. **21**(1-2), pp. 59–74. Cited on p. 22.

Busse, F. and Or, A. 1986. Convection in a rotating cylindrical annulus: thermal Rossby waves. *Journal of Fluid Mechanics*. **166**, pp. 173–187. Cited on p. 21.

Busse, F. and Simitev, R. 2004. Inertial convection in rotating fluid spheres. *Journal of Fluid Mechanics*. **498**, pp. 23. Cited on p. 124.

Busse, F. H. 1970. Thermal instabilities in rapidly rotating systems. *Journal of Fluid Mechanics*. **44**(3), pp. 441–460. Cited on pp. 20 and 74.

Cagney, N. and Lithgow-Bertelloni, C. 2016. Dynamics and excess temperature of a plume throughout its life cycle. *Geophysical Journal International*. **205**(3), pp. 1574–1588. Cited on p. 60.

Cagney, N., Newsome, W. H., Lithgow-Bertelloni, C., Cotel, A., Hart, S. R., and Whitehead, J. A. 2015. Temperature and velocity measurements of a rising thermal plume. *Geochemistry, Geophysics, Geosystems*. **16**(3), pp. 579–599. Cited on p. 60.

Calkins, M. A., Noir, J., Eldredge, J. D., and Aurnou, J. M. 2012. The effects of boundary topography on convection in Earth' s core. *Geophysical Journal International*. **189**(2), pp. 799–814. Cited on p. 125.

Cardin, P. and Olson, P. 1994. Chaotic thermal convection in a rapidly rotating spherical shell: consequences for flow in the outer core. *Physics of the earth and planetary interiors*. **82**(3-4), pp. 235–259. Cited on pp. 19 and 71.

Cardin, P. and Olson, P. 2010. Experiments on Core Dynamics. *Treatise on Geophysics, Volume 8: Core Dynamics*. pp. 319. Cited on p. 19.

Chandrasekhar, S. 1961. Hydrodynamic and hydromagnetic stability. Cited on pp. 9, 14, 15, 18, 29, 31, and 71.

Chen, B., Gao, L., Funakoshi, K.-i., and Li, J. 2007. Thermal expansion of iron-rich alloys and implications for the Earth's core. *Proceedings of the National Academy of Sciences*. **104**(22), pp. 9162–9167. Cited on p. 30.

Cheng, A. and Brebbia, C. A. 2015. *Boundary Elements and Other Mesh Reduction Methods XXXVIII*. Wit Press. Cited on p. 35.

Cheng, J., Stellmach, S., Ribeiro, A., Grannan, A., King, E., and Aurnou, J. 2015. Laboratory-numerical models of rapidly rotating convection in planetary cores. *Geophysical Journal International*. **201**(1), pp. 1–17. Cited on pp. 11, 15, 16, 17, 18, 22, 49, 56, 64, 77, 83, 84, 93, 109, 111, 116, and 122.

Cheng, J. S., Aurnou, J. M., Julien, K., and Kunnen, R. P. 2018. A heuristic framework for next-generation models of geostrophic convective turbulence. *Geophysical & Astrophysical Fluid Dynamics*. **112**(4), pp. 277–300. Cited on pp. 19, 64, and 96.

Cheng, J. S., Madonia, M., Guzmán, A. J. A., and Kunnen, R. P. 2019. Laboratory exploration of heat transfer regimes in rapidly rotating turbulent convection. *arXiv preprint arXiv:1911.04537*. Cited on pp. 18 and 96.

Chillá, F., Ciliberto, S., Innocenti, C., and Pampaloni, E. 1993. Boundary layer and scaling properties in turbulent thermal convection. *Il Nuovo Cimento D*. **15**(9), pp. 1229–1249. Cited on p. 10.

Christensen, U. and Aubert, J. 2006. Scaling properties of convection-driven dynamos in rotating spherical shells and application to planetary magnetic fields. *Geophysical Journal International*. **166**, pp. 97–114. Cited on pp. 45, 84, and 121.

Christensen, U., Aubert, J., Cardin, P., Dormy, E., Gibbons, S., Glatzmaier, G., Grote, E., Honkura, Y., Jones, C., Kono, M., et al. 2001. A numerical dynamo benchmark. *Physics of the Earth and Planetary Interiors*. **128**(1-4), pp. 25–34. Cited on p. 42.

Christensen, U. R. 2002. Zonal flow driven by strongly supercritical convection in rotating spherical shells. *Journal of Fluid Mechanics*. **470**, pp. 115–133. Cited on p. 22.

Christensen, U. R. and Wicht, J. 2015. Numerical dynamo simulations. *Treatise on Geophysics (Second Edition)*. **8**, pp. 245–277. Cited on pp. 95, 96, and 125.

Christensen, U. R., Aubert, J., and Hulot, G. 2010. Conditions for Earth-like geodynamo models. *Earth and Planetary Science Letters*. **296**(3-4), pp. 487–496. Cited on p. 7.

Clarke, A., Davies, C., Ruprecht, D., Tobias, S., and Oishi, J. S. 2020. Performance of parallel-in-time integration for Rayleigh–Bénard Convection. *arXiv preprint arXiv:2001.01609*. Cited on p. 55.

Cordero, S. and Busse, F. 1992. Experiments on convection in rotating hemispherical shells: Transition to a quasi-periodic state. *Geophysical Research Letters*. **19**(8), pp. 733–736. Cited on p. 19.

Courant, R. 1928. On the partial difference equations of mathematical physics. *Mathematische Annalen*. **100**, pp. 32–74. Cited on p. 38.

Couston, L.-A., Lecoanet, D., Favier, B., and Le Bars, M. 2018. The energy flux spectrum of internal waves generated by turbulent convection. *Journal of Fluid Mechanics*. **854**. Cited on p. 35.

Currie, L. K. and Tobias, S. M. 2019. Convection-driven kinematic dynamos with a self-consistent shear flow. *Geophysical & Astrophysical Fluid Dynamics*. **113**(1-2), pp. 131–148. Cited on p. 35.

Davies, C., Silva, L., and Mound, J. 2013. On the influence of a translating inner core in models of outer core convection. *Physics of the Earth and Planetary Interiors*. **214**, pp. 104–114. Cited on p. 42.

Davies, C. J., Gubbins, D., and Jimack, P. K. 2011. Scalability of pseudospectral methods for geodynamo simulations. *Concurrency and Computation: Practice and Experience*. **23**(1), pp. 38–56. Cited on p. 42.

de Wijs, G. A., Kresse, G., Vočadlo, L., Dobson, D., Alfe, D., Gillan, M. J., and Price, G. D. 1998. The viscosity of liquid iron at the physical conditions of the Earth's core. *Nature*. **392**(6678), pp. 805. Cited on p. 2.

Demir, H., Dalkilic, A., Kürekci, N., Duangthongsuk, W., and Wongwises, S. 2011. Numerical investigation on the single phase forced convection heat transfer characteristics of TiO_2 nanofluids in a double-tube counter flow heat exchanger. *International Communications in Heat and Mass Transfer*. **38**(2), pp. 218–228. Cited on p. 106.

Drain, L. E. 1980. *The laser Doppler techniques*. Wiley-Interscience. Cited on p. 106.

Du Puits, R., Resagk, C., Tilgner, A., Busse, F., and Thess, A. 2007. Structure of thermal boundary layers in turbulent Rayleigh–Bénard convection. *Journal of Fluid Mechanics*. **572**, pp. 231–254. Cited on p. 49.

Dziewonski, A. M. and Anderson, D. L. 1981. Preliminary reference Earth model. *Physics of the Earth and Planetary Interiors*. **25**(4), pp. 297–356. Cited on pp. 2 and 3.

Frigo, M. and Johnson, S. G. 2005. The design and implementation of FFTW3. *Proceedings of the IEEE*. **93**(2), pp. 216–231. Cited on p. 36.

Funfschilling, D., Brown, E., Nikolaenko, A., and Ahlers, G. 2005. Heat transport by turbulent Rayleigh–Bénard convection in cylindrical samples with aspect ratio one and larger. *Journal of Fluid Mechanics*. **536**, pp. 145–154. Cited on pp. 11, 47, and 96.

Gastine, T. and Wicht, J. 2012. Effects of compressibility on driving zonal flow in gas giants. *Icarus*. **219**(1), pp. 428–442. Cited on p. 22.

Gastine, T., Wicht, J., and Aurnou, J. M. Sept. 2015. Turbulent Rayleigh–Bénard convection in spherical shells. *Journal of Fluid Mechanics*. **778**, pp. 721–764. Cited on pp. 23, 65, 66, 67, 69, and 85.

Gastine, T., Wicht, J., and Aubert, J. 2016. Scaling regimes in spherical shell rotating convection. *Journal of Fluid Mechanics*. **808**, pp. 690–732. Cited on pp. 21, 22, 23, 50, 65, 66, 67, 69, 73, 74, 75, 79, 83, 84, 86, 88, 90, 91, 93, 96, 100, 108, 115, 117, and 120.

Gauss, C. F. Allgemeine Theorie des Erdmagnetismus. In *Werke*, pp. 119–193. Springer, 1877. Cited on p. 1.

Gibbons, S., Gubbins, D., and Zhang, K. 2007. Convection in rotating spherical fluid shells with inhomogeneous heat flux at the outer boundary. *Geophysical and Astrophysical Fluid Dynamics*. **101**(5-6), pp. 347–370. Cited on pp. 20 and 67.

Gillet, N. and Jones, C. 2006. The quasi-geostrophic model for rapidly rotating spherical convection outside the tangent cylinder. *Journal of Fluid Mechanics*. **554**, pp. 343–369. Cited on pp. 21, 23, 65, 72, and 81.

Gilman, P. A. 1977. Nonlinear dynamics of Boussinesq convection in a deep rotating spherical shell-I. *Geophysical & Astrophysical Fluid Dynamics*. **8**(1), pp. 93–135. Cited on pp. 18, 20, 22, 64, and 73.

Glatzmaier, G. and Coe, R. 2007. *Magnetic polarity reversals in the core*, volume 8. Gerald Schubert. Treatise on Geophysics. Cited on p. 1.

Glatzmaier, G. A. 2013. *Introduction to modeling convection in planets and stars: Magnetic field, density stratification, rotation*. Princeton University Press. Cited on p. 36.

Glatzmaier, G. A. and Roberts, P. H. 1995. A three-dimensional convective dynamo solution with rotating and finitely conducting inner core and mantle. *Physics of the Earth and Planetary Interiors*. **91**(1-3), pp. 63–75. Cited on pp. 7 and 125.

Glazier, J. A., Segawa, T., Naert, A., and Sano, M. 1999. Evidence against 'ultrahard' thermal turbulence at very high Rayleigh numbers. *Nature*. **398**(6725), pp. 307. Cited on pp. 10 and 77.

Goluskin, D. 2016. *Internally heated convection and Rayleigh-Bénard convection*. Springer. Cited on pp. 40 and 45.

Gottlieb, D. and Orszag, S. A. 1977. *Numerical analysis of spectral methods: theory and applications*, volume 26. SIAM. Cited on p. 35.

Greenspan, H. P. G. 1968. *The theory of rotating fluids*. CUP Archive. Cited on pp. 14, 16, 21, 34, 50, 65, and 83.

Grooms, I. and Whitehead, J. P. 2014. Bounds on heat transport in rapidly rotating Rayleigh–Bénard convection. *Nonlinearity*. **28**(1), pp. 29. Cited on pp. 15 and 84.

Grossmann, S. and Lohse, D. 2000. Scaling in thermal convection: a unifying theory. *Journal of Fluid Mechanics*. **407**, pp. 27–56. Cited on pp. 12, 14, 47, 66, 72, 75, 77, 110, 114, and 119.

Grossmann, S. and Lohse, D. 2001. Thermal convection for large Prandtl numbers. *Physical Review Letters*. **86**(15), pp. 3316. Cited on p. 110.

Grossmann, S. and Lohse, D. 2002. Prandtl and Rayleigh number dependence of the Reynolds number in turbulent thermal convection. *Physical Review E*. **66**(1), pp. 016305. Cited on pp. 12, 13, and 47.

Grossmann, S. and Lohse, D. 2011. Multiple scaling in the ultimate regime of thermal convection. *Physics of fluids*. **23**(4), pp. 045108. Cited on pp. 12 and 47.

Grötzbach, G. 1983. Spatial resolution requirements for direct numerical simulation of the Rayleigh-Bénard convection. *Journal of Computational Physics*. **49**(2), pp. 241–264. Cited on p. 38.

Gubbins, D. 2001. The Rayleigh number for convection in the Earth's core. *Physics of the Earth and Planetary Interiors*. **128**(1-4), pp. 3–12. Cited on pp. 3 and 121.

Gubbins, D. and Kelly, P. 1993. Persistent patterns in the geomagnetic field over the past 2.5 myr. *Nature*. **365**(6449), pp. 829–832. Cited on p. 124.

Gubbins, D. and Roberts, P. 1987. Magnetohydrodynamics of the Earth's core. *Geomatik*. **2**, pp. 1–183. Cited on pp. 2 and 42.

Guervilly, C., Cardin, P., and Schaeffer, N. 2019. Turbulent convective length scale in planetary cores. *Nature*. **570**(7761), pp. 368. Cited on p. 85.

Hansen, U., Yuen, D. A., and Malevsky, A. V. 1992. Comparison of steady-state and strongly chaotic thermal convection at high rayleigh number. *Physical Review A*. **46** (8), pp. 4742. Cited on p. 60.

Hawkins, E. K., Cheng, J. S., Pilegard, T., Stellmach, S., Julien, K., and Aurnou, J. M. 2020. Observing geostrophic turbulence in laboratory models of planetary core convection. *Submitted to Geophysical Journal International*. Cited on pp. 9, 12, 13, 60, 99, 106, 109, 110, 115, 116, 117, 120, and 122.

Heimpel, M., Aurnou, J., and Wicht, J. 2005. Simulation of equatorial and high-latitude jets on Jupiter in a deep convection model. *Nature*. **438**(7065), pp. 193. Cited on p. 47.

Hide, R. 1969. Interaction between the Earth's liquid core and solid mantle. *Nature*. **222** (5198), pp. 1055–1056. Cited on p. 125.

Hide, R., Boggs, D., Dickey, J., Dong, D., Gross, R., and Jackson, A. 1996. Topographic core-mantle coupling and polar motion on decadal time-scales. *Geophysical Journal International*. **125**(2), pp. 599–607. Cited on p. 125.

Hollerbach, R. 1996. On the theory of the geodynamo. *Physics of the Earth and Planetary interiors*. **98**(3-4), pp. 163–185. Cited on p. 4.

Holme, R. and Olson, P. 2007. Large-scale flow in the core. *Treatise on geophysics*. **8**, pp. 107–130. Cited on pp. 4, 7, and 63.

Hori, K., Teed, R., and Jones, C. 2018. The dynamics of magnetic Rossby waves in spherical dynamo simulations: A signature of strong-field dynamos? *Physics of the Earth and Planetary Interiors*. **276**, pp. 68–85. Cited on p. 42.

Horn, S. and Shishkina, O. 2014. Rotating non-Oberbeck–Boussinesq Rayleigh–Bénard convection in water. *Physics of Fluids*. **26**(5), pp. 055111. Cited on p. 96.

Hu, Y., He, Y., Wang, S., Wang, Q., and Inaki Schlaberg, H. 2014. Experimental and numerical investigation on natural convection heat transfer of TiO_2–water nanofluids in a square enclosure. *Journal of Heat Transfer*. **136**(2). Cited on p. 106.

Hulot, G., Le Huy, M., and Le Mouël, J.-L. 1996. Influence of core flows on the decade variations of the polar motion. *Geophysical & Astrophysical Fluid Dynamics*. **82**(1-2), pp. 35–67. Cited on p. 125.

Hurle, D., Jakeman, E., and Pike, E. R. 1967. On the solution of the Bénard problem with boundaries of finite conductivity. *Proceedings of the Royal Society of London. Series A. Mathematical and Physical Sciences*. **296**(1447), pp. 469–475. Cited on p. 49.

Iyer, K. P., Scheel, J. D., Schumacher, J., and Sreenivasan, K. R. 2020. Classical 1/3 scaling of convection holds up to $Ra = 10^{15}$. *Proceedings of the National Academy of Sciences*. Cited on pp. 11 and 12.

Jacobs, J. 1953. The Earth's inner core. *Nature*. **172**(4372), pp. 297–298. Cited on p. 1.

Jeffreys, H. 1926. The rigidity of the Earth's central core. *Geophysical Supplements to the Monthly Notices of the Royal Astronomical Society*. **1**(7), pp. 371–383. Cited on p. 1.

Johnston, H. and Doering, C. R. 2009. Comparison of turbulent thermal convection between conditions of constant temperature and constant flux. *Physical Review Letters*. **102**(6), pp. 064501. Cited on pp. 12, 34, 49, 55, and 109.

Jones, C. and Schubert, G. 2007. Thermal and compositional convection in the outer core. *Treatise in Geophysics, Core Dynamics*. **8**, pp. 131–185. Cited on p. 22.

Jones, C., Boronski, P., Brun, A., Glatzmaier, G., Gastine, T., Miesch, M., and Wicht, J. 2011. Anelastic convection-driven dynamo benchmarks. *Icarus*. **216**(1), pp. 120–135. Cited on p. 42.

Jones, C. A. 2011. Planetary magnetic fields and fluid dynamos. *Annual Review of Fluid Mechanics*. **43**, pp. 583–614. Cited on p. 50.

Jones, C. A. Thermal and compositional convection in the outer core. In Schubert, G., editor, *Treatise on Geophysics*, volume 8, pp. 115–159. Elsevier, 2 edition, 2015. Cited on pp. 4, 21, 57, 63, 66, 72, 83, 122, and 123.

Jones, C. A., Soward, A. M., and Mussa, A. I. 2000. The onset of thermal convection in a rapidly rotating sphere. *Journal of Fluid Mechanics*. **405**, pp. 157–179. Cited on pp. 20 and 121.

Julien, K., Legg, S., McWilliams, J., and Werne, J. 1996. Rapidly rotating turbulent Rayleigh-Bénard convection. *Journal of Fluid Mechanics*. **322**, pp. 243–273. Cited on pp. 50, 69, and 96.

Julien, K., Knobloch, E., Rubio, A. M., and Vasil, G. M. 2012a. Heat transport in low-Rossby-number Rayleigh-Bénard convection. *Physical Review Letters*. **109**(25), pp. 254503. Cited on pp. 15, 23, 47, 57, 64, 66, 73, and 79.

Julien, K., Rubio, A., Grooms, I., and Knobloch, E. 2012b. Statistical and physical balances in low Rossby number Rayleigh–Bénard convection. *Geophysical & Astrophysical Fluid Dynamics*. **106**(4-5), pp. 392–428. Cited on pp. 19, 48, 51, 57, 58, 64, 71, 74, 88, 91, 99, 116, and 119.

Kerr, R. M. and Herring, J. R. 2000. Prandtl number dependence of Nusselt number in direct numerical simulations. *Journal of Fluid Mechanics*. **419**, pp. 325–344. Cited on p. 69.

King, E., Stellmach, S., and Aurnou, J. 2012. Heat transfer by rapidly rotating Rayleigh–Bénard convection. *Journal of Fluid Mechanics*. **691**, pp. 568–582. Cited on pp. 9, 11, 17, 19, 22, 39, 49, 64, 73, and 83.

King, E., Stellmach, S., and Buffett, B. 2013. Scaling behaviour in Rayleigh–Bénard convection with and without rotation. *Journal of Fluid Mechanics*. **717**, pp. 449–471. Cited on pp. 12, 13, 17, 18, 39, 40, 49, 50, 52, 57, 64, 65, 71, 73, 75, 99, 108, and 120.

King, E. M. 2009. An investigation of planetary convection: The role of boundary layers. *PhD Thesis*. Cited on pp. 101, 103, and 104.

King, E. M. and Buffett, B. A. 2013. Flow speeds and length scales in geodynamo models: the role of viscosity. *Earth and Planetary Science Letters*. **371**, pp. 156–162. Cited on pp. 6, 68, 70, 84, 90, and 122.

King, E. M., Stellmach, S., Noir, J., Hansen, U., and Aurnou, J. M. 2009. Boundary layer control of rotating convection systems. *Nature*. **457**(7227), pp. 301. Cited on pp. 18, 19, 47, 50, 55, 56, 64, 73, 75, 99, 119, and 122.

King, E. M., Soderlund, K. M., Christensen, U. R., Wicht, J., and Aurnou, J. M. 2010. Convective heat transfer in planetary dynamo models. *Geochemistry, Geophysics, Geosystems*. **11**(6). Cited on pp. 69, 73, 88, 89, and 94.

Kooij, G. L., Botchev, M. A., Frederix, E. M., Geurts, B. J., Horn, S., Lohse, D., van der Poel, E. P., Shishkina, O., Stevens, R. J., and Verzicco, R. 2018. Comparison of computational codes for direct numerical simulations of turbulent Rayleigh–Bénard convection. *Computers & Fluids*. **166**, pp. 1–8. Cited on p. 96.

Korte, M. and Constable, C. 2006. Centennial to millennial geomagnetic secular variation. *Geophysical Journal International*. **167**(1), pp. 43–52. Cited on p. 124.

Kraichnan, R. H. 1962. Turbulent thermal convection at arbitrary Prandtl number. *Physics of Fluids*. **5**(11), pp. 1374–1389. Cited on pp. 11 and 13.

Kuang, W. and Bloxham, J. 1993. On the effect of boundary topography on flow in the Earth's core. *Geophysical & Astrophysical Fluid Dynamics*. **72**(1-4), pp. 161–195. Cited on p. 125.

Kundu, P. and Cohen, L. 1990. Fluid mechanics, 638 pp. *Academic, Calif*. Cited on p. 65.

Kunnen, R. P., Ostilla-Mónico, R., van der Poel, E. P., Verzicco, R., and Lohse, D. 2016. Transition to geostrophic convection: the role of the boundary conditions. *Journal of Fluid Mechanics*. **799**, pp. 413–432. Cited on pp. 16, 52, and 64.

Lallemand, S. and Funiciello, F. 2009. *Subduction zone geodynamics*. Springer Science & Business Media. Cited on p. 8.

Lam, S., Shang, X.-D., Zhou, S.-Q., and Xia, K.-Q. 2002. Prandtl number dependence of the viscous boundary layer and the Reynolds numbers in Rayleigh-Bénard convection. *Physical Review E*. **65**(6), pp. 066306. Cited on pp. 9, 65, and 123.

Landau, L. D. and Lifshitz, E. M. 1987. Fluid mechanics. *Fluid Mechanics. Second Edition. 1987. Pergamon, Oxford*. Cited on pp. 31 and 34.

Larmor, J. 1919. How could a rotating body such as the sun become a magnet. *Rep. Brit. Adv. Sci.* pp. 159–160. Cited on p. 1.

Lehmann, I. 1936. P, publ. *Bur. Centr. Seism. Internat. Serie A*. **14**, pp. 87–115. Cited on p. 1.

Lhuillier, F., Hulot, G., Gallet, Y., and Schwaiger, T. 2019. Impact of inner-core size on the dipole field behaviour of numerical dynamo simulations. *Geophysical Journal International*. **218**(1), pp. 179–189. Cited on p. 67.

Lide, D. R. 2004. *CRC handbook of chemistry and physics*, volume 85. CRC press. Cited on pp. 30 and 101.

Lilly, D. 1971. Numerical simulation of developing and decaying two-dimensional turbulence. *Journal of Fluid Mechanics*. **45**(2), pp. 395–415. Cited on p. 7.

Lister, J. R. and Buffett, B. A. 1995. The strength and efficiency of thermal and compositional convection in the geodynamo. *Physics of the Earth and Planetary Interiors*. **91** (1-3), pp. 17–30. Cited on p. 3.

Liu, Y. and Ecke, R. E. 2009. Heat transport measurements in turbulent rotating Rayleigh-Bénard convection. *Physical Review E*. **80**(3), pp. 036314. Cited on p. 18.

Liu, Y. and Ecke, R. E. 2011. Local temperature measurements in turbulent rotating Rayleigh-Bénard convection. *Physical Review E*. **84**(1), pp. 016311. Cited on pp. 49, 51, and 69.

Long, R., Mound, J., Davies, C., and Tobias, S. 2020a. Scaling behaviour in spherical shell rotating convection with fixed-flux thermal boundary conditions. *Journal of Fluid Mechanics*. Cited on p. ii.

Long, R. S., Mound, J. E., Davies, C. J., and Tobias, S. M. 2020b. Thermal boundary layer structure in convection with and without rotation. *Physical Review Fluids*. **5**(11), pp. 113502. Cited on p. ii.

Malkus, W. 1959. Magnetoconvection in a viscous fluid of infinite electrical conductivity. *The Astrophysical Journal*. **130**, pp. 259. Cited on p. 4.

Malkus, W. V. 1954. The heat transport and spectrum of thermal turbulence. *Proceedings of the Royal Society of London. Series A. Mathematical and Physical Sciences*. **225** (1161), pp. 196–212. Cited on pp. 9, 11, and 48.

Manglik, A., Wicht, J., and Christensen, U. R. 2010. A dynamo model with double diffusive convection for Mercury's core. *Earth and Planetary Science Letters*. **289**(3-4), pp. 619–628. Cited on p. 123.

Masters, T. G., Johnson, S., Laske, G., and Bolton, H. 1996. A shear-velocity model of the mantle. *Philosophical Transactions of the Royal Society of London. Series A: Mathematical, Physical and Engineering Sciences*. **354**(1711), pp. 1385–1411. Cited on p. 124.

Mather, J. F. and Simitev, R. D. 2020. Regimes of thermo-compositional convection and related dynamos in rotating spherical shells. *Geophysical & Astrophysical Fluid Dynamics*. pp. 1–24. Cited on p. 123.

Matsui, H., Heien, E., Aubert, J., Aurnou, J. M., Avery, M., Brown, B., Buffett, B. A., Busse, F., Christensen, U. R., Davies, C. J., et al. 2016. Performance benchmarks for a next generation numerical dynamo model. *Geochemistry, Geophysics, Geosystems*. **17** (5), pp. 1586–1607. Cited on pp. 35 and 125.

McDonough, W. F. and Sun, S.-S. 1995. The composition of the Earth. *Chemical geology*. **120**(3-4), pp. 223–253. Cited on p. 2.

McElhinny, M. and McFadden, P. L. 1998. *The magnetic field of the Earth: paleomagnetism, the core, and the deep mantle*, volume 63. Academic Press. Cited on p. 44.

Miesch, M. S. The coupling of solar convection and rotation (invited review). In *Helioseismic Diagnostics of Solar Convection and Activity*, pp. 59–89. Springer, 2000. Cited on p. 47.

Morelli, A. and Dziewonski, A. M. 1987. Topography of the core–mantle boundary and lateral homogeneity of the liquid core. *Nature*. **325**(6106), pp. 678–683. Cited on p. 125.

Mound, J. E. and Davies, C. J. 2017. Heat transfer in rapidly rotating convection with heterogeneous thermal boundary conditions. *Journal of Fluid Mechanics*. **828**, pp. 601–629. Cited on pp. 21, 22, 23, 42, 65, 68, 84, 111, 122, and 124.

Olafsson, P., Sandstrom, R., and Karlsson, Å. 1997. Comparison of experimental, calculated and observed values for electrical and thermal conductivity of aluminium alloys. *Journal of materials science*. **32**(16), pp. 4383–4390. Cited on p. 103.

Olson, P. Thermal interaction of the core and mantle. In *Earth's Core and Lower Mantle*, pp. 13–61. CRC Press, 2003. Cited on pp. 8 and 124.

Olson, P. 2007. *Core Dynamics: Treatise on Geophysics*. Elsevier. Cited on p. 2.

Orszag, S. A. 1971. Numerical simulation of incompressible flows within simple boundaries. i. galerkin (spectral) representations. *Studies in applied mathematics*. **50**(4), pp. 293–327. Cited on p. 44.

Oruba, L. and Dormy, E. 2014. Predictive scaling laws for spherical rotating dynamos. *Geophysical Journal International*. **198**(2), pp. 828–847. Cited on p. 84.

Otero, J., Wittenberg, R. W., Worthing, R. A., and Doering, C. R. 2002. Bounds on Rayleigh–Bénard convection with an imposed heat flux. *Journal of Fluid Mechanics*. **473**, pp. 191–199. Cited on p. 40.

Pais, M. and Jault, D. 2008. Quasi-geostrophic flows responsible for the secular variation of the Earth's magnetic field. *Geophysical Journal International*. **173**(2), pp. 421–443. Cited on p. 6.

Pedlosky, J. 2013. *Geophysical fluid dynamics*. Springer Science & Business Media. Cited on pp. 7, 14, 29, 31, 50, and 72.

Plumley, M. and Julien, K. 2019. Scaling laws in Rayleigh–Benard convection. *Earth and Space Science*. **6**(9), pp. 1580–1592. Cited on p. 64.

Plumley, M., Julien, K., Marti, P., and Stellmach, S. 2016. The effects of Ekman pumping on quasi-geostrophic Rayleigh–Bénard convection. *Journal of Fluid Mechanics*. **803**, pp. 51–71. Cited on pp. 16, 21, 64, and 83.

Plumley, M., Julien, K., Marti, P., and Stellmach, S. 2017. Sensitivity of rapidly rotating Rayleigh-Bénard convection to Ekman pumping. *Physical Review Fluids*. **2**(9), pp. 094801. Cited on pp. 21 and 83.

Pozzo, M., Davies, C., Gubbins, D., and Alfè, D. 2013. Transport properties for liquid silicon-oxygen-iron mixtures at Earth's core conditions. *Physical Review B*. **87**(1), pp. 014110. Cited on p. 2.

Prandtl, L. 1905. Verhandlungen des III. Internationalen Mathematiker Kongresses. pp. 485–491. Cited on pp. 12 and 34.

Proudman, J. 1916. On the motion of solids in a liquid possessing vorticity. *Proceedings of the Royal Society of London. Series A, Containing Papers of a Mathematical and Physical Character*. **92**(642), pp. 408–424. Cited on p. 6.

Qiu, X.-L. and Tong, P. 2001a. Large-scale velocity structures in turbulent thermal convection. *Physical Review E*. **64**(3), pp. 036304. Cited on pp. 96 and 99.

Qiu, X.-L. and Tong, P. 2001b. Onset of coherent oscillations in turbulent Rayleigh-Bénard convection. *Physical Review Letters*. **87**(9), pp. 094501. Cited on pp. 12, 13, 96, 99, and 110.

Qiu, X.-L. and Xia, K.-Q. 1998a. Spatial structure of the viscous boundary layer in turbulent convection. *Physical Review E.* **58**(5), pp. 5816. Cited on p. 65.

Qiu, X.-L. and Xia, K.-Q. 1998b. Viscous boundary layers at the sidewall of a convection cell. *Physical Review E.* **58**(1), pp. 486. Cited on p. 65.

Quarteroni, A., Canuto, C., Hussaini, M., and Zang, T. 2006. Spectral methods: Fundamentals in single domains. *Springer Verlag.* **4**(8), pp. 16. Cited on p. 36.

Rayleigh, L. 1916. On convection currents in a horizontal layer of fluid, when the higher temperature is on the under side. *The London, Edinburgh, and Dublin Philosophical Magazine and Journal of Science.* **32**(192), pp. 529–546. Cited on p. 8.

Read, P. L. 2001. Transition to geostrophic turbulence in the laboratory, and as a paradigm in atmospheres and oceans. *Surveys in Geophysics.* **22**(3), pp. 265–317. Cited on p. 7.

Rhines, P. B. 1975. Waves and turbulence on a beta-plane. *Journal of Fluid Mechanics.* **69**(3), pp. 417–443. Cited on pp. 66 and 71.

Roberts, P. H. 1968. On the thermal instability of a rotating-fluid sphere containing heat sources. *Philosophical Transactions of the Royal Society of London. Series A, Mathematical and Physical Sciences.* **263**(1136), pp. 93–117. Cited on p. 20.

Rossby, H. 1969. A study of Bénard convection with and without rotation. *Journal of Fluid Mechanics.* **36**(2), pp. 309–335. Cited on pp. 8, 10, 11, 17, 47, 96, and 98.

Sakuraba, A. and Roberts, P. H. 2009. Generation of a strong magnetic field using uniform heat flux at the surface of the core. *Nature Geoscience.* **2**(11), pp. 802–805. Cited on p. 67.

Schaeffer, N., Jault, D., Nataf, H.-C., and Fournier, A. 2017. Turbulent geodynamo simulations: a leap towards Earth's core. *Geophysical Journal International.* **211**(1), pp. 1–29. Cited on pp. 6, 7, 117, and 126.

Schmalzl, J., Breuer, M., and Hansen, U. 2002. The influence of the Prandtl number on the style of vigorous thermal convection. *Geophysical & Astrophysical Fluid Dynamics.* **96**(5), pp. 381–403. Cited on p. 60.

Schmalzl, J., Breuer, M., and Hansen, U. 2004. On the validity of two-dimensional numerical approaches to time-dependent thermal convection. *EPL (Europhysics Letters).* **67**(3), pp. 390. Cited on pp. 52, 53, 56, and 60.

Schmitz, S. and Tilgner, A. 2009. Heat transport in rotating convection without Ekman layers. *Physical Review E.* **80**(1), pp. 015305. Cited on p. 50.

Schmitz, S. and Tilgner, A. 2010. Transitions in turbulent rotating Rayleigh-Bénard convection. *Geophysical and Astrophysical Fluid Dynamics.* **104**(5-6), pp. 481–489. Cited on pp. 10, 19, 64, and 73.

Schubert, G., Turcotte, D. L., and Olson, P. 2001. *Mantle convection in the Earth and planets*. Cambridge University Press. Cited on p. 7.

Schwaiger, T., Gastine, T., and Aubert, J. 2019. Force balance in numerical geodynamo simulations: a systematic study. *Geophysical Journal International*. **219**, pp. S101–S114. Cited on pp. 4, 7, 95, and 126.

Sheyko, A., Finlay, C., Favre, J., and Jackson, A. 2018. Scale separated low viscosity dynamos and dissipation within the Earth's core. *Scientific reports*. **8**(1), pp. 1–7. Cited on pp. 7 and 95.

Shimizu, H., Poirier, J., and Le Mouël, J. 2005. On crystallization at the inner core boundary. *Physics of the Earth and Planetary Interiors*. **151**(1-2), pp. 37–51. Cited on p. 1.

Shishkina, O., Stevens, R. J., Grossmann, S., and Lohse, D. 2010. Boundary layer structure in turbulent thermal convection and its consequences for the required numerical resolution. *New journal of Physics*. **12**(7), pp. 075022. Cited on p. 13.

Shishkina, O., Horn, S., Wagner, S., and Ching, E. S. 2015. Thermal boundary layer equation for turbulent Rayleigh–Bénard convection. *Physical Review Letters*. **114**(11), pp. 114302. Cited on p. 13.

Simitev, R. and Busse, F. 2005. Prandtl-number dependence of convection-driven dynamos in rotating spherical fluid shells. *Journal of Fluid Mechanics*. **532**, pp. 365–388. Cited on p. 124.

Snedecor, G. W. and Cochran, W. G. 1989. Statistical methods, 8^{th} Edn. *Ames: Iowa State Univ. Press Iowa*. **54**, pp. 71–82. Cited on p. 46.

Soderlund, K. M., King, E. M., and Aurnou, J. M. 2012. The influence of magnetic fields in planetary dynamo models. *Earth and Planetary Science Letters*. **333**, pp. 9–20. Cited on pp. 5, 6, 7, and 95.

Soderlund, K. M., Sheyko, A., King, E. M., and Aurnou, J. M. 2015. The competition between Lorentz and Coriolis forces in planetary dynamos. *Progress in Earth and Planetary Science*. **2**(1), pp. 24. Cited on pp. 6 and 7.

Spiegel, E. A. 1971. Convection in stars I. Basic Boussinesq convection. *Annual review of Astronomy and Astrophysics*. **9**(1), pp. 323–352. Cited on pp. 48 and 73.

Spiegel, E. A. and Veronis, G. 1960. On the Boussinesq approximation for a compressible fluid. *The Astrophysical Journal*. **131**, pp. 442. Cited on pp. 29 and 30.

Sprague, M., Julien, K., Knobloch, E., and Werne, J. 2006. Numerical simulation of an asymptotically reduced system for rotationally constrained convection. *Journal of Fluid Mechanics*. **551**, pp. 141–174. Cited on p. 18.

Sprain, C. J., Biggin, A. J., Davies, C. J., Bono, R. K., and Meduri, D. G. 2019. An assessment of long duration geodynamo simulations using new paleomagnetic modeling criteria (QPM). *Earth and Planetary Science Letters*. **526**, pp. 115758. Cited on p. 125.

Stacey, F. D. and Davis, P. M. 2008. *Physics of the Earth*. Cambridge University Press, 4 edition. Cited on p. 1.

Starchenko, S. and Jones, C. 2002. Typical velocities and magnetic field strengths in planetary interiors. *Icarus*. **157**(2), pp. 426–435. Cited on p. 125.

Steinhart, J. S. and Hart, S. R. Calibration curves for thermistors. In *Deep Sea Research and Oceanographic Abstracts*, volume 15, pp. 497–503. Elsevier, 1968. Cited on p. 101.

Stellmach, S. and Hansen, U. 2004. Cartesian convection driven dynamos at low Ekman number. *Physical Review E*. **70**(5), pp. 056312. Cited on p. 96.

Stellmach, S. and Hansen, U. 2008. An efficient spectral method for the simulation of dynamos in cartesian geometry and its implementation on massively parallel computers. *Geochemistry, Geophysics, Geosystems*. **9**(5). Cited on p. 96.

Stellmach, S., Lischper, M., Julien, K., Vasil, G., Cheng, J., Ribeiro, A., King, E., and Aurnou, J. 2014. Approaching the asymptotic regime of rapidly rotating convection: boundary layers versus interior dynamics. *Physical Review Letters*. **113**(25), pp. 254501. Cited on pp. 16, 19, 21, 47, 57, 64, 83, 88, and 98.

Stevens, R. J., Verzicco, R., and Lohse, D. 2010. Radial boundary layer structure and Nusselt number in Rayleigh–Bénard convection. *Journal of Fluid Mechanics*. **643**, pp. 495–507. Cited on pp. 38, 41, and 72.

Stevens, R. J., Zhou, Q., Grossmann, S., Verzicco, R., Xia, K.-Q., and Lohse, D. 2012. Thermal boundary layer profiles in turbulent Rayleigh-Bénard convection in a cylindrical sample. *Physical Review E*. **85**(2), pp. 027301. Cited on p. 13.

Sumita, I. and Olson, P. 2003. Experiments on highly supercritical thermal convection in a rapidly rotating hemispherical shell. *Journal of Fluid Mechanics*. **492**, pp. 271–287. Cited on pp. 19 and 100.

Sze, E. K. and van der Hilst, R. D. 2003. Core mantle boundary topography from short period pcp, pkp, and pkkp data. *Physics of the Earth and Planetary Interiors*. **135**(1), pp. 27–46. Cited on p. 125.

Takahashi, F. 2014. Double diffusive convection in the earth's core and the morphology of the geomagnetic field. *Physics of the Earth and Planetary Interiors*. **226**, pp. 83–87. Cited on p. 123.

Takehiro, S. I., Ishiwatari, M., Nakajima, K., and Hayashi, Y. Y. 1999. Effects of thermal boundary condition on convection in rapidly rotating spherical shells. *Theoretical and Applied Mechanics*. **48**, pp. 415–421. Cited on p. 20.

Tanaka, S. 2010. Constraints on the core-mantle boundary topography from p4kp-pcp differential travel times. *Journal of Geophysical Research: Solid Earth*. **115**(B4). Cited on p. 125.

Tarduno, J. A., Cottrell, R. D., Watkeys, M. K., Hofmann, A., Doubrovine, P. V., Mamajek, E. E., Liu, D., Sibeck, D. G., Neukirch, L. P., and Usui, Y. 2010. Geodynamo, solar wind, and magnetopause 3.4 to 3.45 billion years ago. *science*. **327**(5970), pp. 1238–1240. Cited on p. 1.

Tarduno, J. A., Cottrell, R. D., Davis, W. J., Nimmo, F., and Bono, R. K. 2015. A hadean to paleoarchean geodynamo recorded by single zircon crystals. *Science*. **349**(6247), pp. 521–524. Cited on p. 1.

Taylor, G. I. 1917. Motion of solids in fluids when the flow is not irrotational. *Proceedings of the Royal Society of London. Series A, Containing Papers of a Mathematical and Physical Character*. **93**(648), pp. 99–113. Cited on p. 6.

Tilgner, A. 1996. High-Rayleigh-number convection in spherical shells. *Physical Review E*. **53**(5), pp. 4847. Cited on p. 51.

Tilgner, A. and Busse, F. 1997. Finite-amplitude convection in rotating spherical fluid shells. *Journal of Fluid Mechanics*. **332**, pp. 359–376. Cited on p. 20.

Tilgner, A., Belmonte, A., and Libchaber, A. 1993. Temperature and velocity profiles of turbulent convection in water. *Physical Review E*. **47**(4), pp. R2253. Cited on pp. 49 and 51.

Tobias, S. 2019. The turbulent dynamo. *arXiv preprint arXiv:1907.03685*. Cited on p. 4.

Tobias, S., Oishi, J., and Marston, J. 2018. Generalized quasilinear approximation of the interaction of convection and mean flows in a thermal annulus. *Proceedings of the Royal Society A*. **474**(2219), pp. 20180422. Cited on p. 35.

Umemoto, K. and Hirose, K. 2020. Chemical compositions of the outer core examined by first principles calculations. *Earth and Planetary Science Letters*. **531**, pp. 116009. Cited on p. 2.

Vallis, G. K., Parker, D. J., and Tobias, S. M. 2019. A simple system for moist convection: the Rainy–Bénard model. *Journal of Fluid Mechanics*. **862**, pp. 162–199. Cited on p. 35.

Venugopal, V., De, A. K., and Mishra, P. K. 2020. Significance of Prandtl Number on the Heat Transport and Flow Structure in Rotating Rayleigh–Bénard Convection. *Journal of Heat Transfer*. **142**(1). Cited on p. 123.

Verzicco, R. and Camussi, R. 1999. Prandtl number effects in convective turbulence. *Journal of Fluid Mechanics*. **383**, pp. 55–73. Cited on pp. 12, 13, 49, and 51.

Verzicco, R. and Sreenivasan, K. 2008. A comparison of turbulent thermal convection between conditions of constant temperature and constant heat flux. *Journal of Fluid Mechanics*. **595**, pp. 203–219. Cited on pp. 49, 50, and 59.

Von Hardenberg, J., Parodi, A., Passoni, G., Provenzale, A., and Spiegel, E. 2008. Large-scale patterns in Rayleigh–Bénard convection. *Physics Letters A*. **372**(13), pp. 2223–2229. Cited on p. 49.

Wicht, J. and Christensen, U. R. 2010. Torsional oscillations in dynamo simulations. *Geophysical Journal International*. **181**(3), pp. 1367–1380. Cited on pp. 7 and 68.

Wicht, J. and Sanchez, S. 2019. Advances in geodynamo modelling. *Geophysical & Astrophysical Fluid Dynamics*. **113**(1-2), pp. 2–50. Cited on pp. 95 and 122.

Willis, A. P., Sreenivasan, B., and Gubbins, D. 2007. Thermal core–mantle interaction: exploring regimes for 'locked' dynamo action. *Physics of the Earth and Planetary Interiors*. **165**(1-2), pp. 83–92. Cited on pp. 42 and 124.

Wu, C.-C. and Roberts, P. H. 2013. On a dynamo driven topographically by longitudinal libration. *Geophysical & Astrophysical Fluid Dynamics*. **107**(1-2), pp. 20–44. Cited on p. 4.

Xin, Y. and Xia, K. 1997. Boundary layer length scales in convective turbulence. *Physical Review E*. **56**(3), pp. 3010. Cited on p. 49.

Xiong, Z., Tsuchiya, T., and Taniuchi, T. 2018. Ab initio prediction of potassium partitioning into Earth's core. *Journal of Geophysical Research: Solid Earth*. **123**(8), pp. 6451–6458. Cited on p. 31.

Yadav, R. K., Gastine, T., Christensen, U. R., Duarte, L. D. V., and Reiners, A. 2015. Effect of shear and magnetic field on the heat-transfer efficiency of convection in rotating spherical shells. *Geophysical Journal International*. **204**(2), pp. 1120–1133. Cited on pp. 21, 22, 65, 83, and 111.

Yadav, R. K., Gastine, T., Christensen, U. R., Wolk, S. J., and Poppenhaeger, K. 2016. Approaching a realistic force balance in geodynamo simulations. *Proceedings of the National Academy of Sciences*. **113**(43), pp. 12065–12070. Cited on p. 7.

Zhang, K. and Liao, X. 2017. *Theory and Modeling of Rotating Fluids: Convection, Inertial Waves and Precession*. Cambridge University Press. Cited on p. 34.

Zhang, K.-K. and Busse, F. 1987. On the onset of convection in rotating spherical shells. *Geophysical & Astrophysical Fluid Dynamics*. **39**(3), pp. 119–147. Cited on p. 20.

Zhou, Q., Stevens, R. J., Sugiyama, K., Grossmann, S., Lohse, D., and Xia, K.-Q. 2010. Prandtl–Blasius temperature and velocity boundary-layer profiles in turbulent Rayleigh–Bénard convection. *Journal of Fluid Mechanics*. **664**, pp. 297–312. Cited on p. 13.

Zürner, T., Schindler, F., Vogt, T., Eckert, S., and Schumacher, J. 2019. Combined measurement of velocity and temperature in liquid metal convection. *Journal of Fluid Mechanics*. **876**, pp. 1108–1128. Cited on p. 12.